THE UNIVERSITY *of* EDINBURGH

The Application of Ultrafast Spectroscopic Techniques to Single-molecule Magnets

Kyle Lewis Barlow

For the Degree of Doctor of Philosophy

The University of Edinburgh

2024

Abstract

The photochemical and photophysical properties of transition metal complexes are rich and varied due to the complex interplay between various electronic, vibrational and spin degrees of freedom. The intricate coupling between these leads to complicated dynamic behaviour from the moment of photoexcitation to the final electronic state or photochemical product. This leads to difficulty in tracking the photophysical processes that occur but it is also the source of many features which makes them suitable for light capture and conversion. In particular, the dynamics occurring at the earliest moments after light absorption can often dictate the final outcome of a light-induced process. In this thesis, a range of femtosecond absorption spectroscopies are used to study the electronic, nuclear and spin dynamics within transition metal complexes with a particular focus on single-molecule magnets. Single-molecule magnets are one of the smallest realisable units of magnetic recording media, and therefore combining these with excitation from femtosecond laser pulses could lead to ultrafast and ultradense data storage.

Manganese(III)-based single-molecule magnets were studied as their magnetic properties are strongly coupled to the complex's nuclear structure. Optical transient absorption was used to track coherent vibrational dynamics in manganese(III) complexes. The vibrational motion could be observed as oscillations in light absorption after photoexcitation as a result of a switch in the Jahn-Teller distortion. Three complexes of the form [Mn(2,2';6',2"-terpyridine)X_3] where X = fluoride, chloride, and azide were studied. Upon photoexcitation of a metal-centred transition, a vibrational wavepacket is formed corresponding to a Jahn-Teller pincer-like motion of the terpyridine ligand. The vibrational dephasing times decrease from 620 to 370 fs as the number of vibrational modes with frequencies below the pincer mode increases, suggesting that low-frequency modes are an effective bath to dissipate excess energy.

Despite the utility of optical transient absorption and its ability to identify normal modes that are activated upon excitation, this technique does not provide the direction or magnitude of the change in nuclear coordinates. Therefore, K-edge X-ray transient absorption spectroscopy was performed to study the single-molecule magnet $[Mn(III)_3O(Et{-}sao)_3(\beta{-}pic)_3(ClO_4)]$, where $saoH_2$ and β-pic are salicylaldoxime and 3-methylpyridine, respectively. K-edge X-ray spectroscopy is particularly use-

ful, as it is an element-specific technique and carries more structural information than optical spectroscopies. These measurements were carried out at the Spring-8 Angstrom Compact Free-Electron Laser (SACLA). Coherent vibrational motion of a Jahn-Teller mode was observed with a frequency of 180 cm^{-1} in agreement with the previous optical studies. The K-edge X-ray spectra were simulated at different geometries along this Jahn-Teller mode. Good agreement between the calculated and experimental spectrum was found for bond length changes of only 0.01 Å. This shows the potential capabilities of X-ray absorption to track nuclear motion in large transition metal complexes, perfect for the emerging area of ultrafast molecular magnetism.

Ruthenium(II) polypyridyl complexes display a variety of light-induced functions, ranging from luminescence to photochemical ligand loss. It is well-known that triplet metal-centred states act to quench emission but promote photochemistry. Despite the importance of triplet metal-centred states in these excited state processes, detecting and following the dynamics that occur within these remains a challenge because of their short lifetimes. If the polypyridyl ligands are replaced with triazolyl ligands, this results in a destabilisation of the luminescent metal-to-ligand charge transfer state, which leads to the metal-centred state being the lowest energy excited state. Using femtosecond optical transient absorption, it is shown that triplet metal-centred states are populated within 100 fs, which launches a vibrational wavepacket. This vibrational coherence arises from a Jahn-Teller normal mode that is activated upon population of one of the e_g^* orbitals, similar to manganese(III) complexes. This coherent vibrational motion provides a clear signature of the triplet metal-centred states. In addition, small modifications to the ligand framework have a significant effect on the observed wavepacket dynamics, which suggests that synthetic control of coherent nuclear dynamics could be achieved.

In addition to tracking nuclear motion in single-molecule magnets, it is important to be able to measure spin dynamics to gain insight into changes in the magnetisation. Recently, a broadband time-resolved magnetic circular dichroism setup was developed within the lab. Magnetic circular dichroism describes the differential absorption of left and right circularly polarised light under the application of a magnetic field. Zinc(II) tetraphenylporphyrin has been studied as its static magnetic circular dichroism spectrum and photoinduced dynamics are well understood. After excitation of the porphyrin B-band, there is a fast decay to the lowest excited singlet state, which shows an excited state magnetic circular dichroism spectrum. This is one of the first examples of a femtosecond magnetic circular dichroism spectrum of a molecule and opens up the possibility of studying femtosecond spin dynamics in a range of different systems.

Lay Summary

Controlling and exploiting the properties of magnetic materials is vital for the operation of many modern technologies. Magnets range from huge superconducting coils that are used in magnetic resonance imaging to capture three-dimensional images of organs inside the human body to tiny neodymium magnets that make our phones vibrate when we receive a call. One particularly widespread use of magnetic materials is digital data storage. The cloud storage that saves our most precious memories - photos, videos, etc. - uses magnets to do so. All magnets have a direction associated with them; a simple bar magnet has a north and a south pole, and if an arrow is drawn between them, that is defined as the direction of the magnetisation. In many materials, the magnetisation will prefer to point along certain directions. This is known as magnetic anisotropy. Imagine that the magnetisation only wants to point up or down. In computers, data is stored and transmitted using logical bits. These bits of information can take the binary states of "0" or "1". If we define the magnetisation pointing downward as "0" and pointing upward as "1", then we can store binary data, given that we are able to control and measure the magnetisation. Indeed, society developed magnetic tape recorders in the 1930s to do just that. Despite decades of continuous improvement, the same principle is used today to write magnetic data in devices. A magnetic field is applied to the material to flip the magnetisation from up ("1") to down ("0") or vice versa. Recent research has shown that this method has a maximum speed. If magnetic data storage is to keep up with the increasing demands of data-intensive technologies, then a new method of writing data is required.

In this thesis, the use of ultrashort laser pulses to control the magnetisation in single-molecule magnets is explored. Ultrashort laser pulses that shine light for only a millionth of a billionth of a second can now be routinely generated. These have been shown to be able to control the magnetic anisotropy and, therefore, magnetisation in some materials, showing unprecedented data-recording speeds. However, there is a lack of research concerning single-molecule magnets, which are around a millionth of a millimetre in size. These have the added advantage of being smaller than the magnetic domains used to write data currently and therefore could also increase data storage density as well as read/write speeds. The results herein dis-

cuss methods for both controlling and measuring properties related to magnetic anisotropy in molecular materials on ultrafast timescales. Using advanced experimental techniques, we can see how the atoms in single-molecule magnets move after they are hit by a laser pulse. This motion is discussed in terms of its relationship with magnetic anisotropy and magnetisation control. The conclusions provide potential pathways for exploiting light-controlled data recording in single-molecule magnets.

Declaration

I declare that this thesis has been composed solely by myself and that it has not been submitted, in whole or in part, in any previous application for a degree. Except where stated otherwise by reference or acknowledgement, the work presented is entirely my own.

Signed: Kyle Lewis Barlow

Acknowledgements

First of all, I would like to express my gratitude to my supervisor, Doctor Olof Johansson, for his support, guidance, and invaluable mentorship over the last four years. Your passion for science was contagious and kept me going even when I thought that the lab equipment had a personal vendetta against me. I'm also indebted to my assistant supervisor, Professor Euan Brechin, who provided a lot of insight into the manganese(III) projects and provided space in his lab for me to stumble my way through some basic synthetic chemistry.

I want to thank all of my collaborators who contributed to the work contained in this thesis. The chapters based on the manganese(III) work would not have been possible without Professor Tom Penfold and Doctor Julien Eng at the University of Newcastle. The ruthenium(II) work wouldn't have even started without Professor Paul Elliot, Doctor Paul Scattergood and Samuel Francis at the University of Huddersfield.

A special thanks to my labmates, both past and present, Ryan, Binoy, Hal, Erica and Tom. Not only did you help solve problems that I'd still be stuck on to this day, but you also created an incredibly enjoyable working environment. I extend my appreciation to all of the project students I've worked with during my time here, Ioan, Iona, Euan and Annie, the results in this thesis would not have been possible without your help. A massive thanks to my officemates and lunchmates, Francis, Tom, Julianna, Johanna and Elliot, who were great to take a break and have a laugh with. I have really appreciated the time I have spent demonstrating and doing outreach and that is in no small part due to the people I did it with. So, thank you to Ben, Jenny, Justinas, Jon, Jasmine, Cecilia, Ailsa, Heather and Becky.

Many other people in the department have helped me along the way. Without Lloyd Mitchell and George Steedman in the workshops who built and repaired stuff in record time, I'd have never been able to achieve what I did. Andrei Gromov was a huge help in the Raman Lab. Thank you to Scott Moonie, who trusted me enough to let me use his spectrometers. I'd also like to mention Robert Smith who trained me how to use machines in the analytical lab.

I would be remiss not to mention the support of many of my friends and family. Peter, Callum, Sam, and Flo have always been there to have a chat or a beer. Pool

and pub quiz nights with everyone were always a nice way to wind down after a day in the lab. I'm extremely grateful to my mum and dad, who have always supported me in whatever I want to do. I will miss our weekly phone calls when I'm walking home, I hope that missing The Chase didn't bother you as much as you said.

There are many other people who have either, directly or indirectly, contributed to this thesis and my last four years in Edinburgh. From everyone with whom I've made a mess with running experiments during outreach projects, to the people I've made a different kind of mess with at after-work pub trips, I want to thank all of you for shaping my PhD experience.

List of Publications

K. Barlow, R. Phelps, J. Eng, T. Katayama, E. Sutcliffe, M. Coletta, E. K. Brechin, T. J. Penfold, J. O. Johansson. 2024. Tracking nuclear motion in single-molecule magnets using femtosecond X-ray K-edge absorption spectroscopy. *Nature Communications* (accepted).

K. Barlow, J. Eng, I. Ivalo, M. Coletta, E. K. Brechin, T. J. Penfold, J. O. Johansson. 2022. Photoinduced Jahn-Teller Switch in Manganese(III) Terpyridine Complexes. *Dalton Trans.*, 51: 10751-10757.

K. Barlow, J. O. Johansson. 2021. Ultrafast Photoinduced Dynamics in Prussian Blue Analogues. *Phys. Chem. Chem. Phys.*, 23: 8118-8131.

List of Acronyms

β-pic 3-methylpyridine

BBO . . . . . β-barium borate

bpy . . . . . 2,2'-bipyridine

btz . . . . . 2,2'-bitriazolyl

CASSCF . . . . . complete active space self-consistent field

CCD . . . . . charge-coupled device

cyclam 1,4,8,11-tetraazacyclotetradecane

DFT . . . . . density functional theory

DMF . . . . . dimethylformamide

EXAFS . . . . . extended X-ray absorption fine structure

FEL . . . . . free electron laser

FFT . . . . . fast Fourier transform

GMR . . . . . giant magnetoresistance

HOMO . . . . . highest occupied molecular orbital

IC . . . . . internal conversion

IR . . . . . infrared

IRF . . . . . instrument response function

ISC . . . . . intersystem crossing

IVR . . . . . intramolecular vibrational redistribution

LC . . . . . ligand-centred

LLCT . . . . . ligand-to-ligand Charge Transfer

LUMO . . . . . lowest unoccupied molecular orbital

MC . . . . . metal-centred

MCD . . . . . magnetic circular dichroism

MLCT . . . . . metal-to-ligand charge transfer

NEVPT2. . . . . n-electron valence perturbation theory 2

NOPA . . . . . non-collinear optical parametric amplifier

OD . . . . . optical density

OTF . . . . . trifluoromethanesulfonate

phen . . . . . phenanthroline

SACLA . . . . . Spring-8 angstrom compact free electron laser

saoH$_2$ . . . . . salicylaldoxime

SASE. . . . . self-amplified stimulated emission

SIM . . . . . single-ion magnet

SMM . . . . . single-molecule magnet

terpy . . . . . 2,2':6'2"-terpyridine

tpen . . . . . tetra-kis(2-pyridylmethyl)ethylenediamine

TRMCD . . . . . time-resolved magnetic circular dichroism

TR-XAS . . . . . time-resolved X-ray absorption spectroscopy

ttz . . . . . tris(1-benzyl-1,2,3-triazol-4-yl)-p-anisolylmethane

UV . . . . . ultraviolet

XAS . . . . . X-ray absorption spectroscopy

XFEL . . . . . X-ray free electron laser

XPM . . . . . cross-phase modulation

ZFS . . . . . zero-field splitting

ZnTPP . . . . . zinc(II) tetraphenylporphyrin

Contents

Chapter 1

Introduction

1.1 Magnetism and Data Storage

Magnets have been vital for countless technological developments over the course of history. The needles inside compasses are magnets and have been used for centuries to allow navigation across the oceans. Even in the modern world, magnets are as important as ever. For example, magnets in electrical generators provide a path to convert mechanical energy to electrical energy, which is the basis for almost all energy production. Large cryogenically-cooled superconducting magnets are used in magnetic resonance imaging to generate 3-dimensional maps of organs inside the human body.

One important application of magnets is data storage. By controlling and measuring the direction of the magnetisation of a material, data can be written and read. The key property for non-volatile storage of digital data is magnetic anisotropy. Anisotropy describes any property that is not the same in every direction. Magnetic anisotropy means that the magnetisation of a material will preferentially point along one or more directions. These directions are known as the anisotropy axes. In the simplest case, uniaxial anisotropy describes a material whose anisotropy is symmetric around a single axis. This property can lead to easy axis anisotropy which means the magnetisation will point either up or down along a single axis. In this situation, the material is said to have bistability due to the two possible orientations of the magnetisation. These two orientations can be used to store binary digital data by defining, for example, up as "1" and down as "0". If the material has slow relaxation of magnetisation, that is, it does not switch between pointing up and down without external stimulus, it is perfect for non-volatile data storage.

A material that exhibits bistability and slow relaxation of magnetisation is an excellent platform to store data. However, the direction of the magnetisation must be able to be controlled and measured in order to make this useful. One of the

first developed methods, which is still used today, utilises a small electromagnet that switches the magnetisation depending on the direction of the applied current. To read the data in modern devices, the giant magnetoresistance (GMR) effect is employed. A material that has GMR is brought close to the the surface of a magnetic bit and, depending on the direction of the magnetic field, the resistance of the material is different and can address the state of the data bit. These methods have been implemented in devices and continually improved upon for a few decades.[1]

In today's information *era*, enhancing data storage technologies is crucial due to the escalating volume of data generated by advancements such as artificial intelligence and automation. Meeting this demand may be difficult as the conventional data writing method has a drawback, a constraint on data writing speed.[2, 3] In 2018, there was around 33 zettabytes of data stored in the world, this is expected to rise to 175 zettabytes by 2025 where 50 % of it will be stored on public cloud servers using magnetic data storage.[4] Consequently, there is a risk that the required read/write rate for storing data may surpass its capacity.

Luckily, methods to optically control and measure magnetisation faster than traditional methods have become available. The development of amplified femtosecond titanium sapphire lasers in the 1980s/early 1990s[5, 6] gifted researchers the ability to influence and study matter on previously unobtainable timescales. It is possible to probe the magnetisation of a material using light by employing magneto-optical techniques. The Faraday effect describes the change in the polarisation state of light due to a magnetic field within a material.[7] Therefore, femtosecond lasers can be used to measure magnetisation dynamics faster than ever before. The first ultrafast magneto-optical study was carried out by Beaurepaire et al.[8] The authors excited a thin nickel film with a 630 nm laser pulse that was 60 fs in duration. Using another laser pulse, the magneto-optical signal was recorded, and it was shown that the nickel film demagnetised within 100 fs. Considering that the fastest switching speed for a single switching event in a device without laser excitation is around 200 ps,[9] optical laser pulses seem to be an attractive prospect to significantly increase the rate at which it is possible to manipulate magnetism. This method only produced a demagnetisation as a consequence of thermal effects and therefore cannot be used to write data. But, it did show that optical methods can change the magnetisation of a material orders of magnitude faster than traditional methods.

In recent decades, numerous new methods of magnetisation control using light have emerged, potentially capable of writing data to magnetic materials.[10–16] Circularly polarised laser pulses can generate magnetic fields in a material via the inverse Faraday effect.[17, 18] The high peak powers of femtosecond laser pulses mean that the induced magnetic field can reach around 1–10 T and last for the duration of the laser pulse. Therefore, similar to the traditional electromagnetic

method, these strong induced magnetic fields could be used to flip the direction of a magnetic field. Indeed, these methods have been used to coherently control spin precession[19]. Helicity-dependent all-optical magnetic switching has also been demonstrated.[20] However, it is worth noting that this process relies on a thermal effect tied to magnetic circular dichroism, leading to substantial heat dissipation into the lattice, rendering it inefficient.[21, 22]

Instead of utilising strong magnetic fields to switch the magnetisation, optical excitation can be used to manipulate the magnetic anisotropy directly.[23–25] Magnetocrystalline anisotropy arises from the interaction of a metal ion with its crystal-field environment. Generally, a crystal field will act to quench orbital angular momentum. However, spin-orbit coupling can recreate the orbital angular momentum destroyed by the crystal field.[26] Spin-orbit coupling aligns the spin angular momentum, and consequently, the spin magnetic moment, along the axis of the unquenched angular momentum. Since the direction of the orbital angular momentum is determined by the crystal-field environment, the magnetocrystalline anisotropy is also governed by this environment. Thus, by employing light to manipulate the crystal field, one can alter the magnetic anisotropy, facilitating rapid reorientation of the magnetisation.

The direction of magnetisation has been controlled on ultrafast timescales by optically exciting crystal-field transitions. [23, 24, 27–32] However, in early studies of this process,[23, 24] the new direction of magnetisation was only stable for as long as the crystal-field relaxation time and could not be used to store data. More recently, with the correct choice of material, non-thermal photomagnetic recording after excitation of a crystal-field transition has been achieved with switching speeds of 20 ps in a cobalt-substituted yttrium iron garnet.[29] This was achieved due to a large photoinduced anisotropy with a short lifetime that,[25] after a quarter of a period of the spin precession, left the magnetisation closer to another ground state anisotropy axis. Strong damping of the precession allowed the magnetisation to relax into its new orientation quickly. Therefore, the magnetic moments could be switched between two ground state anisotropy axes. This is schematically shown in Figure 1.1.1 for the case of easy axis anisotropy along the z-axis and a photoinduced anisotropy in the xy-plane. This is not the case in the discussed study,[29] as it contains four anisotropy axes but the dynamics remain largely the same. This was a landmark study in the field, but it relied on a fortuitous cooperation between strong photoinduced anisotropy, the correct crystal-field relaxation time, anisotropy axes and damping of magnetic precession.[33] Designing materials that have the perfect combination of these parameters is paramount to the development of ultrafast optical control of magnetism.

Almost all existing research concerning ultrafast optical control of magnetisation

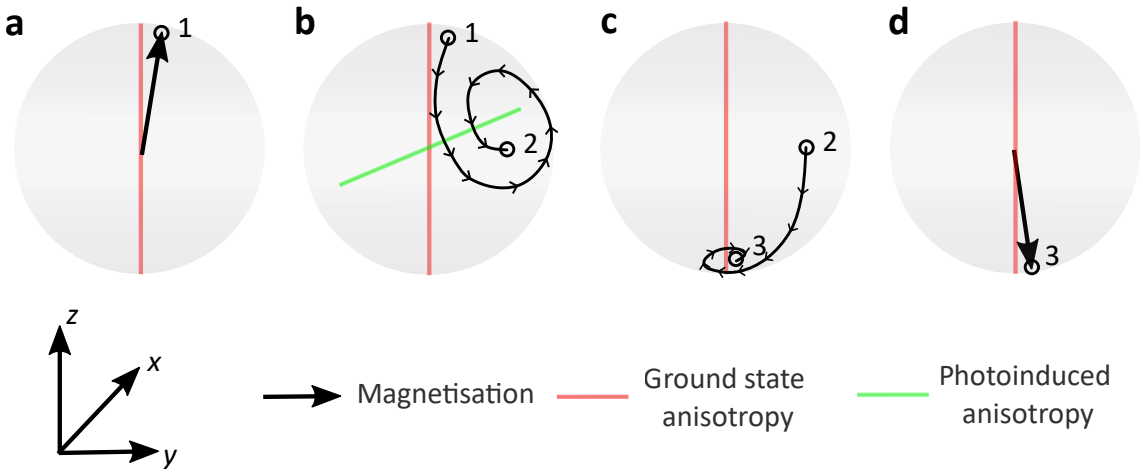

Figure 1.1.1: Schematic of magnetisation switching from photoinduced changes in magnetic anisotropy in a model system. The magnitude of the magnetisation is assumed to be constant so the direction of the magnetisation can be defined by a point on a sphere. **a** Before the interaction with a laser pulse, the magnetisation points along the positive z-direction aligned with the uniaxial magnetic anisotropy corresponding to point 1 on the surface of the sphere. **b** After the interaction with a laser pulse, a new photoinduced anisotropy axis is produced in the xy-plane. Starting from point 1, the magnetisation begins to precess around this new direction for a time dictated by the lifetime of the photoinduced anisotropy. The photoinduced anisotropy turns off, and the magnetisation is in a direction defined by point 2 on the sphere, below the xy-plane. **c** Considering point 2 is closer to the negative z-direction of the ground state anisotropy, it begins to precess around the negative z-direction. **d** The fully relaxed spin after damping arrives at point 3 of the sphere which corresponds to fully switching the magnetisation from the positive z-direction to the negative z-direction.

has investigated traditional condensed matter materials such as metals,[8] semiconductors[34] and dielectrics.[29] However, there is a potential treasure trove of materials for these applications that have been developed by chemists over the past few decades that have yet to be properly utilised. Molecular magnetic materials are compounds that are composed of molecular building blocks and show the same magnetic hysteresis exhibited by traditional magnetic materials.[35–39] Their molecular nature provides a highly tunable platform to study light-induced magnetisation dynamics. If researchers in ultrafast magnetism began exploring the range of synthetic modifications provided by chemists, it could provide even better materials for photomagnetic switching.

A particular class of molecular magnets, single-molecule magnets (SMMs), provide the potential for even more unique properties. SMMs are materials that exhibit slow magnetic relaxation below a certain blocking temperature that is molecular in nature and does not rely on long-range magnetic order.[40–43] In addition to the potential faster switching speeds that are offered via optical control, the ability to store data on a single molecule provides a pathway to massively increasing the data storage density. SMMs therefore represent a huge amount of unexplored territory to expand the capabilities of ultrafast optical control of magnetisation.

The majority of SMMs are transition metal complexes, which consist of one or more metal ion/s bonded to organic ligands. The magnetic anisotropy required for magnetic behaviour arises from the crystal-field environment similar to condensed matter crystals but with the added advantage of easier synthetic tunability.[44] The metal ions and the ligands can be replaced and modified to achieve the desired magnetic anisotropy through known design criteria.[45] External stimulus such as temperature,[46] pressure[47] and magnetic field[48] have already been shown to control the magnetic anisotropy in SMMs. If light can do the same, then there is scope for ultrafast control of magnetisation in single molecules.

This thesis begins to explore the potential of ultrafast photomagnetic switching in SMMs. It begins by discussing the electronic structure of transition metal complexes, of which SMMs are a subset, from the point of view of crystal-field theory and how the electronic structure can be probed spectroscopically. The fundamentals of molecular magnetism are then introduced with particular focus on the relation between the crystal field and magnetic anisotropy. A large section of the thesis is devoted to manganese(III) metal ions and their complexes so these are discussed in detail. The discussion eludes to the possible control of anisotropy using a laser pulse to excite crystal-field transitions to change the Jahn-Teller distortion. Concepts that relate to the ultrafast dynamics of molecules are presented with attention to vibrational wavepackets as a method of tracking nuclear motion after excitation. Finally, existing literature on the ultrafast photoinduced dynamics in transition

metal complexes is reviewed. This is important as the dynamics that occur in single molecules that have localised transitions are very different to those observed in traditional condensed matter materials where excitations tend to be delocalised.

1.2 Electronic Structure and Spectroscopy of Coordination Complexes

1.2.1 Crystal-Field Theory

Crystal-field theory was first developed in the 1930s in an attempt to explain the colours of transition metal complexes.[49, 50] This treats the breaking of the degeneracy of orbitals by considering the ligands introducing a static charge distribution around the metal. The metals and ligands are considered as point charges and do not take part in bonding within complexes. Crystal-field theory primarily describes the splitting of d-orbitals (although p and f-orbitals can also be described), the shape of these is shown in Figure 1.2.1.[51] If a ligand, considered as a point charge, is placed along the direction of one of the orbital lobes, then the energy of that orbital is increased due to electron-electron repulsion. The smaller the metal-ligand distance, the greater the increase. This means that different structures around the metal ions lead to different d-orbital splittings. In an octahedral complex of O_{h} symmetry, the ligands are at an equal distance from the metal centre along both directions of all the principle axes. In this arrangement, the d_{z^2} and $\mathrm{d}_{x^2-y^2}$ orbitals are higher energy as the lobes point directly toward the ligands. The d_{xy}, d_{xz} and d_{yz} orbitals are lower in energy as they point away from the axes.[52] The lower energy set is known as the $t_{2\mathrm{g}}$ orbitals and the upper set are the e_{g} orbitals, referring to their symmetry and degeneracy. There are many other shapes and symmetries of complexes that have different splittings.[52]

This theory explained the bright colours of some complexes. The splitting of the t_{2g} and e_g orbitals allows photon absorption between these sets of orbitals and the energy difference is often in the visible region of the electromagnetic spectrum. This splitting of the levels is called the crystal-field strength (Δ),[53] which follows certain trends. Taking into account the metal ions, a higher oxidation state leads to a larger crystal-field splitting. The greater positive charge causes the ligands to lie closer to the metal centre. Therefore, a metal with a higher oxidation number will have a blueshifted absorption.

The nature of the ligands also determines the crystal-field strength. The spectrochemical series is an empirical list of ligands ordered from ligands that induce the smallest crystal-field splitting (known as weak-field) to those that generate the largest (known as strong-field).[54] The ordering of this list is shown below:

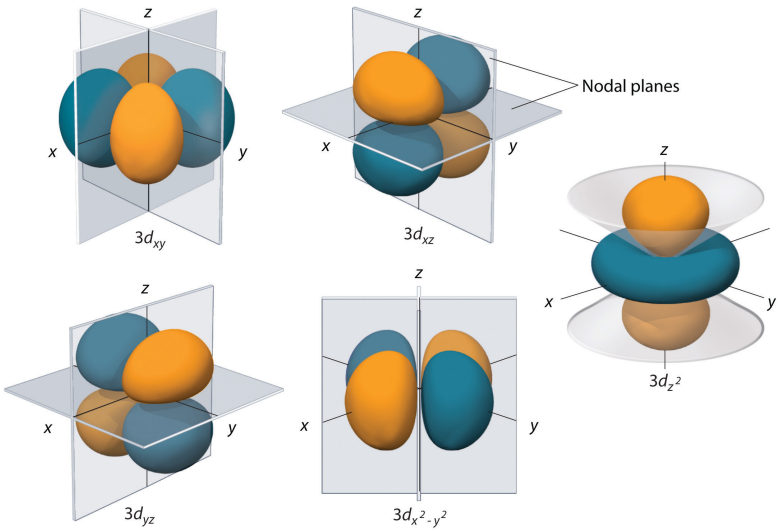

Figure 1.2.1: The shapes of d-orbitals, show the probability density of the electron wavefunction, the blue and orange indicate the opposite phases of the wavefunction. The d_{z^2} and $d_{x^2-y^2}$ orbitals have lobes that point in the z direction and, x and y directions, respectively. Whereas, the d_{xy}, d_{xz} and d_{yz} orbitals have lobes that point between the axes. Figure taken from ref. [51]

$$I^- < Br^- < Cl^- < N_3^- < F^- < NCO^- < C_2O_4^{2-} < O_2^- < H_2O < acac^- < NCS^-$$
$$(\text{N-bonded}) < CH_3CN < \text{pyridine} < NH_3 < \text{bpy (bipyridine)} < \text{phen}$$
$$(\text{1,10-phenanthroline}) < PPh_3 < CN^- < CO$$

Some of the trends in the series can be explained by crystal-field theory. For example, the smaller the halogen, the stronger the crystal field. Smaller halogens have the ability to occupy positions closer to the metal ions, increasing the electron-electron repulsion. However, not all of these can be justified using crystal-field theory. For example, the negatively charged cyanide ligand would be expected to be higher in the series than the neutral CO ligand. A new theory was needed to describe this.

Ligand-field theory was developed by combining crystal-field theory and molecular orbital theory.[55] It explicitly takes into account covalency between the metal and ligand orbitals. Metal-ligand interactions fall into three broad categories shown in Figure 1.2.2. In octahedral complexes, σ-donor ligands donate electrons into the e_g orbitals. Strong σ-donors therefore increase the energy of the e_g orbitals which increases the crystal-field strength. π-donor ligands donate electrons into the t_{2g} orbitals which increases their energy leading to a weaker crystal-field splitting. Finally, π-acceptor ligands remove electron density from the metal t_{2g} orbitals and therefore increase the crystal-field strength. In terms of the spectrochemical series, the weak-field ligands such as the halogens tend to be σ-donors and π-donors due to their filled p-orbitals and produce a small crystal-field splitting. Ligands in the centre of the series such as NH_3 are pure σ-donors. Strong-field ligands such as

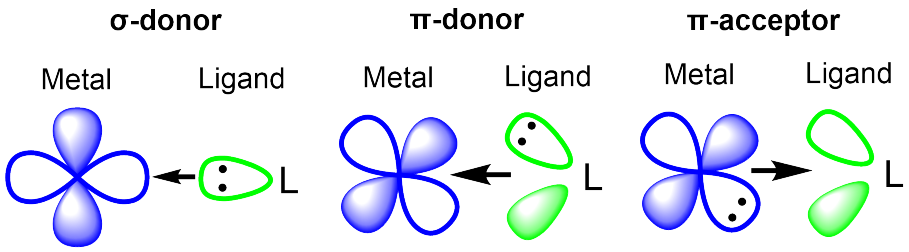

Figure 1.2.2: Types of ligand interactions and the orbitals involved.

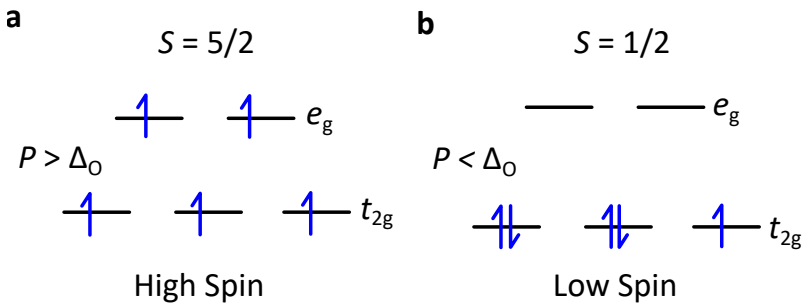

Figure 1.2.3: **a** High and **b** low-spin configurations of a d^5 metal ion. P is electron pairing energy and Δ_O is the crystal-field strength of an octahedral complex.

CN^- and CO are σ-donors and π-acceptors. CO has lower-lying π^* orbitals compared to CN^- and therefore is a better π-acceptor and explains the ordering of the spectrochemical series which cannot be justified in crystal-field theory.

The magnetic properties of transition metal complexes can also be explained using crystal or ligand-field theory. Fe(II) has six d-electrons, following Hund's rule, this ion should have a spin quantum number of $S = 2$ (4 unpaired electrons). In the case of $[Fe(H_2O)_6]^{2+}$ magnetic susceptibility measurements have shown this to be the case.[56] However, in $[Fe(bpy)_3]^{2+}$ and $[Fe(CO)_6]^{4-}$ the spin quantum number was found to be zero,[57, 58] suggesting a violation of Hund's rule. Referring to the spectrochemical series, both bpy and CO are strong-field ligands whereas H_2O is a weak field ligand. There are two competing energy terms that dictate the spin quantum number of the metal ion, one is the crystal-field splitting Δ_O (where the subscript O denotes the octahedral ligand field) and the electron pairing energy P. The pairing energy is the energy cost of adding a second electron into the same orbital. If the pairing energy is larger than the crystal-field splitting the electrons will preferentially occupy the higher lying orbitals before pairing, this gives a high-spin complex, which obeys Hund's rule. If the cost of pairing the electron is less than the crystal-field splitting, the electrons will pair off first and a low-spin complex is formed. The case for a d^5 metal is shown in Figure 1.2.3. This explains the apparent violation of Hund's rule.

1.2.2 High-spin Mn(III) and Jahn-Teller Distortion

Mn(III) complexes often have a high-spin d^4 electron configuration. In this case, there is an electronic degeneracy in the e_g orbitals. The Jahn-Teller theorem states that "any nonlinear polyatomic system in a degenerate electronic state distorts spontaneously so that the degeneracy is lifted and a new equilibrium structure of lower symmetry is attained".[59] Considering a Hamiltonian, $\boldsymbol{H}$ of a polyatomic molecule, the eigenvalues of $\boldsymbol{H}$ describe the potential energy surfaces as functions of the normal mode coordinates Q_i. Jahn and Teller showed that at points of symmetry-induced degeneracy in a nonlinear molecule there are always non-zero first-order expansions in the Hamiltonian that are symmetry-lowering.[59] These linear terms act to distort the molecule away from a point of high-symmetry (any linear term necessitates a gradient in the potential at that point) to one of lower symmetry along a coordinate Q_i. Hence, the point of high-symmetry cannot be the lowest equilibrium nuclear arrangement of a molecule which in turn also lifts the degeneracy. Mathematically, this corresponds to expanding the molecular Hamiltonian in a power series of Q_i. The matrix element $\boldsymbol{H}_{ab}$ of two electronically degenerate states $|\psi_a\rangle$ and $|\psi_b\rangle$ can be written as

$$\boldsymbol{H}_{ab} = \langle\psi_a|\,\boldsymbol{H}\,|\psi_b\rangle = \langle\psi_a|\,\boldsymbol{H}(Q_i = 0) + \sum_i \frac{\partial V}{\partial Q_i} Q_i\,|\psi_b\rangle \tag{1.2.1}$$

where $\frac{\partial V}{\partial Q_i}$ is the derivative of the potential energy surface V along normal mode coordinate Q_i.[60] The expansion has been truncated at first order. Solving this equation leads to adiabatic potential energy surfaces that describe how the potential energy changes with respect to all modes Q_i, this is shown schematically in Figure 1.2.4.

Although the Jahn-Teller effect applies to any non-linear molecule with a degenerate electronic state, it is particularly prominent in transition metal complexes.[61] Jahn-Teller distortion occurs in d^1, d^2, low and high-spin d^4, low-spin d^5, high-spin d^6, low and high-spin d^7 and d^9 configurations. The distortion in the molecule differs depending on the orbitals involved in the degeneracy. For degeneracies in the t_{2g} orbitals, which are non-bonding or weakly bonding/antibonding the change in nuclear coordinates is small. In high-spin Mn(III) (d^4), the degeneracy occurs in the strongly antibonding e_g^* orbitals and this leads to a much larger distortion around the coordination sphere. This distortion leads to a lowering of the symmetry of the complex from O_h to D_{4h}.

The D_{4h} symmetry can manifest itself in two different ways. Firstly, the metal-ligand bonds along the z-axis can expand and the bonds in the equatorial plane can compress. This is called Jahn-Teller elongation and leads to a lowering in

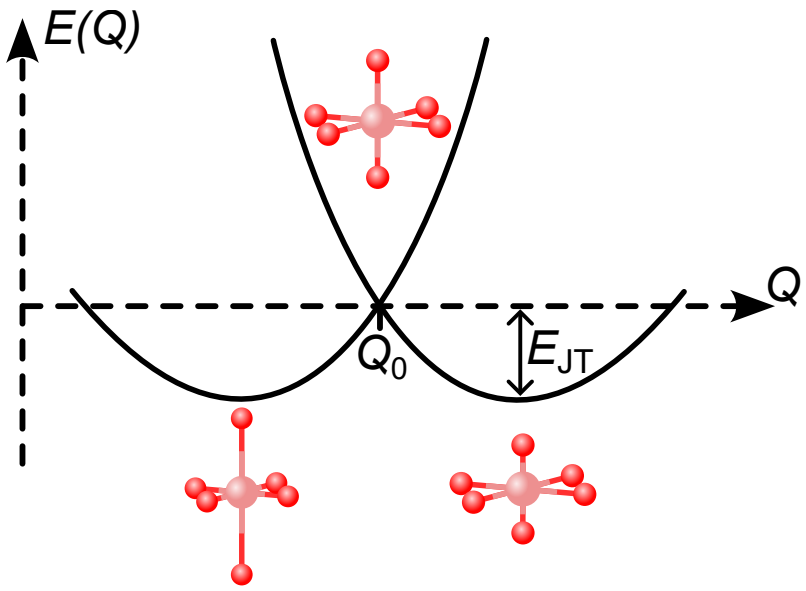

Figure 1.2.4: The diabatic potential energy curve of a molecule exhibiting the Jahn-Teller effect along normal mode coordinate Q. At $Q_0 = 0$ the two states are degenerate and the system is in a high-symmetry arrangement. Here, this is shown as O_h symmetry. The system will distort along normal mode Q until it reaches the minimum of the potential energy curve. These minima are shown as the D_{4h} axially compressed and axially elongated forms of Jahn-Teller distortion E_{JT} is the Jahn-Teller stabilisation energy. Typically, axial Jahn-Teller elongation is found.

energy of the occupied antibonding d_{z^2} orbital and an increase in energy of the unoccupied $d_{x^2-y^2}$ orbital. The opposite can occur where the equatorial bonds are elongated and the axial bonds are compressed, this is Jahn-Teller compression. The compression lowers the energy of the $d_{x^2-y^2}$ and increases the energy of the d_{z^2} orbital. Both Jahn-Teller distortions are shown in Figure 1.2.5 with ground and excited state term symbols. The Jahn-Teller effect does not predict the type of distortion, only the symmetry lowering from O_h to D_{4h}. However, the elongated geometry is overwhelmingly observed due to greater anharmonic contributions to the potential surface[62] and $3d_{z^2}$-4s hybridisation.[63] The above only considers complexes where all the ligands are equivalent, the situation is more complicated if there are ligand inequivalencies in the molecules. It is possible to have systems with even lower symmetries such as C_{2v}, D_{2h} and C_s.[64] For D_{4h} symmetries the electronic states are designated with Mulliken term symbols for transition metal complexes as shown in Figure 1.2.5.

It is possible to change the Jahn-Teller distortion transiently by using light to promote electrons between the $d_{x^2-y^2}$ and d_{z^2} orbitals in Mn(III) on ultrafast timescales.[65] Switching the Jahn-Teller distortion can also be initiated via light-induced spin crossover in Co(II) complexes.[66, 67] It is also possible to induce Jahn-Teller distortion in the excited states when it is absent in the ground state via population of higher-lying doubly degenerate states. This is the case in some

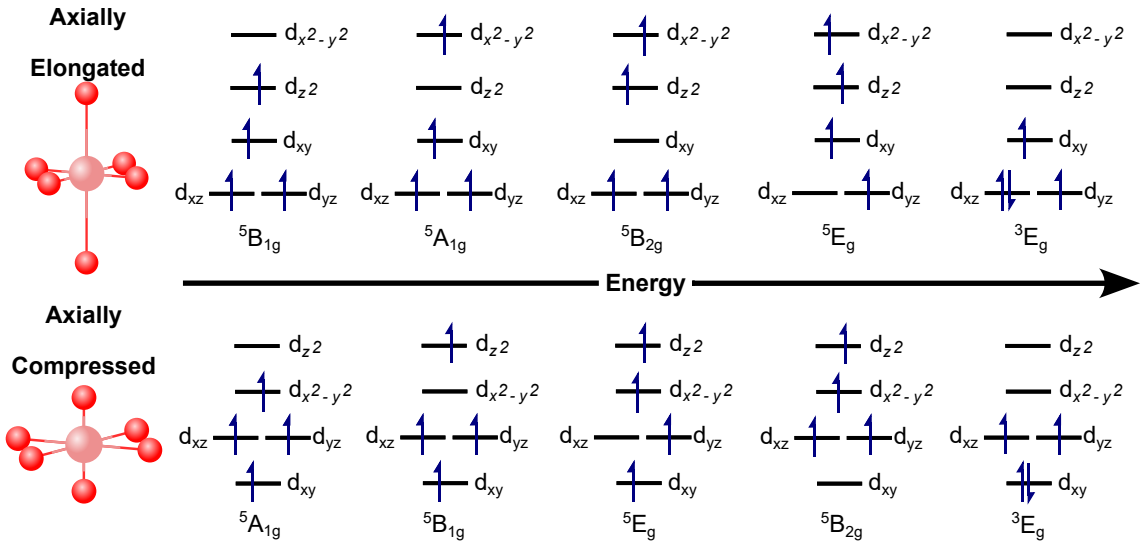

Figure 1.2.5: Valence electronic ligand-field states of Jahn-Teller distorted d^4 high-spin metal ions assuming D_{4h} symmetry. Top: axially elongated geometry. Bottom: axially compressed geometry.

tetrahedral Cu(I) phenanthroline complexes[68–73] and in Ru(II) triazolyl-based complexes discussed in Chapter 5. Similarly, Jahn-Teller distortion can be turned off by exciting to non-degenerate states as observed in charge transfer excited states in MnFe Prussian blue analogues.[74, 75]

1.2.3 UV-Visible Spectroscopy

Ultraviolet-visible (UV-vis) spectroscopy is an experimental technique that uses light in the ultraviolet and visible regions of the electromagnetic spectrum to measure the absorption spectrum of a material. This region corresponds to frequencies that match the difference between energy levels in valence orbitals, which allows the experimentalist to gain information about the d-orbital configuration and low-lying ligand orbitals. In mononuclear transition metal complexes, there are five main types of transition that can be observed in UV-vis spectra: crystal-field or metal-centred (MC) transitions, metal-to-ligand charge transfer (MLCT), ligand-to-metal charge transfer (LMCT), ligand-to-ligand charge transfer (LLCT) and ligand-centred (LC) transitions.

The Beer-Lambert law[76] provides a quantitative description of how much light a material absorbs at a specific wavelength. The absorbance (A) of an isotropic and homogeneous material is given as a function of the concentration (c) of the absorbing species, the path length (l) through which the light traverses the material and the extinction or molar absorption coefficient ($\varepsilon(\lambda)$) which is a function of the wavelength (λ):

$$A = \varepsilon c l. \tag{1.2.2}$$

The extinction coefficient of an absorption peak in a UV-vis spectrum can be used to infer some information about the nature of the transition and the peak position can be used to gain information about the energy difference between states. This information is only useful, provided that there is prior knowledge of typical values of the molar absorption coefficient for different types of transitions. The unit used for absorption is optical density (OD) which is defined as the $A = -\log_{10}(T/T_0)$ where T_0 is the transmission with no sample in the beam and T is the transmission with the absorbing species. Therefore 1 OD corresponds to a transmission of 10 % or an attenuation of 90 %.

Selection rules exist for electronic transitions in transition metal complexes. In the framework of the dipole approximation, the magnitude of the transition dipole moment $\boldsymbol{\mu}$ is how strongly the dipole operator $\hat{\mu}$ couples together the ground electronic (initial) state $|g\rangle$ and the state in which the electrons are excited to $|e\rangle$ (final state). It is defined as

$$\boldsymbol{\mu} = \langle g| \hat{\mu} |e\rangle . \tag{1.2.3}$$

If the transition dipole moment is zero, light cannot couple the two states of the transition within the dipole approximation, and that transition is said to be forbidden.

The Born-Oppenheimer approximation can be introduced to separate the electronic (ψ_{el}) and nuclear (ψ_{n}) parts of the wavefunction.[77] The spin component of the wavefunction (ψ_{s}) can also be separated. Therefore, the total wavefunction can be written as $|\Psi\rangle = |\psi_{\mathrm{el}}\psi_{\mathrm{n}}\psi_{\mathrm{s}}\rangle$. The dipole operator depends on the position and charges of the electrons and nuclei and therefore the dipole operator expressed as a sum of the nuclear and electronic parts of the dipole operator ($\hat{\mu} = \hat{\mu}_{\mathrm{el}} + \hat{\mu}_{\mathrm{n}}$). The transition dipole moment can be expressed as

$$\mu = \langle g| \hat{\mu} |e\rangle = \langle g_{\mathrm{el}} g_{\mathrm{n}} g_{\mathrm{s}}| \hat{\mu}_{\mathrm{el}} + \hat{\mu}_{\mathrm{n}} |e_{\mathrm{el}} e_{\mathrm{n}} e_{\mathrm{s}}\rangle . \tag{1.2.4}$$

This can be simplified by invoking the Condon approximation,[78, 79] which assumes that the integral $\langle g_{\mathrm{el}}| \hat{\mu}_{\mathrm{el}} |e_{\mathrm{el}}\rangle$ does not depend on the nuclear coordinates. This leads to the final expression,

$$\mu = \underbrace{\langle g_{\mathrm{n}}|e_{\mathrm{n}}\rangle}_{\substack{\text{Franck-Condon}\\ \text{Factor}}} \underbrace{\langle g_{\mathrm{el}}| \hat{\mu}_{\mathrm{el}} |e_{\mathrm{el}}\rangle}_{\substack{\text{Orbital Selection}\\ \text{Rule}}} \underbrace{\langle g_{\mathrm{s}}|e_{\mathrm{s}}\rangle}_{\substack{\text{Spin Selection}\\ \text{Rule}}} + \underbrace{\langle g_{\mathrm{el}}|e_{\mathrm{el}}\rangle}_{=0} \langle g_{\mathrm{n}}| \hat{\mu}_{\mathrm{n}} |e_{\mathrm{n}}\rangle \langle e_{\mathrm{s}}|e_{\mathrm{s}}\rangle . \tag{1.2.5}$$

The second term of this equation is equal to zero due to the orthogonality of the electronic states. This equation contains information about the transitions that can be observed in UV-vis spectra.

The orbital selection rule states that the electronic dipole operator must couple the ground and excited states. The electric dipole operator is odd ($\hat{\mu}_{\mathrm{el}} = -e\sum_i \boldsymbol{r}_i$ where e is the charge of an electron and $\boldsymbol{r}_i$ is its position vector), so the electronic states must have a different parity for the transition dipole moment to be non-zero. In transition metal complexes with octahedral symmetry, this means that transitions between the d-orbitals are forbidden as both $t_{2\mathrm{g}}$ and e_{g} orbitals have a centre of inversion. These types of transitions are said to be Laporte forbidden.[80]. This selection rule can be broken in octahedral complexes in a few different ways. If there are ligand inequivalencies that break the centre of inversion, the transition is Laporte allowed. If the molecule has asymmetric vibrations, this transiently breaks the centre of symmetry and the electronic transition can occur. This is known as a vibronic transition because it relies on a vibration mediating the electronic transition. In these cases, the transition is said to be weakly allowed and the transition can be observed in a UV-vis spectrum.

The spin selection rule states that a transition cannot occur if there is a change of spin quantum number associated with that transition. This stems from the fact that the dipole operator does not act on the spin wavefunction and therefore it cannot couple different spin states. These transitions are said to be spin forbidden. However, there is a caveat to this selection rule. Spin-orbit coupling describes the interaction of electron spin with the motion of the electrons inside a potential.[81] The Hamiltonian for spin-orbit coupling ($\hat{H}_{\mathrm{SO}}$) is

$$\hat{H}_{\mathrm{SO}} = \frac{\xi}{2S}\hat{\boldsymbol{L}} \cdot \hat{\boldsymbol{S}} \tag{1.2.6}$$

where ξ is the spin-orbit coupling constant, $\hat{\boldsymbol{L}}$ is the orbital angular momentum operator and $\hat{\boldsymbol{S}}$ is the spin angular momentum operator. This Hamiltonian has the effect of coupling spin states of different spin multiplicity so that L and S are no longer good quantum numbers. Physically, this means that electronic states are no longer pure spin states and have small parts of other spin states mixed in.[82] For example, a "formal" singlet ground state could be 99 % singlet and 1 % triplet and the 1 % triplet part of the ground state can couple to an excited triplet state. Therefore, it is possible to observe spin forbidden transitions in UV-vis spectra but they are often very weak. ξ has a Z^4 (where Z is atomic charge) dependence, which means that spin-orbit coupling is much stronger in heavier ions. This leads to an increase in intensity for spin-forbidden transitions for heavier metal ions, which is observed in $[\mathrm{M(bpy)_3}]^{2+}$ where the Fe(II) complex has the weakest transition and

Os(II) has the strongest spin-forbidden transition.[83] Spin-orbit coupling is also responsible for magnetic anisotropy and intersystem crossing.

The final term in Equation 1.2.5 is the Franck-Condon factor. The Franck-Condon factor is the overlap of the nuclear wavefunctions on the ground and excited electronic states. This overlap must be non-zero in order for a transition to be observed. This also leads to the Franck-Condon principle which states that an electronic transition occurs much quicker than the nuclei can move therefore the outcome immediately after photoexcitation is a molecule with its ground state geometry but in an electronic excited state.[84]

Returning to the Beer-Lambert law, there are rough values that can be referenced to help pinpoint the nature of a transition. These are shown in Table 1.2.1.

Transition	ε /$M^{-1}cm^{-1}$
Spin and Laporte forbidden	0.1
Spin allowed and Laporte forbidden	1 - 10
Spin and Laporte allowed	50 - 200
Spin and Laporte allowed (charge transfer)	> 1000

Table 1.2.1: Transitions that can be observed in transition metal complexes and their extinction coefficient.[85]

1.3 Molecular Magnetism

1.3.1 Magnetic Anisotropy

Magnetic anisotropy provides a preferential direction to the microscopic magnetic moments in a material. A uniaxial magnetic anisotropy leads to the magnetisation pointing up or down along an axis and can constitute a binary logical bit. Reading and writing to magnetic bits (*i.e* knowing what direction the magnetisation is pointing, and being able to change it) is central to magnetic data storage. Therefore, strong magnetic anisotropy is the most important factor for non-volatile memory.

For free magnetic moments in an external magnetic field ($\vec{B}_{\text{ext}}$), the potential energy (V) of a magnetic moment ($\vec{m}$) is given by $V = -\vec{m} \cdot \vec{B}_{\text{ext}}$. Therefore, under the application of a magnetic field, magnetic moments will preferentially align with the field. Even without an external magnetic field, molecules with $S > \frac{1}{2}$ can show magnetic anisotropy known as zero-field splitting (ZFS). In this case, there is breaking of the degeneracy of the different m_s sublevels and therefore different potential energies depending on the direction of the spin in the absence of an external

field. ZFS arises from unquenched orbital angular momentum ($\vec{L}$) that, along with spin-orbit coupling, leads to a preferred direction for the spin angular momentum ($\vec{S}$).[26] The spin-orbit Hamiltonian is shown in Equation 1.2.6. To minimise energy, $\vec{S}$ will always anti-align with $\vec{L}$ leading to the spin magnetic moment favouring certain directions. In general, $\left|\vec{L}\right| \ll \left|\vec{S}\right|$ therefore the dominant contribution to the total magnetisation is spin-only. However, there can be some exceptions to this rule.[86] The direction and magnitude of the orbital angular momentum depends on the geometry and nature of the crystal-field environment. Changing the inner coordination sphere of a transition metal complex can lead to control of the magnetic anisotropy.

The ZFS parameters describe the magnetic anisotropy in ions.[87] The ZFS Hamiltonian for uniaxial anisotropy is

$$\hat{H} = D(\hat{S}_z^2 - \frac{1}{3}S(S+1)) + E(\hat{S}_x^2 - \hat{S}_y^2) \tag{1.3.1}$$

where $S_{x,y,z}$ are the components of the spin operator in the x, y, z-direction and D and E are the axial and equatorial (rhombic) ZFS parameters, respectively. The eigenvalues of S_z are m_s. D and E are strongly related to the ligand-field symmetry and for Mn(III) complexes an equation can be derived for D based on the energies of the ligand-field states. Applying second-order perturbation theory to the spin-orbit coupling operator in d^4 axially elongated Jahn-Teller distorted ions yields Equation 1.3.2 as a function of ligand-field transition energies.[87, 88]

$$D = \frac{\xi^2}{16}\left(\frac{1}{E(^5\mathrm{E}) - E(^5\mathrm{B}_1)} - \frac{4}{E(^5\mathrm{B}_2) - E(^5\mathrm{B}_1)} - \frac{4}{E(^3\mathrm{E}) - E(^5\mathrm{B}_1)}\right) \tag{1.3.2}$$

For Jahn-Teller elongation, D is negative and the minimum energy state is when $m_s = \pm S$ (the maximum value of m_s) leading to an easy axis anisotropy.[89] Jahn-Teller compression leads to a positive D and the energy is minimised when $m_s = 0$ which leads to an easy plane anisotropy where the spin points somewhere in the xy-plane. Changing the Jahn-Teller distortion from elongation to compression using a short laser pulse will transiently change the magnetic anisotropy in Mn(III) complexes. Indeed, there are reports of magnetic anisotropy switching in transition metal complexes using external stimuli such as temperature,[46] pressure[47] and magnetic field.[48] If there is a photoinduced anisotropy, it could lead to methods of ultrafast control of magnetisation in SMMs.

Changes in ZFS parameters have never been measured on an ultrafast timescale in molecular materials. Traditional techniques used to extract these parameters, such as electron paramagnetic resonance (EPR)[87] cannot reach timescales below

a few nanoseconds due to spin precession frequencies.[90] Part of this thesis is concerned with the application of experimental methods that yield information related to the ZFS parameters and attempt to extend them to the ultrafast regime. A consideration of equation 1.3.2 may suggest that D can be extracted by optical spectroscopy and identifying the ligand-field transition energies. However, transitions to the triplet state are forbidden and often completely hidden by charge transfer bands and can only be estimated.[91] Temperature-dependent magnetic circular dichroism (MCD) can be used to calculate the D parameter by fitting different m_s populations using a Boltzmann distribution[92–94] and a time-resolved broadband MCD set-up has been recently developed within the group.[95] There are also reports of using few-cycle pulsed terahertz radiation as a probe of ZFS,[96] which is essentially a frequency-domain version of EPR and direct magnetic (m_s) transition energies are measured. An optical femtosecond pump laser could be coupled into this leading to methods of determination of ZFS parameters on picosecond timescales. If ultrafast control of anisotropy is to be harnessed in SMMs a reliable method to measure D (and to a lesser extent, E) must be developed.

1.3.2 Superexchange

In molecular magnetism, the Kramers-Anderson superexchange interaction,[97, 98] or just superexchange interaction, dictates the relative alignment of spins on different metal ions in a polynuclear transition metal complex. This means it dictates the total magnetic moment of the molecule with $S = \sum_i s_i$ where s_i is the spin quantum number on an individual ion i. So overall, magnetic anisotropy dictates the direction of the magnetisation over all ions (M_S) and the superexchange dictates its strength (S).

Generally, a superexchange interaction can be grouped into two types, ferromagnetic in which the spins on two interacting ions point in the same direction and antiferromagnetic where the spins point in opposite directions. The superexchange Hamiltonian is given by $H = -2J(\vec{s}_1 \cdot \vec{s}_2)$ where J is the coupling constant and $\vec{s}_i$ is the spin on each ion i.[98] If J is positive, the superexchange is ferromagnetic and the spins align. If J is negative, the interaction is antiferromagnetic and the spins anti-align. The sign and magnitude of J is closely related the electronic and nuclear structure of a polynuclear transition metal complex. Superexchange comes from an indirect exchange interaction across two metal ions bridged by an organic ligand.

1.3.3 Single-Molecule Magnets

Single-molecule magnets (SMMs) are molecules with a bistable magnetic ground state and therefore act as one of the smallest realisable units of magnetic memory.[40,

44] As discussed above, uniaxial magnetic anisotropy provides a doubly degenerate ground state where the magnetisation points up or down along an axis ($M_S = \pm S$). For SMMs to be used in data recording media, the memory must be non-volatile and therefore exhibit slow magnetic relaxation between the two states. Magnetic relaxation time is given by $\tau = \tau_0 \exp\left(\frac{E_{\text{bar}}}{k_{\text{B}}T}\right)$ where τ_0 is the attempt time, which is characteristic of a material and $k_{\text{B}}T$ is thermal energy.[99] E_{bar} is the barrier between the two $M_S = \pm S$ states for uniaxial anisotropy and is given by $E_{\text{bar}} = DS^2$, which can easily be seen from Equation 1.3.1, when the rhombic ZFS $E = 0$. Both the axial anisotropy parameter and total spin dictate the relaxation time and therefore both ZFS and superexchange are important to SMMs. Although, there is often a trade off between the magnitude of D and S.[100] Additionally, single-ion magnets can be made without any superexchange interactions if D is large enough.[101, 102]

The first SMM, $[Mn_{12}O_{12}(CH_3COO)_{16}(H_2O)_4]\cdot 2CH_3COOH\cdot 4H_2O$ (Mn_{12}-acetate) was reported in 1993 and exhibits magnetic hysteresis below 4 K.[103] This is an Mn-based SMM with 12 metal centres which shows uniaxial magnetic anisotropy with a barrier of around 60 K.[104] Since 1993, many more SMMs have been synthesised with various blocking temperatures,[44] the largest anisotropy found for an Mn-based system is $[Mn_6O_2(sao)_6(O_2CPh)_2(EtOH)_4]$ ($saoH_2$ = salicylaldoxime or 2-hydroxybenzaldehyde oxime) with a barrier of 86.4 K.[105] More recently, focus has turned to lanthanide-based SMMs due to their large spin-orbit coupling, which can lead to SMMs that have non-volatile magnetisation above liquid nitrogen temperatures.[106]

This thesis primarily concerns Mn-based SMMs as their spin physics and magneto-structural relationships are well understood. As discussed above, axial Jahn-Teller elongation leads to easy axis anisotropy and axial Jahn-Teller compression leads to easy plane anisotropy. Converting between these two geometries is possible using light as shown for Mn complexes,[65] 1-dimensional Cu(I)-based chain magnets[107] and Co(II) complexes.[66, 67] These results open the door to multi-functional SMMs whose magnetic anisotropy could be controlled via ultrashort laser pulses.

1.4 Ultrafast Spectroscopy and Dynamics

1.4.1 Optical Transient Absorption Spectroscopy

Ultrafast transient absorption spectroscopy is a pump-probe technique that measures the change in absorption after a sample interacts with a strong electromagnetic pump pulse. This is a time-resolved extension of UV-visible spectroscopy discussed in Section 1.2.3. Therefore, it has the ability to measure the dynamics that occur in transition metal complexes after light absorption. Generally, the pump is in the

UV-visible regime of the electromagnetic spectrum and therefore excites transitions between different electronic states. After the pump pulse, an excited electronic state is populated, and the probe is used to measure the absorption in this state. The absorption before the pump is subtracted from the absorption after the pump to yield a difference spectrum as a function of wavelength ($\Delta A(\lambda)$). The delay between pump and probe pulses is varied and the progression from the initial excited state to the final photoproduct or state can be monitored.

The different signals that can be measured in transient absorption spectroscopy are described in Figure 1.4.1. After photoexcitation, there is a reduced number of molecules in their electronic ground states. Therefore, there is less absorption in the region of their ground state transitions, which leads to a negative signal known as ground state bleach (GSB). GSB has the same lineshape as the ground state absorption spectrum. Molecules in their excited states have access to new transitions to higher lying energy levels. These transitions create additional absorption features in the excited state which are positive in a difference spectrum and known as excited state absorption (ESA). Finally, an electronic excited state can undergo stimulated emission (SE) to a lower lying state where a probe photon of a certain energy interacts with a sample producing an additional photon of the same energy. As more light reaches the detector, this is recorded as a negative absorption.

1.4.2 Wavepackets and Coherence

Molecules primarily act quantum mechanically and are therefore governed by the time-dependent Schrödinger equation:

$$i\hbar\frac{d}{dt}\left|\Psi(t)\right\rangle = \hat{H}\left|\Psi(t)\right\rangle. \tag{1.4.1}$$

Where $i = \sqrt{-1}$, $\hbar$ is the reduced Planck's constant, $\hat{H}$ is the Hamiltonian or total energy operator of the system and $|\Psi(t)\rangle$ is the state vector of the wavefunction ($\Psi(\boldsymbol{x}, t) = \langle \boldsymbol{x}|\Psi(t)\rangle$) at time t. For time-independent Hamiltonians, the wavefunction can be expressed as a product of a solely time-dependent part and a solely spatially-dependent part. The general solution to a time-independent Hamiltonian can therefore be expressed in terms of the time-dependent solutions:

$$\left|\Psi(t)\right\rangle = \sum_n c_n e^{-i\omega_n t}\left|\phi_n\right\rangle, \tag{1.4.2}$$

where $|\phi_n\rangle$ are the eigenvectors of the time independent solutions with energy eigenvalues E_n, given by the equation $\hat{H}\left|\phi_n\right\rangle = E_n\left|\phi_n\right\rangle$ and $\omega_n = E_n/\hbar$. The coefficients

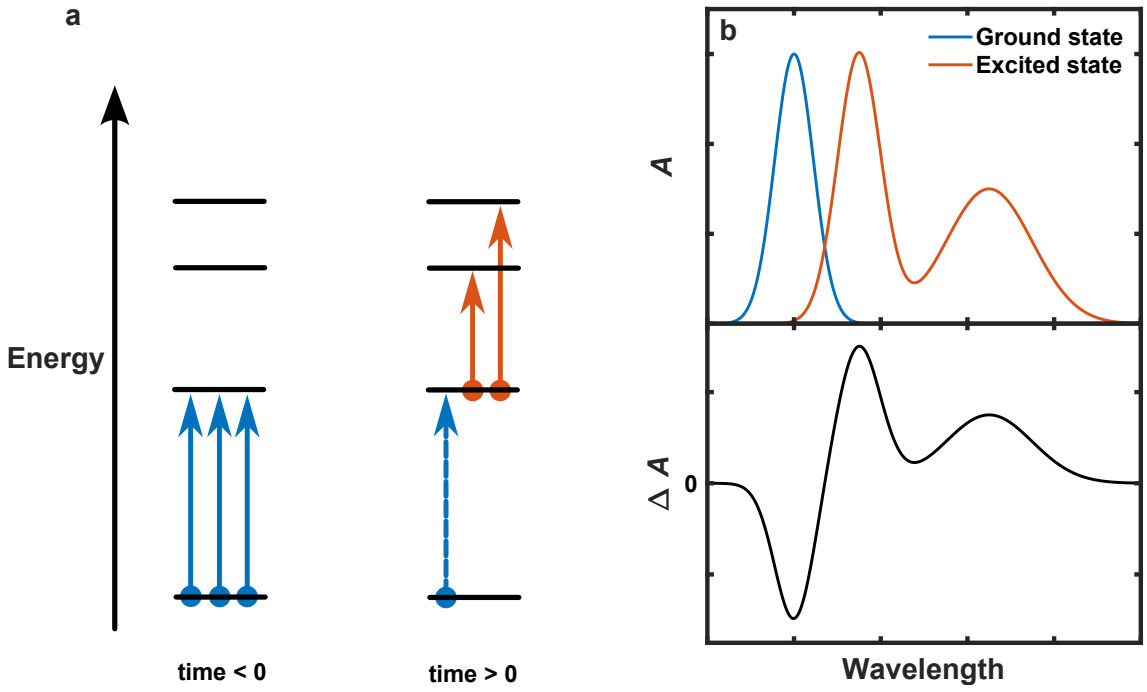

Figure 1.4.1: Features observed in a transient absorption measurement. **a** Energy level diagram of a simple 4-level system. Before the interaction with the pump pulse, all the molecules are in their ground electronic state and have one single absorption band. After the pump, some of the molecules are excited to the first excited state. There are now more energy levels at high energies that the probe can access. This leads to additional ESA features, which are seen in **b**. Additionally, as there are fewer molecules that occupy their ground electronic state after the pump there is less absorption in this region leading to a GSB. The absorption before the pump is subtracted from the absorption after the pump, generating a difference spectrum shown in the bottom panel of **b**. ESA leads to a positive signal and GSB leads to a negative signal.

c_n represent the expansion coefficients. This equation describes a superposition of quantum states, which remains a solution to the time-dependent Schrödinger equation as it is a linear equation. This type of solution is known as a wavepacket, which is a coherent, non-stationary solution of the time-dependent Schrödinger equation constructed from the eigenvectors $|\phi_n\rangle$. The wavepacket is observed to be non-stationary by calculating the probability density $\rho(\boldsymbol{x}, t) = |\langle \boldsymbol{x}|\Psi(t)\rangle|^2$

$$\begin{aligned}\rho(\boldsymbol{x}, t) &= \sum_n |c_n|^2 |\langle \boldsymbol{x}|\phi_n\rangle|^2 + \sum_{n\neq m} c_n^* c_m \langle \phi_n|\boldsymbol{x}\rangle \langle \boldsymbol{x}|\phi_m\rangle e^{i(\omega_n-\omega_m)t} \\ &= \sum_n |c_n|^2 |\langle \boldsymbol{x}|\phi_n\rangle|^2 + 2\sum_{n>m} \mathrm{Re}(c_n^* c_m \langle \phi_n|\boldsymbol{x}\rangle \langle \boldsymbol{x}|\phi_m\rangle e^{i\omega_{nm}t}) \quad (1.4.3)\end{aligned}$$

where $\omega_{nm} = \omega_n - \omega_m$. It is clear to see that the probability density is time dependent due to the oscillatory part of the second term.

A superposition of energy eigenstates generates a non-stationary solution called a wavepacket. This result is highly significant in the context of ultrafast dynamics. There is a significant bandwidth associated with the femtosecond pulses used in ultrafast spectroscopy. This is because a narrow distribution in time corresponds to a wide distribution in frequency according to Fourier transform principles, and thus short pulses encompass a broad spectrum of wavelengths. These pulses can excite multiple states that are close in energy, such as vibrational levels in a molecule. Therefore, a short pulse with a large bandwidth will excite many vibrational levels on an electronic potential energy surface. The superposition of vibrational states generated from the pulse creates a time-dependent wavepacket on the excited state surface. The subsequent propagation of the wavepacket is then governed by the time-dependent Schrödinger equation.

The creation and subsequent motion of a vibrational wavepacket is shown in Figure 1.4.2. A short laser pulse composed of many frequencies excites the ground state wavefunction into a number of different vibrational states that are associated with the electronic excited state dictated by the pulse spectrum and Franck-Condon factors. This coherent superposition of vibrational states leads to a non-stationary wavepacket that oscillates back and forth in the potential well.

Another crucial consideration involves determining the potential surface on which the wavepacket oscillates. Despite tuning the pump pulse on resonance with an electronic transition, a non-stationary wavepacket can still arise on the ground state instead of the excited state.[108] When coherences are generated on an excited state surface, the wavepacket's motion is initiated via a displacive mechanism. As the wavefunction is excited to a region on the excited surface that is not a minimum, the wavepacket will descend to the minimum along the steepest gradient on the

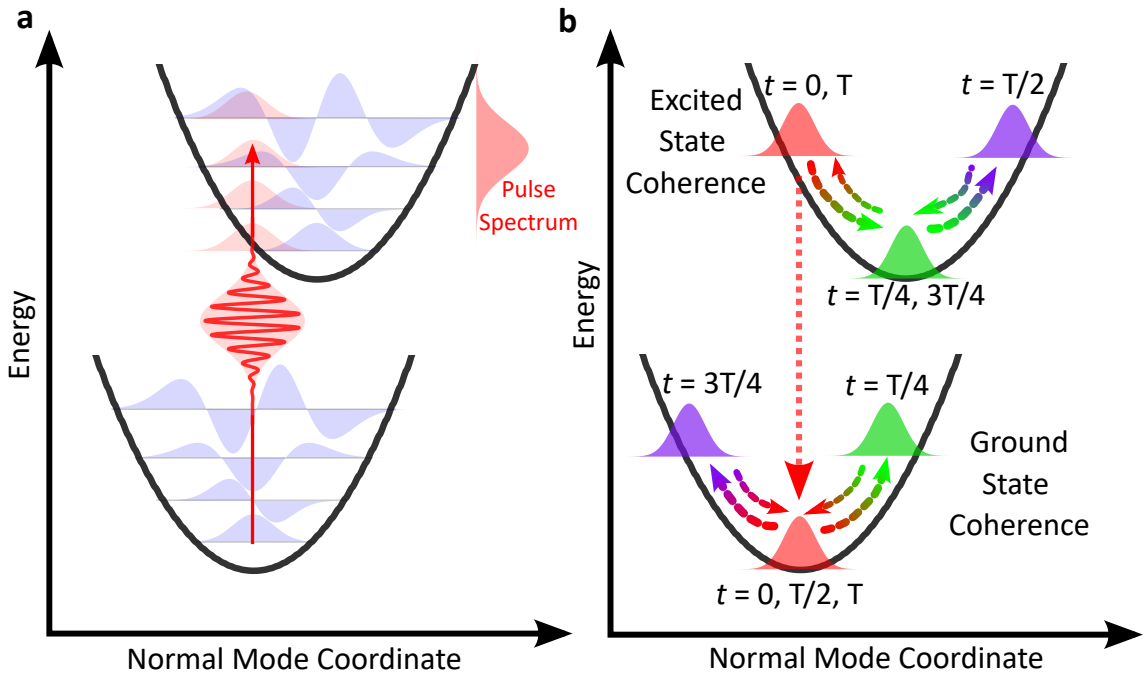

Figure 1.4.2: Generation and propagation of a vibrational wavepacket. **a** Creation of a vibrational coherence. A short laser pulse with a large bandwidth excites more than one vibrational level generating a non-stationary superposition of states. **b** Subsequent motion of the wavepacket. The wavepacket can stay on the excited state potential where it reaches the turning points at $t = T/2$ and $t = T$ where t is the time after excitation and T is the vibrational period. The wavepacket can also quickly fall back down to the ground state potential curve where it will reach the turning points at $t = T/4$ and $t = 3T/4$.

surface and oscillate within that potential well. In contrast, a ground state coherence can be impulsively generated, and instead of displacement, the wavepacket gains momentum from the pump pulse in a Raman-like process.[109] Optical transient absorption is sensitive to both of these coherences, and if a frequency observed in a time-resolved experiment matches that found in a Raman spectrum, it is crucial to differentiate between ground and excited state vibrations.

In general, ground state coherences have a sine-like phase as they start oscillating from the minimum of the potential surface, whilst excited state coherences have a cosine-like phase as they start from a turning point (Figure 1.4.2**b**). Therefore, the measurement of the phase of a coherence in a time-resolved experiment can be a sufficient way to distinguish between these two scenarios. However, coherent artifacts during pump-probe temporal overlap make it difficult to extract absolute phase and processes such as hole-burning can lead to different phases for ground state coherences meaning this method is unreliable.[110] Luckily, broadband transient absorption can be used to discriminate between ground and excited state vibrations.[111] If the oscillations are predominantly observed in areas of ground state bleach where the ground state absorbs then the oscillations are likely to be on the ground state. Whereas if they are found in areas of excited state absorption or stimulated emission they are on the excited state potential surface. It has also been shown that positively and negatively chirped pump pulses can be used to selectively drive a coherent vibrational mode in the ground or excited state.[112]

It should be made clear that the coherence discussed above is a quantum mechanical coherence generated within a single molecule. In pump-probe experiments, the coherence between molecules is also important in order to be able to observe this phenomena in macroscopic samples. Even though a pulse may have sufficient bandwidth to excite a superposition of vibrational states, the pulse duration must still be shorter than the oscillation period of the wavepacket. If the pulse is longer than the period, there is no phase relationship between the ensemble of molecules that have been excited and the coherence cannot be observed. There are two coherences that need to be considered, the coherent superposition of states within a molecule, the wavepacket, and the coherence between the molecules which describes the phase relationship of the wavepacket oscillation in different molecules.[113] For a vibrational wavepacket to be observed, both coherences must exist in the ensemble of molecules.

The process of coherence loss is known as decoherence or dephasing. These two terms are different although, often used interchangeably in the literature. Dephasing is the general term used to describe any loss of coherence. Whereas decoherence is a more specific, single-molecule phenomena when the coherence is lost due to the destruction of the superposition of vibrational states from interactions that depopulate

the higher lying vibrational states. This depopulation can occur when energy is lost to other intramolecular modes or the surroundings.[114] This population relaxation time is denoted T_1.

To differentiate population relaxation and other ensemble dephasing mechanisms, the term pure dephasing is used. Pure dephasing occurs when the phase relationship between the ensemble of vibrating molecules randomises due to interactions with the surroundings. This process involves no population relaxation, only a changes in phase. The time constant for this process is denoted T_2^*. There are two formulations of this process, one developed by Oxtaby[115, 116] based on Kubo's[117] lineshape theories of magnetic resonance. This formulation suggests that solute molecules experience a Gaussian spread of instantaneous frequencies which shifts the vibrational frequencies with respect to one another causing the oscillators to become out of sync.[118] Another interpretation was presented by Yamaguchi,[119] which assumes that intermolecular collisions with solvent molecules induce phase jumps in the solute oscillations with no transfer in energy, as these occur with different phase shifts at different times it destroys the coherence within the ensemble. The total dephasing time T_2 - assuming equal population relaxation times (T_1) from two superposition states - is given by[120]

$$\frac{1}{T_2} = \frac{1}{2T_1} + \frac{1}{T_2^*}. \tag{1.4.4}$$

The discussion above only considers the loss of coherence when considering one set of vibrational states on a single potential energy surface which is vibrationally coupled to other intramolecular modes and/or a bath. However, it does not account for behaviour of the wavepacket as it changes electronic states.[121]

Optical transient absorption can resolve coherent vibrational motion as the nuclear dynamics are coupled to the absorption properties. Two different cases are shown in Figure 1.4.3. Figure 1.4.3**a** shows an oscillation on a lower potential energy curve that has a transition to a displaced potential energy curve at higher energies. The oscillations in transient absorption spectra arise from changes in the transition maximum as the wavepacket oscillates in the potential well. The oscillatory signal's amplitude is strongest where the transition bandshape changes most rapidly with respect to energy, aligning closely with the derivative of the bandshape. Consequently, it exhibits a phase shift at its peak amplitude where the derivative is zero. The second case in Figure 1.4.3**b** corresponds to losing population from an electronic state during vibrational motion. As the wavepacket oscillates, it loses population each time it reaches one of the turning points. Therefore, the oscillatory signal observed in a transient absorption arises from the Beer-Lambert law, where the concentration of a state changes as the wavepacket evolves on the surfaces. The

amplitude of the oscillations more closely follows the bandshape of the transition, rather than its derivative.

In a transient absorption experiment, only the total dephasing time T_2^* can be measured and the individual contributions cannot be separated. It has been shown for I_3^- in solution that pure dephasing dominates this process[122] and this has sometimes been considered to be the case for vibrational dephasing in larger molecules. I_3^- is a small molecule with very few intramolecular vibrational degrees of freedom so one would expect intramolecular vibrational redistribution and therefore population relaxation to be slow, this may not be the case in much larger molecules such as transition metal complexes. It is an open question whether T_2^* dominates in large molecules with hundreds of normal modes and higher density of states. Careful design of experiments may be able to indicate which of these dephasing components is dominant in a molecule, this is explored in Chapter 3. Recently, it has been shown that time-resolved 2D spectroscopy can more effectively decouple the T_1 and T_2^* times.[123]

1.5 Processes after photoexcitation

In addition to the observation of vibrational wavepackets, there are many other processes that can occur after photoexcitation which are shown in Figure 1.5.1. The non-radiative processes that transfer population from one electronic state to another are internal conversion (IC) and intersystem crossing (ISC). IC corresponds to a transition from one electronic state to another of the same spin quantum number. ISC corresponds to transitions between two states of different spin quantum numbers and is therefore forbidden in the absence of spin-orbit coupling. The radiative analogues of these processes are fluorescence and phosphorescence, where fluorescence occurs within the same spin manifold, whilst phosphorescence occurs across two spin manifolds. Finally, there is vibrational relaxation that occurs within the same electronic state where the population is funnelled down a ladder of vibrational states. Vibrational relaxation consists of fast intramolecular vibrational redistribution (IVR) and slower processes where energy is transferred to the surroundings.

Within transient absorption measurements, IC and ISC are expected to lead to the decay and growth of completely new transitions as new electronic states are populated. However, distinguishing between IC and ISC is difficult, there are no criteria for identifying spectra from different spin states. IC and ISC are differentiated from vibrational relaxation through their spectral evolution. Considering there is no change in electronic state during vibrational relaxation, only subtle changes are likely in the experimental spectra. Generally, as lower energy vibrational states are populated, this will blueshift an excited state absorption band as the energy gap

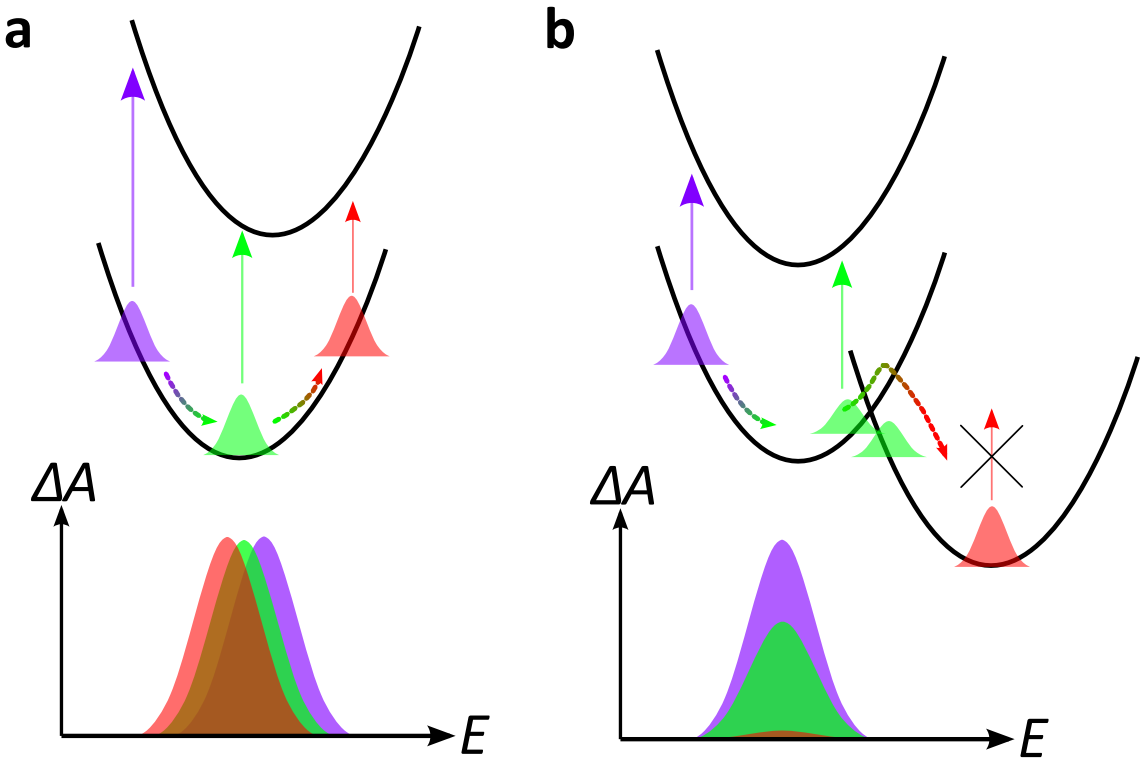

Figure 1.4.3: Schematic of how vibrational coherences can manifest themselves in a transient absorption experiment. This is a simplified view assuming only a single dominant normal mode. The top shows the potential energy surfaces and the wavepacket motion and the bottom shows a cartoon of typical transient absorption spectra that may be observed. **a** shows two displaced potentials. As the wavepacket oscillates back and forth in the lower energy well there is a change in transition energy which shifts the absorption maxima. Therefore, the strongest oscillations are observed on the wings of the peak. **b** shows two nested potential energy surfaces with a third state, which the wavepacket can transfer to. As the wavepacket oscillates and reaches the crossing of potential energy curves it can cross into the next state leading to a reduced absorption. Each pass transfers more population to the lower energy state, causing a change in absorption due to changes in the population of the excited state. Generally, this leads to oscillations that are strongest around the transition peak maximum.

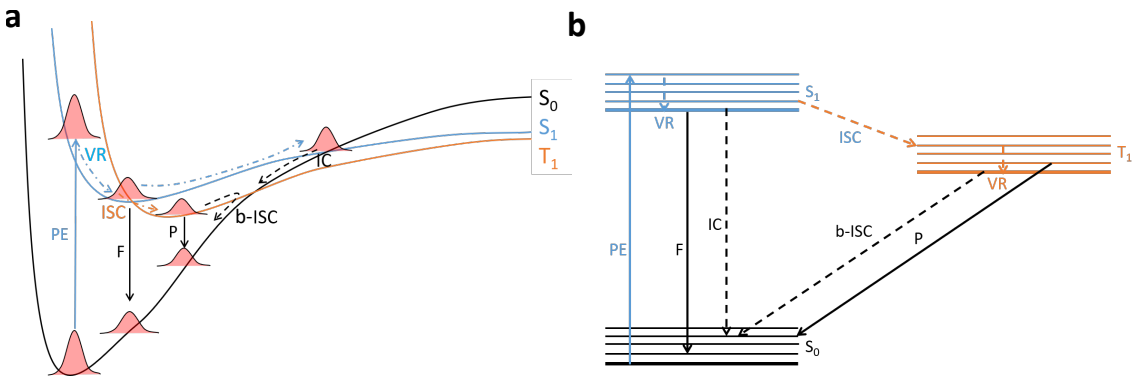

Figure 1.5.1: The processes that can occur after photoexcitation of a molecule. The figure depicts a model system with a singlet ground state (S_0), an excited singlet state (S_1), which is the initial photoexcited state, and an excited triplet state (T_1). **a** Arbitrary potential energy curves of these states, the y-axis corresponds to energy and the x-axis corresponds to an arbitrary nuclear coordinate. **b** The corresponding Jablonski diagram. Filled lines correspond to radiative processes. Dashed lines correspond to non-radiative processes. PE - photoexcitation, F- fluorescence, P - phosphorescence, VR - vibrational relaxation, ISC - intersystem crossing, b-ISC - back-intersystem crossing and IC - internal conversion.

between the populated state and higher-lying energy levels is increased. Second, as the nuclear wavefunction is more localised in lower vibrational states, the transitions tend to become narrower.[124] Fluorescence and phosphorescence are not observed in a transient absorption as light from these processes is emitted incoherently in all directions. However, if either of these processes is dominant, it can certainly lead to a reduction in the signal from the excited state.

1.6 Ultrafast photophysics of coordination complexes

The literature on ultrafast magnetism in single-molecule magnets (SMMs) is limited; however, transition metal complexes offer a wealth of fascinating photoinduced phenomena that have been extensively studied. This review primarily focusses on the dynamics associated with crystal-field transitions, which govern the magnetic anisotropy in SMMs, as well as coherent vibrational wavepackets that can inform on nuclear dynamics. The discussion begins with Fe(II) complexes, well known for their rapid photoinduced spin-crossover, illustrating fundamental aspects of ultrafast photophysics. Comparative analysis between Fe(II) and Ru(II) complexes highlights the impact of altering the excited state order. Vibrational coherences in Cr(III) complexes are discussed to demonstrate the complicated nature of coherent motion. The analysis extends to the photoinduced Jahn-Teller distortion observed in Cu(I) complexes and Co(II) complexes, with a particular focus on ul-

trafast anisotropy changes. Lastly, a review of Mn(III) photophysics sets the stage for subsequent discussion of the results in Chapters 3 and 4.

1.6.1 Iron(II) and Ruthenium(II) Complexes

Fe(II) complexes are discussed as they are one of the most heavily studied systems when investigating ultrafast photoinduced dynamics in transition metal complexes. These molecules show a rich and complex interplay of spin, electronic and nuclear dynamics, which exemplify many of the most important aspects of inorganic photophysics. Fe(II) complexes have a d^6 electron configuration and are generally found in their low-spin form, with all six d-electrons occupying the t_{2g} orbitals. They can undergo spin-crossover (SCO), a change from low-spin to high-spin with the application of external stimulus,[125] including light.[126] They are studied both from a fundamental point of view, to deeply understand photoinduced dynamics and as a possible alternative to more expensive metals (Ru, Ir, Pt etc.) for applications such as photoredox[127, 128] and luminescence.[129] Ru(II) is isoelectronic with Fe(II) but shows a significantly different time evolution after photoexcitation and finds use in countless different applications.[130–132] It is instructive to discuss where the differences in dynamics arise between these two complexes as it provides a basic framework to understand processes that can occur after light absorption. Ru(II) complexes are also discussed in more detail in Chapter 5.

One of the first sub-picosecond ultrafast studies of a transition metal complex was carried out by McCusker et al. in 1993 on solution-phase low-spin Fe(II) complexes.[133] These complexes were chosen as they exhibit optically-induced SCO behavior.[134] In addition to photoinduced SCO, the conversion to high spin can be prompted by the application of pressure or heat.[135] Because of this, the spectrum of high-spin Fe(II) complexes could be measured via temperature-dependent absorption measurements, which can be used as a signature to identify the high-spin state in a time-resolved experiment. The authors used transient absorption spectroscopy with a 700 fs time resolution to investigate $[Fe(tpen)](ClO_4)_2$ in H_2O (where tpen = tetra-kis(2-pyridylmethyl)ethylenediamine) following $^1MLCT \leftarrow {}^1A_1$ excitation. They show that the quintet $^5T_2$ state is formed within 700 fs of photoexcitation before any observed vibrational relaxation (Figure 1.6.1). Similar results were found across other Fe(II) SCO complexes including $[Fe(bpy)_3]^{2+}$ (where bpy = 2,2'-bipyridine). This suggests that spin-orbit coupling in transition metal complexes is sufficient enough to promote changes in spin state rapidly.[136] This could be important to control the magnetisation in SMMs.

In Fe(II) SCO complexes, population of the antibonding e_g^* orbitals in the high-spin, $^5T_2$ state leads to increased metal-ligand bond lengths, indicating that nu-

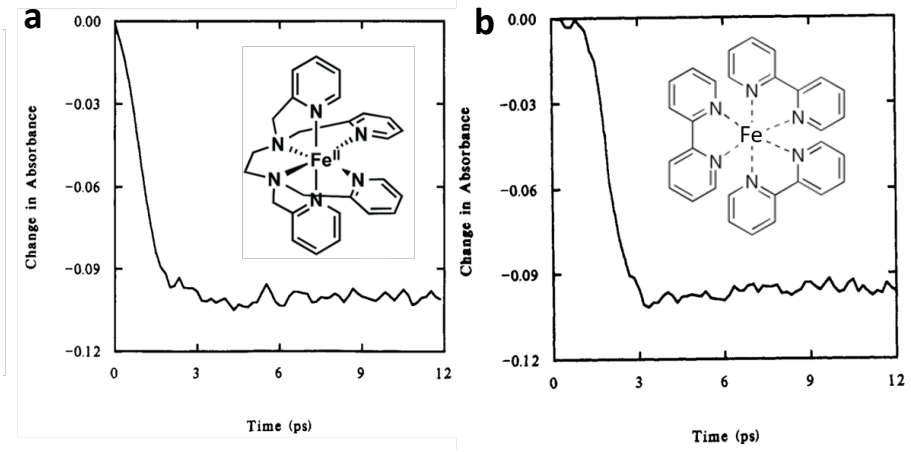

Figure 1.6.1: **a** The kinetic trace monitored at 425 nm of $[Fe(tpen)](ClO_4)_2$ after $^1MLCT \leftarrow {}^1A_1$ excitation. Inset: structure of $[Fe(tpen)](ClO_4)_2$. **b** The kinetic trace monitored at 425 nm of $Fe(bpy)_3^{2+}$ after $^1MLCT \leftarrow {}^1A_1$ excitation. Inset: structure of $Fe(bpy)_3^{2+}$. The kinetic traces show a change of absorbance within 700 fs and this is the signature of the formation of the $^5T_2$ state. Figure adapted from ref. [133].

clear dynamics will be important alongside spin and electronic changes. Coherent vibrational wavepackets were first observed in the high-spin state of $[Fe(bpy)_3]^{2+}$ after MLCT excitation in 2009.[137] Transient absorption measurements revealed oscillations in absorbance, which were Fourier transformed to extract vibrational frequencies. With higher time resolution, additional modes were observed, and the entire SCO process from the initially excited ^{1}MLCT state to the high-spin $^5T_2$ state was found to occur in less than 50 fs.[138] These results are summarised in Figure 1.6.2. After relaxation from the MLCT states into ligand-field states, the nuclear wavepacket oscillates within the $^5T_2$ potential well. The main normal modes (127 and 157 cm^{-1}) likely involve Fe−N bending and stretching modes.[135] These symmetry-breaking modes efficiently couple different electronic and spin states, facilitating fast electronic decay. Time-resolved circular dichroism measurements on enantiopure $[Fe(bpy)_3]^{2+}$ emphasised the importance of non-totally symmetric modes in the conversion from high to low-spin states.[139]

Ruthenium(II) complexes, being isoelectronic with Fe(II) complexes, exhibit similar dynamics, such as the ^{1}MLCT to ^{3}MLCT conversion with identical time constants.[140, 141] However, unlike $[Fe(bpy)_3]^{2+}$, which further relaxes into ligand-field states, $[Ru(bpy)_3]^{2+}$ only relaxes to the ^{3}MLCT state.[142, 143] This difference holds chemical significance, as the long-lived ^{3}MLCT state in $[Ru(bpy)_3]^{2+}$ enables oxidative and reductive chemistry,[144] as well as applications in photovoltaics.[145] Despite these advantages, ruthenium's scarcity and expense have prompted researchers to explore iron as a cost-effective alternative. However, in Fe(II) complexes, the MLCT state is populated for less than 100 fs, precluding diffusion-limited chemistry. The disparity in the lifetimes of the lowest-lying MLCT state between Ru(II)

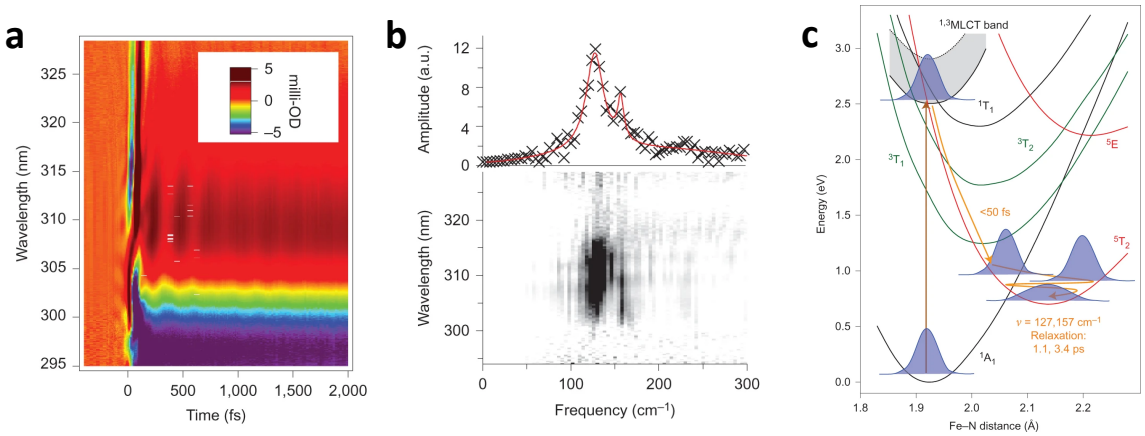

Figure 1.6.2: **a** The transient absorption of $[Fe(bpy)_3]^{2+}$ after exciting at 580 nm (^{1}MLCT $\leftarrow$ $^1A_1$ transition). Oscillations in the signal can be clearly seen in the region around 310 nm. **b** Fast Fourier transform of the residuals after subtracting the kinetic fit from the data identifying the 127 cm^{-1} and 157 cm^{-1} frequencies. **c** The wavepacket dynamics after photoexcitation as a function of Fe−N distance. Figures taken from ref. [138].

and Fe(II) complexes has been attributed to the primogenic effect, wherein the 4d-electron wavefunction extends out further than the 3d-electron wavefunction resulting in an increased crystal-field strength for Ru(II).[146] This leads to the MLCT state being the lowest excited state in $[Ru(bpy)_3]^{2+}$, while in $[Fe(bpy)_3]^{2+}$, the lowest excited state is a ligand-field state.

The question arises: how to engineer an Fe(II) complex with a long-lived MLCT state? One strategy involves creating coordination environments with stronger ligand-fields, inducing state inversion akin to second-row transition metals.[147–149] Alternatively, constraining vibrational degrees of freedom mediating MLCT to ligand-field state conversion could prolong MLCT population. This method, pursued by Paulus et al., employed a polypyridyl-based ligand (L) (Figure 1.6.3**a**) comprised of tethered bpy units and tertiary amine-capped triimines. Time-resolved transient absorption data of $[FeL]^{2+}$ revealed a decay time constant of 110 ± 30 fs for the MLCT to ligand-field state conversion as shown in Figure 1.6.3**c**. Vibrational coherences at 127 and 173 cm^{-1} were identified (Figure 1.6.3**d**), attributed to significant movement of the amine caps. Modification to include copper ions ($[Fe(L)Cu_2]^{4+}$) enhanced rigidity, inhibiting vibrational motion, thereby prolonging MLCT decay to 2.6 ± 0.1 ps, marking the slowest MLCT decay among low-spin polypyridyl-based Fe(II) complexes (Figure 1.6.3**e**–**f**). These results show that knowledge of vibrational motion at the earliest times after light absorption can be used to control the dynamics within transition metal complexes.

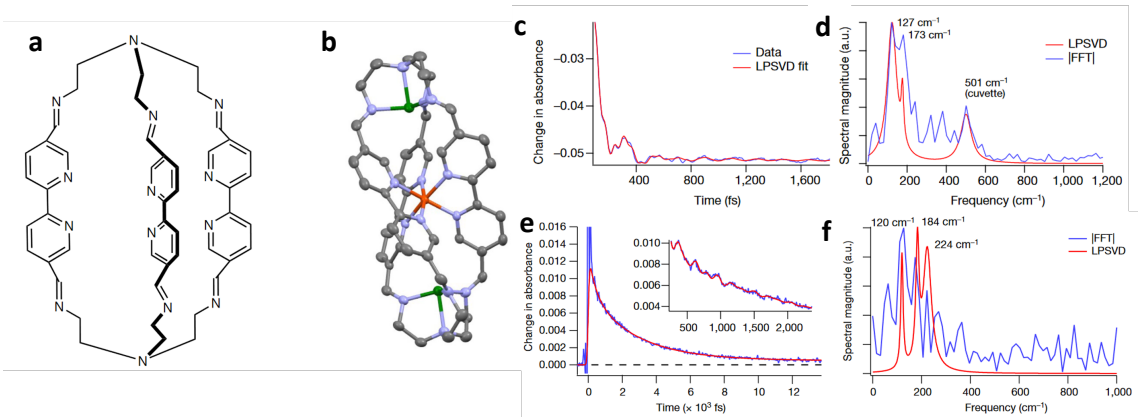

Figure 1.6.3: **a** Structure of polypyridyl-based ligand, L. **b** Structure of $[Fe(L)Cu_2]^{4+}$. Iron, red; nitrogen, blue; copper, green; carbon, gray. **c** Kinetic trace at 608 nm in $[Fe(L)]^{2+}$ showing a fast decay of 110 fs after excitation of a MLCT transition. **d** Linear-predictive singular value decomposition fit and Fourier transform of the residuals in **c** showing two excited state coherences at 127 and 173 cm^{-1}. **e** Kinetic trace at 608 nm in $[Fe(L)Cu_2]^{4+}$ showing a much slower decay of 2.6 ps after the addition of the copper ions into the structure. **f** Linear-predictive singular value decomposition fit and Fourier transform of the residuals in **g** showing a change in frequency of the vibrational coherences after structural modification. Figures taken from ref. [150].

1.6.2 Chromium(III) Complexes

Chromium(III) complexes have been extensively studied since the 1960s for their photophysical and photochemical properties[151–153] and were first subjected to femtosecond transient absorption measurements in 2005 with $Cr(acac)_3$ (Figure 1.6.4**a**).[154] Upon excitation of the $^4A_2$ to $^4T_2$ transition, they observed an ISC to the intraconfigurational ^2E state within 100 fs. Subsequent vibrational relaxation in the hot ^2E state took approximately 1 ps. Further investigation revealed a competition between back-ISC to $^4T_2$ and forward-ISC, resulting in some $^4T_2$ state population that could undergo IC back to the ground state.[155–157] The full Jablonski diagram depicting this process is presented in Figure 1.6.4**b**.

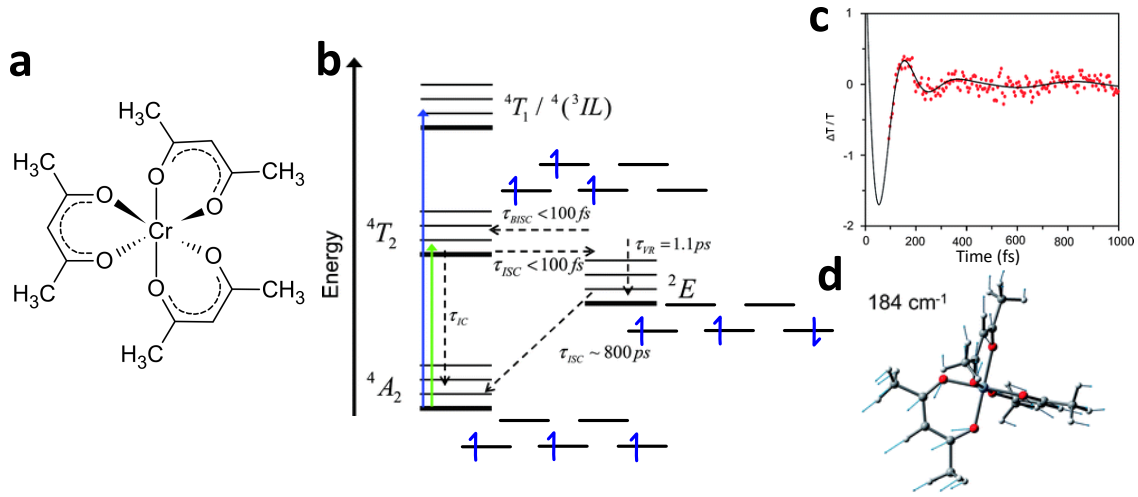

Figure 1.6.4: **a** Structure of $Cr(acac)_3$. **b** Jablonski diagram of dynamics with electronic configuration of ligand-field states. **c** Residuals of a kinetic fit with frequencies of 164 and 75 cm^{-1} after exciting the $^4A_2$ to $^4T_2$ transition. **d** Calculated normal mode that dominates the reaction coordinate. Figures **b**, **c** and **d** taken from ref. [158].

In a subsequent study, the same group investigated $Cr(acac)_3$ with improved signal-to-noise ratio and time resolution, enabling the observation of vibrational coherences in the excited state (Fig. 1.6.4**c**).[158] The strongest oscillation at 164 cm^{-1}, was attributed to a Cr−O breathing mode along with significant motion of peripheral methyl groups of the $acac^-$ ligands whose eigenvectors are shown in Figure 1.6.4**d**. Further experiments replacing methyl groups with bulkier *tert*-butyl groups demonstrated a larger barrier to ultrafast ISC, significantly prolonging the $^4T_2$ state lifetime from 100 fs in $Cr(acac)_3$ to 12 ps in $Cr(tert\text{-butyl-acac})_3$. However, investigations on derivatised $Cr(acac)_3$ ligands revealed a complex relationship between the vibrational coherence frequencies, dephasing times and the IC time constant, which are shown in Figure 1.6.5.[159] Despite changes in the frequencies and dephasing times of the coherent oscillations there is no change in the IC time constant. The

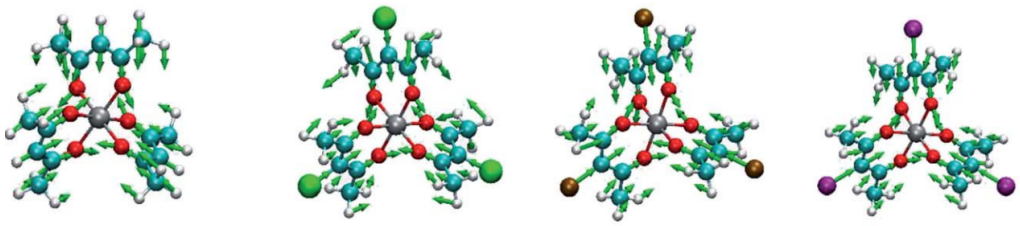

Figure 1.6.5: Nuclear displacements associated with the coherent oscillations identified for the Cr(3-X-acac)$_3$ derivatives. Below each compound's name is the listed frequency associated with the coherence feature, the measured dephasing time, and the time constant (τ_{IC}) corresponding to the observed kinetics for excited-state evolution. Figures taken from ref. [160].

discussion of Fe(II) complexes suggests that coherent vibrational motion can provide insight into influencing dynamics.[150] However, the Cr(III) measurements indicate the exact relationship between vibrational coherences and the lifetimes of states is not so simple.

1.6.3 Copper(I) Complexes

Copper(I) bis-diimine complexes such as $[\mathrm{Cu(dmphen)_2}]^+$ (dmphen = 2,9-dimethyl-1,10- phenanthroline) have long-lived triplet MLCT states useful for photosensitisers and photocatalysts that could be used as an alternative to $[\mathrm{Ru(bpy)_3}]^{2+}$.[161, 162] In the ground state, the Cu(I) ion has a d^{10} configuration with degenerate d_{xz} and d_{yz} orbitals at higher energy than the non-degenerate d_{xy}, d_{z^2} and $d_{x^2-y^2}$ orbitals. Upon MLCT excitation, an electron is removed from the d_{xz} or d_{yz} orbital and the complex has an electronic degeneracy in the excited state, which leads to Jahn-Teller distortion. The ground state of $[\mathrm{Cu(dmphen)_2}]^+$ has a tetrahedron-like $D_{2\mathrm{d}}$ symmetry in which two ligands are attached to the Cu(I) perpendicular to each other. The Jahn-Teller distortion in the excited state, where the copper ion is oxidised, leads to a flattening of the ligands to a more square planar arrangement, which is commonly seen in Cu(II) complexes. Figure 1.6.6**a** shows that the excited state Jahn-Teller distortion decreases the symmetry of the complex from $D_{2\mathrm{d}}$ to D_2.

Tahara and co-workers have extensively studied the ultrafast dynamics in Cu(I) bis-diimine complexes to fully characterise the excited state pathways.[72] Time-resolved fluorescence spectroscopy was used to track the dynamics after excitation of the MLCT band at 550 nm in $[\mathrm{Cu(dmphen)_2}]^+$.[68] The fluorescence spectra shown in Figure 1.6.6**b** clearly show three different processes occurring sequentially. IC occurs first within 300 fs of excitation to the lowest energy singlet excited state

followed by the flattening distortion (FD) occurring over the next picosecond. The fluorescence band redshifts appreciably during the distortion, which is indicative of significant nuclear relaxation. The complex then decays via ISC to the long-lived MLCT triplet state. The dynamics are summarised in Figure 1.6.6**c**.

The same group also carried out transient absorption measurements on $[Cu(dmphen)_2]^+$ with a time resolution of 30 fs. They observed oscillations superimposed on the kinetic traces, which were attributed to vibrational coherences on the excited state potential.[69] A Fourier transform analysis of the oscillations (Figure 1.6.6**e**) showed a significant component at 125 cm^{-1}, which was attributed to a Cu−ligand breathing mode using density function theory calculations (Figure 1.6.6**f**). This breathing mode is due to removing electron density in the antibonding copper orbitals which increases the metal-ligand attraction. Another mode was observed at 290 cm^{-1}, which is a ligand-twisting mode (Figure 1.6.6**g**) with the same symmetry as the flattening distortion. These modes have also been found using time-resolved X-ray K-edge absorption spectroscopy and agree with the assignments made by Tahara and co-workers.[73] As the flattening distortion and ligand twisting mode have the same symmetry they are vibrationally coupled to the first order. It is likely that energy flows efficiently from the ligand-twisting mode, which is coherently excited, to the flattening distortion. This suggests that the symmetries of a coherent vibrations could be important to control the speed of relaxation and dephasing times in transition metal complexes.

1.6.4 Cobalt(II) Complexes

In recent years, research in molecular magnetism has turned to single-ion magnets (SIMs), which are a subset of SMMs that only contain a single metal ion.[101, 163] The magnetic properties of SIMs are solely based on the single-ion anisotropy. Co(II) complexes can have large axial zero-field splittings $|D| \approx 100$ cm^{-1} and therefore have slow magnetic relaxation.[164] In certain crystalline environments, $Co(terpy)_2^{2+}$ exhibits SCO behaviour, where the high-spin quartet state has been shown to exhibit SMM properties.[165, 166] The combination of SCO and SMM behaviour has the potential to create some interesting multifunctional molecular materials.

Biasin et al. have studied an aqueous solution of $Co(terpy)_2^{2+}$ using ultrafast X-ray scattering after excitation of the MLCT transition.[66] In the low-spin state, the complex is axially compressed. After photoexcitation of the MLCT transition, the complex undergoes ISC to the high-spin quartet state leading to anisotropic expansion of all Co–N bonds because of the population of a second antibonding e_g^* orbital. The ultrafast X-ray scattering signal was fitted with a solute, solvent and solvent cage term in order to extract bond length changes over time. Figure 1.6.7**a** shows

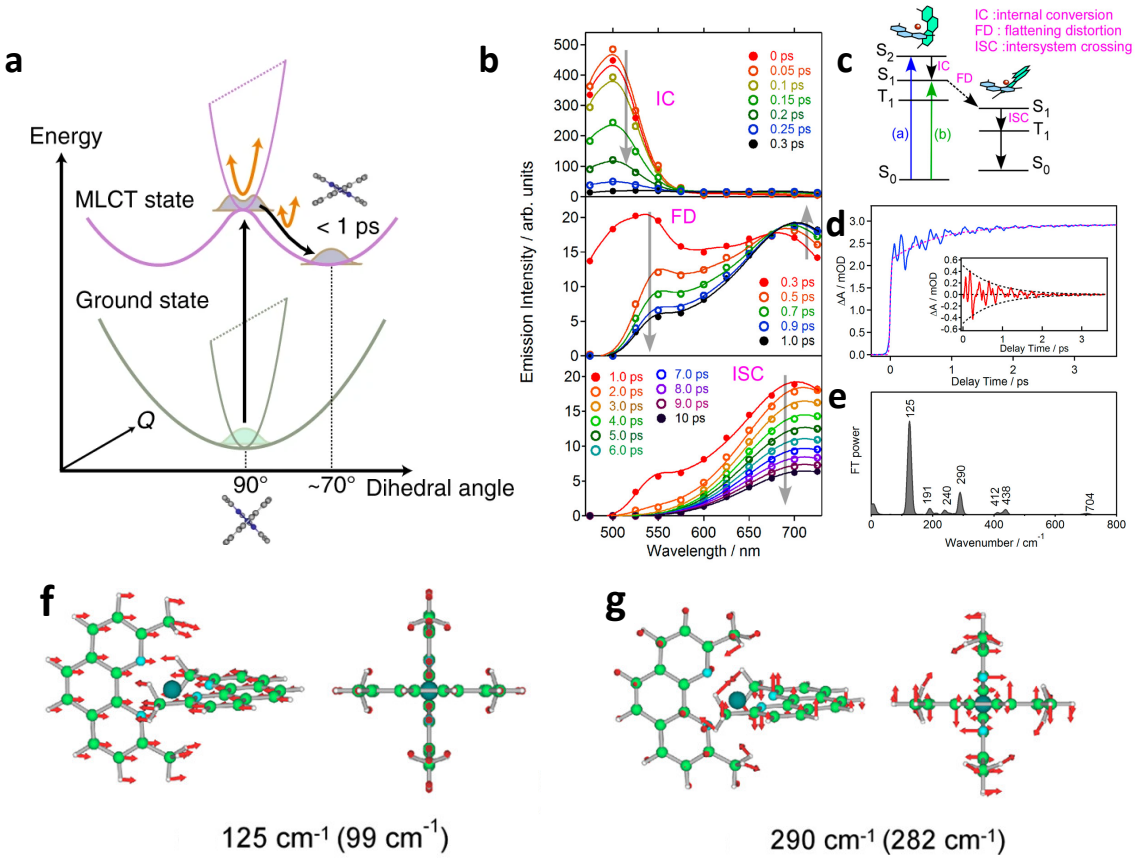

Figure 1.6.6: Summary of photoinduced dynamics in $[Cu(dmphen)_2]^+$. **a** Schematic potential energy curves with respect to the flattening distortion for the ground and MLCT excited state. The Jahn-Teller flattening distortion is shown by the change in the dihedral angle. Taken from ref. [73]. **b** Time-resolved fluorescence upconversion measurement after pumping the MLCT band showing difference spectra for the IC, flattening distortion, and ISC. **c** The proposed excited state pathway exciting to both the S_1 and S_2 state. **d** Transient absorption kinetic trace at 650 nm showing oscillatory signal after excitation to S_1. Inset shows the residuals of a kinetic fit. **e** Fourier transform of the residuals in **e**. **f** Excited state breathing mode with wavenumber from the Fourier transform and the calculated value in brackets. **g** Excited state ligand twisting mode. Figures **b**–**g** are taken from ref. [69].

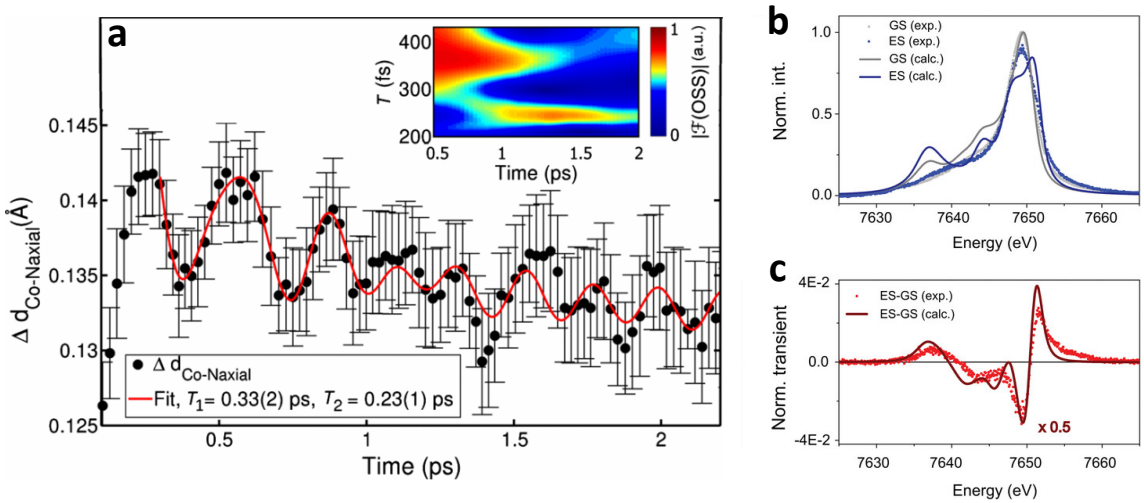

Figure 1.6.7: $Co(terpy)_2^{2+}$ after MLCT excitation in aqueous solution. **a** Change in the axial Co–N distance ($\Delta d_{\text{Co-Naxial}}$) as a function of time measured by X-ray scattering. The data have been fit with two oscillatory components that have periods of 330 fs and 220 fs. Inset: short-time shifting window Fourier transform of $\Delta d_{\text{Co-Naxial}}$ showing the change in frequency over time. Figure taken from ref. [66]. **b** Experimental and calculated ground and excited state Kβ spectrum of $Co(terpy)_2^{2+}$. **c** Experimental and calculated Kβ difference spectrum from data in **b**. Figures **b** and **c** taken from ref. [67].

the change in the axial Co–N distance ($\Delta d_{\text{Co-Naxial}}$) as a function of pump-probe time delay. The Fourier transform in the inset resolved two frequency components. The first with a period of $T_1 = 330$ fs and a second component that grows in as the other decays at $T_2 = 230$ fs. With comparison to DFT calculations, the period T_1 was assigned to a symmetric breathing mode of all the Co–N bonds. Whilst T_2 is in good agreement to a pincer-like mode of the terpyridine ligands. Therefore, upon excitation, the MLCT quickly decays to the high-spin quartet state where the population of a e_g^* orbital immediately initiates a breathing mode. Considering the population of the second e_g^* orbital will lead to a more octahedral coordination sphere, the axial bonds must change more than the equatorial bonds (as the complex is axially compressed in the ground state) which leads to the activation of the more anisotropic terpyridine pincer mode. These results prove that it is possible for vibrational coherence to be transferred between two normal modes.

Photoinduced magnetic anisotropy in the high-spin state of $Co(terpy)_2^{2+}$ was investigated by Canton et al. using ultrafast K-edge X-ray emission spectroscopy.[67] X-ray Kβ emission is particularly sensitive to spin state and the author's results clearly indicated an increase in spin state after excitation in good agreement with the expected increase from $S = 1/2$ to $S = 3/2$ that occurs during SCO. The spectra are shown in Figures 1.6.7**b** and **c**. The splitting between the two peaks in a Kβ spectrum is primarily dependent on 3p-3d exchange energy. Therefore, an increase in S in the

3d orbitals leads to a larger exchange energy and a larger splitting. This can be seen in Figure 1.6.7**c** as the highest energy peak blueshifts and the lowest energy peak redshifts. By fitting to a kinetic model, the transition from MLCT to high-spin quartet state was found to occur with a time constant of 100 fs and the full high-spin lifetime is 6.4 ps. Density functional theory calculations were used to determine the axial ZFS in the high-spin state and found that $D = +120$ cm^{-1}. D is not defined for $S = 1/2$ systems and therefore could not be calculated in the ground state. However, the results do suggest that very strong easy plane anisotropy can be induced via excitation in Co(II) complexes and that these complexes may be good candidates for research in ultrafast molecular magnetism.

1.6.5 Manganese(III) complexes

The results in Chapters 3 and 4 concern dynamics in Mn(III) complexes. The ground and excited state electronic structure of these has been discussed in Section 1.2.2. Mn(III) complexes were used for the first SMMs as their magnetic anisotropy is strongly related to their structure and synthesis could be used to control this. External stimuli can also be used to modulate the magnetic properties. Pressure has been shown to reorientate the Jahn-Teller axis in Mn_{12} to change magnetic anisotropy[167, 168] and some form of magneto-optical control has been demonstrated.[169, 170] There is not much literature on the dynamics of crystal-field excited states in Mn(III) complexes. Work that pertains to ultrafast Mn(III) photophysics has generally looked at donor-acceptor complexes[171] or porphyrins/phthalacyanines that have very different electronic structures.[172–175]

The first ultrafast study on an Mn(III)-based SMM was carried out within the group.[65] Transient absorption spectra were measured after crystal-field excitation of the SMM, $[Mn(III)_3O(Et{-}sao)_3(\beta{-}pic)_3(ClO_4)]$ (where $saoH_2$ and β-pic are salicylaldoxime and 2-methylpyridine, respectively), hereafter Mn_3. This has three Mn(III) ions arranged in a triangle,[176] which are connected with a μ_3-oxo bridge and strong peripheral $-$N$-$O$-$ bonds with the Jahn-Teller axis aligned perpendicular to the plane of the triangle (Figure 1.6.8**a**). This SMM creates difficulty for the theory due to the large spin ground state, so the monomer $Mn(acac)_3$ was also investigated. This is not an SMM but still possesses a Jahn-Teller axis.

The transient absorption results for $Mn(acac)_3$ showed that photoexcitation of a ligand-field transition leads to a coherent vibrational wavepacket in the lowest excited state which corresponds to a switch from axial to equatorial Jahn-Teller distortion with two frequencies of 170 and 208 cm^{-1} and a dephasing time of 325 fs. The authors also fitted the decay to a kinetic model and found a rate constant for the internal conversion to the lowest ligand field state to be 250 fs and the subsequent

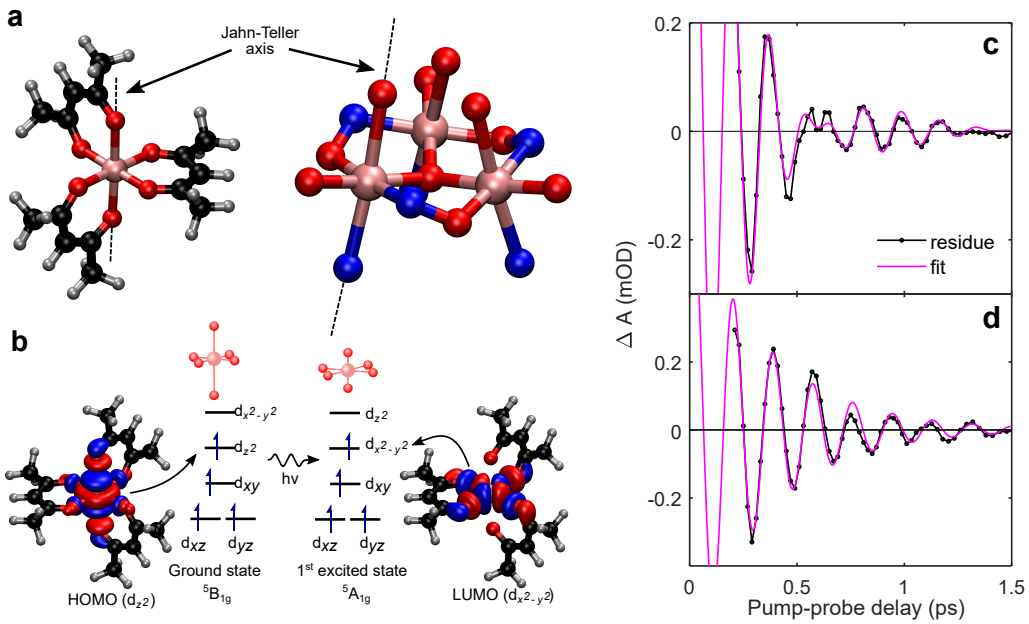

Figure 1.6.8: **a** The structure of $Mn(acac)_3$ and Mn_3 core with the Jahn-Teller axis indicated. Pink, manganese; red, oxygen; blue, nitrogen; black, carbon; grey, hydrogen. **b** The change in electronic configuration upon photoexcitation. The photoexcitation causes an electron to be promoted to the $d_{x^2-y^2}$ orbital which stabilises the axial bonds and destabilises the equatorial bonds. **c** The residuals of the transient absorption spectra of $Mn(acac)_3$ after subtracting the kinetic fit. This is fit the two decaying cosine functions and yielded two frequencies (170 and 208 cm^{-1}) and a dephasing time of 325 fs. **d** The residuals of the kinetic fit of Mn_3 which exhibits one frequency (181 cm^{-1}) and a dephasing time of 360 fs. Figures taken from [65].

vibrational relaxation had biexponential dynamics with time constants of 1.0 and 5.2 ps. There was a plateau in the dynamics indicating that the excited state exists for longer than their experimental timeframe (200 ps).

In Mn_3, the authors observed one single frequency of the vibrational wavepacket in the excited state (181 cm^{-1}). This was attributed to the restriction of in-plane motion created by the strong oxime bridges between the Mn(III) ions. This restriction meant that Mn_3 could not expand in the equatorial plane. Subsequently, the nuclear dynamics were dominated by in-phase out-of-plane motion of all the Mn(III) ions moving back and forth along the Jahn-Teller axis. The rigidity of the Mn_3 triangle also leads to a decrease in excited state lifetime to 9 ps as the bonds in the equatorial plane are unable to expand. To gain deeper insight into the nuclear dynamics that occur upon photoexcitation in Mn_3, time-resolved X-ray K-edge spectroscopy was performed and the results of this are presented in Chapter 4.

To investigate the effect of rigidity in the equatorial plane and its relationship to excited state lifetimes, aqueous solutions of $[Mn(cyclam)(H_2O)_2][OTf]_3$ (cyclam = 1,4,8,11-tetraazacyclotetradecane and OTf = trifluoromethanesulfonate) were studied using transient absorption spectroscopy.[177] The macrocyclic cyclam ligand was

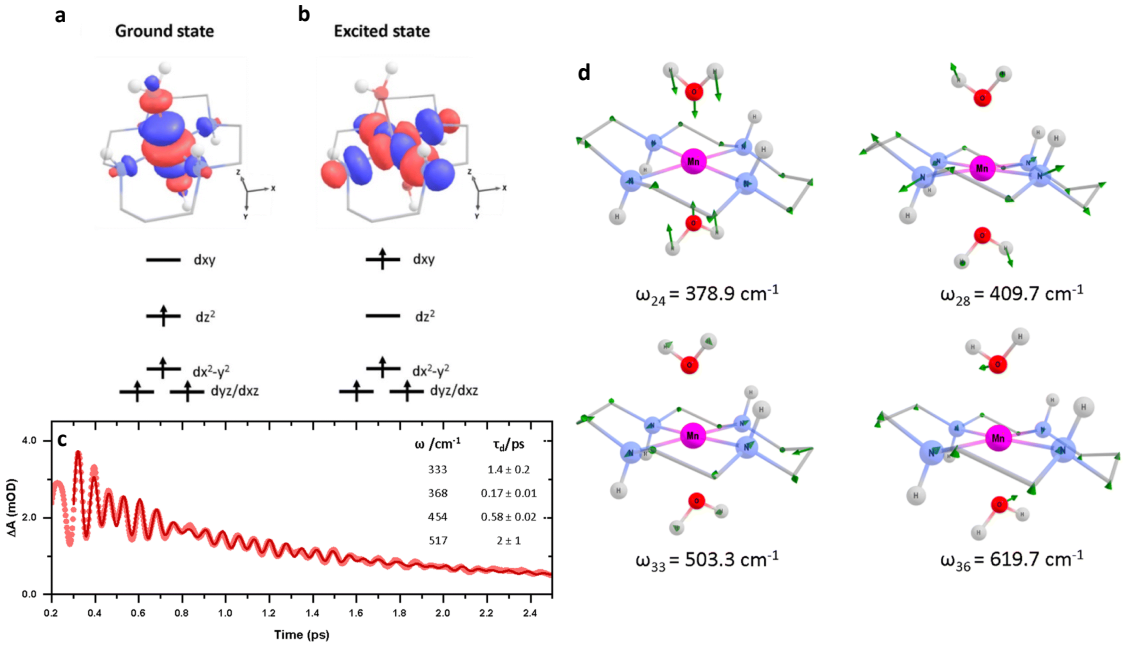

Figure 1.6.9: Dynamics of $[Mn(cyclam)(H_2O)_2][OTf]_3$ in aqueous solution after photoexcitation. **a** Ground state electron configuration and HOMO. **b** Excited state electron configuration and LUMO. **c** Transient absorption after 640 nm excitation monitoring the probe wavelength of 375 nm. The data are fit to a biexponential decay with the sum of four exponentially damped cosine functions. The frequency and dephasing times of these components are shown in the inset. **d** Structural displacements and vibrational frequencies of the normal modes assigned to the coherences observed in **c**. Figures are taken from [177].

chosen to deliberately add rigidity into the equatorial plane. The electron configuration along with the electron densities of HOMO and LUMO are shown in Figure 1.6.9**a** and **b**, respectively. Note that the positions of the d_{xy} and $d_{x^2-y^2}$ orbitals have been switched but this is simply because the x and y-axes have been defined to point in between the metal-ligands bonds and not along them. The change of absorption as a function of time at the maximum of the excited state absorption is shown in Figure 1.6.9**c**. A fit of the exponential population dynamics yielded an excited state lifetime of 3.7 ps, which is several orders of magnitude less than $Mn(acac)_3$. The ability to control excited state lifetimes is vitally important in the efforts to control magnetisation in SMMs. The lifetime of the photoinduced anisotropy needs to be tuned in conjunction with its strength and direction to drive efficient reorientation of magnetisation as described in Figure 1.1.1.

In addition to the short lifetime of the excited state, four different frequency components were observed in the data and are shown in Figure 1.6.9**c** with their respective dephasing times. By comparison to results in the complex $[Mn(cyclam)Cl_2]^{2+}$, the frequencies were assigned to the normal modes in Figure 1.6.9**d**. ω_{24} and ω_{36} mostly involve motion of the axial water ligands whereas the movement in ω_{28} and

ω_{33} is localised to the equatorial cyclam ligand. The motion in the cyclam ligand does not involve much of an expansion in the equatorial bonds as expected from the additional rigidity. Instead, torsional modes are activated to accommodate the population of the d_{xy} orbital. These torsional modes will break the symmetry around the metal-centre and therefore can lead to strong modulations in the optical absorption. Symmetry breaking torsional modes are interesting as they often lead to coupling between different electronic states, which could also be a factor in the complex's short excited state lifetime.

1.7 Aims

Generally, two very broad problems are tackled by the results: (1) can the dynamics in transition metal complexes, and therefore SMMs, be controlled by synthetic design? (2) How can the magnetisation dynamics and other molecular properties that effect the magnetisation be measured on ultrafast timescales in SMMs? Chapters 3 and 5 tackle question 1. Transition metal complexes with only slight modifications in structure are studied after the excitation of a crystal-field transition using ultrafast transient absorption spectroscopy. Vibrational wavepackets are observed after excitation which is a signature of nuclear motion in the crystal-field environment. Chapter 3 discusses the possibility of controlling dephasing times via synthetic design. Chapter 5 shows that minor synthetic modification can create major changes in the wavepacket dynamics. Chapters 4 and 6 focus on question 2. Chapter 4 explores the use of ultrafast X-ray spectroscopy as a method to very accurately track nuclear motion in SMMs. It is shown that the method has a sensitivity to the crystal-field bond lengths below 0.01 Å in large polynuclear complexes and therefore it will be an important method to study dynamics in SMMs. Chapter 6 utilises time-resolved magnetic circular dichroism spectroscopy to study the dynamics of a molecule in solution. There is a lack of spectrally-resolved methods for studying magnetisation dynamics, therefore the development of new methods for studying spin dynamics in molecules is needed. This technique is applied to a model system and it is shown that additional information about the dynamics can be extracted compared to purely optical techniques.

Chapter 2

Methods

2.1 Optical Setup

The time-resolved optical setup uses a Light Conversion Pharos-PH2 regenerative amplifier, which is seeded via a built-in mode-locked oscillator. The laser can deliver pulses that are 330 fs in duration with a spectral centre of 1024 nm at a repetition rate of 25 kHz with energies of 0.4 mJ/pulse. Although the laser can operate at 25 kHz, all the measurements in this thesis were carried out at 1 kHz due to limitations of the detection scheme. The spectrum and autocorrelation of these output pulses are shown in Figure 2.1.1. The spectrum was measured using an Ocean Optics HR2000+ spectrometer and the autocorrelation was measured using an APE Pulsecheck-15 autocorrelator. The spectrum has its peak maximum at 1022 nm and a sech^2 fitting to the autocorrelation provides a peak width of 330 fs. The transient absorption setup is based on the apparatus in ref. [178]. An overview of the entire setup is shown in Figure 2.1.2.

2.1.1 Pump Generation

90 % of the Pharos output is used to pump a Light Conversion Orpheus-F non-collinear optical parametric amplifier (NOPA), which can deliver pulses between 640 and 940 nm with pulse durations around 60 fs. Optical parametric amplification is based on difference frequency generation[179] and supercontinuum generation.[180] In the NOPA, around 1 % of the 1024 nm Pharos output beam is directed into a sapphire plate via a polarising beamsplitter where a supercontinuum is generated. This pulse is chirped and therefore all the wavelength components of the continuum are temporally separated, this is the seed beam. The remaining 99 % of the pump beam is directed into a β-barium borate (BBO) crystal that generates the second harmonic of the beam centred around 512 nm and is split into 2 parts, which will act as the pump for the first and second amplification stages.

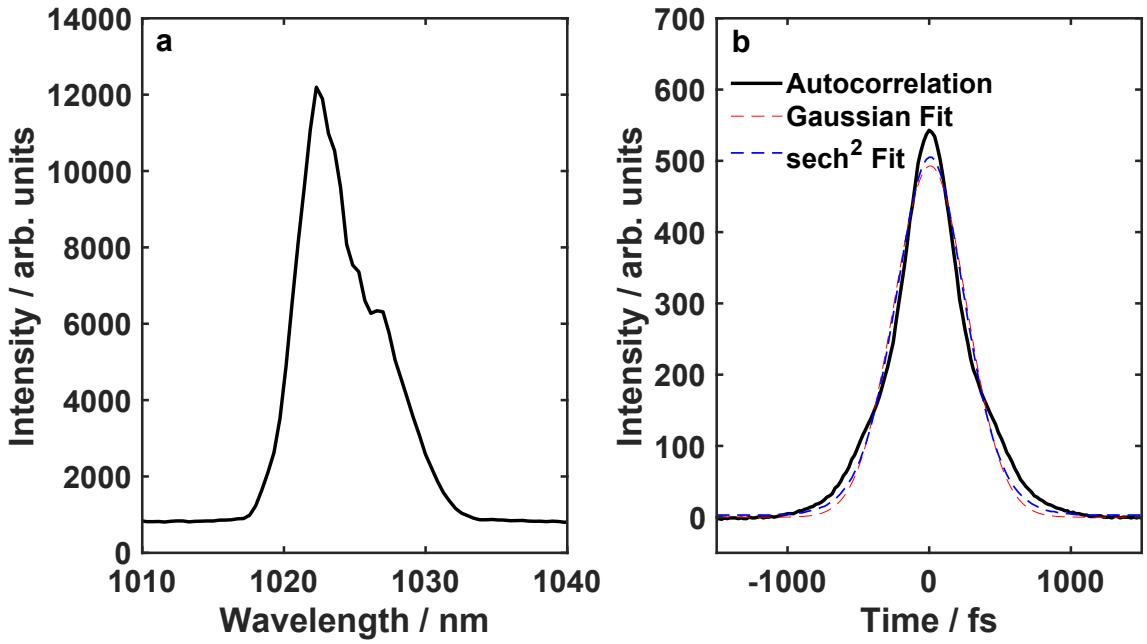

Figure 2.1.1: **a** Spectrum and **b** autocorrelation of Pharos output. The autocorrelation has been fit with both a sech^2 and Gaussian autocorrelation function. The sech^2 function provide the best fit with an autocorrelation width of 508 fs and a pulse width of 330 fs at FWHM.

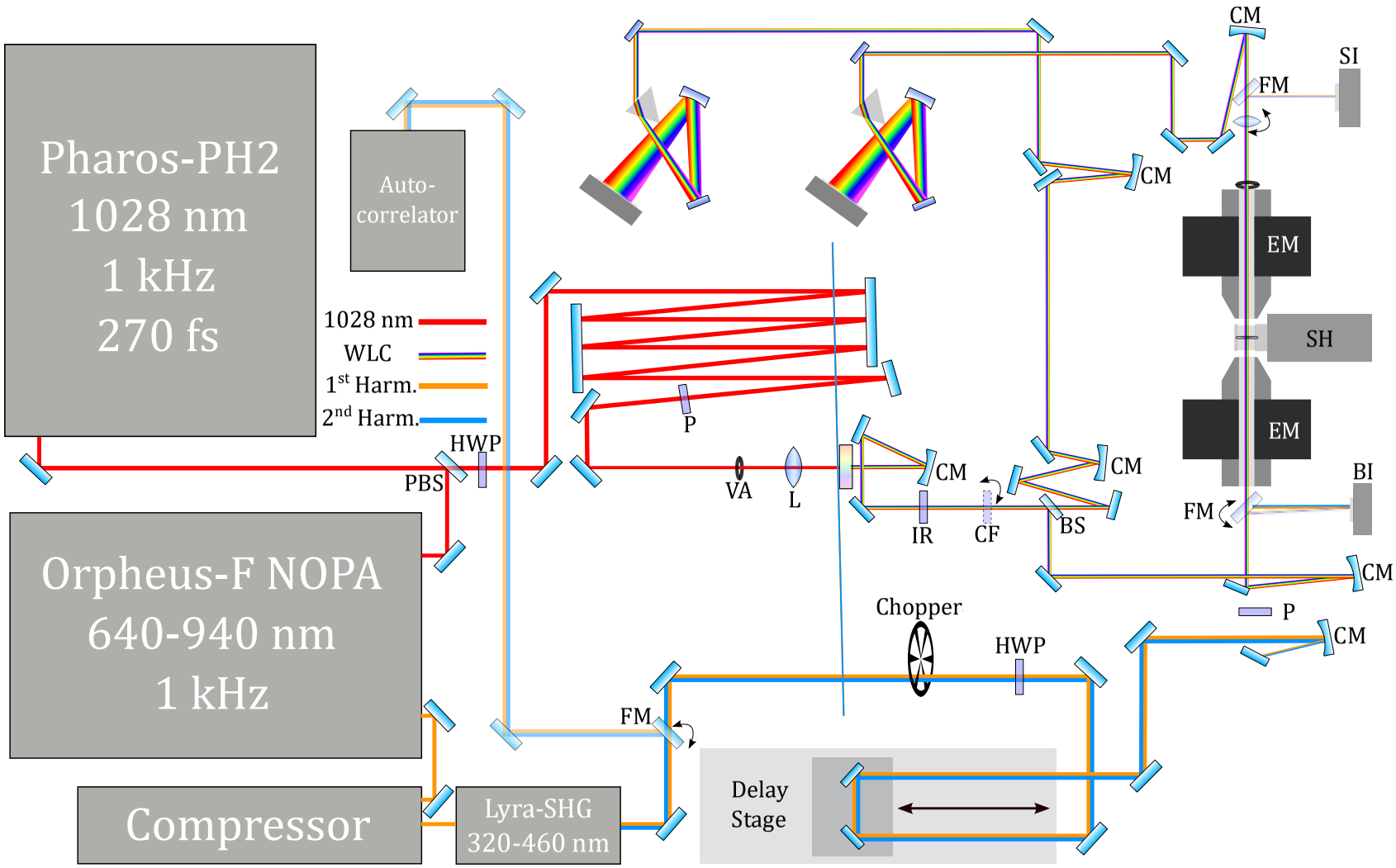

Figure 2.1.2: Schematic of the full optical setup. The small curved double headed arrows indicate a flip mount that can be used to move optics in and out of the beam. Abbreviations: BI; beam imaging, BS; beam splitter, CM; circular mirror, CF; colour filter for wavelength calibration, EM; electromagnet, FM; flip mirror, HWP; half-wave plate, IR; IR filter, L; lens, P; polariser, PBS; polarising beam splitter, SH; sample holder or cryostat, SI; sample imaging camera, VA; variable aperture, WLC; white light continuum.

In the first stage, the supercontinuum and the first part of the pump are overlapped in a BBO crystal facilitating difference frequency generation which creates an idler (the difference frequency of the pump and component of the white-light seed) and a signal (amplified seed beam). Due to the chirp of the supercontinuum, the frequency which is amplified can be selected by altering the temporal overlap of the pump and seed beams via a mechanical delay stage. The second stage operates similarly, the now amplified seed beam which is quasimonochromatic after the first stage is focused into another BBO and combined with the second pump, which further amplifies the seed and also generates a second idler collinear to both the pump and signal beam. Both the signal and idler of the second amplification stage can be taken from the NOPA for use on the optical table although only the signal beam (640–940 nm) is used in this thesis. The signal beam is separated from the pump and idler beams by two dichroic mirrors. The pulse duration is optimised by a double prism compressor. Spectra and autocorrelations for a few selected wavelengths of the NOPA signal are shown in Figure 2.1.3. The spectra were measured using an RGB Laser Systems spectrometer built into the NOPA and the autocorrelations were measured using a APE Pulsecheck-15 autocorrelator. The compressed signal can be frequency doubled in the Light Conversion Lyra, which can produce light with wavelengths 320–470 nm. The compressed signal or its second harmonic is used as the pump pulses in the time-resolved experiments throughout this thesis.

The pump pulses exit the NOPA and are chopped using a Thorlabs MC2000 chopper equipped with the MC1F10 wheel at half the repetition rate of the laser, typically 500 Hz. Every second pump pulse is dumped, which allows the probe to consecutively measure pump-off/pump-on spectra to generate transient absorption difference spectra. A Newport U-BBR2.5-1S corner retroflector mounted on an Aerotech PRO115LM-600 translation stage which is 60 cm long is used to control the timing between pump and probe pulses up to a time delay of around 3 ns. The beam is directed into a half-waveplate-polariser combination to control the power and polarisation of the pump with respect to the polarisation of the probe pulse. A spherical mirror with focal length $f = -50$ cm brings the pump beam into focus just after the sample position. The final mirror before the sample is controlled by a pair of Thorlabs PIAK10 piezoelectric actuators which allows fine adjustment of the spatial overlap of pump and probe horizontally and vertically. The remaining pump after the sample is blocked on the side of an aperture.

2.1.2 Probe Generation

The remaining 10 % of the Pharos output is used to generate the probe beam for use in the transient experiments. The beam first travels through a half-waveplate and

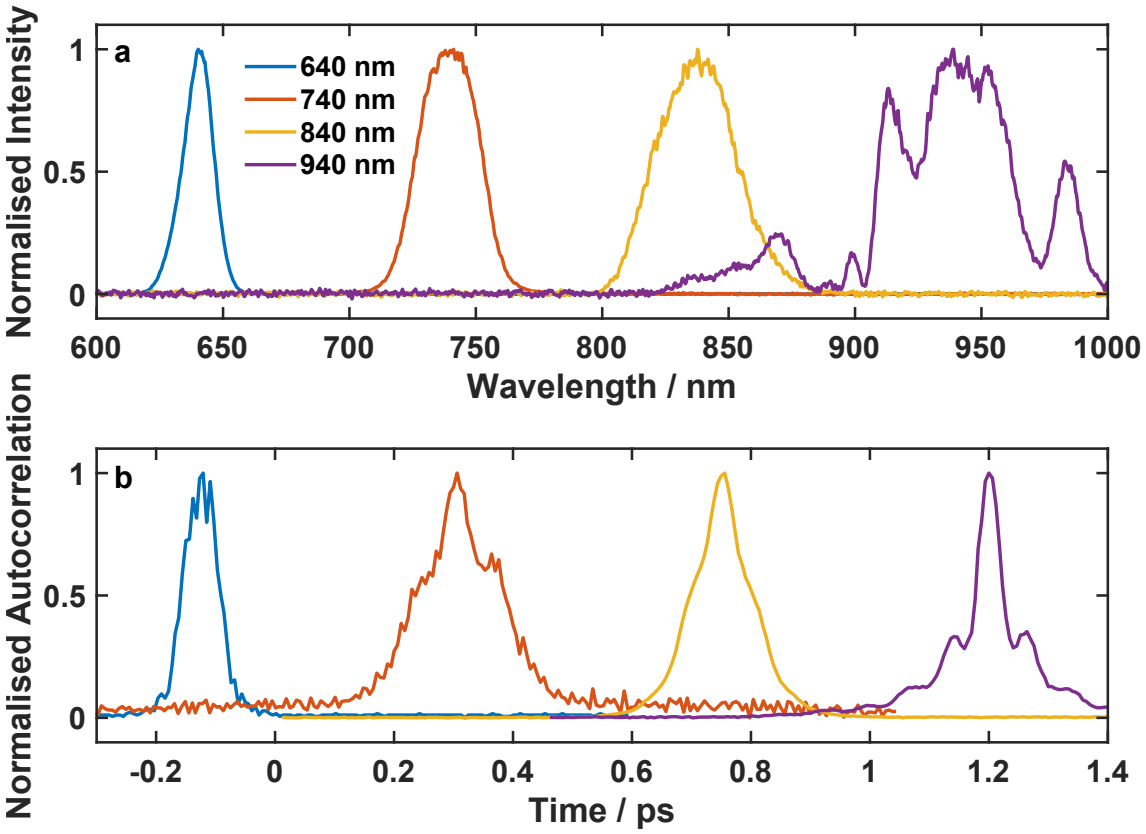

Figure 2.1.3: Selected **a** spectra and **b** autocorrelations of the NOPA output at different wavelengths. The autocorrelations are shifted horizontally to aid visualisation.

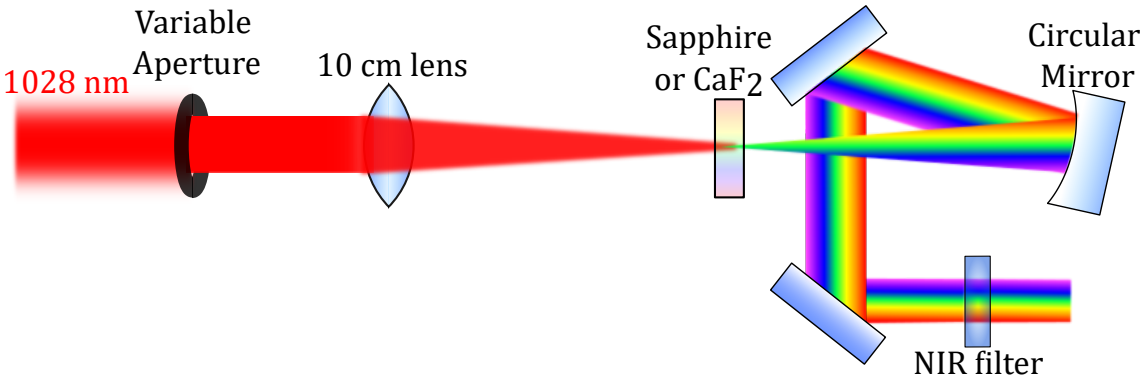

Figure 2.1.4: Optical set-up for white light generation. Around 3 µJ of the 1024 nm Pharos output is used to generate the supercontinuum. The beam travels through a variable aperture to restrict the beam waist and a lens to focus it into the sapphire or CaF_2 plate. Nonlinear optical processes lead to supercontinuum generation and the outgoing beam is recollimated using a spherical mirror and the residual 1024 nm light is removed using a near IR filter. The beam is not dispersed in this process but the rainbow colours are used to signify a white light beam.

polariser to adjust the pulse energy. The polariser (Thorlabs GL10) is set to horizontal (parallel to the optical bench) and the half-waveplate (Thorlabs WPH05M-1030) can be rotated to control the attenuation through the polariser. A pulse energy of around 3 µJ is used. The beam is then directed through a variable aperture set to a diameter of around 5 mm that blocks the outer part of the beam, and a 10 cm convex lens to focus into a nonlinear optical crystal that generates the supercontinuum. The supercontinuum is collimated using a spherical mirror with focal length $f = -10$ cm and the residual pump beam is discarded using a near-IR filter (Newport 10CLVR-1) which cuts off around 850 nm. A diagram of the white-light generation setup is shown in Figure 2.1.4. The angle of the half waveplate, aperture diameter and lens position are used to optimise the supercontinuum spectrum.

The nonlinear optical materials used to generate the white-light probe spectra are sapphire (5 mm) or calcium fluoride (Crystran, 5mm). The average spectrum and standard deviation for 100 pulses are shown for the two materials in Figure 2.1.5. CaF_2 has a wider spectrum extending deeper into the UV (320–850 nm). Although sapphire generates a narrower spectrum (500–850 nm), it has much better stability as evidenced by the lower standard deviation of less than 0.1 %. This is likely due to the need to raster the CaF_2 plate in the plane perpendicular to the beam to prevent thermal damage.[178] Within the region 450–600 nm, white light generation in CaF_2 has a standard deviation of around 0.2 %. However, below 450 nm the standard deviation increases to around 1 %.

Using a beamsplitter, 80 % of the supercontinuum is reflected into the probe line and 20 % is transmitted into the reference line. This double-beam setup allows shot-to-shot spectrally-resolved referencing. The probe beam is directed towards a

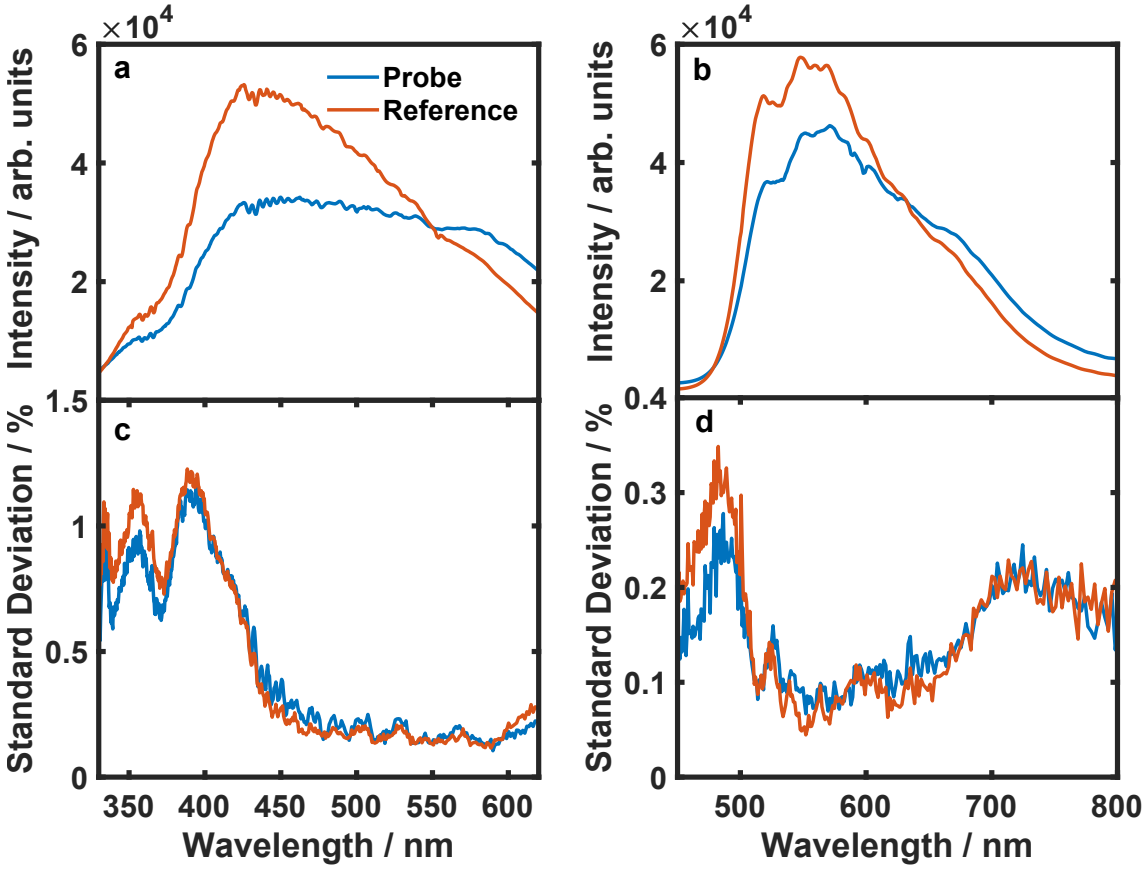

Figure 2.1.5: White light spectra from supercontinuum generation. The figures display the average and standard deviation from 100 laser shots. **a** and **b** show the spectrum obtained from white light generation in CaF_2 and sapphire, respectively. **c** and **d** show the percentage standard deviation at each wavelength obtained from white light generation in CaF_2 and sapphire, respectively.

sample using a spherical mirror with focal length $f = -50$ cm with the sample in the focal position. After the sample, the diverging beam is collimated by another $f = -50$ cm concave spherical mirror and then sent into the spectrometer. Similarly, the reference beam is coupled to the reference spectrometer.

For magnetic circular dichroism measurements, the probe beam must be circularly polarized, and a superachromatic quarter waveplate (Thorlabs SAQWP05M-700) is inserted into the probe line before the entrance to the electromagnet. To ensure circular polarisation, a linear polariser is inserted into the sample position and rotated, pure circular polarisation is achieved when there is no change in beam intensity when the linear polariser is rotated. This is not perfect as the quarter waveplate does not have a retardance of exactly $\frac{\pi}{2}$ or the same fast axis across the spectrum leading to some ellipticity. As long as there are no polarisation optics after the quarter waveplate the signal will be proportional to the magnetic circular dichroism of the sample. The imperfections in the quarter waveplate only allow the MCD intensity to vary up to 5 % across the spectrum.[95]

2.1.3 Detection Scheme

The probe and reference spectrometers spectrally disperse the light using prisms (Eksma Optics 320-1218). The probe enters the spectrometers with horizontal linear polarisation so that it is *p*-polarised with respect to the prism surface. Setting the prism rotation so that the angle of incidence is at the Brewster angle limits the loss of probe intensity through reflection. The spectrally dispersed beams are guided into charge-coupled device (CCD) cameras (Entwicklungsbuero Stresing) equipped with Hammamatsu S7031-0907 sensors. A diagram of the spectrometers is shown in Figure 2.1.6. The sensors are comprised of 512 horizontal and 58 vertical pixels. The probe and reference beams are spectrally dispersed horizontally on the detector and the vertical pixels are binned together which allows synchronised read out of 512 pixels at a rate of 1 kHz. Considering the majority of the supercontinuum is used in the probe line, a graduated neutral density filter is inserted into the beam immediately before the CCD camera to prevent saturation of the detector. A gradient in the neutral density filter attenuates the spectra in the red more than in the blue and therefore it is possible to increase the amount of UV light reaching the CCDs without saturation at longer wavelengths. This can be seen in Figure 2.1.5 as the probe spectrum is more flat than the reference.

The spectrometers must be calibrated to assign a wavelength to the individual horizontal CCD pixels. A 900–1300 nm bandpass filter (Thorlabs, FBG36) is added to the beam before the probe and reference are split. The filter has an intricate absorption spectrum in the UV-visible region and the wavelength of each peak and

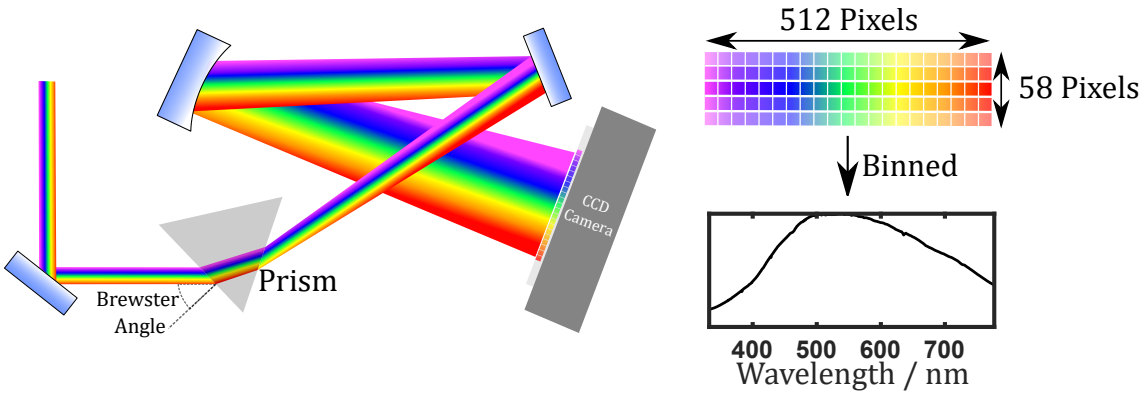

Figure 2.1.6: On the left is the optical layout of reference and probe spectrometers. The right panel shows that the 58 vertical pixels are binned together to get a single 1-dimensional spectrum.

trough is assigned a single pixel (Figure 2.1.7**a**). The corresponding wavelength-pixel data are plotted and fitted with a third-order polynomial as shown in Figure 2.1.7**b**. Consequently, there is a correspondence of pixels to probe and reference wavelengths.

2.1.4 Sample Environment

The sample interaction area is shown in Figure 2.1.8. The pump and probe beams are focused and spatially overlapped within the sample at an angle of around 1 degree. The sample can be solid in the case of thin films or a solution held in a cuvette. In the case of solid samples, they can be mounted inside an Oxford Instruments Microstat-He cryostat with two spectrosil windows to allow propagation of the laser pulses. Within the cryostat, the sample temperature can be controlled between 10–500 K using liquid helium and as low as 77 K using liquid nitrogen. Temperature is adjusted through an Oxford Instruments Mercury iTC controller. The sample is situated between two poles of a water-cooled GMW 3470 electromagnet. Depending on the current supplied, and the distance between the poles, fields up to 0.8 T can be reached. The maximum field when using the cryostat is around 0.5 T as the gap between the poles must be wide enough to accommodate the cryostat (around 2.5 cm). Using a thin cuvette for solution measurements, the gap can be made much smaller (around 3 mm) and fields of around 0.8 T can be reached. Magnetic field strengths are measured using a Hirst GM08 Gaussmeter and are shown as a function of current applied to the electromagnet for pole spacing with the cryostat and with the cuvette in Figure 2.1.9.

While performing MCD measurements, the direction of the current is switched to measure the difference between the two magnetic field orientations. This is equivalent to switching the helicity of light from left to right.[95] Current is supplied to

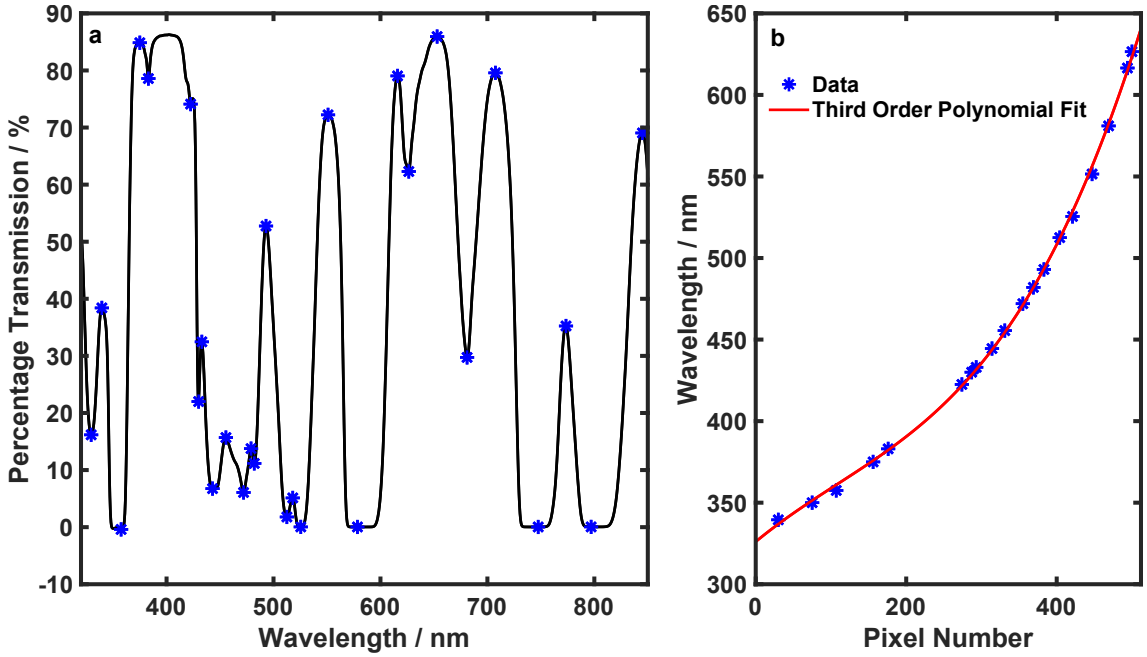

Figure 2.1.7: Wavelength calibration. **a** The transmission spectra of the BG36 filter with the reference points marked at relevant peaks and troughs. The spectrum was measured using a Shimadzu UV-1800 spectrophotometer. **b** Wavelengths at the corresponding pixel number on the CCD detectors. These have been fitted with a third-order polynomial to calibrate the detectors.

the electromagnet by an Aim-TTi CPX400SP power supply which is capable of adjusting current supply and can be controlled using LABVIEW. An Arduino Uno fitted with a relay shield is used to switch the direction of the current and therefore the magnetic field, but this can only handle 4 A. The magnetic field can also be reversed manually using a switch allowing currents up to 5 A to be supplied to the magnet.

Before the sample, a flip mirror can be use to direct the pump and probe into a complementary metal-oxide-semiconductor (CMOS) camera (Basler acA1920-25µm), which is used for beam imaging. The camera sensor is placed at the same

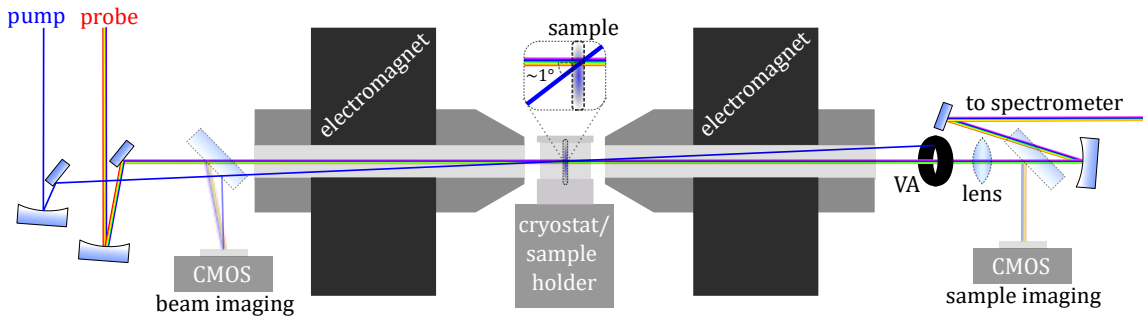

Figure 2.1.8: Diagram of the sample interaction area showing methods of imaging both beam and sample. The transparent optics that are outlined by dotted lines are optional for beam and sample imaging.

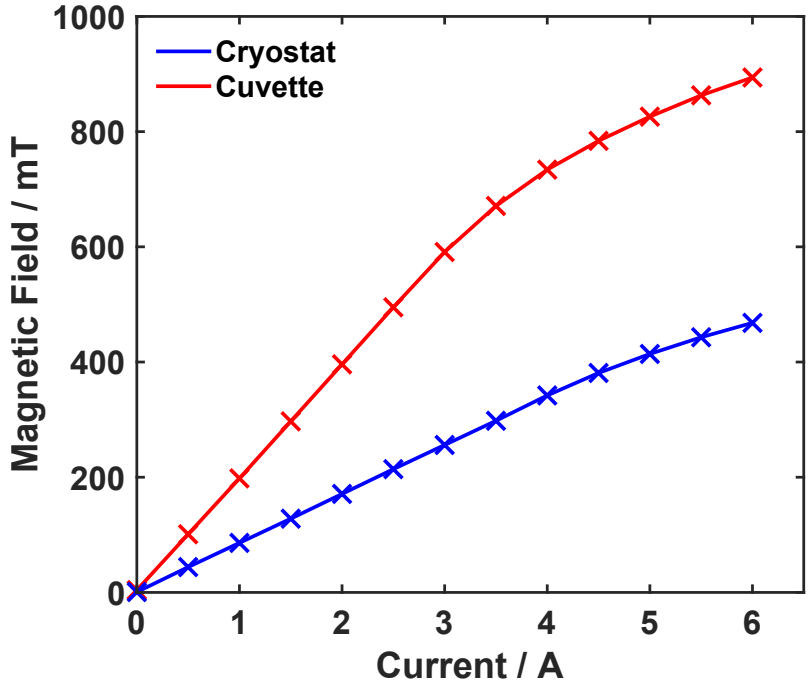

Figure 2.1.9: Magnetic field as a function of current applied to the electromagnet for pole spacing needed for the cryostat and cuvette.

distance away from the focussing mirrors as the sample so the beam morphologies and diameters at the sample can be measured with a resolution of 2.2 µm. The inset in Figure 2.1.10**a** shows a typical beam image taken by the camera. The 2D surface is fitted with the product of two Gaussian functions for the horizontal and vertical directions with different widths, which are used to calculate the area of the beam and therefore the pump fluence. Care must be taken when collimating the probe beam after white light generation as the different wavelength components may not have the same divergence due to processes inherent in supercontinuum generation.[178] Horizontal slices of the beam images are shown for different probe wavelengths in Figure 2.1.10**a** along with the 800 nm pump. In transient absorption, the pump should be larger than the probe to excite all the molecules in the probe diameter and provide as uniform an excitation density as possible across the probe.[181]

Additionally, all the wavelength components of the probe should be around the same size and have maximal overlap with the pump. Assuming the beam profiles of pump and probe are perfect 2D Gaussian functions, in polar coordinates with radial coordinate r, the intensities of the pump (I_{pu}) and probe (I_{pr}) which are separated by distance r_0 in a plane perpendicular to their propagation are given by:

$$I_{\mathrm{pu}} = \frac{A}{2\pi}\exp\left(-\frac{r^2}{2\sigma_{\mathrm{pu}}^2}\right) \quad \text{and} \quad I_{\mathrm{pr}} = \frac{1}{2\pi\sigma_{\mathrm{pr}}^2}\exp\left(-\frac{(r-r_0)^2}{2\sigma_{\mathrm{pr}}^2}\right). \tag{2.1.1}$$

The pump beam has a maximum intensity of $A/2\pi$ and the probe is modelled using a

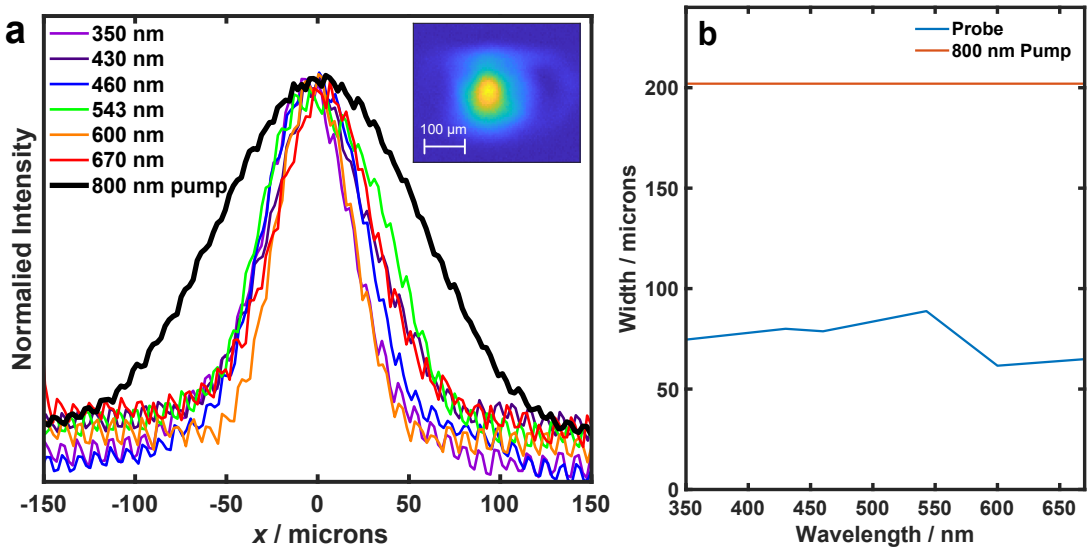

Figure 2.1.10: Beam profiles of the pump and different wavelength components of the probe. **a** Beam intensity of a horizontal slice of the 2D beam profile as a funcion of distance. Inset: Typical image of the beam from the CMOS camera. **b** $1/e^2$ width of the the pump and probe components after fitting the data in **a** with a Gaussian function.

Gaussian with normalised area as it is referenced to the same intensity distribution with pump-on and pump-off. The width of the Gaussian is $\sigma_{\mathrm{pu/pr}}$ for pump and probe beams, respectively. For one-photon excitations, the excitation density and therefore the transient signal is directly proportional to the average pump fluence experienced over the envelope of the probe pulse. This "effective" fluence F_{eff} is given by the area integral over the product of the pump and probe profiles,

$$F_{\mathrm{eff}} \propto \iint_A I_{\mathrm{pr}} I_{\mathrm{pu}}\, dA = \frac{A}{1+(\frac{\sigma_{\mathrm{pr}}}{\sigma_{\mathrm{pu}}})^2} \exp\left[-\left(\frac{r_0}{\sigma_{\mathrm{pr}}}\right)^2 \left(1-\frac{1}{1+(\frac{\sigma_{\mathrm{pr}}}{\sigma_{\mathrm{pu}}})^2}\right)\right]. \qquad (2.1.2)$$

This equation suggests for the maximum transient absorption signal the probe beam should be small compared to the pump to achieve a large fluence. The distribution of probe sizes within our experiment suggests a maximum deviation of 5 % change in F_{eff} over the probe wavelength range (Figure 2.1.10). The best method for ensuring the similarity between probe wavelengths using CaF_2 generated white light was to collimate for wavelengths below 375 nm which yields good circular shapes and similar diameters across the rest of the spectrum, also the UV region is the most difficult to collimate.

After the sample and the electromagnet, there is a second CMOS camera for imaging the position of the probe on the sample and the sample itself. This is particularly useful for inhomogeneous samples and/or samples that are prone to pho-

todamage. The sample can be moved using a Zaber X-LSM025A-E03/X-VSR20A translation stage in the plane perpendicular to the direction of the probe beam and measurements can be made on a homogeneous spot with no damage. This is imaged using a lens and mirror on a flip mount that collimates and directs the probe beam into the CMOS camera. To facilitate the imaging of the sample, a torch is used to illuminate it from behind.

Considering that time-resolved MCD measurements use strong magnetic fields up to 0.8 T that change during measurement, it is important to confirm that the MCD signal does not arise from changing beam positions as the magnetic field switches. Both pump and probe were directed into the beam imaging cameras, and the magnetic field was switched from one direction to another while the beam position on the camera was monitored. There was no change observed so variation in the peak position of the beams was less than the camera resolution ($\leq$ 2.2 µm). Using the typical beam diameters of 100 µm for the probe and 200 µm for the pump, the change in effective fluence for a maximum change in r_0 of 2.2 µm can be estimated with Equation 2.1.2. A change from $r_0 = 0$ to $r_0 = 2.2$ µm reduces F_{eff} by 0.01 %. Taking into account the typical MCD signal of 1 % of total absorbance, movement of the beams due to the magnetic field will have less than a 1 % effect on the magnetic circular dichroism (MCD) intensity.

2.2 Post-Processing and Data Analysis

2.2.1 Post-Processing

The transient absorption data are collected via a LabVIEW program with parameters chosen by the user. The difference spectra are collected at each delay for a total number of n_{t} times for a specified number of laser shots (n_{sh}) which are measured consecutively. The data for n_{sh} shots are averaged for each time delay. This constitutes a single scan. Scans are repeated n_{sc} times. Multiple scans are used to confirm there is no degradation or change of the signal in real time. There is also a filter level to remove the x % highest and lowest intensity CCD signals that can arise from electrical noise or other processes. Typically, this filter is set to 1 %. The LabVIEW program produces a matrix of dimensions $n_\lambda \times n_{\text{t}} \times n_{\text{sc}}$ (where $n_\lambda = 512$ is the number of wavelength points). Therefore, each matrix element contains the differential absorbance at time t, wavelength λ, and for the scan number S. In typical transient absorption measurements, $n_{\text{sh}} \approx 10^3$ and $n_{\text{sc}} = 3$–10. In addition, measurements at negative times are taken ($t_{\text{delay}} < -50$ ps) as background measurements to subtract from the data set. If all scans agree well, they are averaged together to give a final $n_\lambda \times n_{\text{t}}$ dataset.

Typically an MCD signal is less than 1 % of the total absorption signal and therefore MCD measurements are averaged for much longer. Considering a typical sample that has a strong time-resolved absorption signal of around 10-100 mOD, the time-resolved MCD must have a sensitivity in the sub-1 mOD range. In a typical solution-phase MCD measurement, $\geq 10^5$ difference spectra are taken for each field direction and subtracted. Each of the time points in a time-resolved MCD measurement takes around 30 minutes to a few hours to collect. Specific procedures used to handle time-resolved MCD data are provided in Chapter 6.

In the final averaged data set, there are still some corrections to be made. The white light is chirped because of processes inherent in the white-light generation, meaning that each wavelength component arrives at the sample at a different time. To extract a difference spectrum for a single time delay this chirp must be corrected. In transient absorption experiments, there are often extra signals at early times due to nonlinear optical processes. Cross-phase modulation (XPM) occurs when the intense pump induces a variation in the refractive index of the sample as a result of the optical Kerr effect. The consequences of XPM on a transient absorption measurement are shown in Figure 2.2.1. Although this creates problems when attempting to characterise dynamics at early times it provides a good estimate of time zero for each wavelength component. Time zero is chosen at the centre of the XPM signal for around 20 wavelengths across the spectrum and this data is fitted with a 3rd order polynomial with respect to wavelength. The data at each wavelength are shifted in time by the value of that polynomial yielding chirp-corrected transient absorption data (fitting shown in Figure 2.2.1**a**). Generally, XPM is ignored within the fitting as it provides no useful information about the sample being studied.

2.2.2 Data Analysis

Broadband transient absorption measurements produce 2-dimensional data sets of ΔA as a function of both wavelength (λ) and time delay between pump and probe (t). Considering the number of processes that can occur in excited states and their different spectral evolution, there is no standard method of analysing data. Procedures should be chosen based on the features of the particular transient absorption spectra and the goal of the experiment. Generally, one wants to extract time scales for dynamical processes and the nature of those processes (IC, ISC, IVR, *etc.*), and in the process identify different states the molecules access during relaxation.

To extract time scales, the time domain data must be fitted with a kinetic model. Any model can be used if prior knowledge of excited state dynamics is known, but in the absence of this, a parallel or sequential kinetic model is generally used. Schematics of these models are shown in Figure 2.2.2. In a parallel model, it is

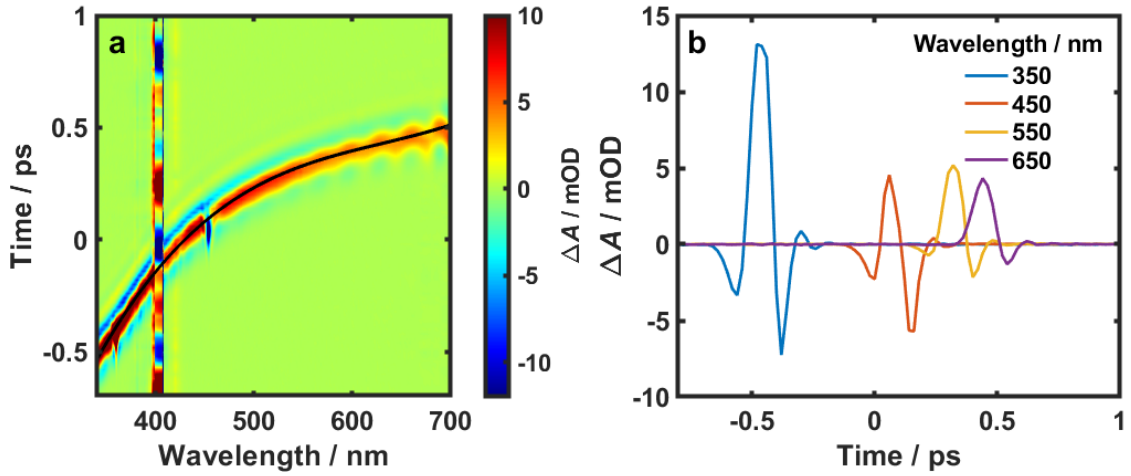

Figure 2.2.1: Transient absorption measurement of pure ethanol in a 200 µm path length cuvette after excitation at 400 nm. **a** Contour plot of the transient absorbance as a function of wavelength and time without chirp correction. The black line overlaid shows a 3rd order polynomial fit to the chirp. The time data is shifted to provide a common time zero for all wavelengths. Pump scatter is seen at 400 nm. **b** XPM signal at different wavelengths as a function of time.

assumed that a number of different states (n) are populated by the pump pulse at $t = 0$ and decay back to the ground state with rate constants k_i where $i = 1$–n. This model is not very physical as it is unlikely that many different electronic states will be populated via a single wavelength excitation; at least there is likely to be one dominant populated state. However, it does give a good estimation of the timescales of the dynamics, particularly if the time constants are well-separated. The sequential model is more physical and describes a relaxation decay without any branching where one species converts to another sequentially until it reaches the ground state. For a parallel model, each component is fitted to the equation:

$$\Delta A(\lambda, t) = \mathrm{IRF}(\sigma, t) \circledast \sum_{i}^{N} A_i \mathrm{e}^{-t/\tau_i} \tag{2.2.1}$$

where A_i is the amplitude of the component with time constant τ_i. The function is convoluted with the instrument response function that is modelled as a Gaussian with width σ that corresponds to the time-domain cross-correlation between the pump and probe pulses. The instrument response takes into account the finite duration of the pump and probe pulses and that all the molecules are not excited simultaneously but over the time profile of the pump pulse and measured over the time profile of the probe pulse.

Global analysis is used to fit the entire 2-dimensional transient absorption data set in Chapter 5. Global analysis fits all wavelength traces at once, sharing the time constants but allowing the amplitude of those components to vary. This relies on

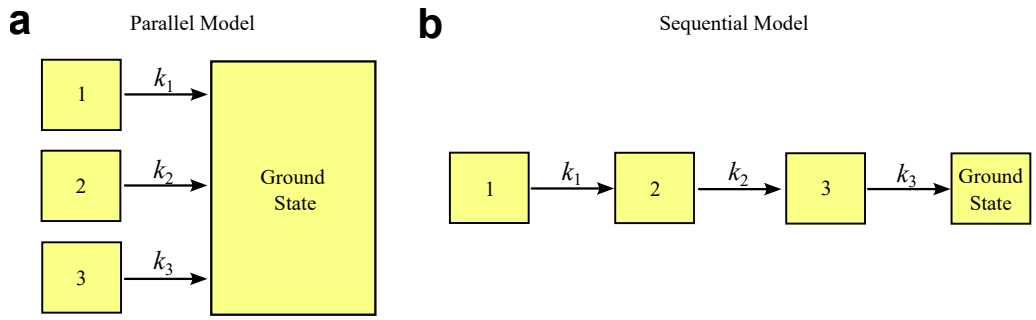

Figure 2.2.2: Schematic of **a** parallel and **b** sequential kinetic models.

the assumption that each species that is accessed during the dynamics has a characteristic spectrum. Therefore, processes such as vibrational relaxation that cause a blueshift and narrowing of excited state absorption bands are not always captured well because the spectra of the species evolves as it redistributes vibrational energy. Global analysis yields decay-associated spectra which describe A_i as a function of wavelength. The features of the decay-associated spectra can be used to identify species when an experimentalist already has prior knowledge of some reference spectra which can be extracted from spectroelectrochemistry or other means.

A significant amount of this thesis is concerned with the observation of coherent vibrational motion that can be identified along the time-domain of a transient absorption measurement. The oscillatory signal cannot be modelled with a sum of exponential components and therefore additional data analysis is required. After fitting a kinetic model to follow the population dynamics, the residuals will contain information about vibrational coherence. To start, the residuals are Fourier transformed to the frequency domain to identify dominant frequency components within the coherence. Simulated data and the corresponding Fourier transform is shown in Figures 2.2.3**a** and **b**. A simple Fourier transform without post-processing often leads to broad peaks due to "spectral leakage" which is caused by the rectangular window over which the Fourier transform is performed due to the finite experimental timescale. If a windowing function is used that limits the discontinuity on the edges of a time-domain signal, it can suppress this leakage. The effects on the time and frequency-domains are shown in Figures 2.2.3**c** and **d** for an applied Hann window. Finally, the data are zero-padded (adding a list of null values at the end of a time-domain signal) which increases the number of points on the frequency axis after Fourier transformation. This does not increase the experimental spectral resolution because this is set by the sampling frequency and the number of steps recorded. However, given the sparseness of points given by a Fourier transform with no zero-padding, it is possible that the maximum value in the spectrum is not the true frequency as it could sit between two discrete points.[111] Zero-padding solves this problem by increasing the density of points in the spectrum. The effect of a

Hann window and 4× zero padding is shown in Figures 2.2.3**e** and **f**.

After the frequencies of the coherent motion have been identified, direct fitting of the oscillations can be carried out. The residuals of the kinetic fit can be fitted to a damped waveform term, $A_{\mathrm{osc}}e^{-t/\tau_{\mathrm{d}}}\cos\left(2\pi c\tilde{\nu}t\right)$. A_{osc} is the amplitude of the oscillations, τ_{d} is the dephasing time of the coherence, c is the speed of light and $\tilde{\nu}$ is the frequency in cm^{-1}. If the oscillations are particularly large in comparison to the exponential population dynamics, then this term can be added to Equation 2.2.1 directly. This is needed for the results in Chapter 3 where the oscillatory part of the dynamics is a magnitude similar to that of the exponential dynamics.

Considering the transient absorption measurements are spectrally resolved a Fourier transform or a waveform fit can be carried out for all wavelength traces in a given measurement. For an entire transient absorption measurement a Fourier transform can be carried out in the time-domain which generates a 2D map of wavelength versus vibrational wavenumber. Alternatively, a global fit of a sum of damped waveforms can be used where the frequency and dephasing times of the coherences are shared between all the wavelengths. Both these methods provides a spectrum associated with a particular vibrational frequency. This spectral-domain information can help distinguish between ground state and excited state vibrational coherences as discussed in Section 1 and it is utilised in Chapters 3 and 5.

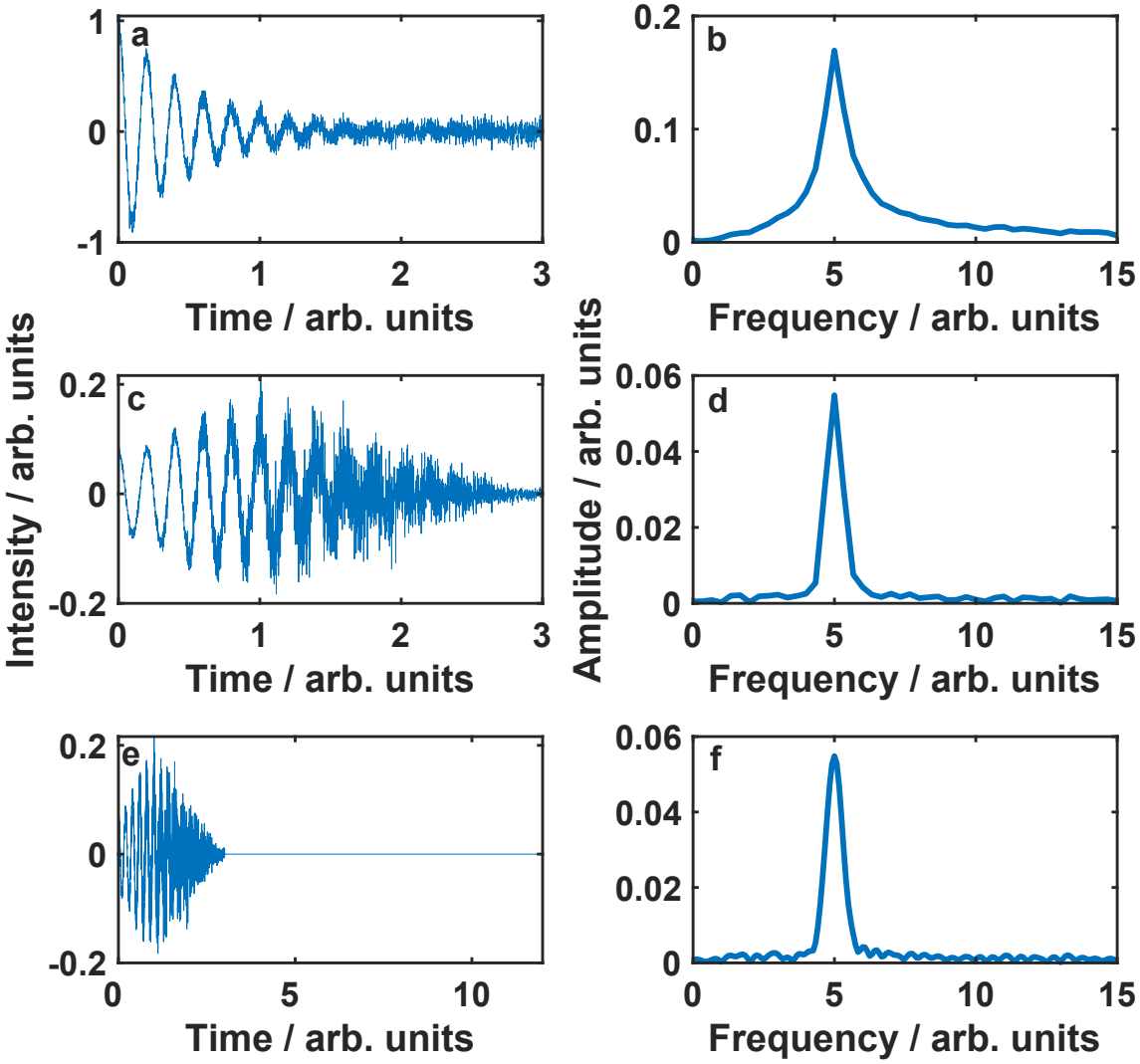

Figure 2.2.3: Effect of post-processing procedures to the fast Fourier transform of simulated oscillatory data. **a** Simulated time domain data of a damped oscillatory waveform with damping time $\tau_{\mathrm{d}} = 0.5$ and frequency $\nu = 5$ with added Gaussian noise $\sigma = 0.05$. **b** Fast Fourier transform of the time domain data in **a** with no post-processing. **c** and **d** Effect of applying a Hann window function to **a** in the time domain and frequency domain showing a reduction of spectral leakage in the Fourier transform. **e** and **f** Effect of applying both a Hann window and 4× zero padding in the time domain and frequency domain, which shows an increase in the density of points in the frequency domain.

Chapter 3

Ultrafast photoinduced Jahn-Teller switch in Mn(III) terpyridine complexes

3.1 Introduction

The first report of vibrational coherences in Mn(III) SMMs after optical excitation was published by the group in 2020.[65] The results of this paper are described in detail in the introduction of this thesis. Considering this was the only report of these coherences in high-spin Mn(III) complexes, there are many open questions about the dynamics of these molecules and the role coherences have within that. How do the ligands affect the frequencies and dephasing times? Does having a dynamic or static Jahn-Teller distortion have an effect? From the previous study,[65] there was a single frequency component and a longer dephasing time in the excited state of the more rigid Mn_3 compared to the more flexible $Mn(acac)_3$, which exhibited two frequency components. Is geometric restriction the reason for the apparent simplification of the reaction coordinate and retention of coherence and, if so, is this still true in mononuclear complexes? Harnessing the information coherences hold may prove vital in controlling the reaction coordinates to influence the magnetic properties in Mn-based SMMs.

Information gathered from coherences has led to synthetic control of ultrafast dynamics in transition metal complexes as shown by Paulus et al.[150] This focused on the frequency of the wavepacket along the reaction coordinate, assigning that to a normal mode and inhibiting that motion via the introduction of structural rigidity. The effect of this rigidity was to increase the MLCT state lifetime 20-fold. Indeed, other studies have shown it is readily possible to influence dynamics by altering molecular structure to disrupt normal modes involved in a reaction coordinate.[114,

158, 159, 182] Although there is an abundance of literature that uses information from coherences to infer details about dynamics, there is a lack of information about how the vibrational dephasing can be changed and/or controlled. Longer vibrational decoherence could be key for magnetic anisotropy control in Mn-based SMMs as it provides a prolonged window where the preferred direction of magnetisation is modulated via Jahn-Teller-active modes.

Vibrational dephasing can occur via population relaxation (T_1) and pure dephasing (T_2^*). Population relaxation is generally controlled by the rate of intramolecular vibrational redistribution (IVR) and vibrational cooling (VC) to the solvent bath. Slow IVR has been suggested as the reason for the long multi-picosecond vibrational dephasing time in cresyl violet where the coherent mode is nearly harmonic and therefore has minimal coupling to the other normal modes of the molecule.[183] The long dephasing time of a Pt−Pt stretching mode in $[Pt_2(P_2O_5H_2)_4]^{4-}$ (PtPOP) was attributed to slow VC. The authors proposed energy loss to the solvent from this mode is suppressed by "shielding" provided by the bulky POP ligand.[184] This is similar to vibrational decoherence of dihalogens in noble gas matrices where the local mode in Br_2 is decoupled from the bulk phonons.[185] Vibrational dephasing times ranging from 0.3 – 2.6 ps have been observed in $Cr(acac)_3$ and its derivatives with no change in lifetimes of electronic states.[159] The reasons for the large range of dephasing times for these structurally similar complexes is not known. These reports imply that synthetic modification could lead to long-lived vibrational coherence but currently there is no solid criteria which can guide molecular design towards this goal.

In order to investigate the effect of synthetic modification on vibrational wavepackets in Mn(III) complexes, a series of $[Mn(terpy)X_3]$ complexes where terpy = 2,2':6',6"-terpyridine and X = Cl, F and N_3 were studied. The molecular structure is shown in Figure 3.3.1**a**. These differ with respect to $Mn(acac)_3$ as the heteroleptic nature of the complexes means there are three distinct bonding axes, which creates a static Jahn-Teller elongation fixed along the N_{eq}−Mn−N_{eq} axis in the ground state.

This chapter presents an investigation of the electronic structure and dynamics of $[Mn(terpy)X_3]$ complexes through a combination of experimental and computational methods. All spectroscopic measurements detailed in this chapter were conducted and analysed by myself and the computation was carried out by Julien Eng and Tom Penfold at the University of Newcastle. The findings presented herein have been the subject of a publication.[186]

Complex	Solvent	c (mM)	λ_{pump} (nm)	d_{pump} (µm)	F (mJ/cm^2)
[Mn(terpy)Cl_3]	DMF	35	400	234	9.4
[Mn(terpy)F_3]	Ethanol	25	750	210	7.9
[Mn(terpy)$(N_3)_3$]	Ethanol	15	800	216	9.8

Table 3.2.1: Experimental parameters for the transient absorption measurements of [Mn(terpy)X_3]. The path length was 0.2 mm. The solution was flowed at 16 µL/min and the probe diameter was 100 µm for all measurements.

3.2 Methods

3.2.1 Synthesis and Characterisation

Synthesis of the complexes was carried out by Iona Ivalo and Marco Coletta at the University of Edinburgh. The synthetic procedures were followed from literature for [Mn(terpy)Cl_3],[187] [Mn(terpy)F_3][188] and [Mn(terpy)$(N_3)_3$][189]. UV-Vis spectroscopy was carried out using a Shimadzu UV-1800 spectrophotometer using a 1 cm quartz cuvette. [Mn(terpy)F_3] and [Mn(terpy)$(N_3)_3$] were dissolved in ethanol and [Mn(terpy)Cl_3] was dissolved in dimethylformamide (DMF). Raman spectra were acquired using a Renishaw Raman microscope with a laser wavelength of 785 nm.

3.2.2 Time-Resolved Measurements

The transient absorption set-up is described in detail in chapter 2, particular experimental parameters used are highlighted here. [Mn(terpy)F_3] and [Mn(terpy)$(N_3)_3$] were dissolved in ethanol and photoexcited at their lowest energy transition $^5B_1 \rightarrow {}^5A_1$ (d_{z^2} to $d_{x^2-y^2}$). [Mn(terpy)Cl_3] could not be photoexcited at this wavelength due to the transition being outside the NOPA wavelength range. Instead, [Mn(terpy)Cl_3] was pumped using 400 nm light which corresponds to the $^5B_1 \rightarrow {}^5E_1$ ($d_{xz/yz} \rightarrow d_{x^2-y^2}$) transition. Furthermore, the low solubility of [Mn(terpy)Cl_3] in ethanol meant that the absorption measurements had to be carried out in DMF. The concentrations of the samples in the transient absorption measurements were such that the optical densities at the pump wavelength were in the region 0.01 – 0.2 OD. The pump polarisation was set to the magic angle (54.7°) relative to the probe. The exact parameters used for excitation are shown in Table 3.2.1. The samples were flowed through a 0.2 mm pathlength Starna flow cuvette at a rate of 16 µL/min during the measurements. The probe beam spectra spanned 320–720 nm and had a beam diameter of around 100 µm at the sample. For each scan, 1500 difference spectra were recorded at each time delay, 5 scans were performed so each average difference spectra consisted of 7500 individual spectra.

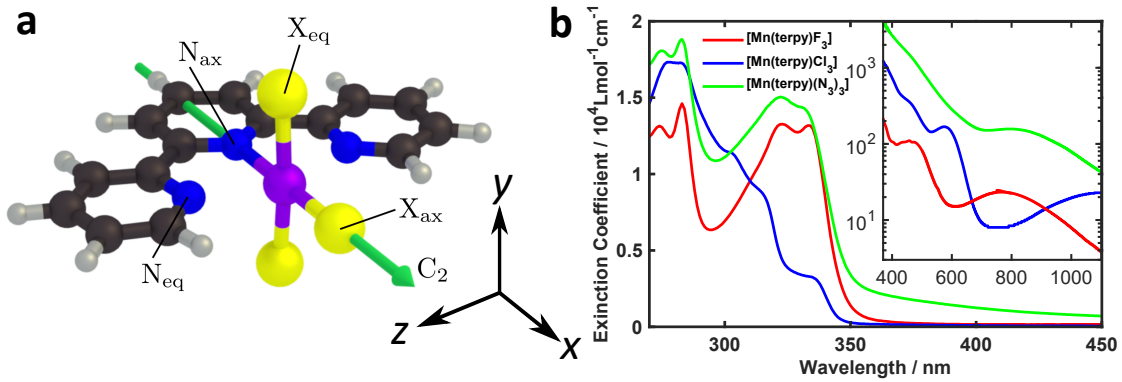

Figure 3.3.1: **a** Structure of [Mn(terpy)X_3] with C_2 axis marked. Mn; purple, N; blue, X; yellow, C; black, H; grey. **b** UV-vis spectra of [Mn(terpy)X_3] where X = F and N_3 were dissolved in ethanol and X = Cl was dissolved in DMF. Inset: ligand-field transitions > 400 nm. Figures are adapted from ref. [186].

Complex	Mn−X_{ax} / Å	Mn−X_{eq} / Å	Mn−N_{ax} / Å	Mn−N_{eq} / Å
[Mn(terpy)Cl_3]	2.23	2.26	2.2	2.25
[Mn(terpy)F_3]	1.78	1.78	1.89	1.97
[Mn(terpy)$(N_3)_3$]	1.92	1.95	2.14	2.27

Table 3.3.1: Ground state structural parameters of the inner coordination sphere for [Mn(terpy)X_3] from from DFT (PBE0) calculations.

3.3 Results and Discussion

3.3.1 Ground State Characterisation

The geometry of [Mn(terpy)X_3] is shown in Figure 3.3.1**a** where the C_2 axis is highlighted, axial (ax) positions are defined along this axis and equatorial (eq) positions are in the plane perpendicular to the C_2 axis. Strictly, there is no C_2 axis in [Mn(terpy)$(N_3)_3$] due to rotation of the azide units but the axial positions are defined similarly. Jahn-Teller elongation is present in all three complexes along the N_{eq}−Mn−N_{eq} bonds in agreement with crystal structures.[187–189] Bond lengths that describe the first coordination sphere of [Mn(terpy)X_3] are given in Table 3.3.1.

UV-visible spectra of the three complexes are presented in Figure 3.3.1**b**. Charge transfer transitions are observed in all three complexes complexes below 350 nm, although [Mn(terpy)$(N_3)_3$] has a long tail in the charge transfer transitions that carries out to the visible region. Charge transfer spectra of [Mn(terpy)F_3] and [Mn(terpy)$(N_3)_3$] are very similar, likely arising from transitions involving the terpyridine unit as this is common to all the complexes. These transitions are different in [Mn(terpy)Cl_3], likely due to the change in solvent which can strongly effect charge transfer transitions,[190] however the peaks remain at roughly the same en-

Complex	$^5B_1 \rightarrow {}^5A_1$ (nm)	$^5B_1 \rightarrow {}^5A_2$ (nm)	$^5B_1 \rightarrow {}^5E_1$ (nm)
[Mn(terpy)Cl_3] (calc.)	1100(925)	580(566)	460(490)
[Mn(terpy)F_3]	750	510	470
[Mn(terpy)$(N_3)_3$]	800	520	450

Table 3.3.2: Electronic transitions of [Mn(terpy)Cl_3], [Mn(terpy)F_3] and [Mn(terpy)$(N_3)_3$] from UV-Vis spectra in Figure 3.3.1**b**. The calculated CASSCF/NEVPT2 transition energies are shown in brackets for [Mn(terpy)Cl_3].

ergy. Ligand-field transitions above 400 nm are displayed in the inset. The C_{2v} symmetry of these complexes means there should be four spin-allowed ligand-field transitions, however, the splitting of the two highest energy transitions is too small to be reliably distinguished.[64] Therefore, three absorptions arising from the lowest energy $^5B_1 \rightarrow {}^5A_1(d_{z^2} \rightarrow d_{x^2-y^2})$, $^5B_1 \rightarrow {}^5A_2$ ($d_{xy} \rightarrow d_{x^2-y^2}$) and the psuedodegenerate $^5B_1 \rightarrow {}^5E_1$ ($d_{xz/yz} \rightarrow d_{x^2-y^2}$) transitions are observed. The extinction coefficients are within 10–100 $M^{-1}cm^{-1}$, which places them firmly as ligand-field transitions. The wavelengths of these transitions are summarised in Table 3.3.2. The energies of the lowest ligand-field transition decrease as X becomes a weaker field ligand ($F^- > N_3^- > Cl^-$), as expected.

Electronic transitions of [Mn(terpy)Cl_3] were computed by Julien Eng and Tom Penfold at the University of Newcastle using a complete active space self-consistent field (CASSCF)/n-electron valence perturbation theory 2 (NEVPT2) approach. The computed transitions of the metal-centred quintet excited states are shown in Table 3.3.2. Along with the transition energies the change in electronic density upon excitation was computed. The electron density difference map of the $^5B_1 \rightarrow {}^5A_1$ ($d_{z^2} \rightarrow d_{x^2-y^2}$) transition is shown in Figure 3.3.2**a**. This clearly indicates a shift of electron density from the d_{z^2} orbital to the $d_{x^2-y^2}$ orbital.

3.3.2 Time-Resolved Measurements

Armed with the knowledge of the electronic transitions and changes in electron configurations associated with them, transient absorption spectroscopy was carried out exciting the lowest energy ligand-field transition in [Mn(terpy)F_3] and [Mn(terpy)$(N_3)_3$] (corresponding to a one-electron transition from the d_{z^2} to the $d_{x^2-y^2}$ orbital) and the d_{xz}/d_{yz} to $d_{x^2-y^2}$ transition in [Mn(terpy)Cl_3].

The transient absorption difference spectra for the three complexes are shown in Figure 3.3.3**a**. All three complexes display strong excited state absorptions occurring around and below 350 nm. In addition to this peak, there is a broad flat absorption in the visible region for [Mn(terpy)Cl_3]. The ESA in [Mn(terpy)$(N_3)_3$] has some peak structure in the visible region perhaps from redshifted LMCTs from the azide

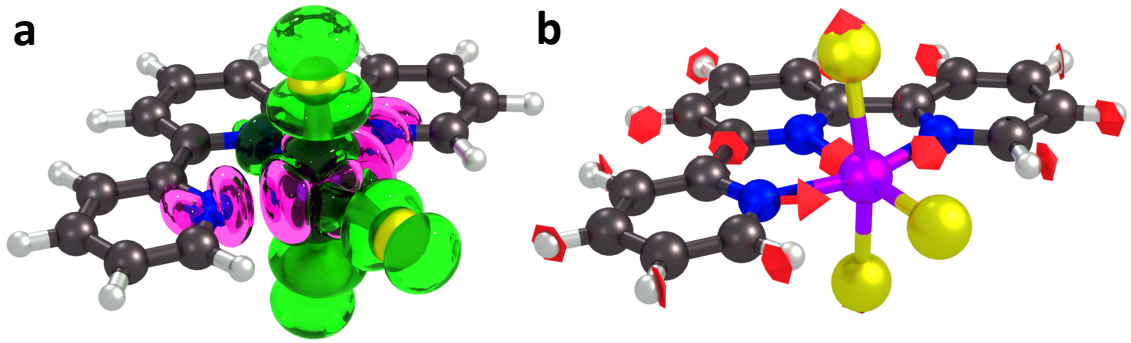

Figure 3.3.2: **a** Change of electron density map after $^5B_1 \rightarrow {}^5A_1(d_{z^2} \rightarrow d_{x^2-y^2})$ photoexcitation in $[Mn(terpy)Cl_3]$. Green; increase, pink; decrease. There is a clear transfer of electron density away from the d_{z^2} orbital into the $d_{x^2-y^2}$. **b** A frequency analysis at the point close to the conical intersection between the first excited state and the ground state reveals one imaginary frequency that corresponds to a combination of q_{10} and q_{21} in $[Mn(terpy)Cl_3]$. The red arrows indicate the vibrational motion that takes the nuclei away from the Franck-Condon region to the conical intersection. The nuclear rearrangement agrees well with the expected change from the change in electron density. Figures are adapted from ref. [186].

ligand after photoexcitation. LMCT transitions from halogen atoms to the Mn(III) centre are likely too far in the UV to observe in the probe region.[191] As the peak at 350 nm is common to all three complexes, this must be a transition arising from the manganese and/or the terpyridine ligand. Considering the intraligand transition is at 290 nm in free terpyridine[192] and ligand-field excitations have little affect on these it is unlikely to be a π–π^* transition. An excited ligand-field transition is also unlikely as the oscillator strength of the band is on the order of the LMCT observed in the $[Mn(terpy)(N_3)_3]$ data. We would expect it to be roughly two orders of magnitude weaker as it would be a Laporte forbidden transition. Additionally, the onset of the charge transfer transitions in the ground state is around 350 nm, if the excited state absorption of these complexes was a ligand-field transition the charge transfer GSB would completely dominate any excited ligand-field transitions leading to a negative signal. MLCT or LMCT involving the terpyridine ligand therefore must be be the origin of this band.

Kinetic traces are shown in Figure 3.3.3**b** for each of the complexes. The probe wavelength is at the peak of the 350 nm absorption. As well as the exponential population dynamics, large oscillatory modulations of the absorption are superimposed on the signal. Both components were fitted using Equation 3.3.1 which comprises two exponential components to take into account the population dynamics and a decaying cosinusoid to fit the vibrational wavepacket.

$$\Delta A = \mathrm{IRF}(\sigma, t) \circledast \left(\sum_{i=1}^{2} A_i e^{-t/\tau_i} + A_{\mathrm{osc}} e^{-t/\tau_\mathrm{d}} \cos\left(2\pi c \tilde{\nu} t\right) \right) \tag{3.3.1}$$

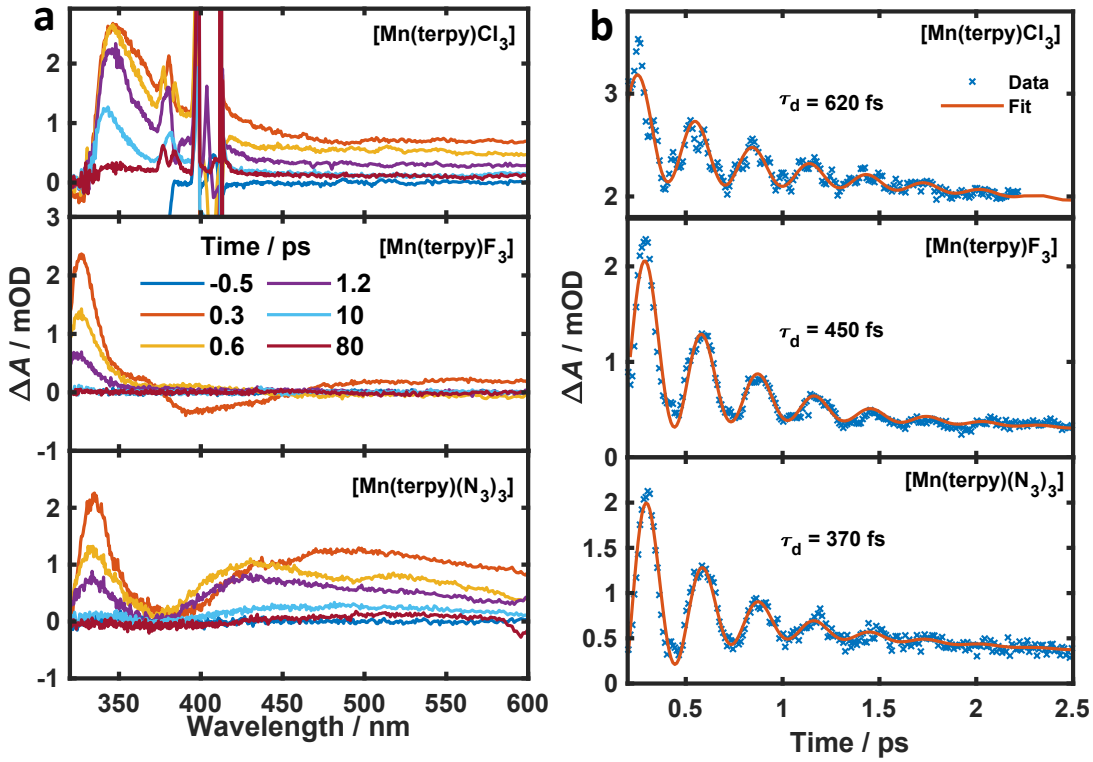

Figure 3.3.3: Results of the transient absorption experiments after exciting $[Mn(terpy)Cl_3]$ at 400 nm, $[Mn(terpy)F_3]$ at 750 nm and $[Mn(terpy)(N_3)_3]$ at 800 nm. **a** Differential absorbance spectra of all three complexes at selected time delays. **b** Kinetic traces taken at the excited state absorption maxima with fit using Equation 3.3.1. The probe wavelength is 350, 340 and 343 nm for $[Mn(terpy)Cl_3]$, $[Mn(terpy)F_3]$ and $[Mn(terpy)(N_3)_3]$, respectively. Figures are adapted from ref. [186].

This equation takes into account the finite pulse duration of the pump and probe via the instrument response function (IRF(σ, t)), which is the time-domain cross-correlation function of the pump and probe pulses. It is modelled as a Gaussian function with width σ ($\sigma \approx 80$ fs). A_i is the amplitude of an exponential decay with a time constant τ_i, the parameters for the oscillatory part of the fit are the amplitude A_{osc}, frequency $\tilde{\nu}$ and dephasing time τ_{d}.

The fit gave oscillation frequencies of $\tilde{\nu} = 113 \pm 1$, 115 ± 1, and 115 ± 1 cm^{-1} for [Mn(terpy)Cl_3], [Mn(terpy)F_3], and [Mn(terpy)$(N_3)_3$], respectively. The corresponding dephasing times were $\tau_{\mathrm{d}} = 620 \pm 40$, 450 ± 20 and 370 ± 10 fs. The kinetics in the UV decayed with two components with time constants $\tau_1 = 330 \pm 40$ fs and $\tau_2 = 11.7 \pm 0.1$ ps for [Mn(terpy)Cl_3]; $\tau_1 = 450 \pm 20$ fs and $\tau_2 = 4.0 \pm 0.2$ ps for [Mn(terpy)F_3]; and $\tau_1 = 850 \pm 60$ fs and $\tau_2 = 9 \pm 1$ ps for [Mn(terpy)$(N_3)_3$]. These parameters are summarised in Table 3.3.3. The transient absorption of [Mn(terpy)F_3] showed no signal in the visible, and none of the complexes showed significant oscillations in the visible region from the sample. The visible ESA is likely to originate from a different transition than the UV peak observed in [Mn(terpy)Cl_3] and [Mn(terpy)F_3] and the visible region is only marginally sensitive to the wavepacket in [Mn(terpy)$(N_3)_3$] at 460 nm (Figure 3.3.4). The visible traces, fits and Fourier transform of residues are shown in Figure 3.3.4. The time constants for traces at 460 nm were the same as the peak of the ESA apart from [Mn(terpy)Cl_3] where τ_2 was smaller, 2.4 ± 0.3 ps.

Considering the lowest energy transition was excited in [Mn(terpy)F_3] and [Mn(terpy)(N_3)], the only processes that can occur are IVR/VC and relaxation to the ground state. Considering τ_1 is accompanied by a slight blueshift of the ESA this is assigned to IVR in the first excited state as vibrational cooling to the solvent bath tends to occur over a few picoseconds not hundreds of femtoseconds.[193] τ_2 is accompanied by a return to zero signal and is assigned as IC back to the ground state. The transient absorption spectra of [Mn(terpy)Cl_3] can have extra components arising from IC between higher lying levels due to the population of higher excited states. τ_1 is likely a combination of IC between these states along with IVR. τ_2 is defined as return to the ground state although there is a small offset to the signal at longer times which suggests some population may get trapped in the lowest excited state.

Interestingly, the frequency of the oscillations was found to be essentially the same for all three complexes. Immediately, it is possible to infer that the normal mode associated with the oscillations in the kinetic traces is overwhelmingly dominated by motion of the terpy ligand and/or the metal-centre. If the normal mode involved significant motion of Cl, F or N_3 we would expect the frequency to be different for each of the three complexes. Returning to the one electron picture of transitions which involves a transfer of electron density from d_{z^2} to $d_{x^2-y^2}$ (this

Complex	τ_1 / fs	τ_2 / ps	$\tilde{\nu}$ / cm^{-1}	τ_d / fs
[Mn(terpy)Cl_3]	330 ± 40	11.7 ± 0.1	113 ± 1	620 ± 40
[Mn(terpy)F_3]	450 ± 20	4.0 ± 0.2	115 ± 1	450 ± 20
[Mn(terpy)$(N_3)_3$]	850 ± 60	9 ± 1	115 ± 1	370 ± 10

Table 3.3.3: Calculated fitting parameters from Equation3.3.1. The fits were carried out at the excited state absorption maxima and are shown in Figure 3.3.3**b**.

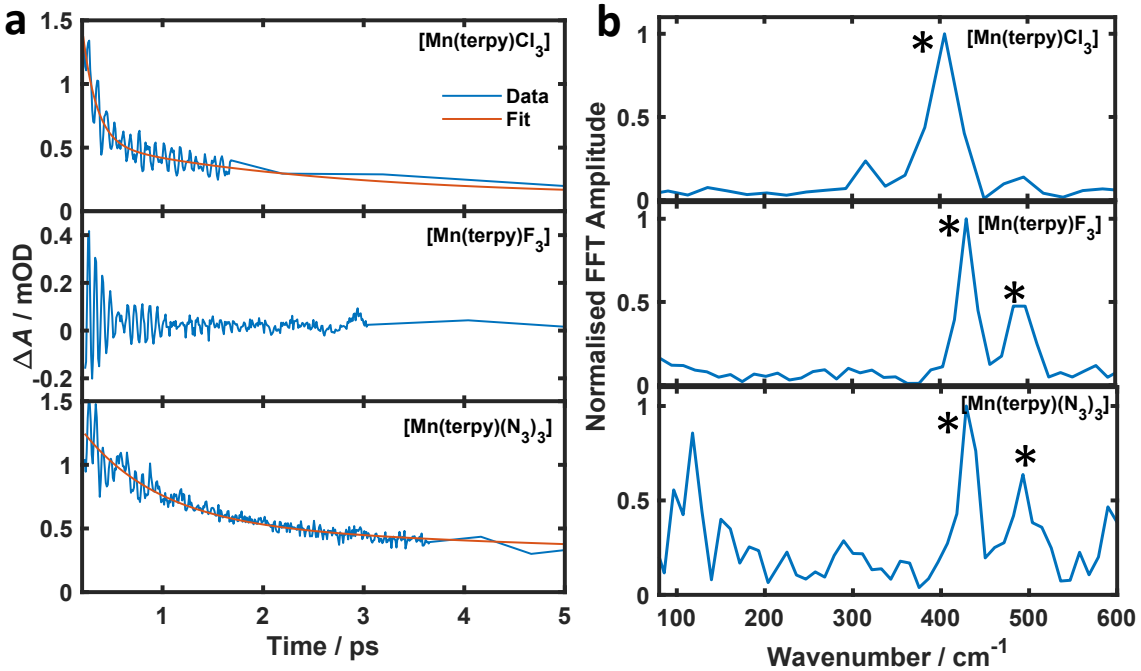

Figure 3.3.4: Dynamics observed at a probe wavelength of 460 nm. **a** Kinetic trace data and fit for [Mn(terpy)X_3]. [Mn(terpy)Cl_3] and [Mn(terpy)$(N_3)_3$] were fitted with just 2 exponential components reflecting the population dynamics. [Mn(terpy)F_3] was not fitted as it shows no population dynamics at this wavelength. The fitted time constants agreed with those found fitting the peak of the excited state absorption (Table 3.3.3) apart from τ_2 for [Mn(terpy)Cl_3] which was 2.4 ± 0.3 ps. **b** Fourier Transform of the residuals following subtraction of the population dynamics. The asterisk (*) denotes signals arising from solvent and cuvette only measurements. There are no oscillations from the sample for [Mn(terpy)Cl_3] and [Mn(terpy)F_3] in this region. The same 115 cm^{-1} frequency seen in Figure 3.3.3 is observed for [Mn(terpy)$(N_3)_3$], however. The step size of the time delay was changed during the measurements. Figures are adapted from ref. [186].

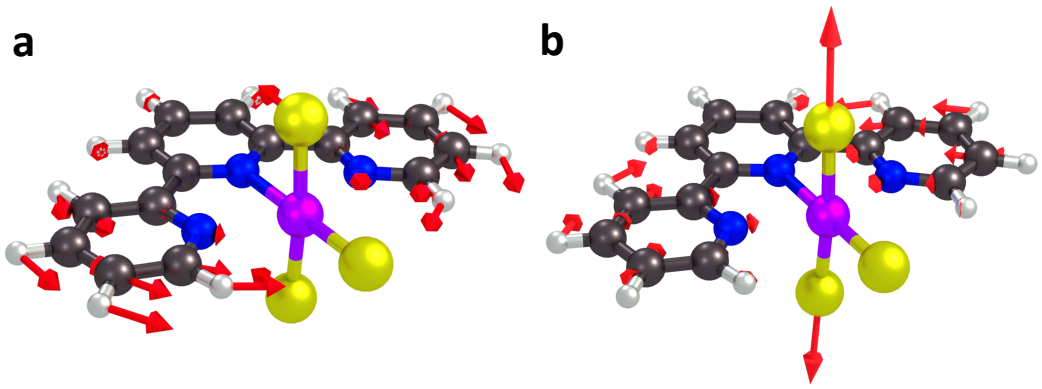

Figure 3.3.5: Eigenvectors of normal modes that decrease the energy gap between $^5B_1$ and $^5A_1$ states in [Mn(terpy)Cl_3]. **a** The pincer-like mode q_{10} ($\omega_{10} = 97.8$ cm^{-1}) which is observed in the transients. **b** the symmetrical breathing mode q_{21} ($\omega_{21} = 273.4$ cm^{-1}). Figures are adapted from ref. [186].

is clearly seen in the electron density difference map for the lowest energy transition in Figure 3.3.2**a**), these are both antibonding e orbitals suggesting that the excitation will lead to an extension of the N_{ax}−Mn bond and a contraction of the N_{eq}−Mn bonds. From this we can hypothesise that the vibrational wavepacket observed in the transient spectra arises from a pincer-like motion of the terpyridine ligand around the metal ion where a shortening of the N_{eq}−Mn bonds is accompanied by a lengthening of the N_{eq}−Mn bond and *vice versa* (Figure 3.3.5**a**). This mode has previously been observed in $[Co(terpy)]^{2+}$ in an ultrafast X-ray scattering experiment with a frequency of 150 cm^{-1} where Jahn-Teller distortion is activated by photoexcitation.[66] Pincer-like modes have also been observed in the ground state of [Pt(terpy)(S−glutathionato)]$^{2+}$[194] and $[Ru(terpy)_2]^{2+}$[195] at 111 and 80 cm^{-1}, respectively. 113–115 cm^{-1} therefore seems reasonable for these modes in [Mn(terpy)X_3].

For additional verification of this mode, electronic structure calculations were carried out along normal modes (q_i, where i is the number of the normal mode starting from the lowest frequency) in [Mn(terpy)Cl_3] to find which modes decreased the energy between $^5A_1$ and $^5B_1$ the most. Two modes are significant in lowering the energy gap, q_{10} ($\omega_{10} = 97.8$ cm^{-1}) and q_{21} ($\omega_{21} = 273.4$ cm^{-1}). The eigenvectors of these modes are shown in Figure 3.3.5. q_{10} involves a pincer-like motion of the terpyridine ligand with a small modulation of the Cl_{eq}−Mn−Cl_{eq} angle and has a frequency close to the experimental frequency suggesting that it is indeed the mode observed in the transient spectra and supports the hypothesis based on purely experimental observations discussed in the previous paragraph.

The second mode, q_{21} consists mostly of a symmetrical stretch of the two Mn−Cl_{eq} and a small symmetrical breathing motion of the terpyridine. This is not observed

in the transient spectra but is likely seen in the Raman spectra (Figure 3.3.7**a**). The lack of sensitivity to this mode in the transient absorption may stem from the weak ligand field of Cl, F and N_3 compared to the terpyridine ligand. As q_{21} (and corresponding modes in [Mn(terpy)F_3] and [Mn(terpy)$(N_3)_3$]) involve large changes in the Mn−X_{eq} bonds, but minimal motion of the other bonds, there will only be a slight modulation of the electronic structure due to the weak-field nature of Cl, F and N_3. Secondly, the breathing mode is more symmetrical than the pincer-mode, which is likely to modulate the oscillator strength of a transition significantly less.

To further support the assignment of these modes as part of the reaction coordinate, computations to calculate the geometry of the conical intersection between the ground state and first excited state were carried out. This was composed of one imaginary frequency corresponding to a combination of q_{10} and q_{21} (Figure 3.3.2**b**), suggesting these are the distortions that take place upon excitation and define the majority of the reaction coordinate. Indeed, the nuclear rearrangement in the excited state is consistent with change of electron density. The contraction of the axial N_{ax}−Mn bonds accompanied by the expansion of the equatorial bonds confirms a Jahn-Teller switch on ultrafast timescales.

Using Kubo's lineshape theory,[117] Raman spectra can be used to estimate dephasing times of coherent vibrations and therefore validate some conclusions made thus far. The linewidth of a Raman peak is inversely proportional to dephasing times due to the Fourier transform relationship between signals in the time and frequency-domain. The equation $\tau_d = \frac{\pi}{c \times \sigma}$ where σ is the full width half maxima (FWHM) of a Lorentzian fit can be used to calculate dephasing times.[196] The peaks between 100–200 cm^{-1} were fitted (Figure 3.3.6**a**), the dephasing times from both the transient absorption and Raman linewidth measurements are plotted in Figure 3.3.6**b**. The dephasing times from both methods are well-correlated and provide a strong indication that the peaks at 113–115 cm^{-1} in the Raman spectra are the same mode observed in the excited state transient absorption signal. Although there is a good linear correlation with the three data points they do deviate from the theoretical values. There may be a few reasons for this, the vibration in the transient experiment is likely on the excited state potential (see below) whilst the Raman probes the ground state. Secondly, the Raman spectrum was measured with powdered samples whereas the absorption measurements were in solution.

As discussed in the introduction, vibrational coherences in transient absorption spectra can arise from both a coherence generated on the excited state potential through a displacive mechanism and a coherence on the ground state potential produced via an impulsive Raman process. The peak in the Fourier transform of the kinetic trace, after subtracting the exponential population dynamics, is found close to peaks in the ground state Raman (Figure 3.3.7**a**) and the linewidth in the ground

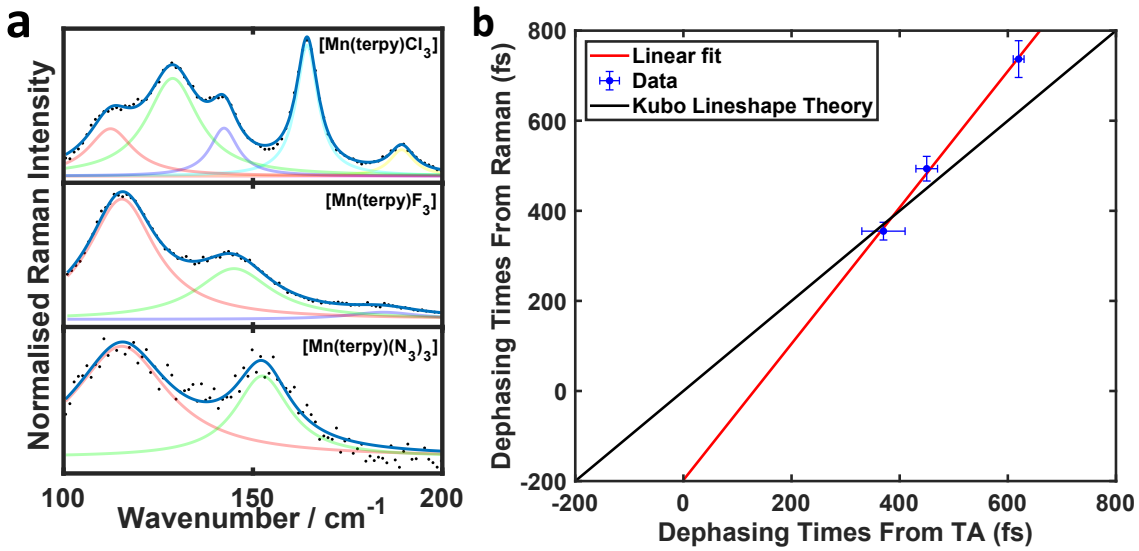

Figure 3.3.6: Correlation between the linewidth of Raman peaks and dephasing time from transient experiments. **a** Raman spectra of the three complexes in the region 100-200 cm^{-1}. The data (black dots) are fitted with multiple Lorentzian functions (transparent coloured lines). The cumulative fit is shown by the bold blue line. **b** Plot of the dephasing times fitted directly from the transient absorption spectra against calculated values from the FWHM of the Lorentzian fit of the 113–115 cm^{-1} mode (red transparent line) in the Raman spectra for each of the complexes. The black line shows the expected values if the analysis from both these methods match exactly. The red line shows a linear fit to the raw data points.

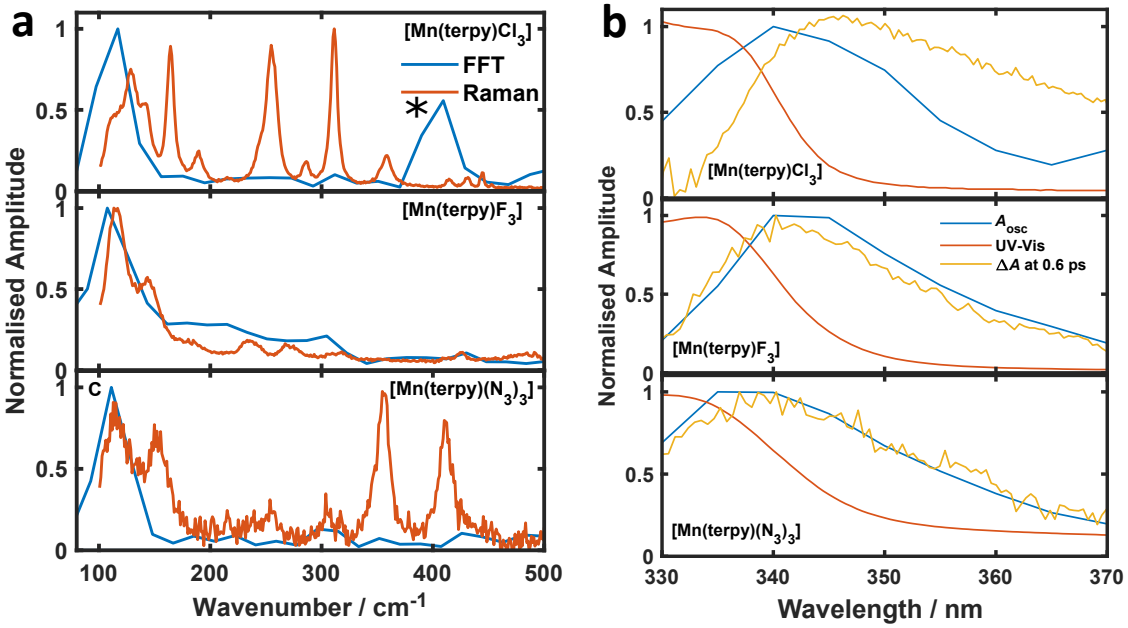

Figure 3.3.7: **a** Ground state Raman spectra of crystalline powders and fast Fourier transform of the kinetic traces after subtraction of population dynamics from 0.2 to 2 ps. The asterisk (*) indicates a signal arising from the solvent. **b** A_{osc} from fitting equation 3.3.1 to different probe wavelengths, ground state UV-Vis spectra and ΔA at 0.6 ps. A_{osc} follows the shape of the excited state absorption much more closely than the ground state spectra suggesting the observed vibration is coupled to the transition at 350 nm and that the wavepacket propagates on the excited state potential.

state correlates well with the dephasing time in the time-domain (Figure 3.3.6**b**). It is therefore important to confirm the coherence observed in the transient spectra arises from vibrational states in the first excited state rather than the ground state. Figure 3.3.7**b** shows the ground state UV-vis spectra, the difference spectra at 0.6 ps and the A_{osc} from fits of different probe wavelengths as a function of wavelength. For a ground state coherence it is expected that the oscillation amplitude should follow the ground state spectrum and similarly, an excited state coherence would follow the excited state absorption. It is clear in the figure that A_{osc} follows the excited state spectra much closer than the ground state spectra, confirming the observed vibrational wavepacket is generated and propagates on the electronic excited potential.

Returning to the loss of coherence, although the frequency of the vibration is the same for all three complexes the dephasing times decrease from $[Mn(terpy)Cl_3]$ to $[Mn(terpy)F_3]$ to $[Mn(terpy)(N_3)_3]$. As discussed in the introduction, vibrational dephasing occurs from two main mechanisms, decoherence, which describes the loss of quantum superposition due to vibrational energy loss and pure dephasing, due to interactions that involve no energy transfer just phase shifts that are randomised

within the ensemble of molecules due to solvent fluctuations. Most of the vibrational energy will be concentrated within the pincer-like mode, as time progresses, energy in this mode will be lost due to IVR to other normal modes in the molecule. IVR occurs preferentially to modes of lower frequency.[195] Ground state frequency calculations show that the pincer mode is the 10th, 12th and 18th lowest energy normal mode when X = Cl, F and N_3, respectively. As the number of normal modes with frequencies lower than the pincer mode increases the dephasing time decreases, which is consistent with vibrational dephasing times in [Mn(terpy)X_3] being dominated by population relaxation (T_1), with IVR being the dominant reason for depopulation of the vibrational states. This is similar to decoherence in cresyl violet where slow IVR leads to multi picosecond vibrational dephasing times.[183] It should be noted that although the trends here indicate low-frequency modes act as an effective bath for IVR to take place leading to dephasing, a full normal mode-normal mode coupling calculation would need to be carried out to confirm this. This is outside the scope of the calculations presented in this chapter. In addition, there were attempts to synthesise the bromide, cyanate and thiocyanate salts of [Mn(terpy)X_3] to increase the sample size. Unfortunately, these efforts failed.

In comparison to $Mn(acac)_3$,[65] the [Mn(terpy)X_3] complexes may have a simpler reaction coordinate in the excited state due to the static Jahn-Teller distortion compared to the dynamic distortion in $Mn(acac)_3$. In [Mn(terpy)X_3], only one frequency is observed in the transient absorption spectra which corresponds to the pincer-like mode of the terpyridine ligand. Whereas in $Mn(acac)_3$, two frequencies are observed in the results. This is could be due to $Mn(acac)_3$ possessing dynamic Jahn-Teller distortion where the Jahn-Teller axis can lie along any of the three bond axes due to all the coordination sites being equivalent. [Mn(terpy)X_3] does not have equivalent ligands at all coordination sites and therefore the Jahn-Teller axis in the ground state is fixed along the N_{eq}–Mn–N_{eq} bonds. When photoexcited, there are two separate nuclear trajectories that $Mn(acac)_3$ can take to reach the compressed state. The axial bonds can compress and the equatorial bonds can expand or only two of the equatorial bonds that lie opposite each other can elongate. Both these routes lead to the same geometry for the compressed Jahn-Teller distortion in the excited state but involve different trajectories to do so. Since [Mn(terpy)X_3] has a fixed Jahn-Teller axis there is only one main trajectory for the nuclear relaxation. This may explain the observation of two frequency components in the dynamics in $Mn(acac)_3$ but only one in [Mn(terpy)X_3], suggesting a simpler reaction coordinate can be generated via restriction of the Jahn-Teller axis similar to the strong oxide and oxime bonds which constrained the wavepacket motion in Mn_3.[65]

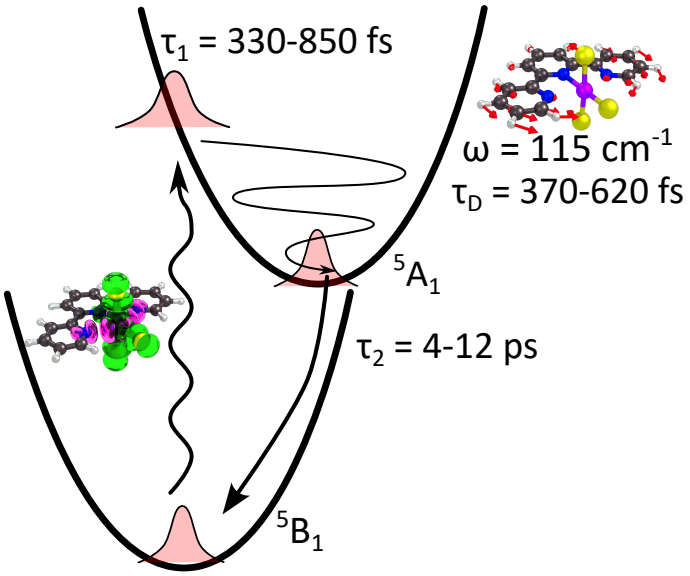

Figure 3.4.1: Summary of the photoinduced dynamics of [Mn(terpy)X_3] after $^5B_1$ $\rightarrow$ $^5A_1$ excitation.

3.4 Conclusion and Future Work

Femtosecond transient absorption spectra of [Mn(terpy)X_3] where X= Cl, F, and N_3 after exciting ligand-field transitions have been measured. The lowest energy transition was assigned using multiconfigurational calculations and corresponds to an excitation from the d_{z^2} to the $d_{x^2-y^2}$ orbital, which leads to an ultrafast switch in the Jahn–Teller distortion from axial elongation to compression. During the subsequent nuclear motion, all three complexes show evidence of a vibrational wavepacket with frequencies 113–115 cm^{-1}, which corresponds to a pincer-like motion of the terpyridine ligand. This is identified in the computations as one of the main reaction coordinates along the first excited electronic potential energy surface. The single frequency observed potentially indicates a simpler reaction coordinate due to fixing the Jahn-Teller axis to one dimension in contrast to $Mn(acac)_3$.[65] The dephasing times are inversely correlated with the number of normal modes with frequencies lower than that of the pincer-mode, implying the coherent motion dephases primarily due to population relaxation from intramolecular vibrational redistribution. A summary of the photoinduced dynamics is shown in Figure 3.4.1 These results represent a strategy to increase vibrational dephasing times in transition metal complexes by limiting the number of low-frequency vibrational modes. Extending these coherence lifetimes may lead to methods of optical control of magnetic anisotropy in SMMs.

Further work should focus on determining the generality of limiting the number of low-frequency modes to increase dephasing times. Efforts were made to synthesise more complexes of the form [Mn(terpy)X_3] where X = Br^-, NCO^- and NCS^- to

increase the sample size. However, following the same procedure as literature[187–189] but using reagents with different counterions, the synthesis always generated the Mn(II) complexes rather than the Mn(III) complexes. Another interesting direction would be to synthesise complexes with different terpyridine derivatives to also change the frequency of the pincer-like mode. If a heavier terpyridine derivative was used where bulky groups were attached to the rings, then the pincer-mode would have a lower frequency. This could lead to an increase in dephasing times due to a lower number of normal modes of energy lower than the pincer-like mode. On the other hand, localised modes of bulky groups attached to the terpyridine rings may couple strongly to the reaction coordinate and speed up dephasing. Establishing solid molecular design criteria to increase dephasing times will be beneficial. In fact, a greater focus on vibrational wavepacket dynamics of large molecules in general will lead to a fuller understanding of the photophysics of complex systems.

Chapter 4

Femtosecond K-edge X-ray absorption spectroscopy of Mn(III) SMM

4.1 Introduction

The group has previously explored the photoinduced dynamics of the Jahn-Teller distortion in the SMM $[Mn(III)_3O(Et{-}sao)_3(\beta{-}pic)_3(ClO_4)]$, where $saoH_2$ and β-pic are salicylaldoxime and 3-methylpyridine, respectively, now referred to as Mn_3.[65] In this molecule, three Mn(III) ions are arranged in a triangle and the spins of each ion ferromagnetically couple to form an $S = 6$ ground state.[176] Optical transient absorption spectroscopy which was used in the previous study and is discussed in the Introduction,[65] was limited to a convoluted picture of the electronic and nuclear dynamics because valence electronic spectra are composed of a complicated overlap of many different transitions. Important nuclear motions in the reaction coordinate were inferred from the observed vibrational wavepacket and quantum chemical calculations. Only one normal mode was observed in the optical transient absorption corresponding to motion of the three Mn ions along the Jahn-Teller axis. However, the calculations indicated that there are more nuclear degrees of freedom than just motion along the Jahn-Teller axis, such as the flattening of the triangle.[65] This motion will have important consequences for magnetic properties, as the 3d-2p-3d orbital overlap between magnetic Mn(III) ions in the triangle determines the sign and strength of superexchange interactions.[176]

Despite the information that can be obtained from vibrational wavepackets and tracking excited state lifetimes, using optical transient absorption spectroscopy to directly identify electronic, spin and structural dynamics is much more challenging. In this case, vibrational coherences generated with an ultrashort pulse in a

molecule with more than a few nuclear degrees of freedom usually do not permit direct interpretation of changes in bond lengths and angles. Alternatively, to directly address the crystal field around the metal ions, X-ray spectroscopies are an excellent technique because they offer the elemental specificity and direct structural insight that optical spectroscopies cannot. In particular, time-resolved X-ray spectroscopies on femtosecond timescales carried out at X-ray free electron lasers (XFELs) are uniquely suited to tackle such problems as they track the dynamics on and around the metal ion, exclusively. This could make time-resolved X-ray K-edge spectroscopy of metal ions an incredibly useful technique in the area of ultrafast molecular magnetism.

The elemental specificity has led to many important insights into the dynamics of photoactive transition metal complexes.[197–200] X-ray K-edge spectra focus on transitions originating from the 1s to valence and continuum states of an atom. The elemental specificity arises from the K-edges of different atoms being well-separated in energy. The K-edge can be divided into three regions:[201–203] (1) The pre-edge occurs at energies lower than the edge and is primarily composed of 1s-to-3d electronic transitions and carries information on d-orbital occupation and ligand-field strength. These s-to-d transitions are formally forbidden and generally very weak. However, non-centrosymmetric symmetry can lead to d-p mixing and increase the intensity of these transitions. Therefore, the pre-edge is also sensitive to coordination symmetry. (2) The rising edge occurs as the energy reaches near the 1s ionisation threshold and is composed of 1s to 4p transitions. The position of this edge is particularly sensitive to electron density on the metal and therefore is a good marker of oxidation state. (3) Extended X-ray absorption fine structure (EXAFS) region is found at energies above the edge and involves the ionisation and ejection of an electron. The ejected electron scatters off nearby atoms, which can create standing waves. This signal can contain information on the local structure around the metal ion.

The high brilliance and femtosecond duration of hard (>5 keV) X-ray pulses at XFELs have opened up new avenues to explore photoinduced dynamics at the earliest timescales in photophysical processes.[204–206] The first study showing femtosecond K-edge X-ray spectroscopy was possible at XFELs was carried out by Lemke et al.[207] Monitoring the kinetics of the iron K-edge in $[Fe(bpy)_3]^{2+}$ after MLCT excitation, it was found that the lowest energy excited state, $^5T_2$, was populated in 160 fs. Since this landmark study, many improvements have been made, such as increasing shot-to-shot stability and timing diagnostics to ensure accurate pump-probe delay times. Only a few years later, the same experiment on $[Fe(bpy)_3]^{2+}$ was performed but with a much higher signal-to-noise ratio and time resolution.[208] This allowed the observation of vibrational coherences imprinted on the X-ray ki-

netic traces. In comparison to simulations, the authors concluded that the dynamics must involve a passage through an intermediate ^{3}T state, which had been an open question for a long time.[138, 209] This was one of the first studies to show that X-ray spectroscopies at femtosecond timescales have the opportunity to answer questions that are inaccessible by optical means.

Direct structural information has previously been extracted from K-edge absorption spectroscopy by analysing vibrational wavepackets in mononuclear complexes. Katayama *et. al.* studied the Cu(I)-phenanthroline complex $[Cu(dmphen)_2]^{2+}$ (dmphen is 2,9-dimethyl-1,10-phenanthroline) and showed multiple different nuclear motions could be decoupled using time-resolved X-ray absorption spectroscopy (TR-XAS) at the Cu K-edge.[73] By following the change in XAS after photoexcitation at the pre-edge and rising edge, the measurement is sensitive to coordination symmetry and electron density on the copper atom, respectively. The time-dependence of the rising edge probe showed one frequency of a vibrational wavepacket corresponding to a symmetric breathing mode that modulates the total electron density around the copper ion. In addition to this breathing mode, the pre-edge exhibited two more frequencies that correspond to a flattening motion of the two phenanthroline ligands due to the activation of Jahn-Teller distortion in the excited state. Only the pre-edge is sensitive to this motion as it is symmetry breaking and leads to 3d-4p mixing increasing its intensity. From comparison to simulations, they showed that the inner coordination sphere bond lengths contract by 0.02 Å which shows the potential sensitivity of TR-XAS to minute bond length changes. Considering the structural rigidity of Mn_3 implied from the previous optical study,[65] it is likely that a method as sensitive as TR-XAS is needed to track the changes in nuclear structure. In addition, it is interesting to find out if as much structural detail can be elucidated in a molecule as large as Mn_3 as can be for a smaller mononuclear complex such as $[Fe(bpy)_3]^{2+}$ or $[Cu(dmphen)_2]^{2+}$.

As evidenced by the previous paragraphs, a high level of detail can be gained from K-edge TR-XAS of transition metal complexes. Therefore, this chapter presents results from time-resolved K-edge X-ray absorption spectroscopy at the Spring-8 Ångstrom Compact free-electron Laser (SACLA) to gain deeper insight into the photoinduced dynamics of Mn_3 after metal-centered photoexcitation. With complimentary simulations, a detailed and cohesive picture of the nuclear dynamics of Mn_3 after photoexcitation has been developed. Most aspects of the TR-XAS measurement can be interpreted considering motion along a single Jahn-Teller mode with a frequency of 181 cm^{-1}. The changes in the main and pre-edge regions were simulated with good agreement to experimental data. These calculations suggest very small changes in the nuclear structure with one of the largest being only a 0.05 Å elongation of the Mn—O (oxime) bond lengths. Using the time dependence

of the dynamics at the main edge, good agreement with the optical transient absorption is found. TR-XAS also provides further evidence of coherent motion at a frequency of 181 cm^{-1}, which further supports its assignment as the dominant mode in the reaction coordinate. Measurements focussing on the pre-edge region, which provides sensitivity to the coordination symmetry, agree well with the changes in the inner coordination sphere suggested from the main edge. The results in this chapter show that TR-XAS is an excellent technique for tracking crystal field dynamics in large polynuclear complexes and therefore is an important tool in the emerging field of ultrafast photoswitchable SMMs.

Considering travel restrictions in place at the time of the experiment, visiting SACLA was not possible. Therefore, the experiment was ran by Tetsuo Katayama with remote participation from myself. The data analysis of the experimental results presented was carried out by myself. Simulations of the TR-XAS spectra were performed by T. J. Penfold and J. Eng at the University of Newcastle. The contents of this chapter has been accepted for publication in Nature Communications.

4.2 Methods

4.2.1 X-ray Free Electrons Lasers (XFELs)

An accelerating charge generates electromagnetic radiation, which is the basis for any particle accelerator based light sources such as synchrotrons and FELs. The peak brightness and photon energies of some X-ray light sources are shown in Figure 4.2.1**a** which shows FELs have a much greater brightness than synchrotron sources. In FELs, the method of accelerating charges is provided by undulators, which are a series of dipolar magnets that create a periodic structure of oscillating magnetic fields along an axis. The fundamental wavelength of the radiation emitted by the electrons travelling along this axis is on the order of λ_u/γ^2, where λ_u is the undulator period and γ is the Lorentz factor.[210] Undulator periods of a few centimetres are typical for XFELs and the Lorentz factor is on the order of several thousand which can take the radiation into the hard X-ray regime. Experimental realisation of FEL radiation was first demonstrated in 1953[211] and since then there have been several substantial breakthroughs.[212, 213]

Despite the successful generation of FEL light, the emitted radiation was initially incoherent, which substantially reduced its ability to create high-intensity and short pulses. These two properties are vital for the development of femtosecond spectroscopy using X-rays. To create coherent light, the phases of all the electric fields must be the same. This has been achieved by periodically "bunching" groups of electrons at the same wavelength as the radiation.[215] This is the high-gain regime

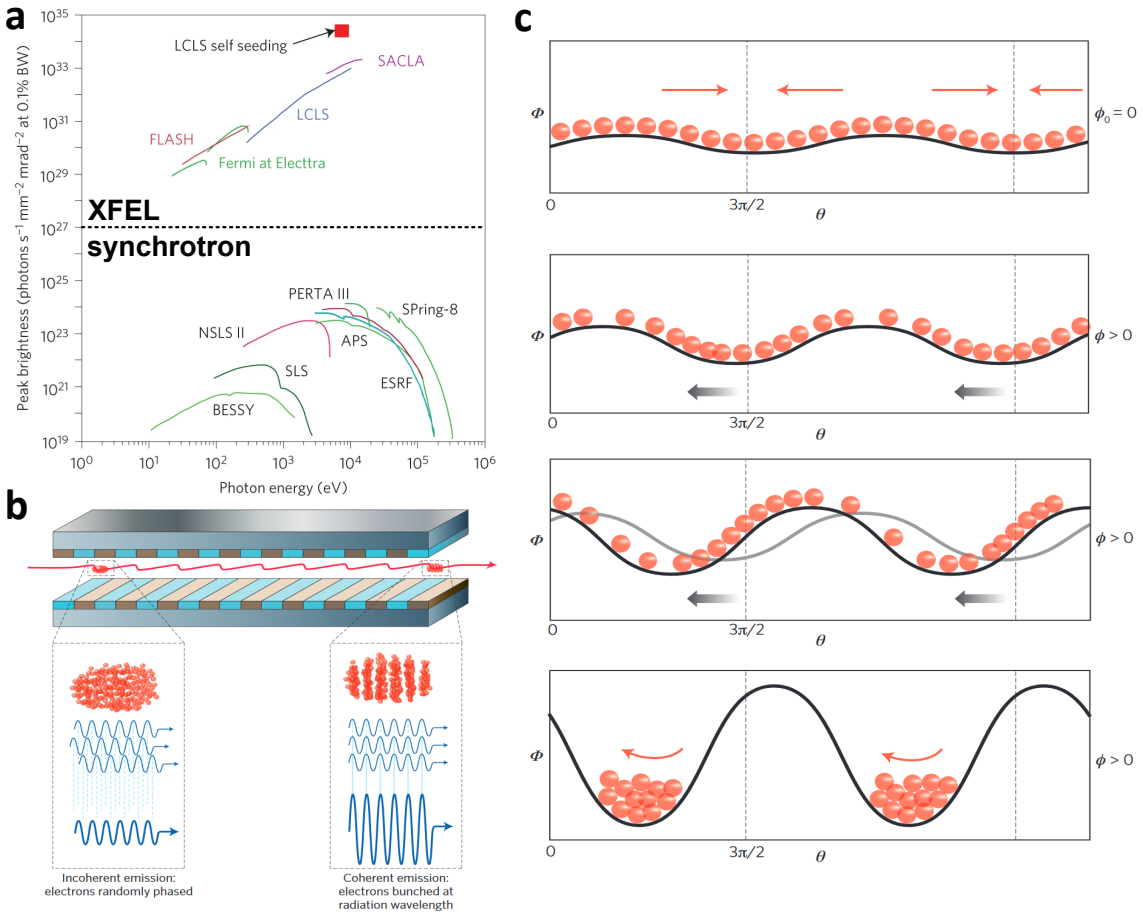

Figure 4.2.1: Overview of X-ray sources and the schematic of the operation of FEL lasing. **a** Photon energies and peak brightness of X-ray sources as of 2015 show the improvement of the brightness of FEL-based sources over synchrotrons. Taken from ref. [214] **b** Schematic of the undulator emission showing the creation of incoherent radiation due to the acceleration of charges. After some time in the undulator, the charges microbunch creating coherent radiation that has high brilliance. Figure taken from ref. [215]. **c** Potential energy (Φ) as a function of undulator distance (θ) viewed from the rest frame of the electron. The phase, ϕ is shown on the right-hand side of the figures. From top to bottom: the development of microbunching across two potential wells of the radiation field. The electrons initially experience a small force from the initial field that causes them to fall into the potential well around $\theta = 3\pi/2$ and $7\pi/2$. This drives a small phase shift ϕ in the position of the wells. The weakly bunched electrons (that is electrons that are near the peak of the potential) begin to fall into the well and lose their kinetic energy to the radiation field. This process continues, increasing the amplitude of the radiation field exponentially. This growth stops when the electrons are strongly bunched and surf in the potential wells along the remainder of the undulator. Figure taken from ref. [215]

of FEL operation and is shown schematically in Figure 4.2.1**b** and 4.2.1**c**. The process is known as self-amplified stimulated emission (SASE). Overall, this process generates ultra-bright X-ray pulses that can be tens of femtoseconds in duration, which are necessary for pump-probe X-ray spectroscopy on ultrafast timescales.

4.2.2 Time-resolved K-edge X-ray absorption spectroscopy

The experimental procedure for time-resolved X-ray K-edge spectroscopy at SACLA utilises a total fluorescence yield detection method.[216, 217] This assumes that, over the spectral region of interest, the quantum yield of X-ray fluorescence is constant regardless of the absorbed photon energy. Therefore, by scanning the incoming X-ray photon energies and measuring the total intensity of the X-ray fluorescence emitted from the sample, an absorption spectra can be generated. In an experiment, the XFEL radiation is monochromated by a crystal to select the photon energy. Under the total fluorescence yield detection method, the number of photons at each monochromator position must be the same to achieve a true absorption spectrum. In reality, due to the inherent noise in FEL lasing there is large fluctuations in pulse intensities which need to be corrected for. For X-ray absorption spectra the total fluorescence yield is normalised with respect to the pulse intensity that is measured shot-to-shot. Overall, the X-ray absorption at one photon energy can be measured on a shot-to-shot basis by normalising to pulse intensity and a monochromator can be scanned to produce a spectrum of the entire region.

A time-resolved X-ray absorption difference spectrum is acquired in a manner analogous to how an optical difference spectrum is measured. An optical pump laser is overlapped spatially with an X-ray beam and chopped at half the repetition rate of the X-ray probe. Therefore, each two probe pulses measure the pump-on and pump-off absorption at one probe photon energy. A difference spectrum can be produced by scanning the probe photon energy. A change of absorption over time at one photon energy (an X-ray kinetic trace) can be acquired by scanning the delay between the pump and probe. To achieve accurate time delays, timing jitter of the FEL pulses must be corrected for using timing diagnostics.[218]

4.2.3 Sample Preparation

Mn_3 was synthesised according to literature procedures with the aid of Marco Coletta.[176] A 9 mM ethanol solution of Mn_3 was injected into the sample chamber[73] using a glass nozzle that produced a 50 µm cylindrical jet at a speed of 12 ms^{-1}, which was constantly circulated. The X-ray repetition rate was 60 Hz and therefore new sample was probed every pulse.

4.2.4 Time-Resolved Measurements

The TR-XAS measurements were performed at beamline 3 of SACLA[216, 217]. The X-ray absorption was measured using the total fluorescence detection method as discussed above. Two Si(111) crystals in the (+,–,–,+) geometry were used to monochromate the beam and a Be lens was used to focus the X-rays at the sample position to a size of 10 × 10 µm^2 at FWHM. At the interaction point, 400 nm laser pulses were focused down to 210 × 215 µm^2 at FWHM and interleaved with the X-ray pulses to measure both optical laser on and off spectra to acquire the pump induced difference spectra. The timing jitter was measured using the beamline diagnostics[218] and corrected in the data analysis, to improve the time resolution.

Considering the small signals that arise from X-ray spectroscopy, high pump-pulse intensities are used to achieve high excitation yields. To ensure the pump energy is within the one-photon absorption regime, a pump-power dependence of the transient signal was carried out. Figure 4.2.2**a** shows the transient signal monitored at 700 fs and a probe energy of 6548.5 eV. The signal is linear up to a fluence of 124 mJcm^{-2}. Despite the linearity of the signal up to a fluence of 124 mJcm^{-2}, this pump power suggests there are around 7 photons absorbed per molecule. Considering the unusually high absorbed photon number, a pump power dependence was carried out also scanning pump-probe time delay. This is shown in Figure 4.2.2**b**. When normalising the signal to the pump power the signal is indeed linear when only monitoring at 700 fs, however the early time kinetics are dependent on pump power. These measurements suggest that it is not enough to only check a power dependence at a single time delay and care should be taken to check the power titrations at different time delays. This has important consequences for many studies where photon numbers exceed 100 % excitation but show linear signal strengths with respect to pump pulse energy. Subsequent measurements were performed at a pump fluence of 13.3 mJcm^{-2} which, with a 9 mM ethanol solution of Mn_3, path length of 50 µm and extinction coefficient of 12500 M^{-1}cm^{-1} at 400 nm, provides an excitation yield of 74 %.

4.3 Results and Discussion

The experimental (red) and simulated (blue) K-edge X-ray absorption spectra of Mn_3 are presented in Figure 4.3.1**a**. The two spectra are in good agreement, and show a weak pre-edge (1s-to-3d transitions) at 6539 eV and the main edge at 6549 eV, matching what is expected from Mn(III) ions.[219] The absorption difference spectrum at 700 fs, obtained after photoexcitation of Mn_3 at 400 nm, is shown in Figure 4.3.1**b** and the pump-on and pump-off spectra are shown in Figure 4.3.2**a**. The

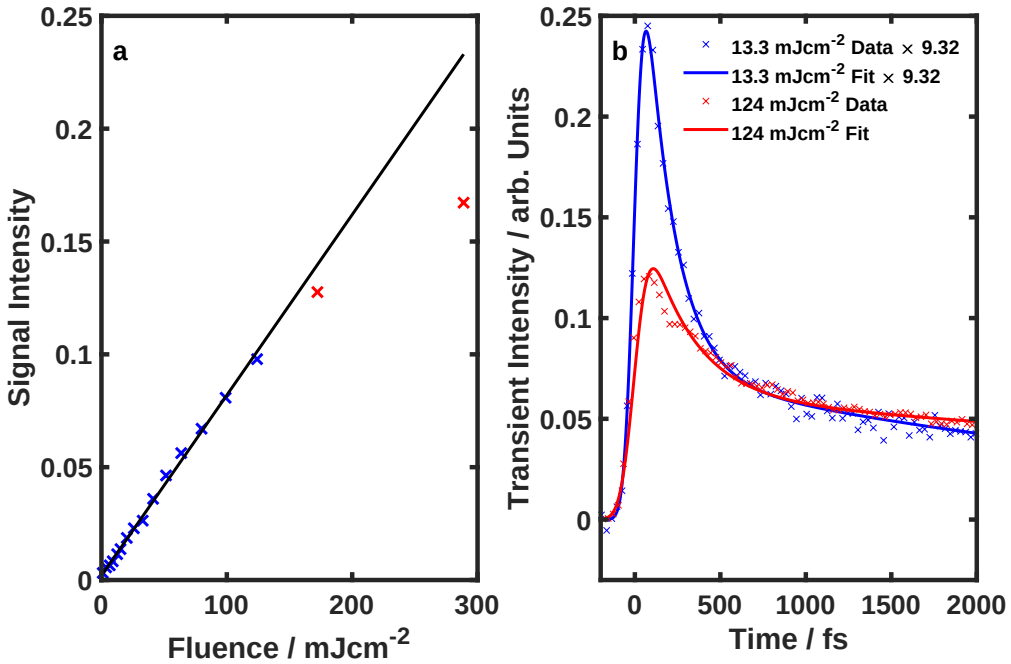

Figure 4.2.2: Power titration of the transient XAS signal at 6548.5 eV. **a** The transient signal as a function of pump fluence measured at 700 fs. The data show a loss of linearity above 124 mJcm^{-2}. **b** The kinetic traces measured at fluences of 13.3 mJcm^{-2} and 124 mJcm^{-2}. The 13.3 mJcm^{-2} data has been multiplied by 9.32 to aid comparison with the high fluence measurement.

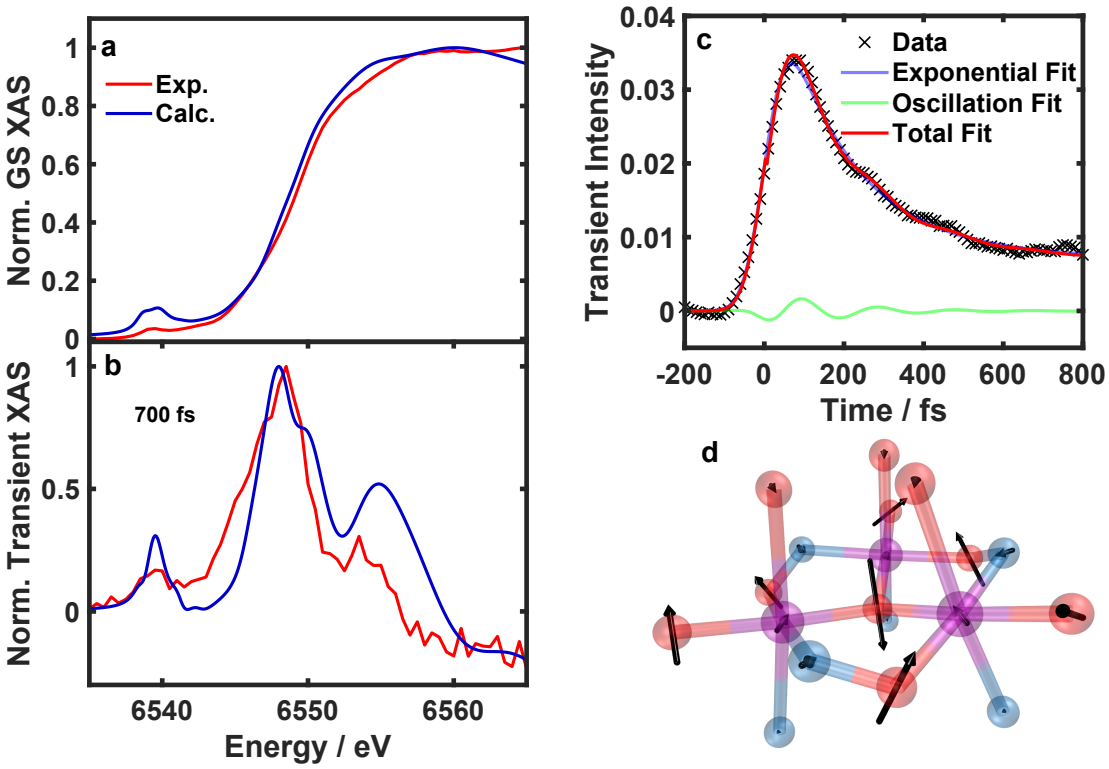

Figure 4.3.1: X-ray K-edge absorption spectra of Mn_3. **a** The experimental (red) and calculated (blue) ground state K-edge XAS of Mn_3. **b** XAS difference spectra at 700 fs after 400 nm photoexcitation. The calculated spectrum was simulated using the 74 % excitation yield and calculating the XAS at a new geometry along ν_{60} to give the best match to the experimental results. **c** Time evolution of the TR-XAS signal at an X-ray probe energy of 6548.5 eV with 5-point adjacent averaging. The fitted line is made up of two exponential decay components with time constants τ_1= 180 fs and τ_2 = 9000 fs. There is also a small oscillatory component with a frequency of 181 cm^{-1} that is a signature of a vibrational coherence. **d** Schematic of the mode (ν_{60}) that is responsible for to oscillation seen in **c**, where the peripheral ligands of the Mn_3 complex have been removed for clarity.

400 nm excitation wavelength corresponds to the highest energy crystal-field transition. In a simplified D_{4h} coordination symmetry, this corresponds to the $^5E_g \leftarrow ^5 A_{1g}$ transition. At this pump-probe delay, there is an increase in the pre-edge intensity and a small redshift of the main edge of around 0.2 eV (Figure 4.3.2**b**) at 700 fs. From the optical study,[65] it is known that Mn_3 reaches the lowest energy electronic excited state with a time constant of 180 fs. Therefore at 700 fs, most of the molecules will have undergone internal conversion to the lowest excited state. This is confirmed by the plateau of the kinetic trace shown in Figure 4.3.1**c**.

Figure 4.3.3**a** displays a spectrum of the pre-edge of the Mn K-edge XAS spectrum. Subtracting the background of the main edge generates a pure pre-edge spectra that is composed of two peaks. These have been fitted by the sum of two Gaussian functions as shown in Figure 4.3.3**b**. Simulations suggest the lower energy

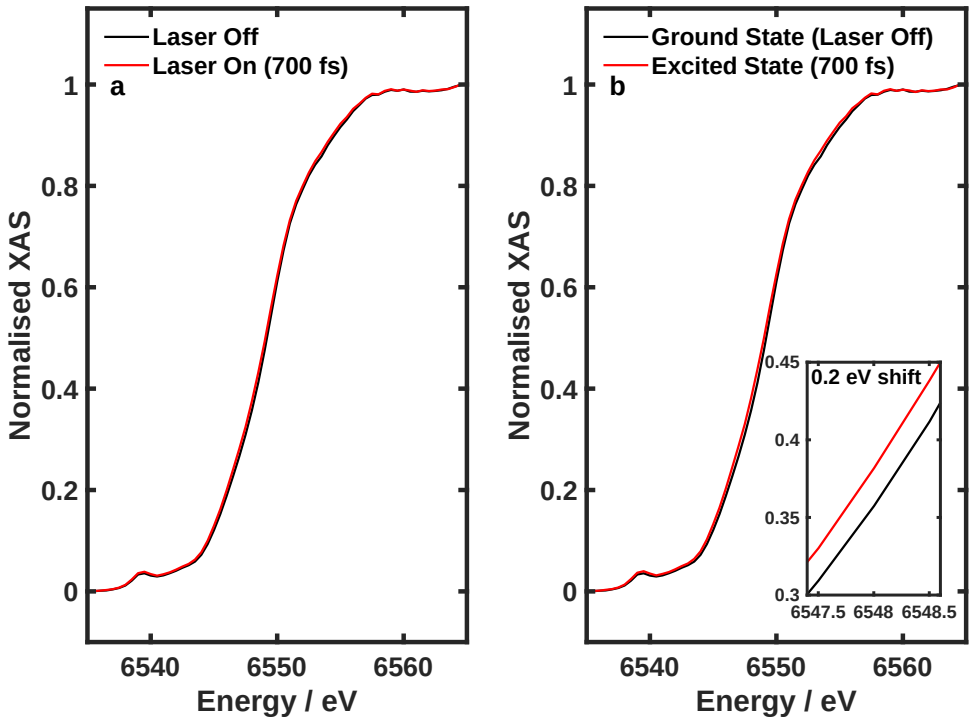

Figure 4.3.2: K-edge X-ray absorption spectra of 9 mM ethanoic Mn_3 solution with and without 400 nm photoexcitation. **a** The laser on and laser off XAS spectra showing a small pump induced signal at 700 fs. **b** Ground and excited state XAS spectra. The excited state spectra have been calculated using the estimated proportion of excited state molecules generated by the pump pulse (74 %). Inset: Edge region showing an edge shift of around 0.2 eV in the excited state at 700 fs.

transition at 6539.5 eV is made up of 1s-to-3d transitions. The higher energy transition at 6542 eV is composed of transitions from the 1s-orbital to the 3d-orbitals mixed with the ligand p-orbitals and will be referred to as the MLCT peak. The assignment of these two peaks is in agreement with previous literature on Mn K-edge spectroscopy.[219] The 1s-to-3d electronic transition is forbidden and therefore the pre-edge is significantly weaker than the main edge. In an idealised D_{4h} symmetry the pre-edge is purely made up of electric quadrupole transitions as the 1s-to-3d transition is dipole forbidden.[220] However, symmetry breaking geometries can lead to 3d-4p orbital mixing and contribute dipole allowed character to the 1s-to-3d transition. 1s-to-3d transition intensities therefore hold information on the symmetry of inner coordination spheres. The MLCT peak includes details on the amount of 3d-ligand orbital mixing and therefore covalency, which will also be an indirect measure of inner coordination sphere structure.

To extract kinetic information, the largest pump-induced transient at 6548.5 eV was measured as a function of time delay. The decay signal could be fitted with

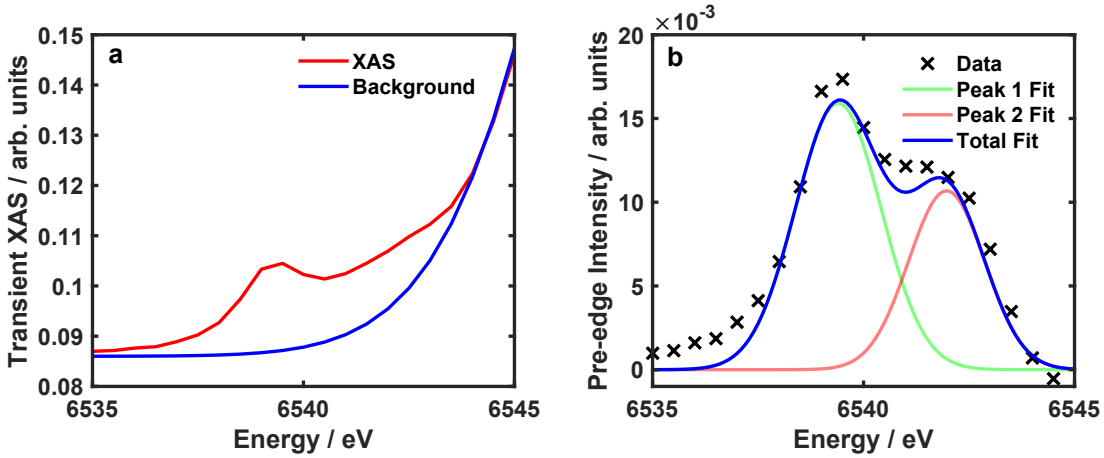

Figure 4.3.3: Ground state pre-edge region. **a** Ground state pre-edge region with the background from the rising edge. **b** Pure pre-edge spectra with background from **a** subtracted. This has been fitted with two Gaussian functions.

a biexponential function, as shown in Figure 4.3.1**c**. The data was processed with a five-point adjacent averaging filter, the effect of this is shown in Figure 4.3.4. Interestingly, there are oscillations superimposed on the transient signal. Similar to the optical experiment, this type of behaviour is indicative of coherent vibrational motion induced by the pump pulse. A term was included to capture this vibrational wavepacket using the same equation provided in Chapter 3:

$$\Delta A = \mathrm{IRF}(\sigma, t) \circledast \left(\sum_{i=1}^{2} A_i e^{-t/\tau_i} + A_{\mathrm{osc}} e^{-t/\tau_{\mathrm{d}}} \cos\left(2\pi c \tilde{\nu} t\right) \right) \tag{4.3.1}$$

where A_i and τ_i are the exponential decay amplitudes and decay times, respectively. A_{osc} and τ_{osc} are the wavepacket amplitude and dephasing time, respectively. The wavepacket frequency is given by $\tilde{\nu}$ and c is the speed of light. The equation is convoluted with an instrument response function (IRF) modelled as a Gaussian of width $\sigma = 42 \pm 2$ fs from the fitting, which takes into account the finite width of the pump and probe pulses. The fitting yielded a decay constant of $\tau_1 = 178 \pm 6$ fs in agreement with the optical data[65] ($\tau_1 = 180 \pm 10$ fs) and the excited state lifetime was fixed at $\tau_2 = 9000$ fs.[65] The value of the oscillation frequency was $\tilde{\nu} = 172 \pm 8$ cm^{-1}. The observed mode was assigned to ν_{60} and involves an in-phase oscillation of the three Mn(III) ions along their Jahn-Teller axis (Figure 4.3.1**d**) and was also observed in the optical transient absorption with a frequency of $\tilde{\nu} = 181 \pm 3$ cm^{-1} and has a computed frequency of 210 cm^{-1}. The vibrational dephasing time was found to be shorter than in the optical data at $\tau_{\mathrm{osc}} = 170 \pm 80$ fs. This is likely due to the lower amplitude of the oscillations in comparison to the optical data which means the oscillations fall below the noise level at earlier pump probe

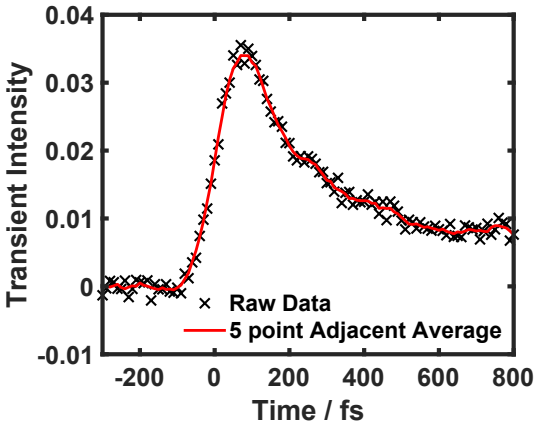

Figure 4.3.4: Effect of 5 point adjacent averaging on the main edge probe (6548.5 eV) transient kinetic trace.

delay times compared to the optical data ($\tau_{osc} = 360 \pm 15$ fs). The XAS investigates core-to-valence transitions whilst the optical measurements only look at valence transitions. It is possible that the sensitivity of the optical transient absorption to the wavepacket is primarily due to changes in the HOMOs whilst the XAS only investigates the LUMOs. The 1.9 ps vibrational cooling component found in the optical data was not observed. Again, this could be due to the vibrational cooling occurring on the potential energy surface of the highest populated electronic state and therefore XAS would not be sensitive to this as it probes unpopulated states.

It was previously proposed that the structural rigidity of Mn_3 constrains the reaction coordinate to a single dominant mode, ν_{60}, in contrast to the more flexible monomer $Mn(acac)_3$.[65] Considering the agreement in the optical and X-ray data, the aim is to interpret the TR-XAS data within the normal mode framework by simulating XAS spectra of Mn_3 at different geometries along mode ν_{60} in the electronic ground state. It could not be calculated in the excited state due to the difficulty in modelling exchanged-coupled polynuclear complexes with large spin angular momentum. It is expected that the electronic effect of metal-centred excitation would lead to only small modulations of the overall X-ray spectrum as there is no formal change in oxidation state of the metal ions. The calculated difference spectrum shown in Figure 4.3.1**b** was generated by calculating the XAS spectrum at the ground state geometry and at different points along ν_{60} corresponding to very small geometry changes. The proportion of excited molecules (74 %) was taken into account to compare with experiment. Considering the complexity of the molecule, there is an excellent agreement with experiment showing the peaks at the pre-edge, rising edge and post-edge and also the negative signal above 6560 eV. This strongly suggests that the TR-XAS data can be accurately described by structural changes along the dominant ν_{60} mode.

Structural Parameter	Franck-Condon	Distorted Structure	Change
Ave. Mn–O (ClO_4) bond length (Å)	2.367	2.415	0.048
Ave. Mn–N (β-pic) bond length (Å)	2.369	2.342	−0.027
Ave. Mn–N (Et-sal) bond length (Å)	1.995	2.003	0.008
Ave. Mn–O (OH) bond length (Å)	1.875	1.883	0.008
Ave. Mn–N (oxime) bond length (Å)	1.929	1.938	0.009
Ave. Mn–O (μ_3-O) bond length (Å)	1.911	1.922	0.011
Plane of Mn_3 to μ_3-O distance (Å)	0.333	0.374	0.041
Ave. Mn–N–O–Mn dihedral angle (°)	42.94	42.39	-0.55

Table 4.3.1: Computed structural parameters for Mn_3 at the Franck-Condon geometry and distorted excited-state geometry. The difference in bond lengths involving the three manganese ions does not vary more than 0.01 Å and the dihedral angles only vary by 0.2 °.

The changes in nuclear coordinates are detailed in Table 4.3.1. In particular, the axial Mn—O bond length increases by around 0.05 Å and the Mn—N axial bond length decreases by 0.03 Å suggesting the manganese ions move down along the Jahn-Teller axis. Equatorial bonds change by < 0.011 Å suggesting restriction of in-plane motion as previously suggested.[65] The effect of other modes alongside ν_{60} is shown in Figure 4.3.5 and the eigenvectors of these modes are shown in Figure 4.3.6. While the combination of multiple modes can improve the agreement with the experimental difference spectrum, these additional modes only give to rise small modulations of the spectra with ν_{60} being the dominant contribution.

In order to explore the structural changes in more detail, energy scans were carried out at different time delays in the pre-edge region 6535–6545 eV. Pre-edge spectra are particularly sensitive to coordination sphere symmetry and therefore are an excellent marker of crystal-field nuclear dynamics in a time-resolved experiment.[73] Figure 4.3.9**a** displays pre-edge spectra, with the background from the tail of the main edge subtracted (this background is shown in Figure 4.3.7), of the excited state at different pump-probe delay times. The pure excited state spectra were calculated by adding the ground state contribution to the difference spectra. To calculate the ground state contribution, the 74 % excitation yield calculated in the methods section was scaled by $e^{-\frac{t}{9000}}$ where t is the time delay between pump and probe. This is to take into account the recovery of the ground state which occurs with a time constant of 9000 fs. The same features that occur in the ground state occur in the excited state with the 1s-to-3d peak and the MLCT peak. The data show a small decay and slight blueshift in the MLCT peak and a much more pronounced decay in the 1s-to-3d peak. Kinetic scans at three probe wavelengths were also performed and are shown in Figure 4.3.11. These can be fitted to the

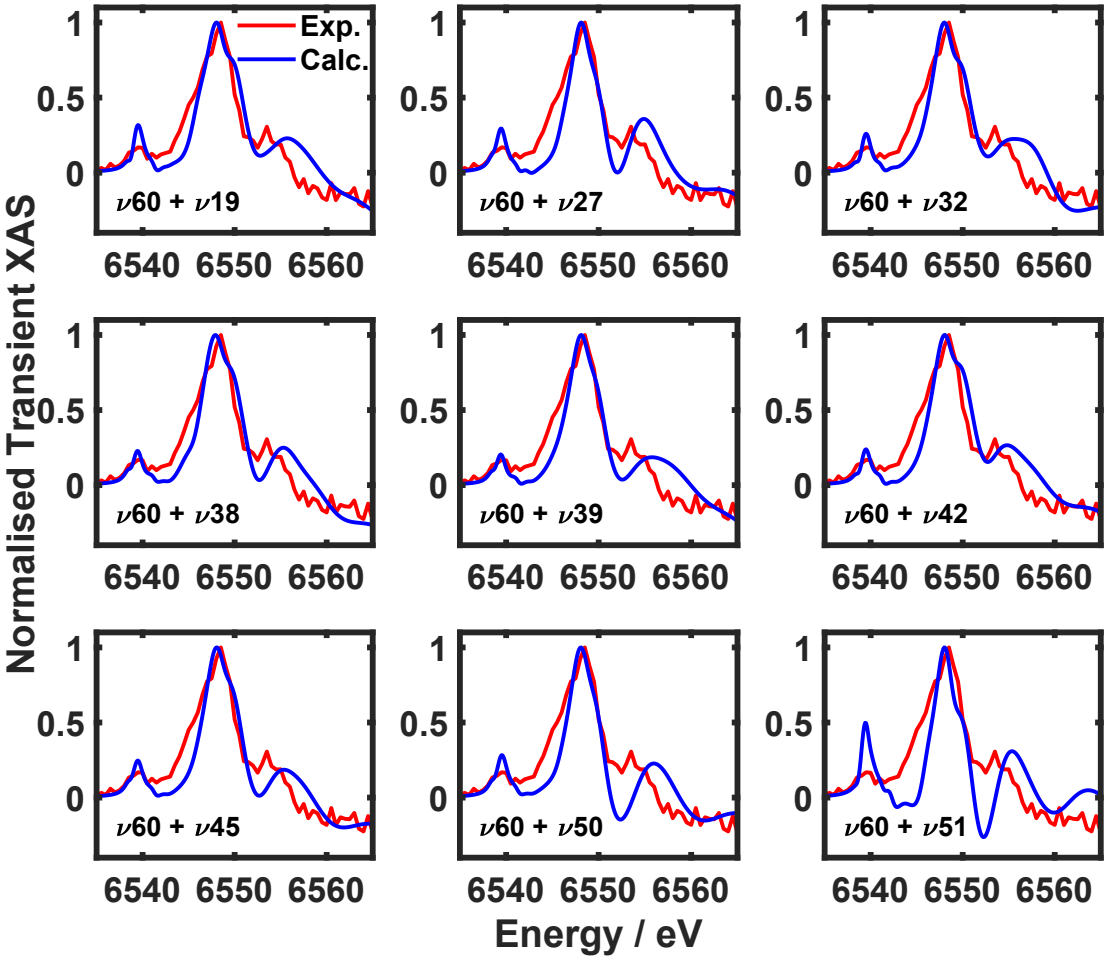

Figure 4.3.5: Experimental and simulated transient XAS signal for different combinations of normal modes. Only motion along ν_{60} creates a spectrum that matches well with experiment and all other modes only show small modulations to that signal. These scans were carried out with the first 100 modes but only the ones that effect the XAS spectrum are shown.

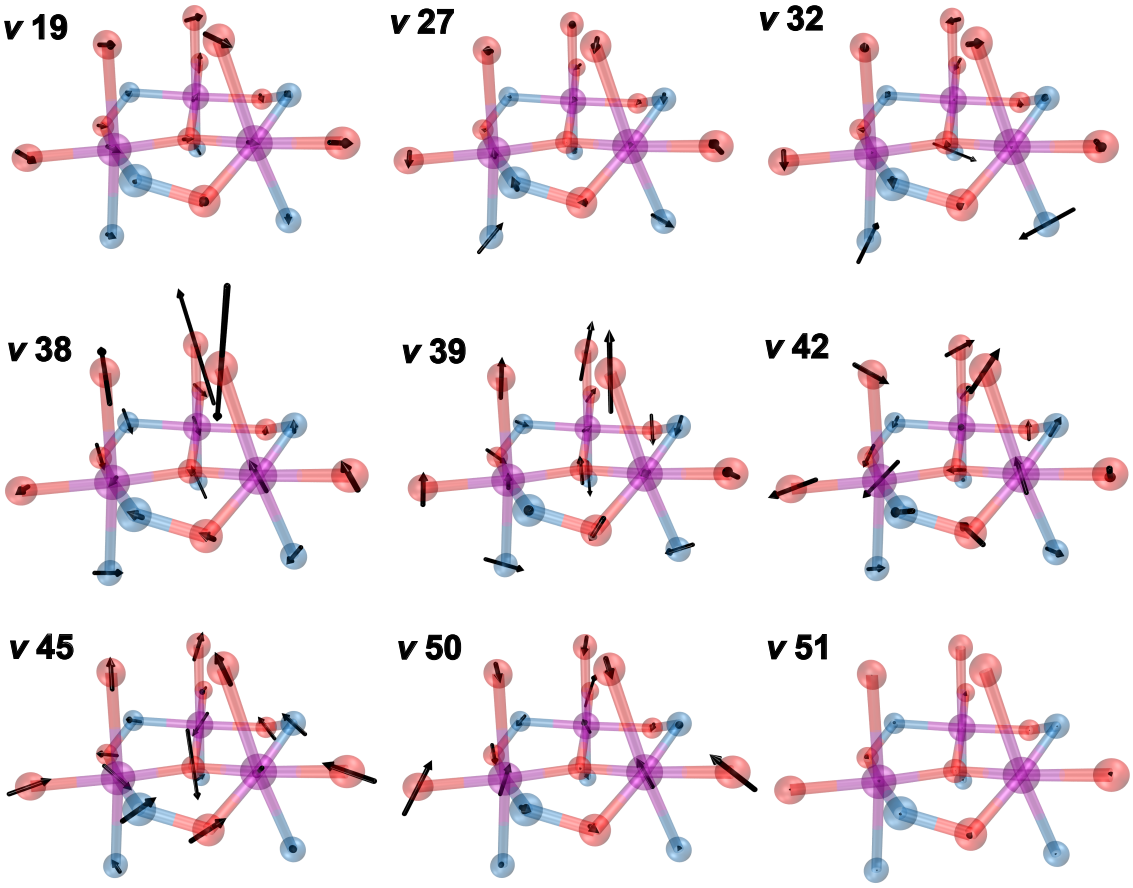

Figure 4.3.6: Eigenvectors for the modes involved in calculating the transient XAS signals in Figure 4.3.5. Mode ν_{51} has small arrows as the nuclear motion is mostly localised on the peripheral ligands.

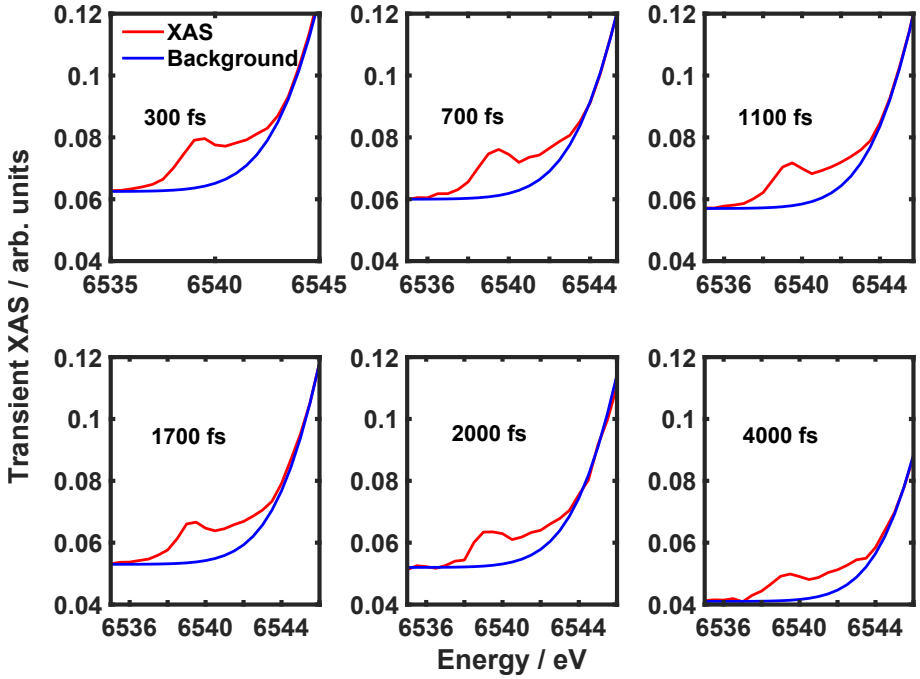

Figure 4.3.7: Pure excited state pre-edge region and the background that is subtracted to yield only the pre-edge transitions for each pump-probe time delay. The background is modelled as a Gaussian rising edge and was done by eye.

same time constants as the main edge and prove that there is consistency across the whole K-edge spectral region.

Returning to the calculations and focussing on just the pre-edge transitions calculated using time-dependent density functional theory, there is qualitative agreement with experimental data (Figure 4.3.10). There is a decrease in intensity of the 1s-to-3d peak and a blueshift of the MLCT peak moving from the distorted structure back to the ground state.

To quantify these changes, the spectra were fit with the sum of two Gaussian functions (fits shown in Figure 4.3.8) with the peak centre of the 1s-to-3d transition fixed at 6539.4 eV. The time evolution of the fitting parameters is shown in Figures 4.3.9**b-d** along with the ground state values. Figure 4.3.9**c** shows the peak areas as a function of time. The 1s-to-3d peak decays at the same rate as the MLCT peak grows showing they are likely sensitive to the same dynamical process. Considering the pump pulse only excites a ligand-field transition, the total d-orbital occupation is constant and the change in the 1s-to-3d peak is likely due to coordination symmetry. Returning to the structural parameters calculated by the simulations there are very small changes in the equatorial plane (Table 4.3.1) due to the rigid in-plane bonds. The axial bonds in the ground state are about equal at 2.37 Å but in the excited state the Mn–O bonds increase by about 0.05 Å and the Mn-N bonds decrease by around 0.03 Å. This suggests a reduction in symmetry along the z-axis, which will cause the 1s-to-3d peak to increase in intensity due to 3d–4p mixing in good

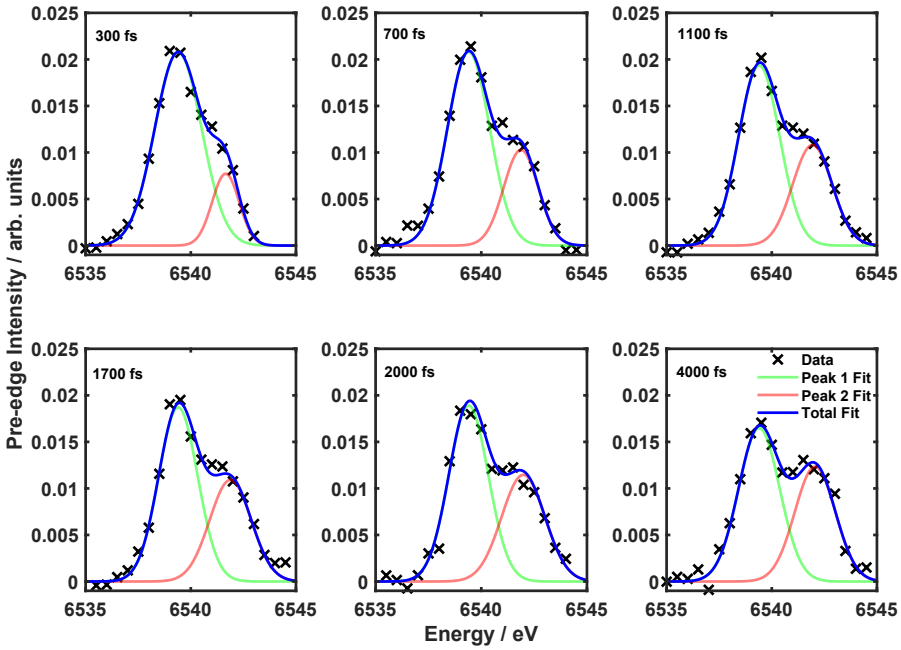

Figure 4.3.8: Pure pre-edge spectra of the excited state at different time delays. These have been fit with two Gaussian functions with the 1s-to-3d peak centre fixed at 6539.4 eV.

agreement with the experimental peak area. The energy of the 1s-to-3d transition does not shift. There is no change in the Mn oxidation state and so the average energy of the 3d orbitals would be expected to shift only by a very small amount.

Changes in peak widths are shown in Figure 4.3.9**d**. This shows a small increase in the width of the 1s-to-3d transition. Considering this band is composed of transitions to all the 3d orbitals it could suggest a slightly greater energy splitting amongst them and a stronger ligand field. Indeed, the Mn–N bonds to the strong-field ligand (β-pic) decrease by 0.03 Å. There is very little change in the equatorial bonds and the other axial ligand (ClO_4^-), despite an increase in the Mn–O bond length, is unlikely to have much effect as it is a weak-field ligand. Therefore, there could be a small increase in ligand field strength on the order of 1500 cm^{-1} in the excited state upon contraction of the Mn–β-pic distance.

The peak centre, area and width of the MLCT transition also change with time. Upon photoexcitation, all metal-ligand bonds elongate apart from the β-pic ligand (Table 4.3.1). Compared to the Franck-Condon structure, there is worse overlap between the ligand and metal 3d orbitals in the excited state distorted structure, which leads to the MLCT transitions having more 1s-to-3d character than 1s-to-ligand character. This has two effects; the peak centre redshifts as the 3d orbitals are at lower energy than the ligand orbitals and the intensity of the transition will decrease as the 1s-to-3d transition is more forbidden than the 1s-to-ligand transition. Both these effects are observed in the experimental data at early times, the centre

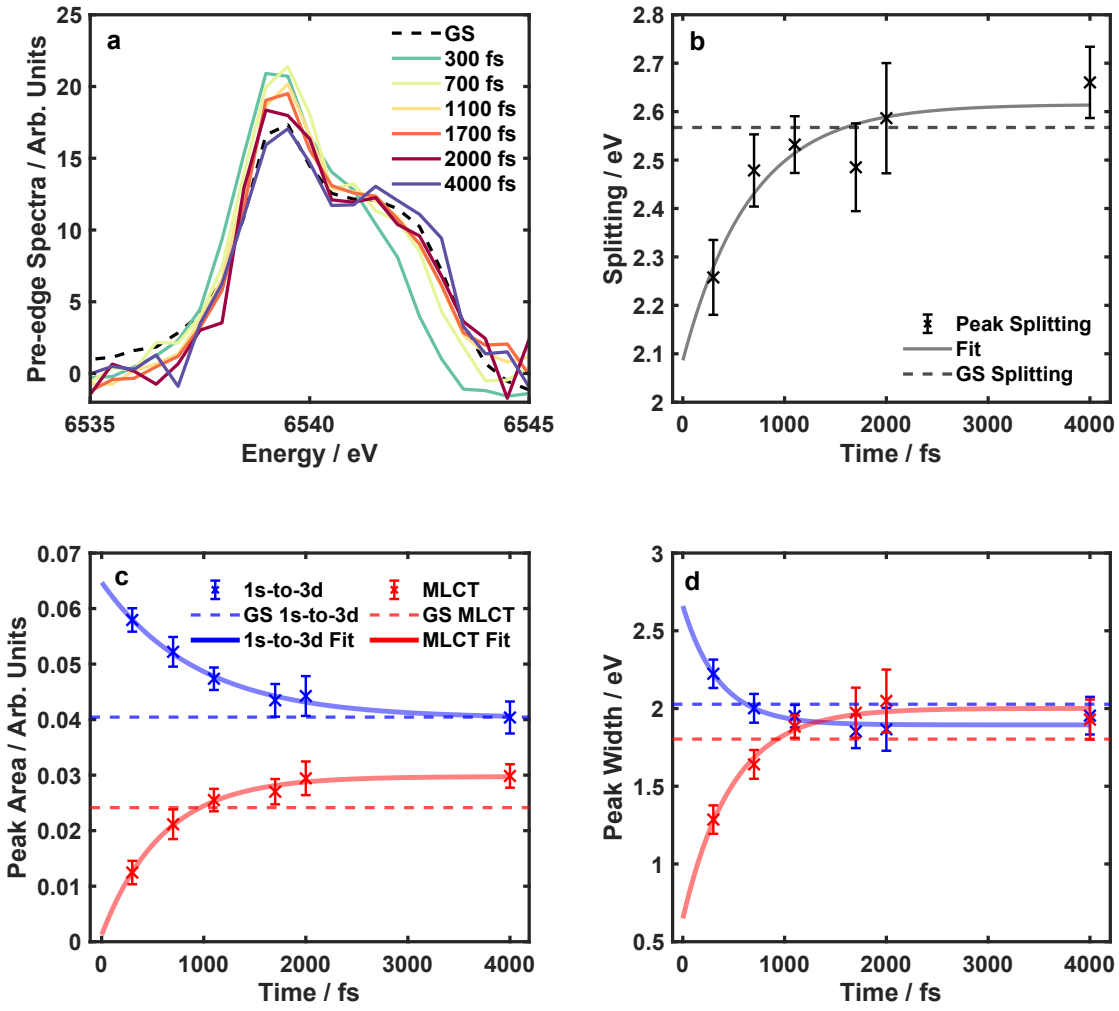

Figure 4.3.9: Pre-edge dynamics after photoexcitation. (a) Ground and excited state pre-edges after subtracting the background of main edge. There is a clear increase in the low-energy 1s-to-3d band after photoexcitation that then decays. There is a blueshift of the high-energy MLCT peak initially that then blueshifts back to the ground state value. (b) Energy splitting of the two peaks as a function of time calculated using Gaussian fits (Figure 4.3.9**c**). (c) Peak areas of the two pre-edge peaks as a function of time calculated using Gaussian fits (Figure 4.3.9**c**). (d) Peak widths of the two pre-edge peaks as a function of time calculated using Gaussian fits (Figure 4.3.9**c**). The fitted lines are an exponential decay with a time constant of around 500 fs and is provided as a guide for the eye. The dashed horizontal lines show the values for the ground state (GS) pre-edge

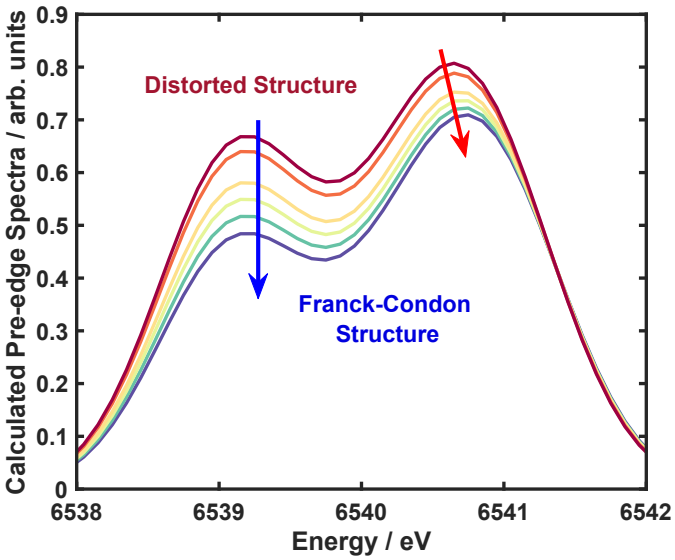

Figure 4.3.10: TD-DFT simulated pre-edge as the molecule moves along the reaction coordinate to the distorted excited state structure. The intensity of the low energy 1s-to-3d transition decreases and the MLCT transition blueshifts moving along this pathway.

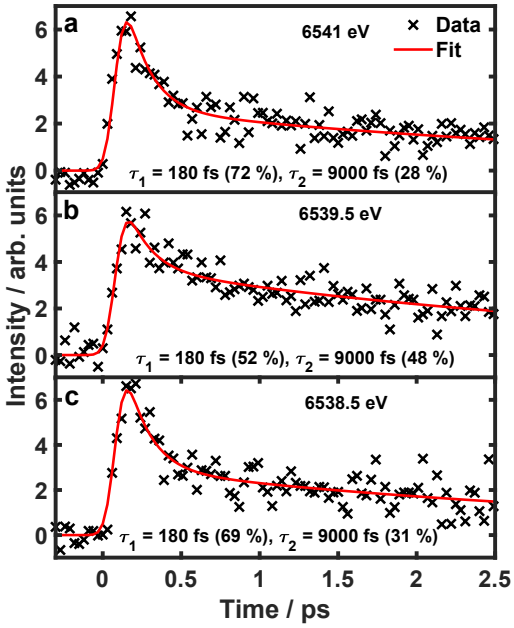

Figure 4.3.11: Pre-edge kinetic traces. All three traces exhibit the same time constants as the optical and main edge data. The number shown in brackets is the fractional amplitude of that time constants' component. Probe X-rays have energies of (a) 6541 eV, (b) 6539.5 eV and (c) 6538.5 eV.

and area then return to near their ground state values over the next few picoseconds.

Similar dynamics are found in the 1s-to-3d and MLCT peak as changes arise from the same dynamics associated with the inner coordination sphere. As the MLCT peak is a marker of metal 3d-ligand 2p orbital overlap it acts as an indirect measure of metal-ligand covalency. The sharing of the unpaired metal 3d electrons with ligand 2p orbitals dictates the superexchange interaction between the metal ions. Therefore, a reduction in the MLCT peak could be an indication of mildly weaker magnetic coupling.

The peak width of the MLCT peak decreases upon excitation. Considering all other bond lengths apart from the Mn–N(β-pic) increase, it is likely that the MLCT peak is predominantly 1s-to-β-pic character in the excited state. The peak is now composed of one dominant transition, which likely sharpens the distribution of energies that the peak is composed of.

In the context of photomagnetism, there are generally two important structural parameters that will dictate the magnetic properties in Mn_3.[176] In the ground state, the magnetic property is dominated by ferromagnetic superexchange between the three Mn(III) sites, yielding a total spin of $S = 6$. The superexchange interaction is dictated mostly by the dihedral Mn–N–O–Mn angles.[176] From the ground state to the distorted structure these decrease from 43 to 42.5 °. Antiferromagnetically-coupled Mn(III) triangles generally have dihedral angles smaller than 20 °,[176] therefore, it is very unlikely that photoexcitation changes the superexchange interaction. The second parameter is the Mn-ligand bond lengths, particularly the difference in the equatorial and axial bond lengths as these determine the magnetic anisotropy through their influence on the crystal field. The average equatorial bond length only increases by around 0.01 Å from the Franck-Condon to the distorted structure, whilst the axial bonds change by around 0.05 Å. Therefore, there is likely a very small change in the magnetic anisotropy. The metal-ligand bond lengths in $Mn(acac)_3$ are calculated to change by around 0.2 Å, which is an order of magnitude more than Mn_3. This is further evidence that this molecule is very rigid and is likely the reason for the short 9 ps excited state lifetime in comparison to the much more flexible $Mn(acac)_3$, which has a lifetime well over 1 ns.[65]

In light of these very small structural changes, it is unlikely that changes in nuclear structure alone will lead to methods of magnetisation control in such a rigid polynuclear complex. If control of magnetisation is to be achieved in these large metallic Mn(III) clusters by influencing the geometry of the crystal field, perhaps more focus should be given to flexible molecules that will be able to accommodate larger changes in nuclear coordinates. There is some evidence that light can influence the magnetic properties in some Mn_{12} SMMs,[169] and so with the right molecular structure femtosecond magnetic manipulation might be possible. It has

been previously shown in Mn(III) monomer model systems, i.e. not SMMs, that it is possible to simplify the reaction coordinate to a reduced number of normal modes by introducing a static rather than dynamic Jahn-Teller axis as shown in Chapter 3.[186] In addition, excited state lifetimes can be reduced by adding structural rigidity into the equatorial plane which restricts the in-plane expansion and favours ground state recovery.[177] These suggest that, through targeted synthetic design, reaction coordinates in the excited state could be engineered to create the most efficient path to control the magnetisation in SMMs. Using pressure as the external stimulus has already been shown to be an effective method to switch the Jahn-Teller distortion to access different magnetic properties.[168] The results presented here show that light can also be used to influence the bond lengths in the inner coordination sphere.

Considering the discussion of the TR-XAS results presented in the previous paragraphs, all of the data can be explained by motion along one reaction coordinate dominated by mode ν_{60}. This may be a general finding for molecules where there are only small transient XAS signals due to the excitation of metal-centred transitions, which do not change oxidation state or spin state but can cause geometrical distortions. To the best of our knowledge, all previous work using femtosecond K-edge TR-XAS studied metal complexes after generation of a charge-transfer state, where there is a formal change in metal oxidation state and therefore large transient signals due to large shifts in the main edge. The measurements presented here, show that even upon excitation of metal-centred transitions in large polynuclear exchange-coupled complexes, conclusions can be drawn from comparison to computation with sensitivity to bond-length changes on the order of hundredths of Ångströms.

4.4 Conclusions and Future Work

In this chapter, it has been demonstrated that time-resolved K-edge X-ray absorption spectroscopy is an excellent method for tracking the nuclear dynamics in complex polynuclear transition metal complexes. The whole K-edge difference spectrum, after metal-centred excitation, can be interpreted using geometric changes occurring predominantly along a single Jahn-Teller active mode, which is crucial for the magnetic anisotropy in these systems. The signature of this mode was also observed as an oscillation with a frequency of around 180 cm^{-1} in the kinetic trace, suggesting a coherent excitation of this mode, in excellent agreement with the optical time-resolved measurements.[65] Spectral changes in the pre-edge also agree well with the changes across the whole K-edge region with motion along one Jahn-Teller mode being dominant. The good agreement between computation and experiment allowed us to estimate bond length changes from the Franck-Condon structure to

the excited state on the order of hundredths of ångströms demonstrating the sensitivity of TR-XAS. Changes in the axial Jahn-Teller bonds were greater than 0.03 Å whereas equatorial bonds elongated only by around 0.01 Å, indicating structural rigidity in the equatorial plane. In light of these small geometry changes upon excitation, it would be instructive to look at more flexible SMMs as a platform to direct nuclear motion using light in order to control the magnetisation direction in SMMs. Although only the nuclear structure has been studied in this chapter, electronic and spin dynamics will certainly play a role in magnetisation dynamics.

In terms of further X-ray spectroscopies, studying these dynamics with methods that are more sensitive to d-orbital occupation such as resonant inelastic X-ray scattering[221, 222] to follow the electronic dynamics would be useful. Using known magneto-structural relationships, it is possible to infer likely changes in the magnetic properties after photon absorption using the structural data obtained in this chapter. However, more direct measures of the superexchange interaction and magnetic anisotropy will be crucial in the emerging field of ultrafast single-molecule magnetism. A tentative connection between the MLCT peak intensity and metal-ligand covalency has been made that will have an influence on the superexchange interaction but more detailed information is needed. In terms of other aspects of X-ray absorption spectroscopy, the ligand K-edge,[223] metal shakedown transitions and metal L-edge spectra[224] are good markers of metal-ligand covalency. Considering exchange interactions (and therefore superexchange interactions) depend heavily on orbital overlap and covalency, these transitions could be used to gather information on coupling between metal centres. The spin quantum number and direction of magnetisation can be found by angle-dependent X-ray magnetic circular dichroism at metal L-edges[225] which would be an excellent technique to study single-molecule magnetism on ultrafast timescales particularly for bimetallic SMMs where the spin dynamics could be followed independently at each edge. But, the first measurements using this technique at femtosecond timescales at XFELs have only just been published.[226]

Time-resolved X-ray K-edge emission spectroscopy has already been carried out at the European Union XFEL by the group, which should provide further information on the electronic and spin dynamics of Mn_3. Preliminary data are shown in Figure 4.4.1 which shows the Kα (2p to 1s) and Kβ (3p to 1s) emission difference spectra as a function of pump-probe time delay. The Kα emission is primarily sensitive to 2p-3d spin-orbit coupling as the two peaks arise from the $2p_{1/2}$ and $2p_{3/2}$ states. Kβ emission is sensitive to the 3p-3d exchange interaction. Therefore, K-edge emission has been used to track changes in spin state in transition metal complexes.[205, 209, 227, 228] But importantly, as there is no formal changes in spin state upon photoexcitation of Mn_3, it is specifically sensitive to spin density

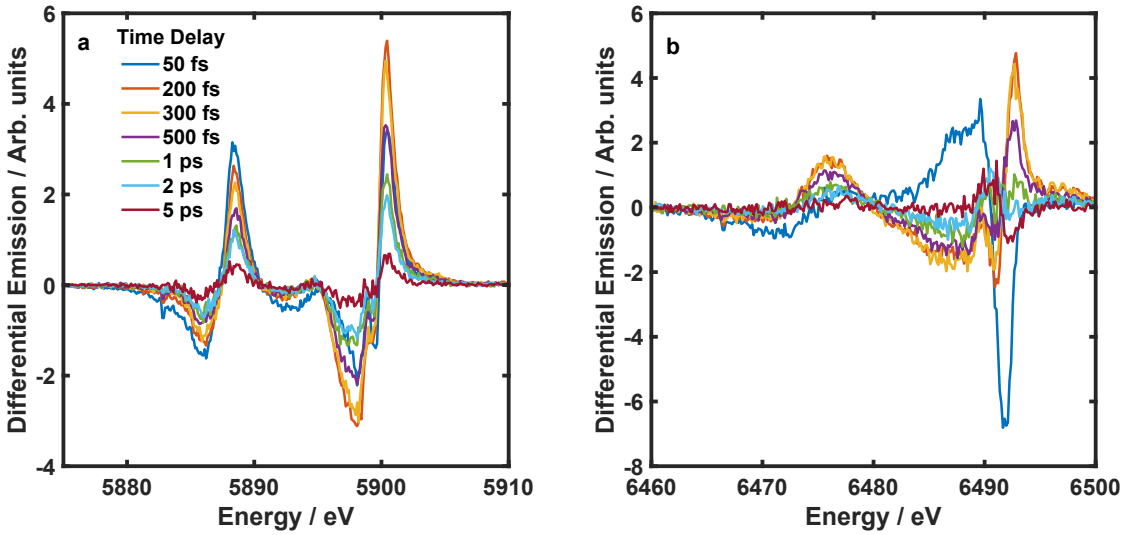

Figure 4.4.1: Femtosecond K-edge emission difference spectra of a 5 mM ethanoic solution of Mn_3 after photoexcitation with a 400 nm pump with a fluence of 120 mJcm^{-2}. **a** Kα emission spectra. **b** Kβ emission spectra.

on the metal ions. Therefore, careful analysis of the K-edge emission spectra could yield information on the spin dynamics and spin density after photoexcitation.

Chapter 5

Ligand-field excited states in Ru(II) triazolyl complexes

5.1 Introduction

Ruthenium(II) polypyridyl complexes have been utilized for a variety of photophysical applications, from solar energy conversion[229, 230] to photodynamic therapy.[231, 232] The broad applicability of these complexes to photochemical problems is due to their strong MLCT transitions in the visible region, which can initiate a wide range of processes. One of the most extensively studied chromophores is $Ru(bpy)_3^{2+}$ (where bpy = 2,2'-bipyridine).[233] A search of "$Ru(bpy)_3^{2+}$ photophysics" on Google Scholar yields more than 20,000 results.

A scheme of the dynamics after MLCT excitation of $Ru(bpy)_3^{2+}$ is shown in Figure 5.1.1. Excitation of the $^1A_1$ ground state to the ^{1}MLCT state leads to a fast ISC to the famous luminescent and photoredox active ^{3}MLCT state.[234, 235] This process occurs in 20 fs[236, 237] and the lifetime of the ^{3}MLCT state is 600 ns in aqueous solution at room temperature.[141, 238] Temperature-dependent emission studies indicate that the ^{3}MLCT state is quenched at higher temperatures via the thermal population of the ^{3}MC state which is around 3000 cm^{-1} higher in energy compared to the ^{3}MLCT state.[239] The ^{3}MC potential energy minimum is distorted with respect to the $^1A_1$ ground state so that the ^{3}MC minimum is close to the crossing with the ground state potential energy surface. This leads to fast nonradiative decay to the ground state, which quenches the emission. The relative energies of the ^{3}MC and ^{3}MLCT states can be tuned by applying pressure[240] or chemical modification of the bpy ligands.[241] In cases where the ^{3}MC state is shifted below that of the ^{3}MLCT state, the emission is completely quenched.

Although long-lived MLCT states are beneficial for photoredox and solar cells, low-lying metal-centred states such as the ^{3}MC state offer additional avenues for

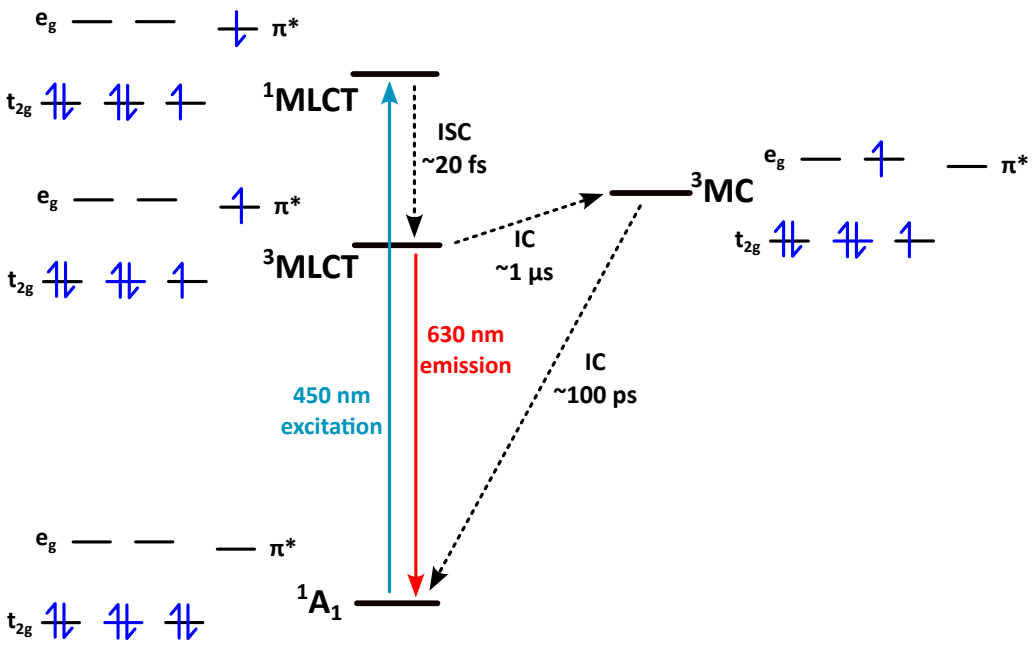

Figure 5.1.1: Depiction of the photoinduced dynamics of $Ru(bpy)_3^{2+}$ after excitation of the MLCT transition. Unbroken lines correspond to radiative processes and dotted lines correspond to nonradiative processes. IC is internal conversion and ISC is intersystem crossing. The orbital configurations of the states is also given where π^* refers to the antibonding orbital centred on the bipyridine ligands.

light-triggered chemistry. The population of antibonding e_g^* orbitals in the ^{3}MC state can lead to ligand loss photochemistry with potential applications in light-activated drug release.[160, 242, 243] The ^{3}MC has a $t_{2g}^5 e_g^1$ electron configuration that is electronically degenerate and therefore is subject to Jahn-Teller distortions. Taking into account the antibonding character of the e_g^* orbitals, the distortion manifests itself as tetragonal, similar to the Mn(III) complexes discussed in the previous sections. Theoretical modelling of $Ru(bpy)_3^{2+}$ shows two distorted structures of the ^{3}MC state.[244] There is a $^3MC_{trans}$ state that shows an elongation of two metal-ligand bonds along the same axis, which is equivalent to the axially elongated Jahn-Teller distortion and can lead to the dissociation of monodentate ligands of Ru(II) polypyridyl complexes.[245] The $^3MC_{cis}$ state is equivalent to an axially compressed Jahn-Teller distortion with four longer bonds in the plane. The $^3MC_{cis}$ state can lead to bidentate ligand loss.[246] However, some new experimental evidence has emerged suggesting that ligand-loss photochemistry can also occur directly from MLCT states.[247] Considering the variety of ligand-field and MLCT states, it is vitally important to understand their behaviour on ultrafast timescales to control the outcome of photochemical transformations.

Despite evidence for the existence of the ^{3}MC state from temperature-dependent emission and photochemistry experiments,[239] direct spectroscopic detection of this state has remained fairly elusive. The difficulty arises from the fact that the popu-

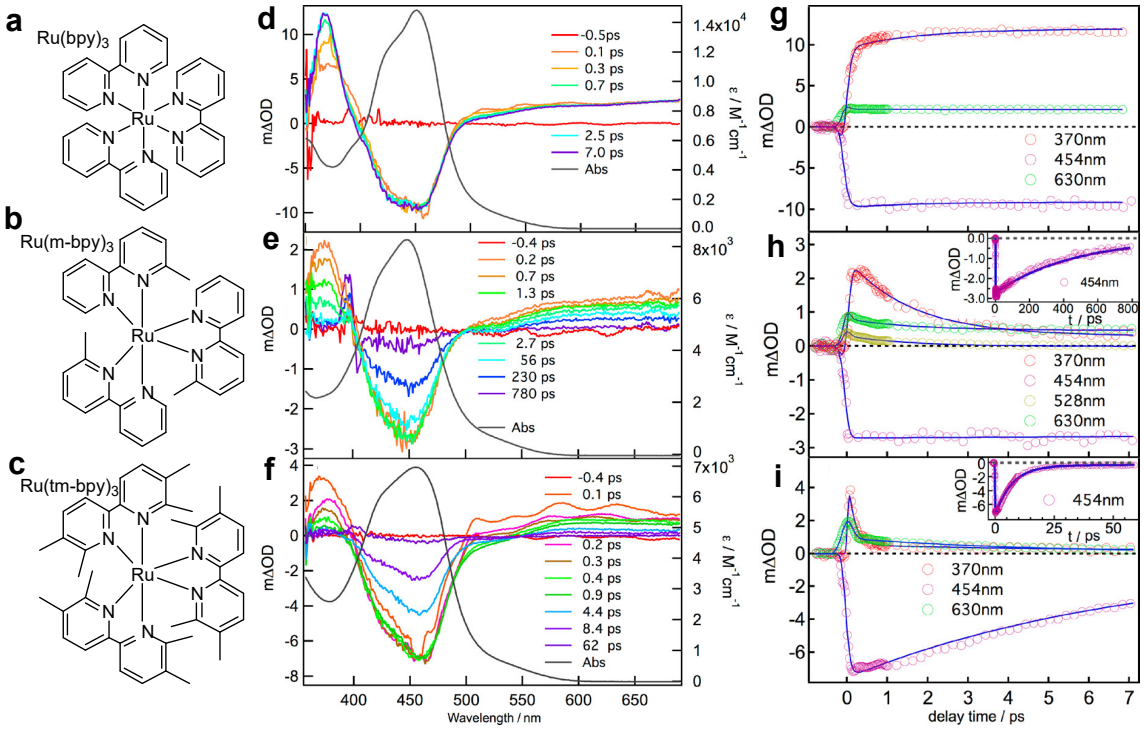

Figure 5.1.2: Optical transient absorption spectroscopy of $Ru(bpy)_3^{2+}$ and its sterically encumbered derivatives. **a**–**c** show the chemical structures of $Ru(bpy)_3^{2+}$, $Ru(m-bpy)_3^{2+}$ and $Ru(tm-bpy)_3^{2+}$. **d**–**f** show the optical transient absorption difference spectra at a range of time delays for acetonitrile solutions of $Ru(bpy)_3^{2+}$, $Ru(m-bpy)_3^{2+}$ and $Ru(tm-bpy)_3^{2+}$. The black line shows the corresponding absorption spectrum with the axis on the left. **g**–**i** show the optical transient absorption kinetic traces at a range of wavelengths for acetonitrile solutions of $Ru(bpy)_3^{2+}$, $Ru(m-bpy)_3^{2+}$ and $Ru(tm-bpy)_3^{2+}$. Figures **d**–**i** are taken from ref. [249]

.

lation of the ^{3}MC state is much slower ($\approx$ 1 µs) than its depopulation back to the ground state ($\approx$ 100 ps). Therefore, there is a fleeting population of the ^{3}MC state that exists only at extremely low concentrations that prevents its identification in time-resolved experiments. Additionally, in complexes where the ^{3}MC state is the lowest energy excited state, it is expected that the ^{3}MC to ^{3}MLCT transition intensity will be much weaker than its singlet counterpart due to longer metal-ligand bond lengths in the ^{3}MC state,[248] which leads to difficulty observing it in transient absorption experiments.

Detection of the MC state in $Ru(bpy)_3^{2+}$ still remains elusive, however, observation of this state has been inferred in some Ru(II) complexes with derivatised bpy ligands by Sun et al.[249, 250] The regular bpy ligands were replaced by m-bpy and tm-bpy which are 6-methyl-2,2'-bipyridine and 4,4',6,6'-tetramethyl-2',2'-bipyridine, respectively as shown in Figure 5.1.2**a**–**c**. The steric bulk of the extra hydrocarbon substituents leads to longer metal-ligand bonds, which reduces the strength of the ligand field and pushes the ^{3}MC state below the ^{3}MLCT state, as shown by

their complete lack of photoluminescence. Further transient absorption measurements show very different excited state lifetimes for $Ru(bpy)_3^{2+}$, $Ru(m{-}bpy)_3^{2+}$ and $Ru(tm{-}bpy)_3^{2+}$. Results are shown in Figure 5.1.2**d**–**i**. $Ru(bpy)_3^{2+}$ shows the expected fast population of the ^{3}MLCT state and then no change over the first few hundred picoseconds after photoexcitation due to its microsecond lifetime.[238] However, there are stark differences in the dynamics of $Ru(bpy)_3^{2+}$ compared to $Ru(m{-}bpy)_3^{2+}$ and $Ru(tm{-}bpy)_3^{2+}$. In $Ru(m{-}bpy)_3^{2+}$, there is a fast decay of 1.6 ps of the transition at 380 nm due to the absorption of the radical $bpy^{\bullet-}$ anion, while the bleach of the ground state persists before decaying with a time constant of 450 ps. $Ru(tm{-}bpy)_3^{2+}$ shows very similar spectral features, but the timescales are much faster. The fast time component which defines the decay of the 380 nm peak is only 160 fs and the total excited state lifetime is just 7.5 ps.

Consolidating the information in the previous paragraph, the authors suggest the following interpretation, summarised in Figure 5.1.3. Upon substitution of the two hydrogens for methyl groups in the ligands of $Ru(bpy)_3^{2+}$, the metal-ligand bond lengths increase, decreasing the ligand-field strength, which stabilises the ^{3}MC state with respect to the ^{3}MLCT state. This leads to a fast non-radiative decay from the ^{3}MLCT state into the ^{3}MC state. Due to the population of antibonding e_g^* orbitals, the metal-ligand bond lengths elongate in the metal-centred state, and the minimum of the ^{3}MC state occurs at a geometry different from that of the ground state. Now, there is a small barrier to deactivation to the ground state as the curve crossing between the ^{3}MC state and the ground state is close to the ^{3}MC state minimum, leading to a fast nonradiative return to the ground state. The addition of more methyl groups to form $Ru(tm{-}bpy)_3^{2+}$ generates greater stabilization in the ^{3}MC state due to even longer metal-ligand bonds. The lower energy ^{3}MC state speeds up both the ^{3}MLCT deactivation and the ^{3}MC decay back to the ground state.

Despite the strong evidence for accessing the ^{3}MC state, there is no experimental observable in a transient absorption measurement that defines it.[250] The peak at 380 nm decays with the radical $bpy^{\bullet-}$ anion. There is a flat excited state absorption above 500 nm once the ^{3}MC state has been populated but this absorption also occurs in the ^{3}MLCT state and therefore cannot serve as a good marker for the population of the ^{3}MC state.

In previous paragraphs, steric bulk has been shown to effectively lower the energy of the ^{3}MC state. Electronic effects can also be used the change excited state ordering. The ability to synthesise 1,2,3-triazoles opened the door to many new ligands for coordination chemistry.[251] These ligands have led to many interesting developments in the photophysics of transition metal complexes.[252, 253] Compared to their bpy analogues, they tend to show a blueshifted absorption spectrum and highly quenched emission spectra. These properties are expected since the electron-

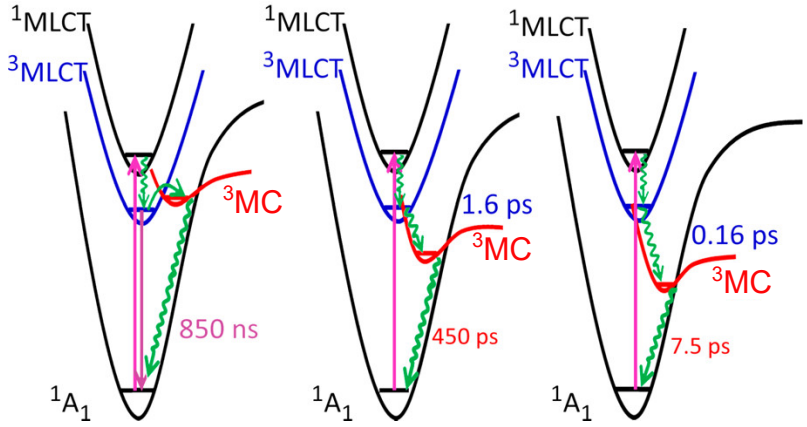

Figure 5.1.3: Schematic representation of the potential energy surfaces of the ground state and the relevant excited states of $Ru(bpy)_3^{2+}$, $Ru(m-bpy)_3^{2+}$ and $Ru(tm-bpy)_3^{2+}$ (from left to right). Radiative and non-radiative processes are indicated by smooth and wavy lines, respectively. For $Ru(bpy)_3^{2+}$, the lifetime given is associated with the ^{3}MLCT lifetime. For $Ru(m-bpy)_3^{2+}$ and $Ru(tm-bpy)_3^{2+}$, the lifetimes given reflect the ^{3}MC to ^{3}MLCT conversion and ^{3}MC to ground state conversion, respectively. Figure taken from ref. [249].

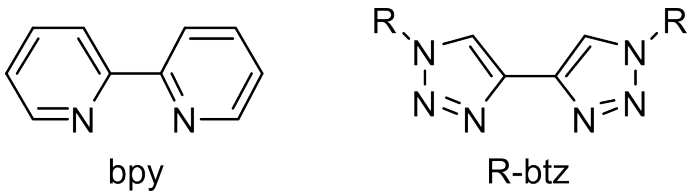

Figure 5.1.4: Structure of bpy (left) and R-btz (right) where R phenyl or benzyl.

rich triazolyl rings are likely to destabilise the MLCT states relative to the MC states when compared to pyridyl ligands.

The effect of the symmetric 4,4'-bi-1,2,3-triazolyl (btz) ligand (a direct analogue of bpy) on the electronic structure of Ru(II) complexes has been studied by Welby et al.[254] The chemical structure of bpy and btz are shown in Figure 5.1.4. Welby et al. studied the photophysics of complexes $[Ru(bpy)_{3-n}(Bn-btz)_n]^{2+}$ (where $n = 0$–3 and Bn = benzyl) to investigate the effect of sequentially replacing pyridyl with triazolyl ligands. The UV-visible absorption spectra of the four complexes are shown in Figure 5.1.5**a**. For $n = 0$, the usual $Ru(bpy)_3^{2+}$ spectrum is shown with the strong ^{1}MLCT transition at 450 nm and the bpy $\pi \rightarrow \pi^*$ transition at 290 nm. On replacement of bpy with btz ligands, the MLCT energy blueshifts as n increases from zero to two, suggesting a destablisation of the MLCT state. Upon substitution of the final bpy ligand with btz, the 450 nm MLCT and sharp 290 nm $\pi \rightarrow \pi^*$ transition disappear and a broad peak centred at 315 nm appears. Additionally, when $n = 0$–2, there is detectable emission from the complexes, however, for $n = 3$, there is no emission even at 77 K.

Quantum chemical calculations suggest that the 450 nm peak for all bpy-containing

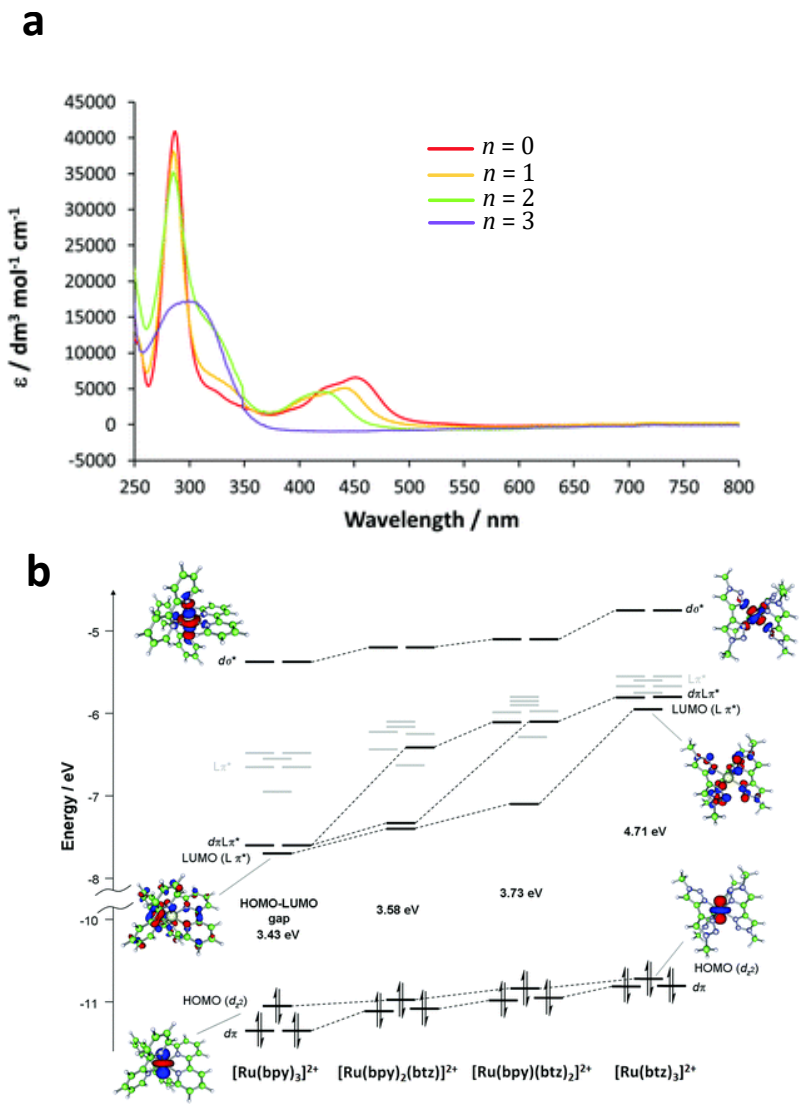

Figure 5.1.5: **a** UV-visible spectra of $[Ru(bpy)_{3-n}(Bn{-}btz)_n]^{2+}$ in acetonitrile solution. **b** Computed energies of valence states showing the destabilsation of the MCLT state upon replacing bpy with btz in $[Ru(bpy)_{3-n}(Bn{-}btz)_n]^{2+}$. Figures taken from ref. [254].

complexes has significant MLCT character from the Ru(II) to the bpy ligands (Figure 5.1.5**b**). Upon replacing the final bpy ligand with btz, there can no longer be MLCT transitions to a bpy ligand and the lowest energy spin-allowed transition is now of metal-centred character. Considering the excited ^{1}MC state is below the ^{1}MLCT state it is also likely that the ^{3}MC state sits below the ^{3}MLCT for $[Ru(btz)_3]^{2+}$. To confirm this, a geometry optimisation was carried out fixing the spin multiplicity to three. Compared to the ground state singlet, the triplet geometry displays an elongation of two mutually *trans* Ru−N bonds. Partial dechelation of these two bonds leads to the formation of $[Ru(\kappa^2\text{-btz})(\kappa^1\text{-btz})]^{2+}$. This structural change is due to Jahn-Teller distortion in the ^{3}MC state due to an electronic degeneracy in the e_g^* orbitals.

As discussed throughout this thesis, the population of electronic states with displaced potential energy minima can lead to coherent vibrational motion along that potential energy surface. Photoexcitation into the ^{1}MLCT state of $[Ru(R{-}btz)_3]^{2+}$ will lead to fast, potentially coherent crossing to the ^{3}MC state, which may allow the observation of a vibrational wavepacket in a transient experiment. This would be the first observation of coherent motion in the metal-centered state of a Ru(II) complex. Compared to the Mn(III) complexes discussed elsewhere in this thesis, excitation leads to a change from no Jahn-Teller distortion to distortion in the excited state.

This chapter contains results from a collaboration with Paul A. Scattergood and Paul I. P. Elliot's groups at the University of Huddersfield. All syntheses and computations were performed at the University of Huddersfield. All time-resolved measurements were carried out and analysed by myself.

5.2 Experimental

The complexes, $[Ru(Ph{-}btz)_3][PF_6]_2$ and $[Ru(Bn{-}btz)_3][PF_6]_2$ were synthesised at the University of Huddersfield. For transient absorption measurements, the complexes were dissolved in acetonitrile at a concentration of 1.2 mM. A 0.2 mm path length Starna flow cuvette was used to replenish the sample every few seconds using a flow rate of 8 µL/min.

The samples were excited using a 330 nm pump pulse. Although it is possible to generate this from the Light Conversion Lyra, the light was manually generated using the second harmonic of the 660 nm NOPA output after the optical delay stage. The delay stage uses silver mirrors, and therefore, a lot of UV light is lost as it passes through the stage. Much higher powers could be achieved by frequency doubling the 660 nm beam close to the sample. A 0.2 mm thick BBO was placed in a rotation mount that also allowed fine adjustment of the crystal angle to optimise phase matching conditions. The crystal axes were aligned with the polarisation of light and the incident angle tuned to achieve maximum second harmonic generation efficiency of around 10 %. Most of the residual 660 nm light was removed by the polariser before the sample (the second harmonic has a polarisation perpendicular to the fundamental beam), but a 275–375 nm band-pass filter was used to remove the remaining 660 nm light.

The pump-probe polarization angle was set to the magic angle (54.7 °) for all measurements to ensure that there are no anisotropic contributions. A fluence of 1.3 mJcm^{-2} was used for the pump with a beam diameter of 160 µm. The diameter of the probe was 110 µm.

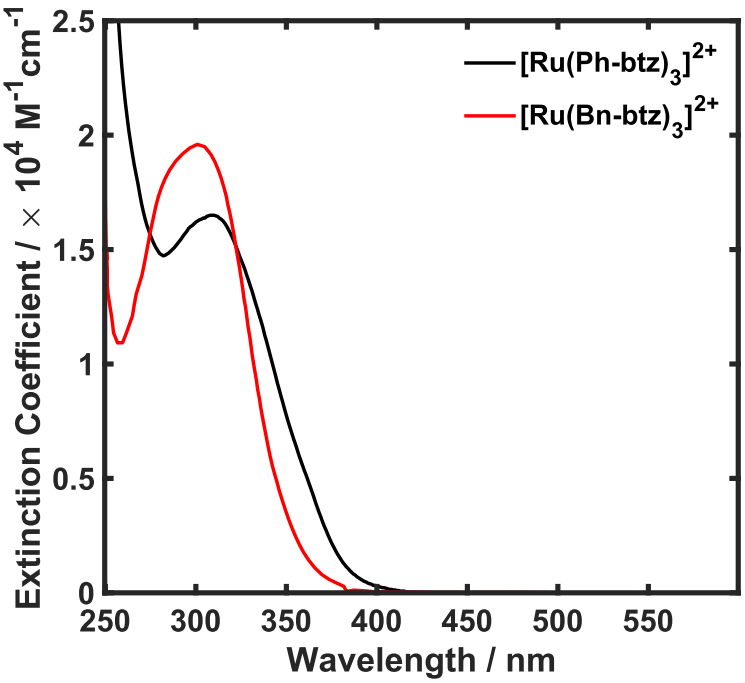

Figure 5.3.1: UV-Vis spectrum of $[Ru(Ph{-}btz)_3]^{2+}$ and $[Ru(Bn{-}btz)_3]^{2+}$ in acetonitrile.

5.3 Results and Discussion

The UV-vis spectra of $[Ru(Ph{-}btz)_3]^{2+}$ and $[Ru(Bn{-}btz)_3]^{2+}$ in acetonitrile are shown in Figure 5.3.1. This is composed of one large broad MLCT transition centred around 300 nm. The spectrum of $[Ru(Ph{-}btz)_3]^{2+}$ is slightly redshifted with respect to $[Ru(Bn{-}btz)_3]^{2+}$. This is likely due to the higher amount of conjugation in Ph-btz which will shift the ligand π^* orbitals to lower energies. Calculations suggest that the singlet metal-centred transition is at lower energies than the MLCT transition but it is likely obscured by the much stronger charge transfer transition.[254] Considering the ^{1}MC state is at lower energies than the ^{1}MLCT state, it is expected the ^{3}MC state will be lower energy than the ^{3}MLCT state.[254] Therefore, in the transient absorption experiment, the sample was pumped at the low-energy edge of the ^{1}MLCT transition and it is expected this would quickly decay to the lowest energy triplet metal-centred state, which is Jahn-Teller distorted.

Differential absorption spectra at different time delays for $[Ru(Ph{-}btz)_3]^{2+}$ and $[Ru(Bn{-}btz)_3]^{2+}$ in acetonitrile are shown in Figures 5.3.2**a** and **b**. They display very similar features with the GSB arising from the MLCT transition below 400 nm and a broad ESA at longer wavelengths. At the earliest pump-probe delays, there is an additional feature at 600 nm and around 700 nm for $[Ru(Ph{-}btz)_3]^{2+}$ and $[Ru(Bn{-}btz)_3]^{2+}$, respectively. The spectra of $[Ru(Bn{-}btz)_3]^{2+}$ also display a small ESA at 380 nm at 2.5 ps that does not have an analogue in $[Ru(Ph{-}btz)_3]^{2+}$. The ground state recovery is complete within hundreds of picoseconds for both

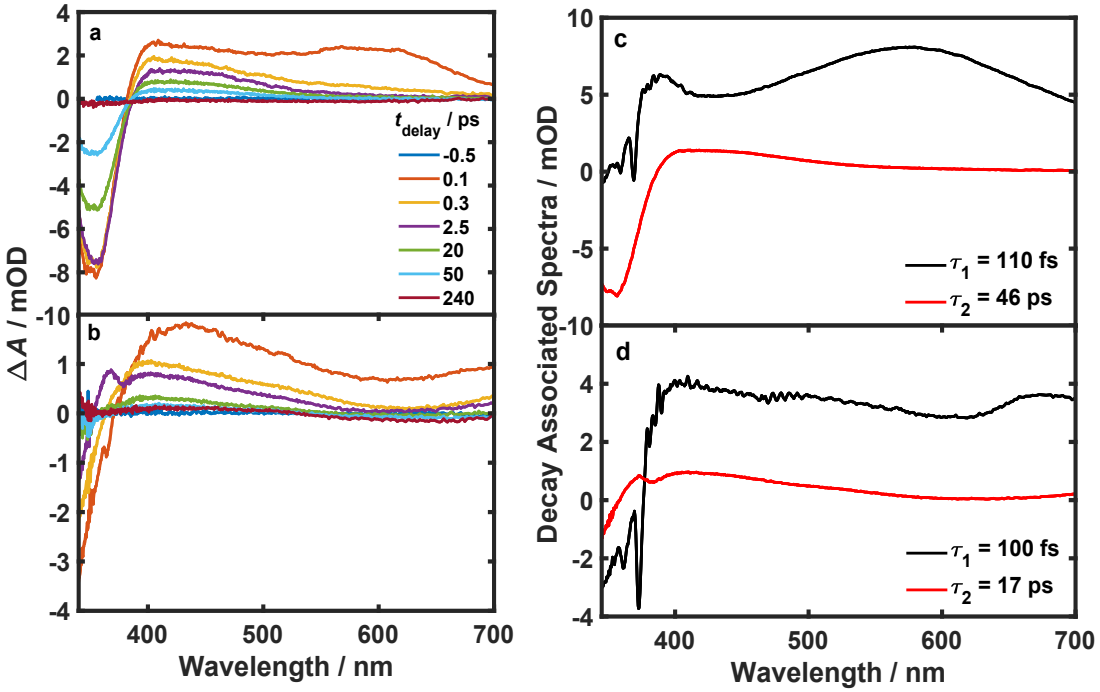

Figure 5.3.2: Difference absorption spectra and decay associated spectra for the two Ru(II) complexes. Transient absorption spectra at various pump-probe time delays after 330 nm excitation of acetonitrile solutions of $Ru(Ph{-}btz)_3^{2+}$ and $Ru(Ph{-}btz)_3^{2+}$ are shown in panels **a** and **b**, respectively. Decay-associated spectra from the global fitting of acetonitrile solutions of $Ru(Ph{-}btz)_3^{2+}$ and $Ru(Ph{-}btz)_3^{2+}$ are shown in panels **c** and **d**, respectively. The time constants associated with the decay-associated spectra are given in the legend.

complexes.

To further characterise the dynamics, a global fitting procedure was carried out for every wavelength trace using a sequential model in Glotaran, which is a kinetic modelling tool that enables one to fit data to a global kinetic model.[255] A selection of the data and fits are shown in Figure 5.3.3. The decay-associated spectra of this fit are shown in Figure 5.3.2**c** for $[Ru(Ph{-}btz)_3]^{2+}$ and 5.3.2**d** for $[Ru(Bn{-}btz)_3]^{2+}$. The global fit produced time constants of $\tau_1 = 110 \pm 1$ fs and $\tau_2 = 46 \pm 1$ ps for $[Ru(Ph{-}btz)_3]^{2+}$ and $\tau_1 = 100 \pm 1$ fs and $\tau_2 = 17 \pm 1$ ps for $[Ru(Bn{-}btz)_3]^{2+}$. Considering τ_2 is accompanied by a decay to zero for all wavelengths, this is assigned to recovery of the ground state. This value is comparable to the recovery of the ground state of $Ru(m{-}bpy)_3^{2+}$ which was assigned to the decay of the triplet metal-centered state back to the $^1A_1$ ground state.[249] The decay-associated spectra of τ_1 for the $[Ru(Ph{-}btz)_3]^{2+}$ data show no change in the bleach region, which suggests that it is simply a conversion between excited states with no ground state recovery.

The sequential global fit describes the transient absorption data of $[Ru(Ph{-}btz)_3]^{2+}$ well at all wavelengths. However, the probe region around 370–400 nm in the

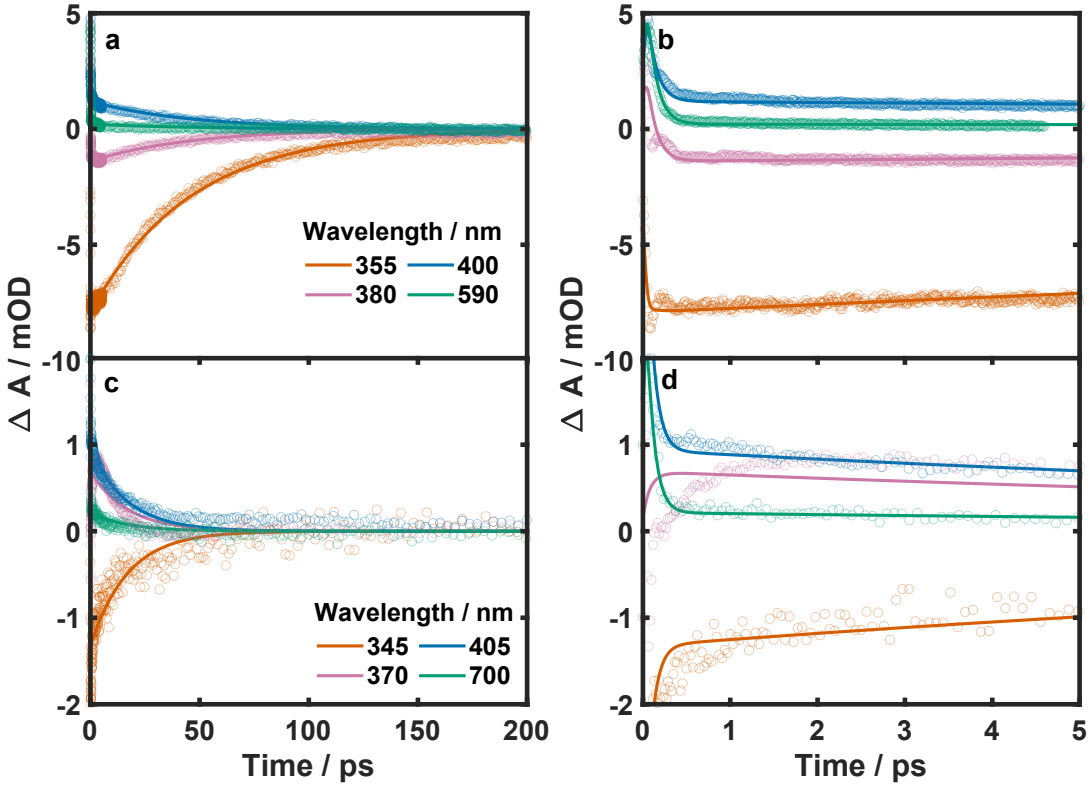

Figure 5.3.3: Transient absorbance as a function of time delay for selected wavelengths. The circles correspond to data points and the lines to the global fit. **a** and **b** show the data for $[Ru(Ph{-}btz)_3]^{2+}$ and **c** and **d** show the data for $[Ru(Bn{-}btz)_3]^{2+}$.

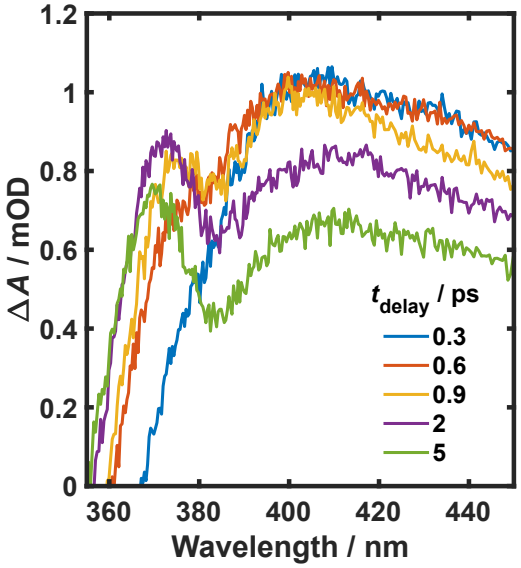

Figure 5.3.4: Transient absorption spectra of $Ru(Bn{-}btz)_3^{2+}$ in acetonitrile in the region 355–445 nm. The peak at 370 nm grows in and blueshifts within the first 5 ps after photoexcitation at 330 nm.

$[Ru(Bn{-}btz)_3]^{2+}$ data set is not well modeled by the fitting. This can be seen clearly in the 370 nm trace in Figure 5.3.3**d**. The reason for the discrepancy between the model and the data likely arises from the additional ESA peak that is observed around 370 nm. Figure 5.3.4 shows the transient absorbance in the region 355-445 nm for delay times up to 5 ps, which clearly shows a growth and blueshift of this peak over the first few picoseconds after excitation. Global analysis is unable to capture shifting of transition maxima,[256] which is likely the source of the mismatch between the model and data around this region. Considering this peak blueshifts over a few picoseconds it is likely due to vibrational relaxation.

The values for τ_1 in both complexes are around 100 fs and the molecules exhibit similar features in the decay-associated spectra with a peak above 600 nm and a lower signal around the ground state bleach. It is likely that this time constant is associated with the same dynamics in $[Ru(Ph{-}btz)_3]^{2+}$ and $[Ru(Bn{-}btz)_3]^{2+}$. After excitation to the ^{1}MLCT state, the ^{3}MLCT state is likely to be formed in around 20 fs through ISC, which cannot be observed due to the experimental time resolution.[236] Therefore, τ_1 is attributed to the internal conversion from the ^{3}MLCT state to the ^{3}MC state, although this could also have some contributions from intramolecular vibrational redistribution. Further evidence of the population of the ^{3}MC state is given in subsequent paragraphs. τ_2 is associated with a return to the baseline and is assigned to the recovery of the $^1A_1$ ground state. The timescales shown here are very similar to the data shown by Sun et al. in the introduction with a sub-picosecond relaxation of the ^{3}MLCT state to the ^{3}MC state and then recovery

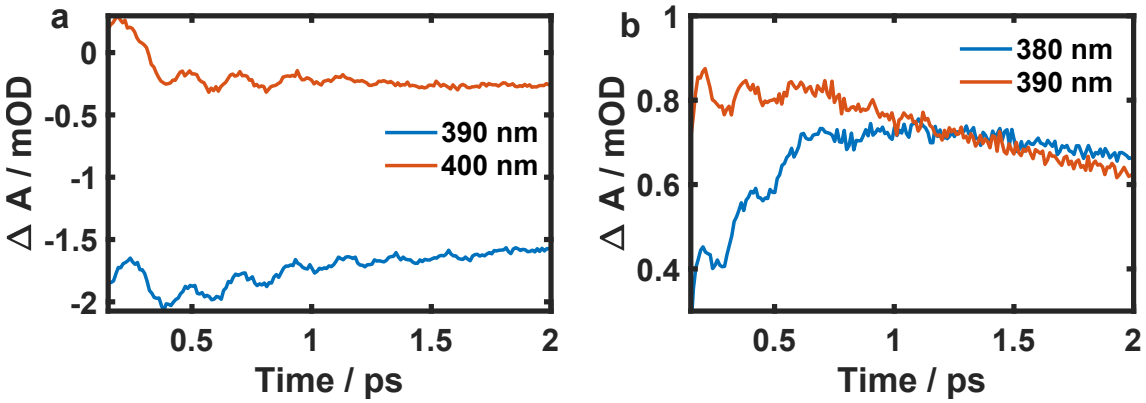

Figure 5.3.5: Kinetic traces up to 2 ps (**a**) $[Ru(Ph{-}btz)_3]^{2+}$ and (**b**) $[Ru(Bn{-}btz)_3]^{2+}$ showing the oscillatory motion at early times.

of the ground state over the next tens of picoseconds.[249] This strongly suggests that the ^{3}MC state is the lowest-energy ground state that is populated in around 100 fs and followed by ground state recovery in 10–50 ps.

Considering the ^{3}MC state is populated within 100 fs, it is possible that coherent vibrational motion is triggered in this state. To establish if this is the case, transient absorption measurements were carried out with higher signal-to-noise (2000 laser shots for each time scan with 5 repeats) up to 3 ps to resolve any possible vibrational coherence. Kinetic traces up to 2 ps are shown in Figure 5.3.5. Figure 5.3.5**a** refers to data for $[Ru(Ph{-}btz)_3]^{2+}$, which clearly exhibits oscillations that have a period of around 200 fs. The situation for $[Ru(Bn{-}btz)_3]^{2+}$ in panel **b** is more complex, oscillatory behaviour can be observed but the period of the waveform appears to increase as time progresses. The coherence also decays to below the noise level much quicker.

The residuals after global analysis were Fourier transformed in the time domain and the corresponding wavelength-wavenumber map is shown in Figure 5.3.6. The bottom panels in this figure show the Fourier transform at a particular wavelength. The frequency of the oscillation for the $[Ru(Ph{-}btz)_3]^{2+}$ data is 156 cm^{-1} and it is strongest around 390 nm. This is shifted away in energy from the ground state transition maximum, therefore this is likely an excited state vibrational coherence. For $[Ru(Bn{-}btz)_3]^{2+}$, the map shows no obvious frequency components, although there may be a signal below 100 cm^{-1} and also a broad peak between 100 and 200 cm^{-1}. The lack of a single obvious frequency component could be due to the short lifetime and apparent shift in frequency of these oscillations.

To further investigate the change in frequency over time, a shifting-window Fourier transform was performed in the region where the oscillations appear the strongest for both complexes. A shifting-window Fourier transform involves Fourier transforming a window of time-domain data and then shifting that window along

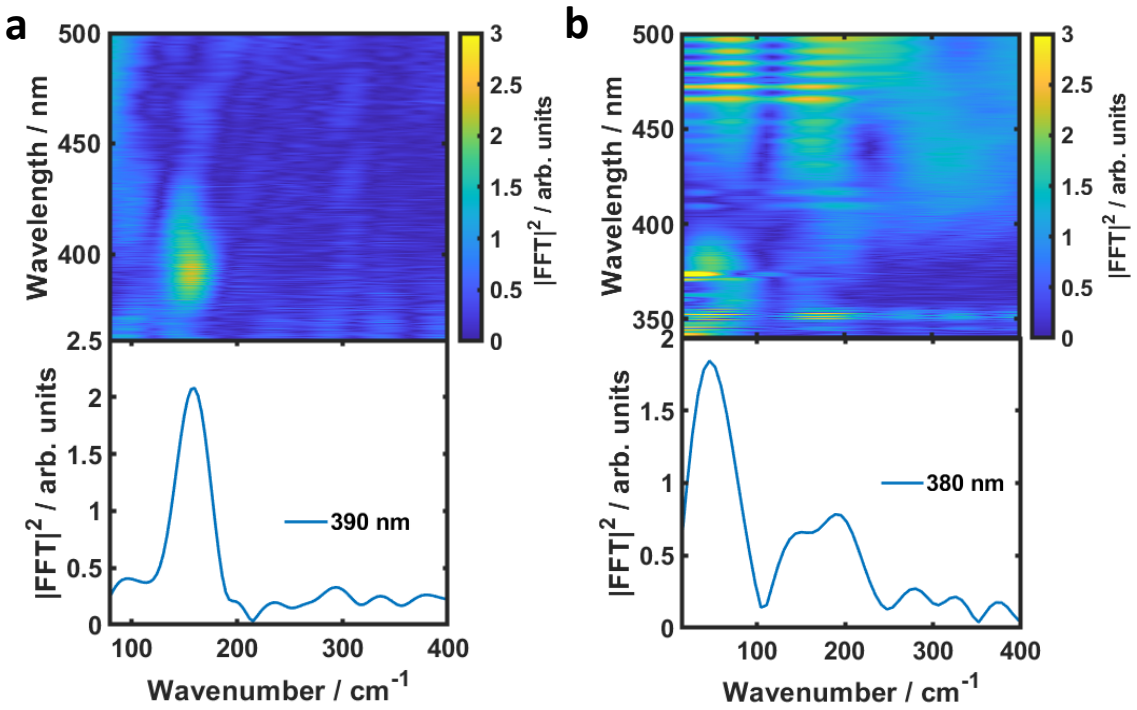

Figure 5.3.6: Fourier transform of the global fit residuals for **a** $[Ru(Ph{-}btz)_3]^{2+}$ and **b** $[Ru(Bn{-}btz)_3]^{2+}$. The FFT is performed along the time axis yielding a wavelength-wavenumber map. The bottom panel shows a slice of the Fourier transform spectrum for one wavelength.

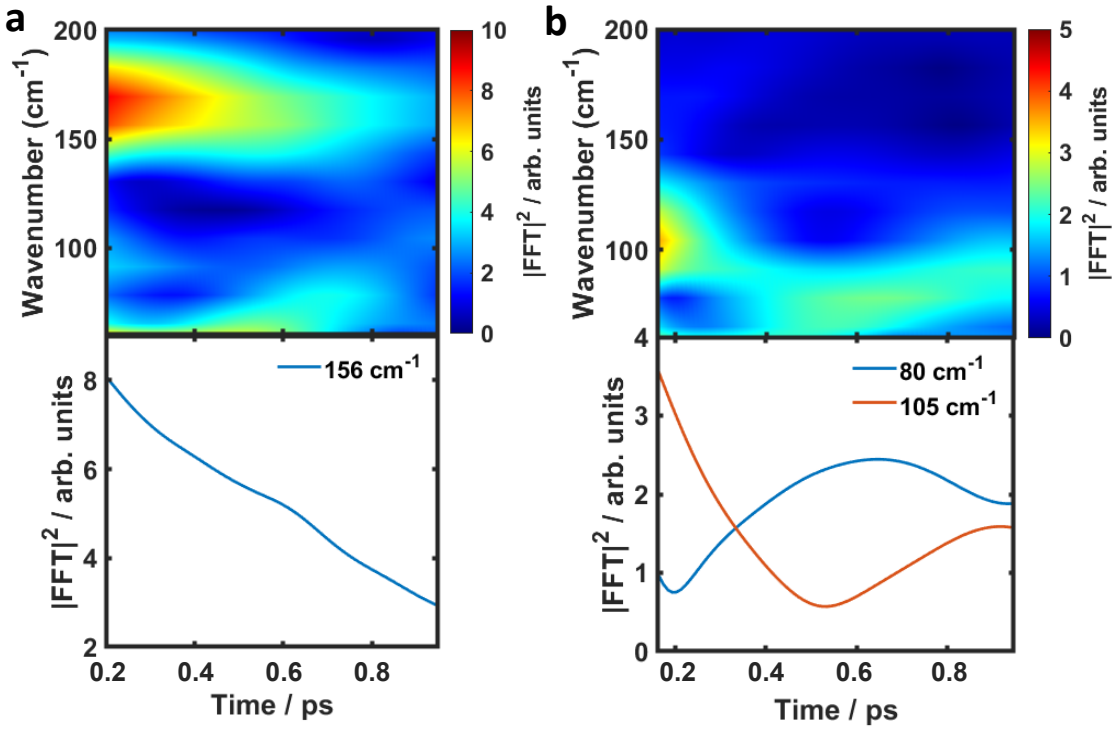

Figure 5.3.7: Shifting-window Fourier transform of the residuals for global fitting with a 1.2 ps Hann window. The values along the time axis correspond to the start of the window. **a** Data for $[Ru(Ph{-}btz)_3]^{2+}$ the Fourier transform has been performed over an average of the residuals between 380 and 410 nm. The bottom panel shows the time evolution of the 156 cm^{-1} component. **b** Data for $[Ru(Bn{-}btz)_3]^{2+}$. The Fourier transform has been performed over an average of the residuals between 365 and 400 nm. The bottom panel shows the time evolution of the 80 and 105 cm^{-1} components.

one time point and performing the transform again. With the continuation of this process, the time evolution of a Fourier spectrum can be visualised, which is shown in Figure 5.3.7. The results for $[Ru(Ph{-}btz)_3]^{2+}$ are shown in Figure 5.3.7**a** which displays the decay of a single frequency at 156 cm^{-1} as expected. However, Figure 5.3.7**b** shows the data for $[Ru(Bn{-}btz)_3]^{2+}$ is more complicated. It suggests an initial high-frequency component around 105 cm^{-1} that quickly decays, during which time a low-frequency component (80 cm^{-1}) grows.

Considering the simplicity of the oscillatory signal in the data of $[Ru(Ph{-}btz)_3]^{2+}$, the trace at 400 nm was fitted directly with the sum of two exponential components and a damped waveform as described by Equation 5.3.1:

$$\Delta A = \mathrm{IRF}(\sigma, t) \circledast \left(\sum_{i=1}^{2} A_i e^{-t/\tau_i} + A_{\mathrm{osc}} e^{-t/\tau_\mathrm{d}} \cos\left(2\pi c \tilde{\nu} t\right) \right). \tag{5.3.1}$$

This equation takes into account the finite pulse duration of the pump and probe via the instrument response function ($\mathrm{IRF}(\sigma, t)$), which is the time-domain cross-

correlation function of the pump and probe pulses. It is modelled as a Gaussian function with width $\sigma \approx 80$ fs. A_i is the amplitude of an exponential decay with a time constant τ_i, the parameters for the oscillatory part of the fit are the amplitude A_{osc}, frequency $\tilde{\nu}$ and dephasing time τ_{d}. This is the same equation used to fit the kinetic data in Chapters 3 and 4. The data and fit are shown in Figure 5.3.8**a**. The time constants were fixed to the values obtained from the global fit (τ_1= 110 fs and τ_2= 46 ps). The fitting yielded a frequency of $\tilde{\nu} = 156 \pm 1$ cm^{-1} and a dephasing time of $\tau_{\mathrm{d}} = 610 \pm 60$ fs.

To fit the $[\mathrm{Ru(Bn{-}btz)_3}]^{2+}$ data, the following model was assumed. The dynamics initially are dominated by the oscillatory signal with frequency $\tilde{\nu}_1$ which decays with the same time constant, τ_{d1} as the second $\tilde{\nu}_2$ component grows. The second, low-frequency component decays with a time constant, τ_{d2}. Equation 5.3.2 describes the fitting function used for this model with the addition of the exponential population terms. This equation was not convoluted with the IRF due to the difficulty in calculating this for the rise and decay of the second frequency component.

$$\Delta A = \sum_{i=1}^{2} A_i e^{-t/\tau_i} + A_{\mathrm{osc1}} e^{-t/\tau_{\mathrm{d1}}} \cos\left(2\pi c\tilde{\nu}_1 t\right) + A_{\mathrm{osc2}} e^{-t/\tau_{\mathrm{d2}}} (1 - e^{-t/\tau_{\mathrm{d1}}}) \cos\left(2\pi c\tilde{\nu}_2 t\right) \tag{5.3.2}$$

The fit is shown in Figure 5.3.8**b**. The frequencies obtained from the fitting are $\tilde{\nu}_1 = 131 \pm 1$ cm^{-1} and $\tilde{\nu}_2 = 83 \pm 1$ cm^{-1}, which agree well with the Fourier transform in Figure 5.3.7**b**. The decay of the $\tilde{\nu}_1$ and rise time of $\tilde{\nu}_2$ was found to be $\tau_{\mathrm{d1}} = 112 \pm 1$ fs and the decay time of the $\tilde{\nu}_2$ component is $\tau_{\mathrm{d2}} = 295 \pm 2$ fs. The time constants for the population dynamics were found to be $\tau_1 = 280 \pm 5$ fs and $\tau_2 = 7.7 \pm 0.1$ ps, which are different from those obtained in the global fit. However, this is expected due to the transition around 380 nm shifting, which was previously discussed and shown in Figure 5.3.4.

The dynamics of $[\mathrm{Ru(Ph{-}btz)_3}]^{2+}$ can be explained well by a model very similar to what was proposed by Sun et al. for $[\mathrm{Ru(m{-}bpy)_3}]^{2+}$. The 330 nm pump pulse initially excites the molecule to the ^{1}MLCT state which quickly undergoes ISC to the ^{3}MLCT state faster than the experimental time resolution. The ^{3}MLCT impulsively populates the ^{3}MC state with a time constant of $\tau_1 = 110$ fs. This state has a single electron that populates one of the e_g orbitals which activates the Jahn-Teller distortion on an ultrafast timescale. The population of this state launches a vibrational wavepacket along the potential energy surface of the ^{3}MC state with a frequency of 156 cm^{-1}, which dephases in 610 fs. The subsequent ground state recovery occurs with a time constant of $\tau_1 = 46$ ps. These dynamics are summarised in Figure 5.3.9**a**.

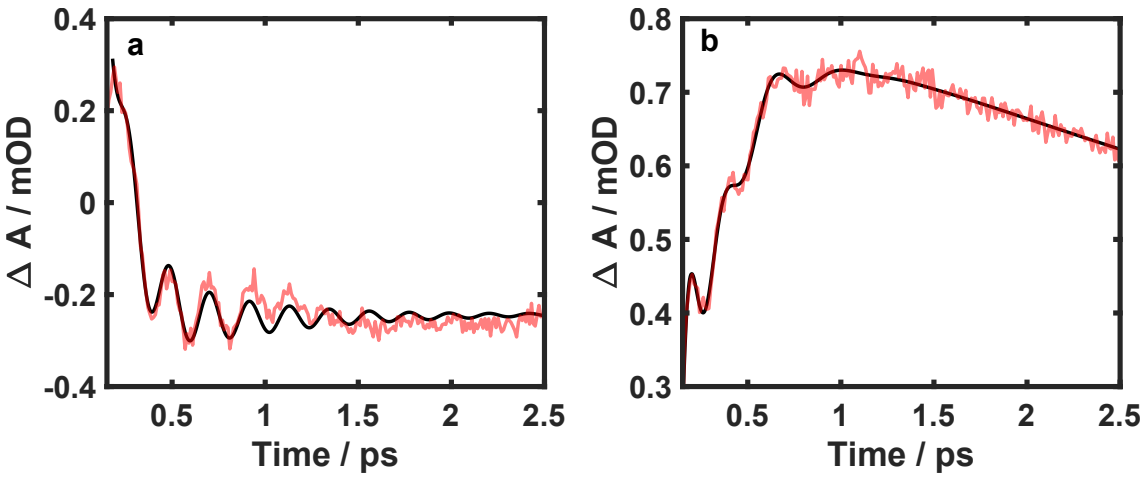

Figure 5.3.8: Kinetic traces (red line) and fit (black line) including the oscillatory components. **a** Transient absorption of $[Ru(Ph{-}btz)_3]^{2+}$ at a probe wavelength of 400 nm fit with Equation 5.3.1. **b** Transient absorption of $[Ru(Bn{-}btz)_3]^{2+}$ at a probe wavelength of 380 nm fit with Equation 5.3.2.

The dynamics of $[Ru(Bn{-}btz)_3]^{2+}$ are more complex. The population dynamics consist of a fast 100 fs time constant and a delayed ground state recovery with a time constant of 17 ps. This suggests the same kinetic model as $[Ru(Ph{-}btz)_3]^{2+}$, with a fast ^{3}MLCT to ^{3}MC state conversion and then subsequent recovery of the ground state. Assuming this scheme, there are two possible origins for the loss of one frequency and the growth of another. The first possibility is shown in Figure 5.3.9**b**. This assumes that the ^{3}MLCT state has a different potential minimum from the ground state and that the initial high-frequency component of 131 cm^{-1} oscillates on the ^{3}MLCT potential energy curve. With a time constant of 100 fs the wavepacket transitions to the ^{3}MC state that has a wider potential well, which leads to the lower frequency oscillations of 83 cm^{-1}. The molecule then returns to the ground state with a time constant of 17 ps. This picture is supported as the fast time constant associated with the decay of the ^{3}MLCT to the ^{3}MC state ($\tau_1 = 110 \pm 10$ fs) is within the error of the decay of the 130 cm^{-1} oscillations and growth of the 90 cm^{-1} oscillations ($\tau_{d1} = 112 \pm 1$ fs). A similar transfer of vibrational coherence between states in the impulsive limit has been observed in other systems.[257–259] MLCT states are generally nested with the ground state with only very small shifts from the ground state potential energy minima. This is because the t_{2g} orbitals are non-bonding, so the removal of an electron from these orbitals has minimal effect on the structure and therefore does not normally lead to coherent motion in the initial excited state. However, recently a coherence with a frequency of around 120 cm^{-1} has been observed in the ^{3}MLCT state of $[Ru(bpy)_3^{2+}]$, which is a similar magnitude to the 112 cm^{-1} frequency observed for $[Ru(Bn{-}btz)_3]^{2+}$.[260]

The second possibility assumes that vibrational wavepacket dynamics only occur

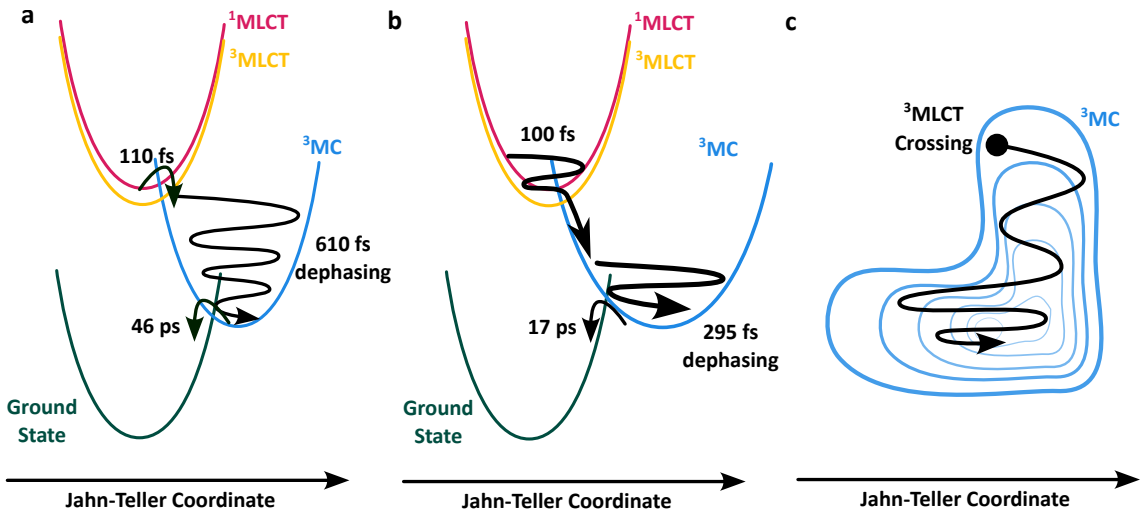

Figure 5.3.9: Schematic of the proposed dynamics for the Ru(II) bistriazolyl complexes. **a** The proposed dynamics for $[Ru(Ph{-}btz)_3]^{2+}$ after MLCT excitation. **b** and **c** Two different possibilities of the proposed dynamics for $[Ru(Bn{-}btz)_3]^{2+}$ after MLCT excitation. In **b**, all the dynamics occur along a single Jahn-Teller normal mode and the two different frequencies arise from the width of the potential energy curves in the ^{3}MLCT and ^{3}MC state. In **c**, only the ^{3}MC state is considered to contribute to the vibrational wavepacket dynamics. In this case, a multidimentional surface is required, with the wavepacket initially oscillating within a narrow well that moves into a well that is wider leading to a lower frequency vibration.

within the ^{3}MC state. In this case, the decay of one frequency and the growth of another can only be described by a multidimensional potential energy surface with at least two different normal mode coordinates. A cartoon of the ^{3}MC surface and trajectory of the wavepacket is shown in Figure 5.3.9**c**. The wavepacket populates the ^{3}MC state where it crosses with the ^{3}MLCT surface and is initially within a narrow well that corresponds to the high-frequency mode. As the wavepacket evolves it moves into an area that has a wider well and therefore the wavepacket begins to oscillate with a lower frequency. The nature of the wavepacket mode is still likely to be a Jahn-Teller-like coordinate but the character of the other mode is unknown. It could be that this slower, non-oscillatory motion along the second normal mode is responsible for the peak shifting that is observed in the transient absorption spectra shown in Figure 5.3.4. The only difference in the structures of $[Ru(Ph{-}btz)_3]^{2+}$ and $[Ru(Bn{-}btz)_3]^{2+}$ is the replacement of the phenyl substituent by the benzyl substituent. Considering that the phenyl moiety is conjugated with the triazolyl ring, it is likely that the rings lie in the same plane and the rotational motion of the phenyl ring is restricted. Whereas, the benzyl substituent is not conjugated and therefore will be more flexible. The second coordinate axis could be some form of twisting of the benzyl ring with respect to the triazolyl ring. A process similar to this is observed in some Cu(I)-phenanthroline complexes.[70, 72]

5.4 Conclusions and Future work

The photoinduced dynamics of triazolyl-based structural analogues of $Ru(bpy)_3^{2+}$ have been studied with the aim of a more direct identification of the ^{3}MC excited state. By replacement of the bpy with the triazolyl equivalent, 4,4'-bi-1,2,3-triazolyl, the excited state ordering of the ^{3}MLCT and ^{3}MC state can be inverted, which changes the nature of the lowest-energy excited state to metal-centred. This ^{3}MC state has a single electron in the metal e_g orbitals which leads to Jahn-Teller distortion. In the two complexes studied, $[Ru(Ph{-}btz)_3]^{2+}$ and $[Ru(Bn{-}btz)_3]^{2+}$, the photoexcitation of the MLCT transition leads to an ultrafast and impulsive population of the ^{3}MC state which drives coherent vibrational motion within the ^{3}MC state. This is one of the first observations of vibrational coherence in the ^{3}MC state in a Ru(II) complex. The dynamics of $[Ru(Ph{-}btz)_3]^{2+}$ show a single vibrational mode that is activated with a frequency of 156 cm^{-1} with a dephasing time of 610 fs, which is assigned to the motion of a Jahn-Teller normal mode as it moves to its new elongated geometry in the ^{3}MC state. Calculations are underway to calculate the normal modes in the lowest energy triplet state to confirm this assignment.

Despite having the same fast ^{3}MLCT to ^{3}MC (100 fs) conversion and slow ground state recovery (17 ps), the vibrational wavepacket dynamics in $[Ru(Bn{-}btz)_3]^{2+}$ differ significantly from those observed in $[Ru(Ph{-}btz)_3]^{2+}$. There is an initial 131 cm^{-1} component that decays into a 83 cm^{-1} component with a time constant of 112 fs. The second component then dephases with a time constant of around 295 fs. These wavepacket dynamics could arise from two different cases: (1) The 131 cm^{-1} wavepacket is initiated in the ^{3}MLCT state and upon impulsive internal conversion to the ^{3}MC state the second 90 cm^{-1} wavepacket is activated along the same normal mode trajectory. (2) The wavepacket dynamics only occur within the ^{3}MC state, which necessitates the dynamics occur on a multidimensional surface with at least two independent vibrational normal modes. The wavepacket initially oscillates within a narrow well that opens up into a wider well leading to the change from a higher frequency to a lower frequency.

In the context of this thesis, the initial wavepacket dynamics are interesting. One broader aim is to harness some control over the photoinduced dynamics that influence the magnetic properties of a molecule. As discussed in Chapter 1, the magnetic anisotropy is closely related to the Jahn-Teller distortion in Mn(III) SMMs. In Chapters 3 and 4, the nuclear motion after excitation is tracked and there is some suggestion that synthetic modification can be used to control wavepacket dynamics after excitation. The data presented here do indeed suggest that, even with relatively minor synthetic modification (replacing a phenyl for a benzyl group), it is possible to drive very different vibrational motion after light absorption. Control of the

wavepacket dynamics has not been achieved here as it is unknown what causes the change in vibrational motion between the two complexes. However, it certainly suggests that with the correct choice of complexes, design criteria could be developed to direct nuclear motion along chosen coordinates. The development of these design criteria could be crucial in controlling the magnetisation of SMMs where the nuclear coordinates are coupled strongly to the magnetic anisotropy.

In this vein, further work on the triazolyl ligand framework has been carried out. The bistriazolyl ligands were replaced with two molecules of tris(1-benzyl-1,2,3-triazol-4-yl)-p-anisolylmethane (ttz).[261] Two of these molecules form an octahedral complex with with Ru(II) ($Ru(ttz)_2^{2+}$), as shown in Figure 5.4.1**a**. The two ligands form a tripodal chelation that is staggered with respect to one another. The transient absorption of $Ru(ttz)_2^{2+}$ in acetonitrile after exciting the MLCT is shown in Figure 5.4.1**b**. This is very similar to the data for $[Ru(Ph{-}btz)_3]^{2+}$. $[Ru(Ph{-}btz)_3]^{2+}$ decays back to the ground state within tens of picoseconds, whilst $Ru(ttz)_2^{2+}$ shows a similar tens of picosecond decay (42 ps), it plateaus and does not return to zero (Figure 5.4.1**c**). In fact, the molecule does not decay within our measurable 3 ns time delay. Further nanosecond transient absorption measurements carried out by Owen Woodford and Elizabeth Gibson at the University of Newcastle show that the full excited state lifetime of this molecule is 30 ns. This was initially thought to be a solvento complex due to the dechelation of one of the triazolyl rings and the chelation of an acetonitrile molecule. However, the dynamics also show a plateau around the same value when the same experiment was performed in dichloromethane (Figure 5.4.1**d**). Therefore, the proposed nature of this state is a pseudo-five-coordinate complex shown in Figure 5.4.1**e**. After relaxation to the ^{3}MC state the elongation provides room for one of the triazolyl rings to rotate and form a π-interaction with the Ru(II) ion to loosely obey the 18-electron rule. Indeed, preliminary density functional theory calculations performed at the University of Huddersfield show a local minimum around this geometry. $Ru(ttz)_2^{2+}$ exhibited no evidence of coherent vibrational motion after excitation but with synthetic modification, a completely different structure was induced in the final excited state. This provides further evidence that molecules can be designed to have specific desired excited state nuclear geometries.

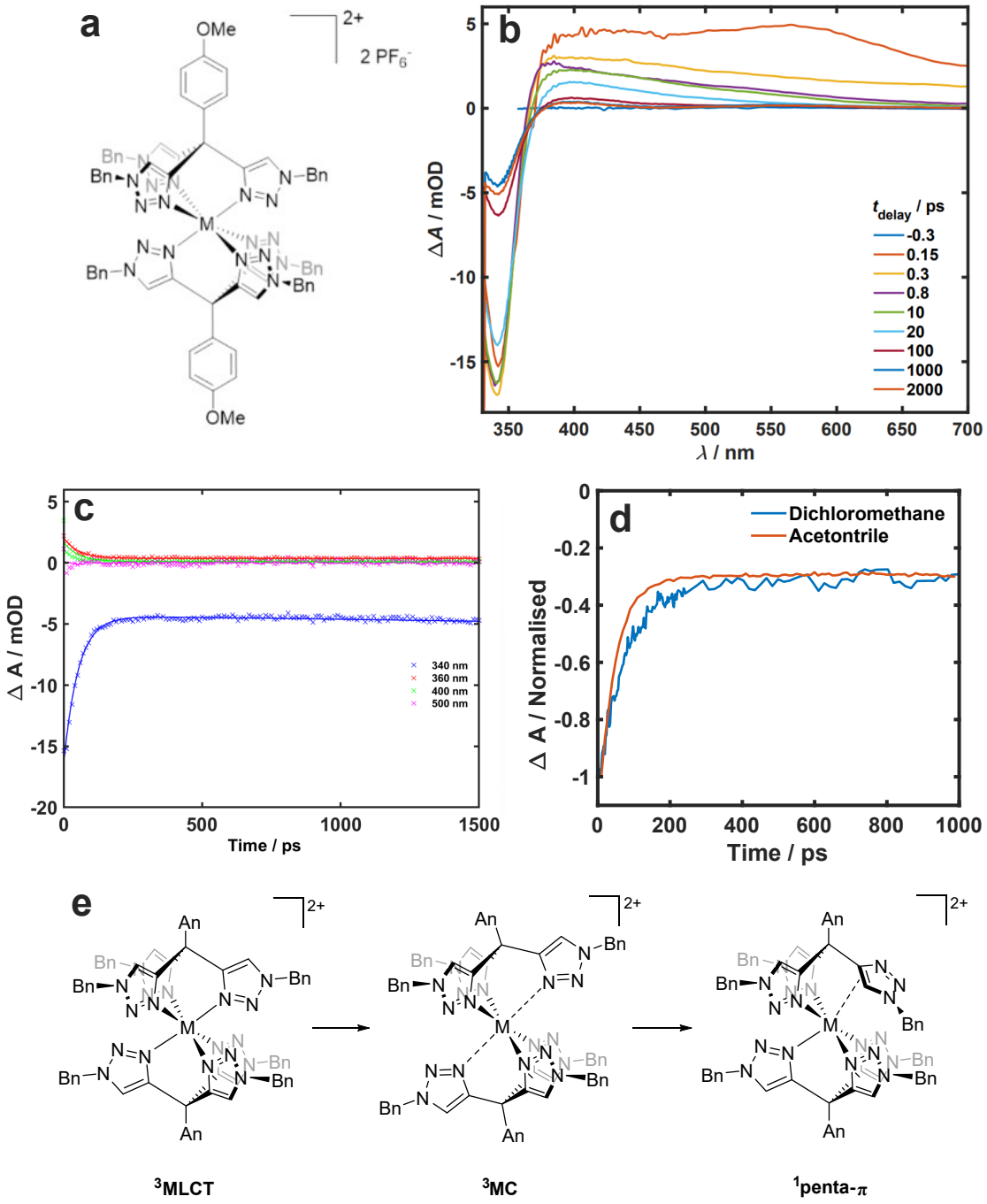

Figure 5.4.1: Overview of the dynamics of $Ru(ttz)_2^{2+}$ after MLCT excitation. **a** Chemical structure of $Ru(ttz)_2^{2+}$. **b** Transient absorption difference spectra at selected time delays after MCLT excitation. **c** Kinetic traces at selected wavelengths. The 340 nm trace shows a long-lived plateau. **d** Kinetic traces for a probe wavelength of 340 nm in dichloromethane and acetonitrile showing the same plateau level. The data have been normalised to the maximum ground state bleach at that region to compare. **e** Schematic of the proposed dynamics after photoexcitation to the MLCT state.

Chapter 6

Femtosecond Broadband Magnetic circular Dichroism Spectroscopy of Zinc Tetraphenylporphyrin

6.1 Introduction

One objective of this thesis is to observe and monitor the magnetic state of a molecule with femtosecond time resolution. Currently, there is extensive research focused on studying magnetisation dynamics in metals, semiconductors, and dielectrics.[10, 13, 15] These studies typically employ a quasi-monochromatic optical probe to measure Faraday rotation or ellipticity.[8, 262] This approach is highly effective for traditional condensed-phase magnets, as they exhibit absorption spectra that lack distinctive features, making it unnecessary to expand the energy range of the probe.[263] However, transition metal-based SMMs often possess complex optical absorption spectra due to various charge transfer, metal-centered, and ligand-centered transitions. Consequently, it is crucial to develop magneto-optical spectroscopies that are broadband and spectrally-resolved for the study of ultrafast molecular magnetism. Additionally, ultrafast spectroscopies that have greater spin-state sensitivity will be useful in cases where different spin manifolds can play a role in the dynamics such as photocatalysis,[264] solar cells[265] and thermally activated delayed fluorescence.[266]

A broadband femtosecond MCD spectrometer has been developed within the group to measure time-resolved magnetic circular dichroism (TRMCD),[95] which is described in Chapter 2. To test the utility of this setup, the ultrafast dynamics of zinc(II) tetraphenylporphyrin (ZnTPP) are investigated. This molecule was chosen as its dynamics after light absorption have already been heavily investigated[267, 268] and the complex shows a strong ground state MCD spectrum at room temperature. The following chapter contains results from a project that was started by

Doctor Erica Sutcliffe.[269] The results section contains a replication of the solution-phase measurements from their thesis,[269] with higher signal-to-noise. The thin film and temperature-dependent measurements presented here are reported for the first time.

6.1.1 Theory of Magnetic Circular Dichroism

Magnetic circular dichroism (MCD), often referred to as Faraday ellipticity, is the differential absorption of left and right circularly polarised light (σ^+ and σ^-, respectively) under the application of a magnetic field.[270] This effect arises as photons carry $\pm 1\hbar$ of angular momentum depending on whether they are left or right circularly polarised. Therefore, photons preferentially excite transitions with $\Delta m_J = +1$ or $\Delta m_J = -1$ depending on their helicity, to conserve angular momentum. Linearly polarised light does not exhibit the MCD effect as it represents the superposition of the two circular polarisations.

The microscopic origins of MCD arise from the Zeeman effect.[271] Upon application of an external magnetic field, the Zeeman effect leads to changes in the energy of magnetic sublevels depending on their angular momentum quantum numbers. The perturbation from the magnetic field is $\hat{V} = -\boldsymbol{m} \cdot \boldsymbol{B}$ where $\boldsymbol{m}$ is the magnetic moment of the state and $\boldsymbol{B}$ is the magnetic field. Both the spin and orbital angular momentum contribute to the magnetic moment,

$$\boldsymbol{m} = \frac{\mu_\mathrm{B}}{\hbar}(\hat{L}_z + 2\hat{S}_z) \tag{6.1.1}$$

where μ_B is the Bohr magneton and the factor of 2 arises from the gyromagnetic ratio of the electron spin. In the case where spin-orbit coupling dominates over the effect of the external field and the magnetic field points along the z-axis, the pertubation is given by $\hat{V} = \mu_\mathrm{B} g_J B \hat{J}_z$ where $\hat{J}_z$ is the total angular momentum (J) projection operator and g_J is the Landé g-factor. Overall, the change in energy is directly proportional to B and depends on the z-projection (m_J) of the total angular momentum. The energy difference (ΔE) is is given by

$$\Delta E = \left\langle n^{(0)} \right| \hat{m}_z B \left| n^{(0)} \right\rangle = \left\langle n^{(0)} \right| \mu_\mathrm{B} g_J B \hat{J}_z \left| n^{(0)} \right\rangle = \mu_\mathrm{B} g_J B m_J \tag{6.1.2}$$

for an unperturbed zeroth-order wavefunction $\left|n^{(0)}\right\rangle$ with angular momentum quantum numbers J and m_J.

In addition to the change in energy, the application of a magnetic field also leads to new perturbed wavefunctions. To first order, the perturbed wavefunction ($\left|n^{(1)}\right\rangle$) is formed from the unperturbed wavefunction ($\left|n^{(0)}\right\rangle$) mixed with all other zeroth-order wavefunctions, $\left|k^{(0)}\right\rangle$. The expression for this is

$$\left|n^{(1)}\right\rangle = \left|n^{(0)}\right\rangle - \sum_{k \neq n} \frac{\left\langle k^{(0)}\right| \hat{V} \left|n^{(0)}\right\rangle}{E_n^{(0)} - E_k^{(0)}} \left|k^{(0)}\right\rangle \tag{6.1.3}$$

where $\hat{V}$ is the Zeeman perturbation and $E_i^{(0)}$ is the energy of the unperturbed states. The denominator suggests that significant magnetic field-induced mixing occurs only when two states are close in energy.

Transitions occur from an electronic ground state $|g\rangle$ with sublevel γ to an excited state $|e\rangle$ with sublevel ϵ. The sublevels γ and ϵ encompass the magnetic states with quantum numbers J and m_J. The MCD signal for such a transition is given by

$$\Delta A_{\mathrm{MCD}} = C \sum_{\gamma,\epsilon} N_{g,\gamma} (|\langle e_\epsilon| \hat{\mu}_- |g_\gamma\rangle|^2 - |\langle e_\epsilon| \hat{\mu}_+ |g_\gamma\rangle|^2) \rho(\nu) \tag{6.1.4}$$

where the prefactor C is a collection of constants, $N_{g,\gamma}$ is the population of the state $|g\rangle$ with sublevels γ, $\hat{\mu}_\pm$ is the electric dipole operator for $\sigma^\pm$ light and $\rho(\nu)$ is the lineshape of a transition with frequency ν. This assumes that the electronic energy difference between $|g\rangle$ and $|e\rangle$ is very large compared to thermal energy so only the ground state sublevels are populated.

Substitution of the results from perturbation theory into Equation 6.1.4 and neglecting terms that are second-order in B leads to the expression[270]

$$\Delta A_{\mathrm{MCD}} = CB \left(\mathcal{A}_1 \left(-\frac{\partial \rho(\nu)}{\partial \nu} \right) + \left(\mathcal{B}_0 + \frac{\mathcal{C}_0}{k_{\mathrm{B}} T} \right) \rho(\nu) \right) \tag{6.1.5}$$

with three distinct MCD terms: $\mathcal{A}_1$, $\mathcal{B}_0$ and $\mathcal{C}_0$-terms. This equation also makes use of the rigid-shift approximation, which assumes that the Zeeman effect only leads to an energy shift of a transition and no change in the transition lineshape ($\rho(\nu) = \rho(\nu - \nu_0)$).

The $\mathcal{A}_1$-term is given by

$$\mathcal{A}_1 = \sum_{\gamma,\epsilon} (\langle e_\epsilon| \hat{\mu}_z |e_\epsilon\rangle - \langle g_\gamma| \hat{\mu}_z |g_\gamma\rangle)(|\langle e_\epsilon| \hat{\mu}_- |g_\gamma\rangle|^2 - |\langle e_\epsilon| \hat{\mu}_+ |g_\gamma\rangle|^2) \tag{6.1.6}$$

which describes a transition from a ground state to a degenerate excited state with split Zeeman sublevels. This splitting leads to small changes in the transition band positions depending on whether the light is left or right circularly polarised. Therefore, after taking the difference, the shape of the MCD signal has a derivative-like form as shown in Figure 6.1.1.

The $\mathcal{B}_0$-term is given by

$$\mathcal{B}_0 = \sum_{\gamma,\epsilon}\left[\sum_{k\neq e,\kappa}\frac{\langle e_\epsilon|\,\hat{\mu}_z\,|k_\kappa\rangle}{E_k - E_e}(\langle e_\epsilon|\,\hat{\mu}_+\,|g_\gamma\rangle\,\langle g_\gamma|\,\hat{\mu}_-\,|k_\kappa\rangle - \langle e_\epsilon|\,\hat{\mu}_-\,|g_\gamma\rangle\,\langle g_\gamma|\,\hat{\mu}_+\,|k_\kappa\rangle)\right.$$
$$\left. + \sum_{k\neq g,\kappa}\frac{\langle k_\kappa|\,\hat{\mu}_z\,|e_\epsilon\rangle}{E_k - E_g}(\langle g_\gamma|\,\hat{\mu}_-\,|e_\epsilon\rangle\,\langle e_\epsilon|\,\hat{\mu}_+\,|k_\kappa\rangle - \langle g_\gamma|\,\hat{\mu}_+\,|e_\epsilon\rangle\,\langle e_\epsilon|\,\hat{\mu}_-\,|k_\kappa\rangle)\right] \tag{6.1.7}$$

where $|k_\kappa\rangle$ denotes all other electronic states k with sublevels κ. From the denominators in Equation 6.1.7, this term is only large if two states lie close in energy to each other. This effect arises from the first-order perturbation theory and the resultant mixing of zeroth-order wavefunctions shown in Equation 6.1.3.

The $\mathcal{C}_0$-term is given by

$$\mathcal{C}_0 = \sum_{\gamma,\epsilon}\langle g_\gamma|\,\hat{\mu}_z\,|g_\gamma\rangle \times \left(|\langle g_\gamma|\,\hat{\mu}_-\,|e_\epsilon\rangle|^2 - |\langle g_\gamma|\,\hat{\mu}_+\,|e_\epsilon\rangle|^2\right) \tag{6.1.8}$$

which describes the signal arising from a Zeeman split ground state to a non-degenerate excited state. This term is sensitive to the population of the ground state levels. For high temperatures, all ground-state Zeeman sublevels are equally populated, and therefore no $\mathcal{C}_0$-term is observed. However, at low temperatures, the lowest energy sublevel is preferentially populated because of the Boltzmann distribution and $\mathcal{C}_0$-terms dominate the MCD spectrum. $\mathcal{C}_0$-terms necessitate a Zeeman splitting in the ground state, and therefore do not play a role in the spectrum of diamagnetic complexes. However, these terms dominate the spectrum of paramagnetic compounds at low temperatures because of their $1/k_\mathrm{B}T$ dependence.

Finally, the absorption term $\mathcal{D}_0$ is given by

$$\mathcal{D}_0 = \frac{1}{2}\sum_{\gamma,\epsilon}\left(|\langle g_\gamma|\,\hat{\mu}_-\,|e_\epsilon\rangle|^2 + |\langle g_\gamma|\,\hat{\mu}_+\,|e_\epsilon\rangle|^2\right). \tag{6.1.9}$$

This is simply the average of the absorption of both the left and right-handed circularly polarised light. This does not contribute to the MCD spectrum but rather to the absorption spectrum.

A schematic of all the terms and the spectral shape they produce is shown in Figure 6.1.1. Importantly, the features of all these terms allow their identification in an experimental spectrum. $\mathcal{A}_1$-terms are characterised by a derivative-like shape that is generally insensitive to temperature changes. Both $\mathcal{B}_0$-terms and $\mathcal{C}_0$-terms have a shape that matches the absorption band. However, they can be distinguished through their temperature-dependent behaviour, where the intensity of $\mathcal{C}_0$-terms will increase with $1/T$. The relative contribution of the $\mathcal{A}_1$, $\mathcal{B}_0$ and $\mathcal{C}_0$ terms scale

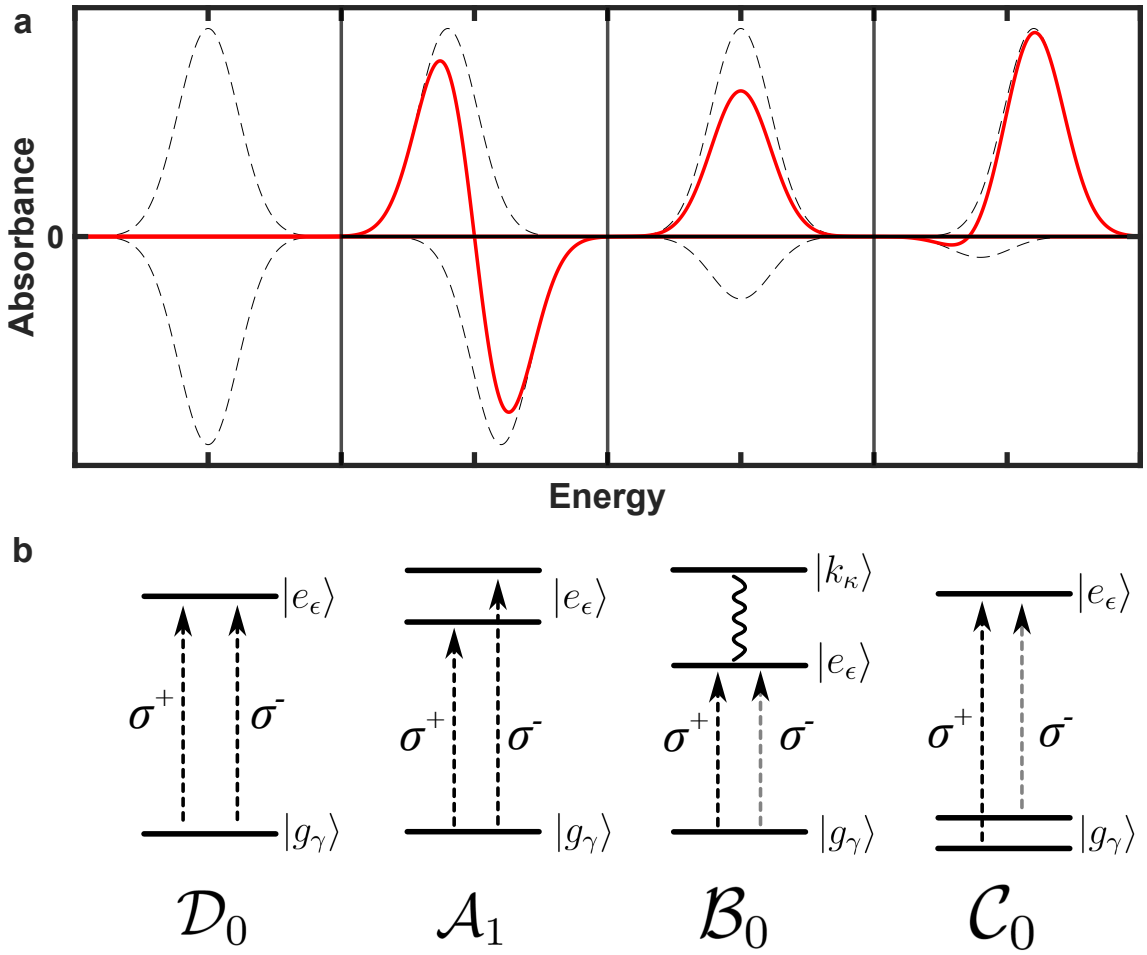

Figure 6.1.1: Origin of MCD terms. **a** The shape of the $\mathcal{D}_0$, $\mathcal{A}_1$, $\mathcal{B}_0$ and $\mathcal{C}_0$ from left to right. The dotted line in the upper and lower panels shows the absorption of σ^+ light and the absorption of the σ^-, respectively. The red line shows the corresponding MCD spectrum. **b** The transitions associated with each MCD term.

with linewidth ($\Delta\Gamma$), energy splitting between electronic states (ΔE), and thermal energy, respectively: $\frac{1}{\Delta\Gamma} : \frac{1}{\Delta E} : \frac{1}{k_\mathrm{B}T}$. Typically, $\Delta\Gamma \approx 1000$ cm^{-1}, $\Delta E \approx 10000$ cm^{-1} and $k_\mathrm{B}T \approx 100$ cm^{-1} (at room temperature) therefore the ratio of the $\mathcal{A}_1$, $\mathcal{B}_0$ and $\mathcal{C}_0$-terms is 0.1:0.01:1, respectively. Even at room temperature, $\mathcal{C}_0$-terms are the strongest component of MCD of paramagnets. At temperatures around 10 K, the intensity of the $\mathcal{C}_0$-terms will increase 10-fold and completely dominate over the $\mathcal{A}_1$ and $\mathcal{B}_0$-terms.

6.1.2 Metalloporphyrins and their Electronic Structure

Porphyrins are large organic macrocycles composed of four pyrrole units connected via methine bridges. The structure of free base porphyrin is shown in Figure 6.1.2. Porphyrins are vital for many biological functions, from heme proteins that transport oxygen around the body to one of the main substituents of vitamin B12.[272] They also exhibit incredibly strong optical absorption bands in the visible region of

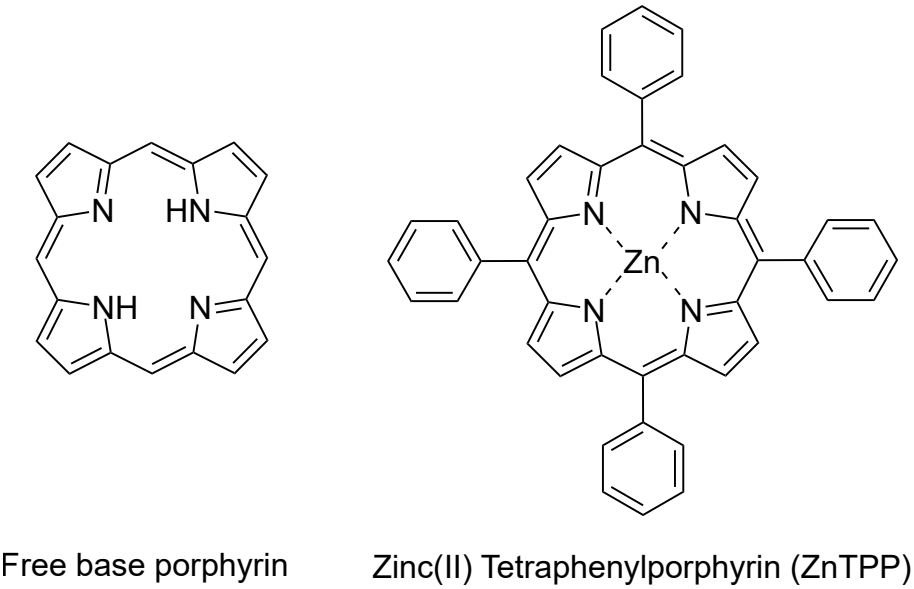

Figure 6.1.2: Chemical structure of free base porphyrin (left) and zinc(II) tetraphenylporphyin (right).

the spectrum that, when excited, can lead to various light-triggered processes. In biology, magnesium porphyrin is the light-absorbing antenna for photosynthesis in plants.[273] Porphyrins are also being studied for use in photodynamic therapy,[274] dye-sensitised solar cells[275] and photocatalysis.[276]

The porphyrin's interesting optical properties arise from the combination of four valence orbitals. As described by Gouterman's four orbital model,[277, 278] the valence states are composed of two HOMOs and two LUMOs. In the D_{4h} symmetry of ZnTPP, the HOMOs and LUMOs are degenerate which leads to the description given in Figure 6.1.3. Figure 6.1.3**a** displays the molecular orbital picture showing two degenerate HOMOs with $1e_u$ symmetry and two degenerate LUMOs with $1e_g$ symmetry. These molecular orbitals mix and give rise to the state picture in Figure 6.1.3**b** with a non-degenerate ground state and two doubly degenerate excited states. The electronic structure leads to an optical absorption spectrum that is composed of two main bands, the Q-band and B-band. In a free electron model, the Q-band transitions occur with a change in orbital angular momentum of $\Delta M_L \pm 9$, which is forbidden. The B-band is associated with a change in orbital angular momentum of $\Delta M_L \pm 1$, which is allowed. The B-band typically occurs around 400 nm and has an extinction coefficient of $\varepsilon > 10^5$ $M^{-1}cm^{-1}$. The Q-band occurs around 600 nm and despite its forbidden nature, the transition has a relatively large extinction coefficient of $\varepsilon \approx 10^4$ $M^{-1}cm^{-1}$. Taking into account the non-degenerate ground state and doubly degenerate excited states, the ground state MCD spectrum is composed of only $\mathcal{A}_1$-terms in diamagnetic ZnTPP.

The Jablonski diagram after 400 nm excitation (S_0 to S_2) is shown in Figure

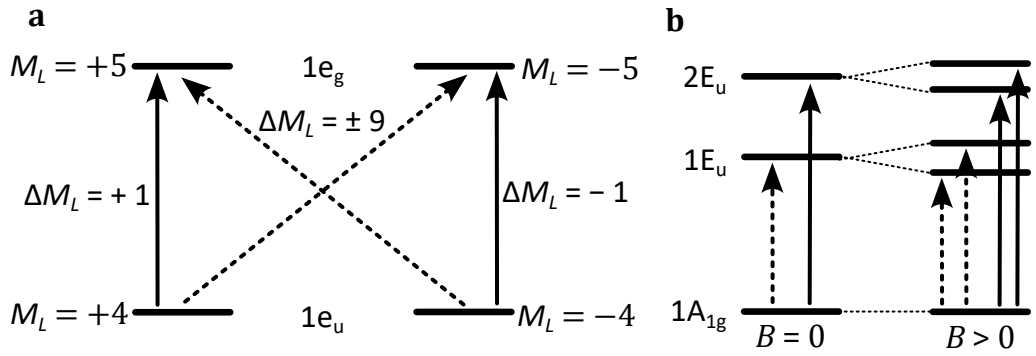

Figure 6.1.3: Gouterman's four orbital model. **a** Molecular orbital picture. The fully populated HOMOs are degenerate $1e_u$ orbitals with $M_L = \pm 4$ and the LUMOs are composed of empty $1e_g$ orbitals with $M_L = \pm 5$. Two different transitions can arise from this, the dotted arrows denote the Q-band with $\Delta M_L = \pm 9$ and the solid arrow show the B-band transitions with $\Delta M_L = \pm 1$. **b** The state picture that is equivalent to the molecular orbital picture. The two excited states are doubly degenerate and can be split with the application of a magnetic field leading to $\mathcal{A}_1$-terms in an MCD spectrum. The figure is adapted from ref. [279].

6.1.4. Vibrational relaxation and the subsequent IC to the S_1 state occur in 70 fs and 1.5 ps, respectively.[267] The results obtained in this chapter only focus on dynamics occurring after 20 ps and therefore dynamics associated with the S_2 state do not need to be considered. Within the S_1 state, vibrational relaxation occurs with time constants of around 10 ps and 100 ps and the ISC to the T_1 state with a time constant of around 2 ns.[268] In the measurements, the pump-probe time delay is 20–3000 ps and therefore it investigates vibrational relaxation in the S_1 state and the ISC to the lowest energy triplet state.

6.2 Methods

6.2.1 Experimental

The TRMCD set-up is described in detail in Chapter 2, and particular experimental parameters are highlighted here. A supercontinuum generated in sapphire was used as the probe pulse with a spectrum spanning 500–800 nm. The probe diameter was 100 µm at the sample position. The pump wavelength was 400 nm, which excited the molecule to the second vibrational level of the S_2 state. The pump diameter was 210 µm and the fluence was 1.4 mJcm^{-2} at the sample. The pump polarisation was linear and the applied magnetic field was 750 mT. Each presented spectrum is composed of 200,000 individual time-resolved difference spectra measured at each field. For the solution-phase measurements, ZnTPP was dissolved in toluene at a concentration of 780 µM and flowed through a 200 µm cuvette at a rate of 32 µL/min.

The excited state features of the TRMCD spectrum need to be assigned to $\mathcal{A}_1$,$\mathcal{B}_0$

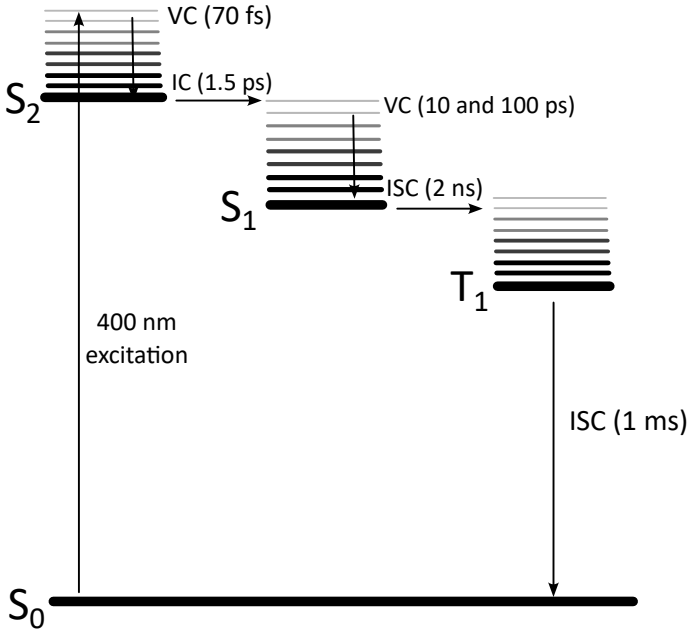

Figure 6.1.4: Jablonski diagram of the ultrafast dynamics of ZnTPP in toluene after 400 nm excitation. Values extracted from refs. [267, 268, 280].

or $\mathcal{C}_0$-terms. In order to fully characterise the spectrum, temperature-dependent measurements are required to differentiate $\mathcal{B}_0$ and $\mathcal{C}_0$-terms as the latter exhibit a $1/T$ dependence. If samples are to be mounted in the cryostat, they must be solid, and therefore this necessitates the synthesis of solid thin films.

Thin film samples were synthesised by Ioan Jenkins at the University of Edinburgh. A small amount of ZnTPP powder was mixed with Loctite superglue and pressed between two glass coverslips. Most of the ZnTPP dissolved in the superglue, however, there were some small crystals left in the film. The UV-vis spectrum of the Q-band in film and solution is shown in Figure 6.2.1. The spectra are similar but the thin film spectrum is redshifted by around 4 nm and also has a much higher baseline. The shift in the spectrum could be due to miscalibrations between the two spectrometers that were used or due to the different chemical environments. The higher baseline is likely due to scattering from small crystals in the films.

The samples were mounted in an Oxford Instruments Microstat HE2 cryostat. All of the time-resolved measurements of thin films were carried out with the sample mounted in the cryostat and pumped out to a high vacuum. The sample was continually moved in a grid pattern during the measurements to prevent sample damage. For every measurement, a fresh grid was used to ensure the undamaged sample was probed. The measurements were carried out at 293 K and 80 K.

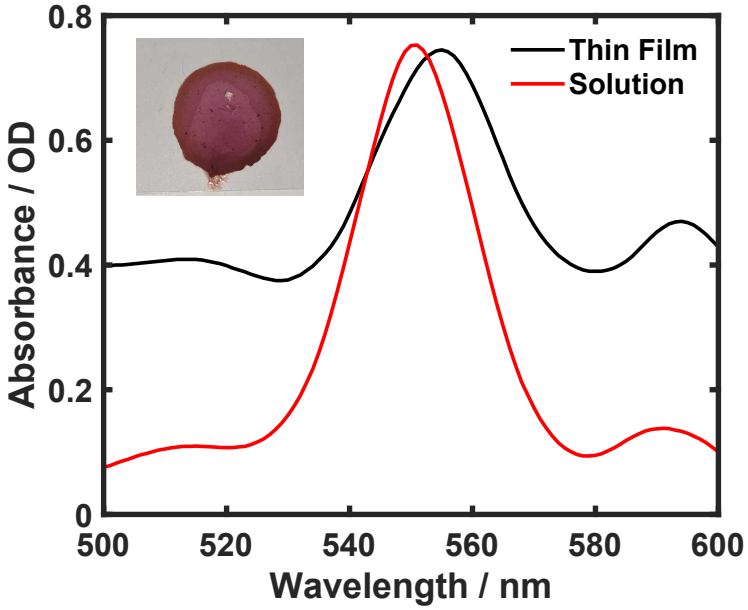

Figure 6.2.1: UV-vis spectrum of ZnTPP in toluene and superglue thin films. The solution-phase measurement was carried out by Erica Sucliffe at the California Institute of Technology using a JASCO J-1700 spectrometer. The ZnTPP was dissolved in toluene at a concentration of 38 µM. The path length of the cuvette was 1 cm. The spectrum of the thin film was measured on a Shimadzu 1800-UV spectrophotometer. Inset: Image of thin film.

6.2.2 Post-Processing

An MCD signal is typically around 1 % of the total absorption signal. A strong signal in a transient absorption measurement is around 10–100 mOD and therefore a sensitivity of under 1 mOD is required. This can be difficult because the MCD measurements are not performed shot-to-shot like the transient absorption measurements. It is impossible to switch the magnetic field at 1000 Hz with the electromagnet. In theory, a transient absorption measurement with a circularly polarised probe can be performed with one field direction and then another with the field reversed, and the difference between these would be the MCD signal. However, even a slight drift in laser parameters (such as pump fluence) between these two measurements could completely dominate the signal over the true MCD effect. Generally, the magnetic field is switched about every second to cancel out the effect of long-term drift of laser parameters. This is a good compromise between minimising the effect of drift and the increase in measurement time due to the time it takes to flip the magnetic field (around 200 ms).

Considering the signal-to-noise required, the TRMCD measurements are averaged for much longer than the equivalent transient absorption measurements. For the solution phase measurements, a single TRMCD spectrum at one time delay takes around 1 hour. The equivalent transient absorption spectrum would take seconds.

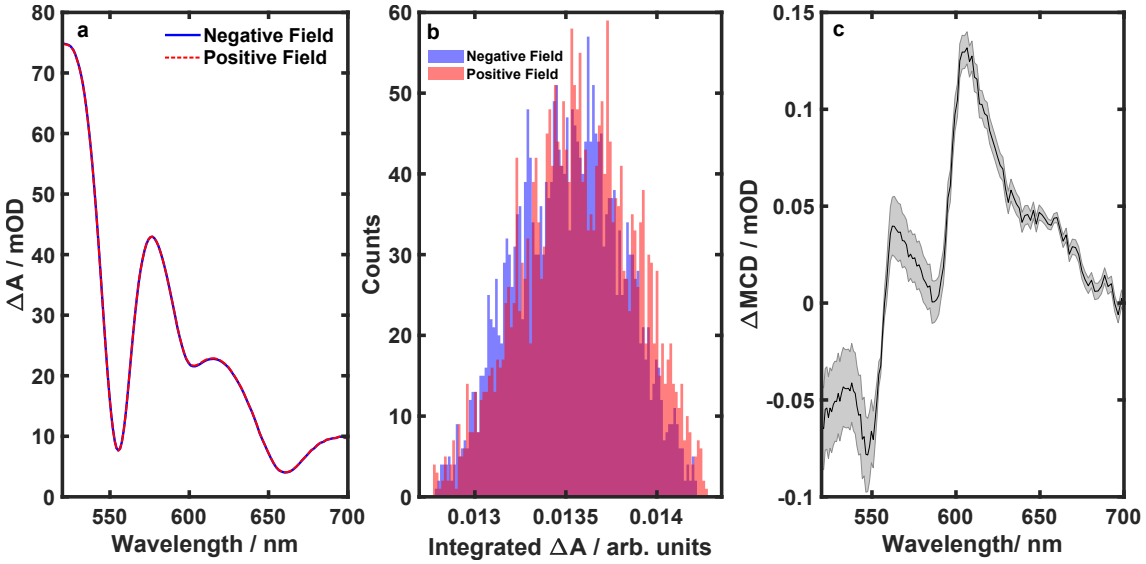

Figure 6.2.2: Measurement of a TRMCD spectrum at a 20 ps pump-probe delay. The measurement is composed of 4000 difference spectra for each field direction. Each individual difference spectra is the average of 200 laser shots which are not individually resolved. The sample was excited with a 400 nm pump pulse with a fluence of 1.4 mJcm^{-2}. The sample concentration was 780 µM, the optical path length was 200 µm and the solution flowed at 8 µL/min. **a** The average transient absorption difference spectrum for each field direction with a circularly polarised probe. **b** Histogram of the integrated intensity between 600 and 700 nm of the 4000 spectra that constitute the average spectra shown in **a**. **c** The TRMCD spectrum at a 20 ps pump-probe delay. The shaded area describes the standard error of the mean.

Figure 6.2.2**a** shows the transient absorption spectrum with a circularly polarised probe at 20 ps in a 780 uM toluene solution of ZnTPP in a 200 µm path length cuvette after photoexcitation using a 400 nm pump with a fluence of 1.4 mJcm^{-2}. The spectra shown are the average of 4000 difference spectra, which are the mean of 200 consecutive laser shots each at positive and negative magnetic fields. Figure 6.2.2**b** shows a histogram of the integrated signal between 600 and 700 nm for the 4000 difference spectra. These are mostly overlapped, but there is a slight shift of the positive field spectra to higher intensities. Figure 6.2.2**c** shows the TRMCD spectrum at 20 ps, the positive field spectrum in Figure 6.2.2**a** subtracted by the negative field spectrum. The shaded area is the standard error of the mean, $\delta\Delta\text{MCD} = \frac{\sigma}{\sqrt{N}}$ where σ is the standard deviation and N is the number of measurements.

To confirm the setup truly measures TRMCD and does not show a difference due to sample damage between the two field directions, the measurement is taken twice. Starting first with a positive field direction and reversing the field back and forth during the measurement. Then we begin instead with a negative field direction and flip the magnetic field back and forth. If the signal arises from sample damage we would expect the same results in both cases. If the effect is due to

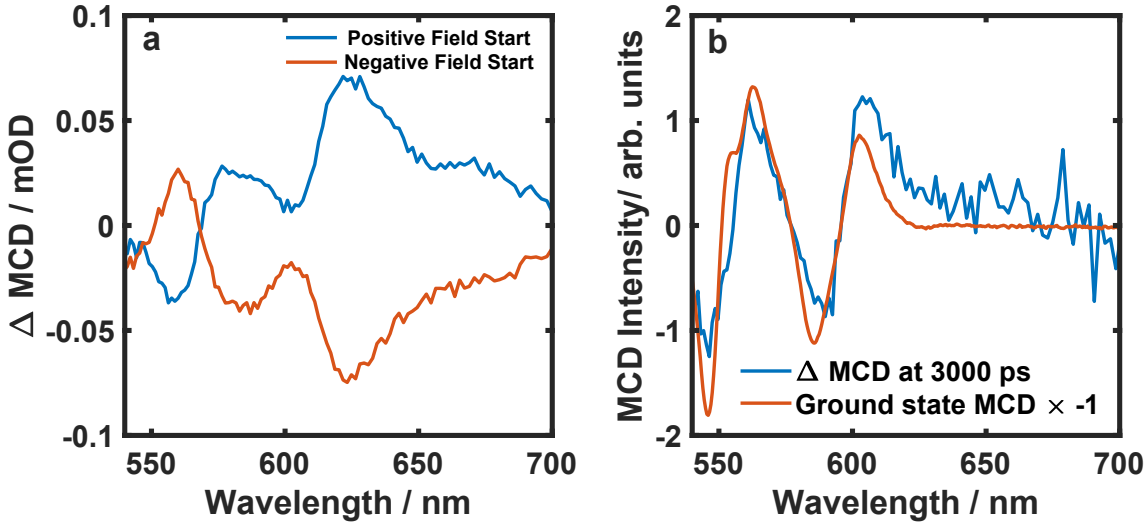

Figure 6.2.3: **a** Comparison of TRMCD spectrum with a positive and negative starting field at a pump-probe delay of 200 ps. **b** Comparison of the ground state MCD spectrum with the TRMCD spectrum at 3000 ps when most of the first excited singlet state has decayed.

MCD, the measurements will be mirror images of one another as shown in Figure 6.2.3**a**. Another good marker that a given signal is true TRMCD, analogous to GSB in a transient absorption measurement, a bleach will also occur at the position of the ground state MCD in a TRMCD measurement. The ground state MCD and TRMCD are shown in Figure 6.2.3**b**. There is good agreement between the shapes of the MCD and TRMCD which suggests the MCD bleach is captured well. However, they are not expected to match exactly given that there will be some excited state signals in the spectrum but it still suggests there is a ground state MCD contribution to the spectrum as expected.

6.3 Results and Discussion

The UV-vis spectrum and the MCD spectrum of ZnTPP in toluene are shown in Figure 6.3.1. Figure 6.3.1**a** shows the B-band, which corresponds to the S_0 to S_2 transition. The strongest transition is centred at 430 nm, which originates from the transition to the lowest vibrational level of S_2. The smaller shoulder at 400 nm corresponds to the transition to the first vibrationally excited level of S_2. The MCD displays one dominant $\mathcal{A}_1$-term at 430 nm and a much weaker $\mathcal{A}_1$-term from the vibronic transition. The sample is excited at 400 nm in the time-resolved experiments and the S_2 state is populated. The Q-band (S_0 to S_1 transition) is shown in Figure 6.3.1**b**. The strongest transition is at 555 nm and displays additional peaks corresponding to transitions to other vibrational levels in the S_1 state. The MCD spectrum contains two dominant $\mathcal{A}_1$-terms from different vibrational levels in the

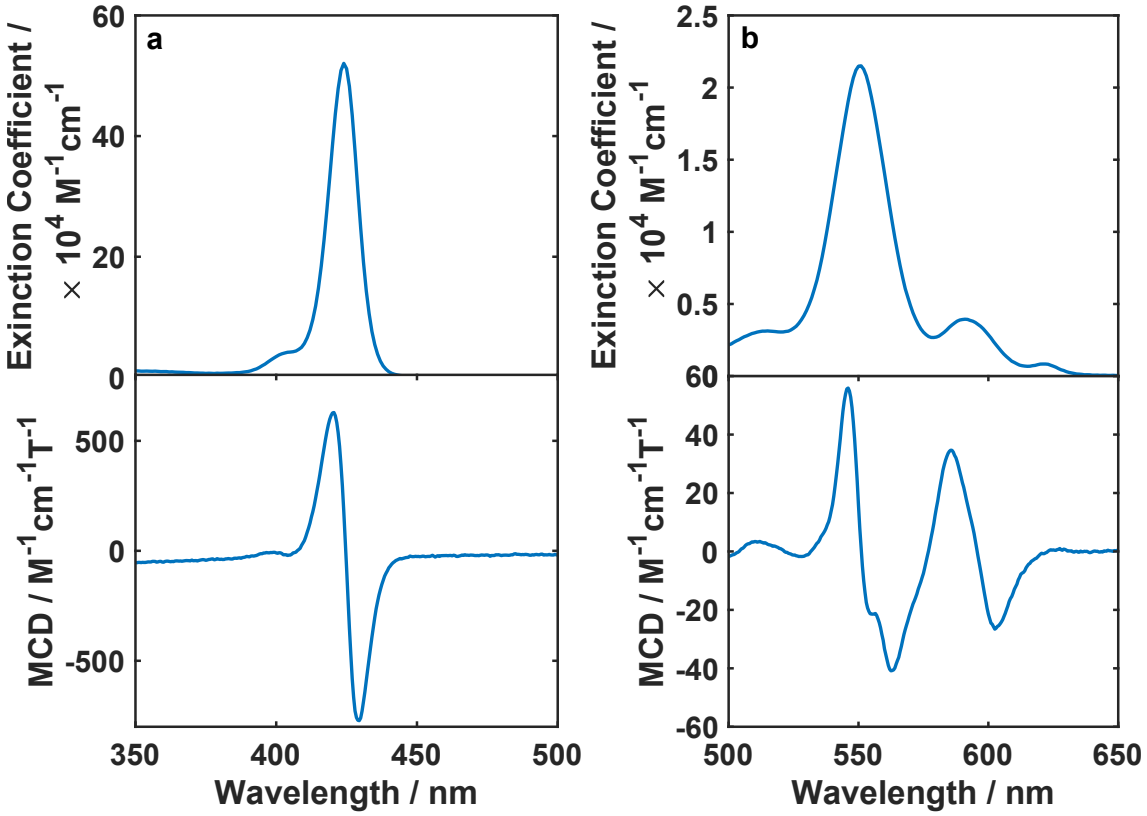

Figure 6.3.1: UV-vis and MCD spectrum of ZnTPP in toluene. **a** UV-vis absorption spectrum and MCD of the B-band centred around 420 nm. **b** UV-vis absorption spectrum and MCD of the Q-band centred around 550 nm. The data were obtained by Dr Erica Sutcliffe at the California Institute of Technology using a JASCO J-1700 spectrometer in Prof. Ryan Hadt's lab. The measurements were carried out at room temperature with an applied magnetic field of 1.4 T.

same electronic excited state.

The transient absorption and TRMCD spectra after 400 nm excitation are shown in Figure 6.3.2. After 400 nm excitation, ZnTPP undergoes IC to the S_1 state with a time constant of 1.5 ps and subsequent vibrational relaxation in that state with a time constant of around 100 ps. The ISC to the T_1 state occurs in 2.3 ns. Figure 6.3.2 shows pump-probe time delays between 20–3000 ps, which will follow the vibrational relaxation in S_1 and the S_1 to T_1 ISC.

The transient absorption spectra in Figure 6.3.2**a** exhibit GSB at 555 and 600 nm, which corresponds well to the absorptions in the ground state spectrum shown in 6.3.1**b**. Additionally, there is a small dip in the transient spectra at 660 nm, which likely arises from stimulated emission as it matches with the peak of the fluorescence spectrum.[267] The remaining signals arise from ESA. From 20 to 3000 ps there is a decay at all wavelengths apart from 660 nm where there is a small growth due to the depopulation of the S_1 state and therefore a reduction of stimulated emission.

The TRMCD spectra at various time delays are shown in 6.3.2**b**. There is a large peak at around 610 nm, which shows very little change in the first 100 ps and

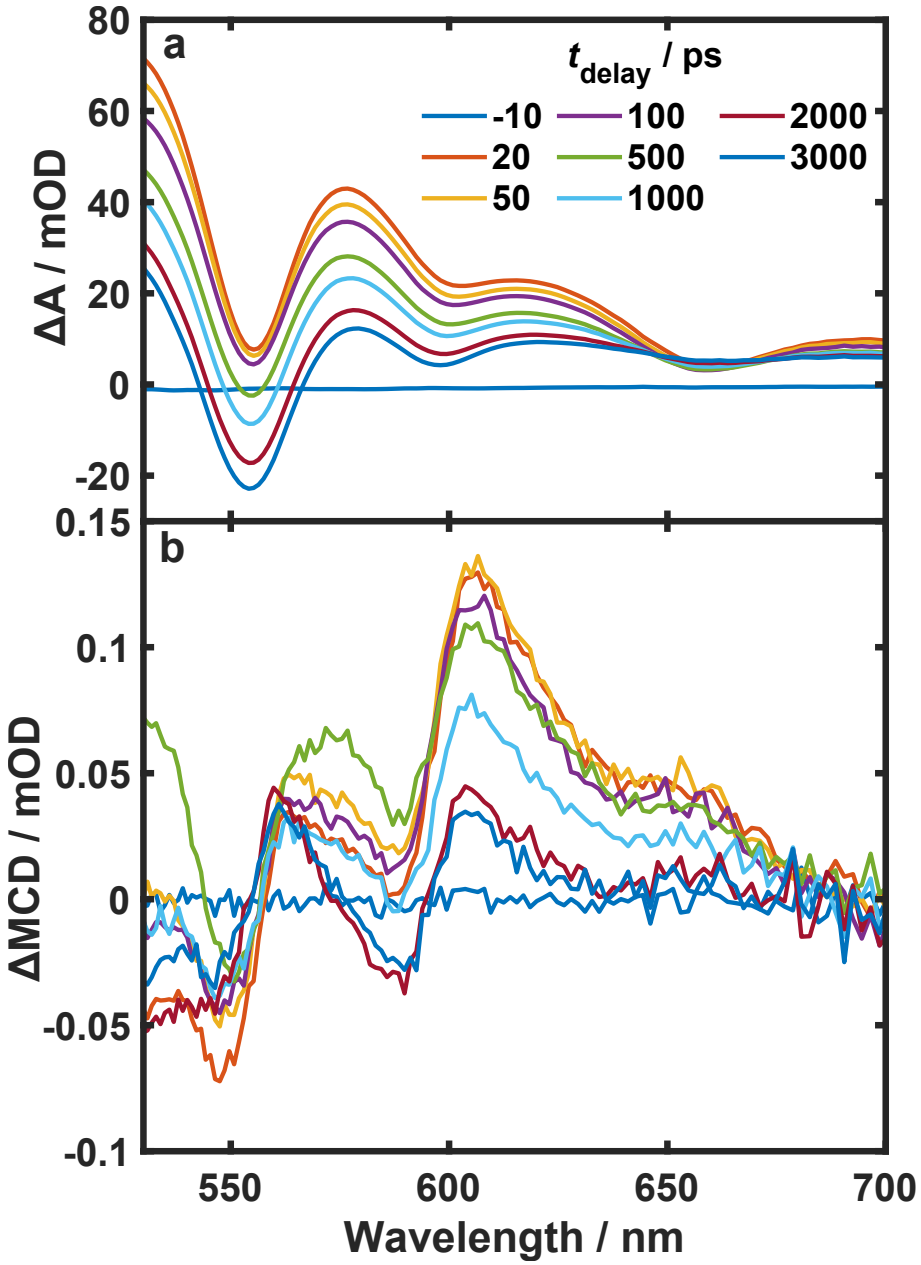

Figure 6.3.2: **a** Transient absorption and **b** TRMCD spectra at different pump-probe time delays. The concentration of ZnTPP was 780 µM in toluene. The sample has a path length of 200 µm and was pumped at 400 nm with a fluence of 1.4 mJcm^{-2}. The applied magnetic field was 750 mT.

then decays to almost a plateau at 2000 ps. Similar dynamics occur at the small shoulder around 660 nm. At times after 2000 ps, the TRMCD spectra strongly resemble the ground state MCD spectra suggesting that the spectra are dominated by an MCD GSB. Considering the triplet state is populated with a time constant of approximately 2000 ps, it is likely the T_1 state has a very weak MCD spectrum in the spectral region measured. Based on their decay, the 610 and 660 nm peaks are likely associated with the S_1 state.

In an attempt to isolate the pure S_1 MCD spectrum for characterisation, the ground state MCD spectrum was subtracted from the TRMCD spectra. The contribution of the ground state MCD to the TRMCD was estimated by scaling the ground state MCD to match, as closely as possible, with the TRMCD at 3000 ps. The comparison between the ground state MCD and TRMCD at 3000 ps is shown in Figure 6.2.3**b**. The estimated excited state MCD spectra at various times are shown in Figure 6.3.3. At 3000 ps, the signal is not exactly zero, which is expected as there will still be some population of the S_1 state given its 2000 ps lifetime. Despite the incomplete subtraction of the ground state signal, it is clear the 580, 610 and 660 nm peaks do not possess derivative-like bandshapes and therefore are unlikely to be $\mathcal{A}_1$-terms. The 610 and 660 nm peaks are separated by around 1200 cm^{-1}, which is the same splitting between the vibrational shoulders in the ground state spectrum. These two peaks could arise from a transition to the same electronic state but a different vibrational state.

To further characterise the timescales of vibrational relaxation within the S_1 state and the ISC to the T_1 state, the transient absorption and TRMCD signals were integrated from 600 to 700 nm and plotted as a function of time. This is shown in Figure 6.3.4. The integrated intensities as a function of time, $I(t)$ were globally fit with a biexponential decay described by:

$$I(t) = A_1 e^{-t/\tau_1} + A_2 e^{-t/\tau_2} + A_0 \tag{6.3.1}$$

where A_i are the amplitudes associated with time constants τ_i and A_0 is an offset term at long times. The fit provided time constants, $\tau_1 = 70 \pm 30$ ps and $\tau_2 = 2000 \pm 1000$ ps, which agree well with the previously measured vibrational relaxation and ISC time constants, respectively.[267] All fitting parameters are shown in Table 6.3.1. The amplitude of the first time constant associated with the vibrational relaxation is significant in the transient absorption data, around 27 % of the total signal. However, the amplitude of the vibrational relaxation component in the TRMCD data is less than 1 %. Considering the molecular temperature of ZnTPP decreases during vibrational relaxation, this suggests that the TRMCD between 600 to 700 nm is not sensitive to temperature. An excited state $\mathcal{A}_1$-term has already

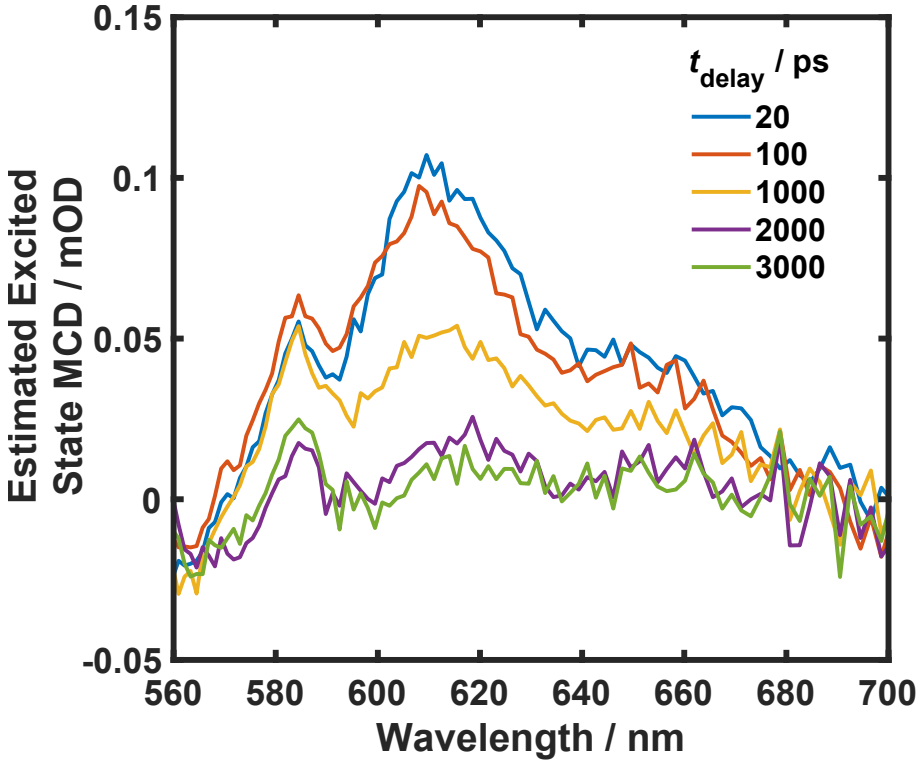

Figure 6.3.3: Estimated excited state MCD spectra at different pump-probe delays. These have been generated by subtracting the ground state MCD spectrum.

been dismissed due to the shape of the spectrum. The origin of the excited state MCD must be a $\mathcal{B}_0$ or $\mathcal{C}_0$-term. Because the TRMCD is insensitive to the cooling of the molecule during vibrational relaxation, it suggests the excited state MCD is dominated by $\mathcal{B}_0$-terms.

To confirm the assignment that the excited state MCD signal arises from $\mathcal{B}_0$-terms, a TRMCD measurement was carried out at 80 K. To do this, a thin film sample was used and mounted within the cryostat. The UV-Vis of the film is shown in Figure 6.2.1 in the methods. The time-resolved data at a time delay of 100 ps are

Parameter	MCD	Transient Absorption
τ_1 (ps)	70 ± 30	70 ± 30
τ_2 (ps)	2000 ± 1000	2000 ± 1000
A_1	0.003 ± 0.100	0.33 ± 0.10
A_2	0.90 ± 0.17	0.27 ± 0.09
A_0	0.10 ± 0.10	0.40 ± 0.09

Table 6.3.1: Fitting parameters extracted from the global fit of the transient absorption and TRMCD kinetic fit in Figure 6.3.4. The amplitudes A_i are given as a fraction of the maximum amplitude of the signal.

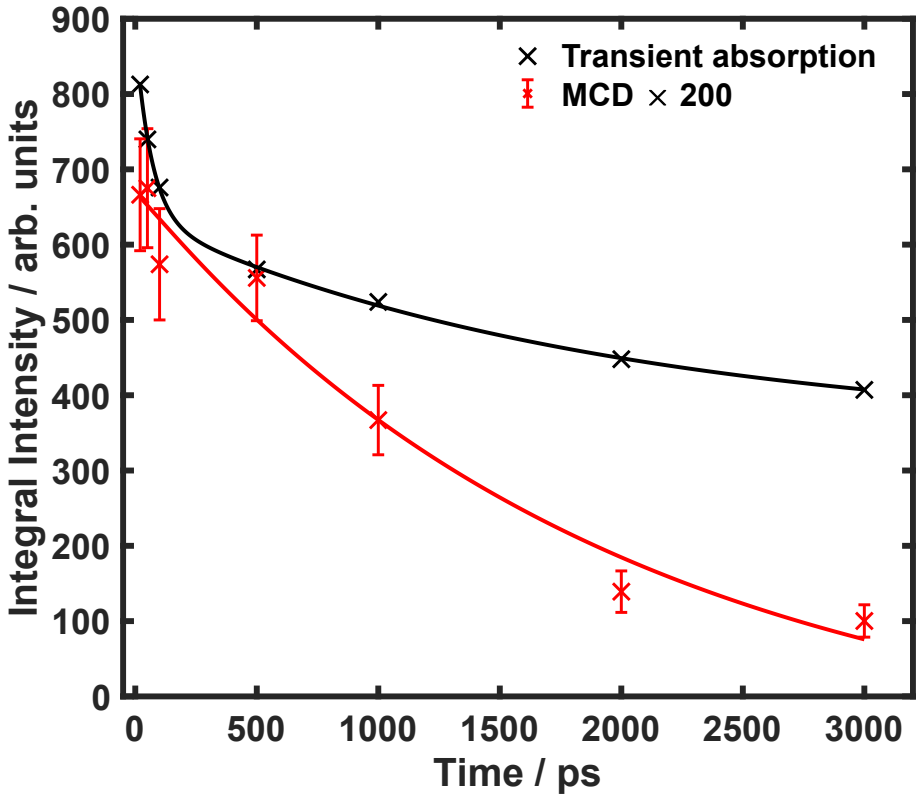

Figure 6.3.4: Integrated intensity of the transient absorption and TRMCD spectra shown in Figure 6.3.2 from 600 to 700 nm as a function of pump-probe time delay. The TRMCD data has been multiplied by 200 to aid visualisation. The data are globally fitted with a biexponential decay with time constants 70 ± 30 ps and 2000 ± 1000 ps. The errorbars of the transient absorption data are too small to see.

shown in Figure 6.3.5 together with the solution-phase data at room temperature for comparison. The transient absorption spectra in thin films are largely the same as in toluene solution. Peaks and troughs occur within a few nanometres of each other, apart from the additional structure in the thin-film measurements between 600 and 650 nm, which suggests a splitting of peaks. Comparing the 293 K and 80 K transient absorption spectra, the absorption in the region 600–650 nm is roughly the same, which should allow a reasonable comparison between the TRMCD spectra at the two temperatures.

The TRMCD spectra at room temperature in solution and temperature-dependent thin film measurements are shown in Figure 6.3.5**b**. Taking into account the $1/T$ dependence of $\mathcal{C}_0$-terms, a reduction in temperature from 293 K to 80 K should increase the magnitude of a $\mathcal{C}_0$-term by 3.5 times. Despite the low signal-to-noise ratio of the data, it is clear that the MCD does not increase by 3.5 times and remains roughly constant, suggesting no temperature dependence associated with the excited state MCD term. This is in agreement with the apparent insensitivity to vibrational relaxation processes suggested by the kinetic data. Therefore, the excited state MCD likely arises from a $\mathcal{B}_0$-term.

In ground state MCD spectra, the $\mathcal{B}_0$-terms tend to be much weaker than the other terms. Considering that $\mathcal{B}_0$-terms are inversely proportional to the energy difference between two states that are mixed by the magnetic field, one could expect these terms to be more intense as electronic states are more closely spaced at higher energies. It could be that the $\mathcal{B}_0$-terms are much more common in the excited states of molecules. Indeed, the energy difference between the closest excited state in the S_0 state is 1.57 eV to the T_1 state whereas in the S_1 state the closest states are separated by only 0.54 eV.[281]

6.4 Conclusion

Using a newly developed TRMCD setup, the MCD spectrum of the first singlet excited state in ZnTPP was measured. By comparison to the ground state MCD spectrum, it is shown that the S_1 MCD spectrum is dominated by peaks at 580, 610 and 660 nm. Given that the bandshape of these signals do not have a derivative-like shape, it is unlikely these are $\mathcal{A}_1$-terms. It was observed that the S_1 state MCD signal is not sensitive to vibrational cooling dynamics suggesting that the signal does not depend on molecular temperature. These observations indicate that the S_1 state MCD signal in the 550–700 nm region is dominated by $\mathcal{B}_0$-terms. To confirm this, temperature-dependent TRMCD measurements were conducted that showed no change in the S_1 state MCD signal down to 80 K.

Although nothing new about the dynamics that occur after photoexcitation of

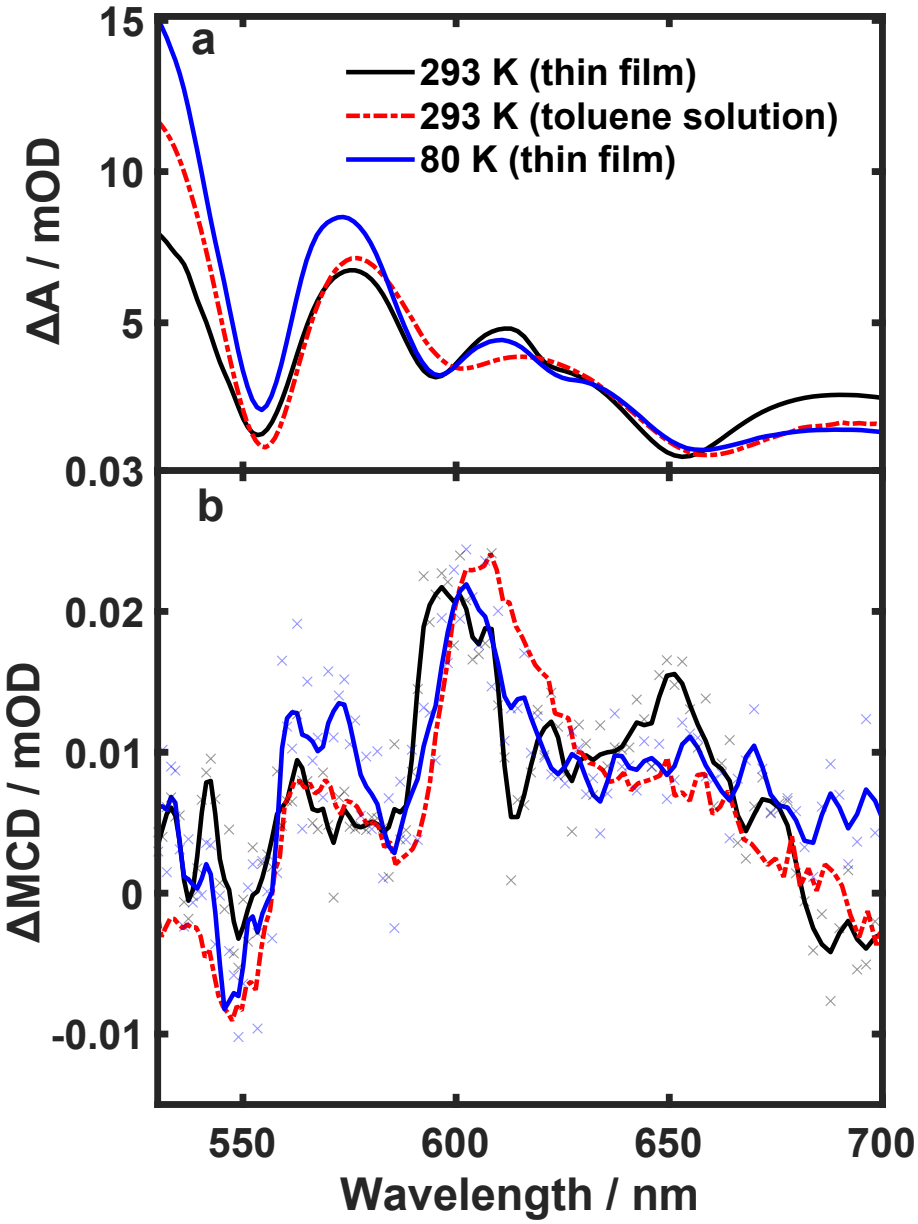

Figure 6.3.5: Temperature-dependent transient absorption and TRMCD spectra after 400 nm excitation in solution and thin film samples. The pump-probe time delay is 100 ps. The solution phase data has been multiplied by 0.2 to aid comparison to the thin film measurements. **a** Transient absorption spectra. **b** TRMCD spectra. The lines have been smoothed with 7 point adjacent averaging and the markers display the unsmoothed data points for the thin film measurements.

ZnTPP was discovered, the results still show that TRMCD is an interesting technique to investigate the excited states of molecules. $\mathcal{B}_0$-terms are generally the most difficult MCD terms to analyse as they rely on wavefunction mixing rather than Zeeman shifts. The analysis of $\mathcal{A}_1$ and $\mathcal{C}_0$-terms can yield the value of magnetic moments in the excited states.[282] A direct measurement of the magnetic moment in the excited state of a molecule on these timescales will be important to develop light-controlled magnetisation in SMMs. Additionally, temperature-dependent MCD measurements have been used to calculate ZFS parameters of transition metal complexes.[283] This would be interesting to extend to electronic excited states, particularly to measure the change in ZFS parameters after Jahn-Teller switching in Mn(III) complexes.

Chapter 7

Conclusions

This thesis examined the application of ultrafast spectroscopic techniques to single-molecule magnets and related transition metal complexes. One main focus was to follow how the magnetic anisotropy of metal ions might change upon light absorption on femtosecond timescales and to explore the possibilities of controlling this. Given that nuclear, electronic, and spin degrees of freedom are intimately related to the magnetic anisotropy, methods that were sensitive to these were applied. Two very broad questions were asked: (1) could the dynamics in transition metal complexes, and therefore SMMs, be controlled by synthetic design? (2) How could the magnetisation dynamics, magnetic anisotropy, and other molecular properties that have an effect on the magnetisation be measured on ultrafast timescales?

In Chapters 3 and 5, optical transient absorption spectroscopy was used to investigate nuclear wavepackets after the population of crystal-field excited states in Mn(III) terpyridine and Ru(II) triazolyl complexes. Nuclear structure is important to SMMs, as the geometry of the crystal-field environment can dictate the magnetic anisotropy. In [Mn(terpy)X_3] where X = F, Cl, N_3, the excitation of the lowest energy crystal-field transition leads to the activation of a pincer-like mode on the terpyridine ligand with a frequency of 110 cm^{-1}. This mode is activated due to the transfer of an electron from the d_{z^2} to the $d_{x^2-y^2}$ orbital that drives a Jahn-Teller switch from axial elongation to compression. The dephasing times of the pincer-mode increase moving from X = F to Cl to N_3. With the aid of computations, it was found that as the number of vibrational normal modes with energies below the pincer mode increases, the dephasing times decrease. This suggests that low-frequency modes act as an effective bath to dissipate energy through intramolecular vibrational redistribution. It could be possible to harness some control over vibrational relaxation and dephasing in SMMs.

In Chapter 5, the photoinduced dynamics of triazolyl-based structural analogues of $Ru(bpy)_3^{2+}$ were investigated with the aim of directly identifying the ^{3}MC excited state. By substituting the bipyridine ligand with the triazolyl equivalent, 4,4'-bi-

1,2,3-triazolyl, the excited state ordering of the ^{3}MLCT and ^{3}MC state could be inverted, thereby transforming the nature of the lowest-energy excited state to metal-centered.[254] This ^{3}MC state contains a single electron in the metal e_g orbitals, inducing Jahn-Teller distortion. In the two complexes studied, $[Ru(Ph{-}btz)_3]^{2+}$ and $[Ru(Bn{-}btz)_3]^{2+}$, photoexcitation of the MLCT transition resulted in impulsive population of the ^{3}MC state, driving coherent vibrational motion. In $[Ru(Ph{-}btz)_3]^{2+}$, relatively simple wavepacket dynamics with one single dominant mode were observed, which dephases over time. Even with relatively minor synthetic changes (replacing a phenyl with a benzyl group), significant variations in vibrational motion after light absorption were observed. The findings suggest that, with the correct design criteria, coherent vibrational motion could be controlled in the excited states of molecules, including SMMs.

Chapter 4 utilised femtosecond K-edge X-ray absorption spectroscopy to accurately track nuclear dynamics after photoexcitation in a trinuclear Mn(III) SMM to investigate question (2). The whole K-edge difference spectrum, after metal-centred excitation, could be interpreted using geometric changes occurring predominantly along a single Jahn-Teller active mode. The signature of this mode was also observed as an oscillation in the X-ray kinetic trace with a frequency of around 180 cm^{-1}, suggesting a coherent excitation of this mode. This was in excellent agreement with the optical time-resolved measurements.[65] Spectral changes in the pre-edge also agreed well with the changes across the whole K-edge region, with motion along one Jahn-Teller mode being dominant. The good agreement between computation and experiment allowed the determination of bond length changes that occurred in the excited state. Changes in the axial Jahn-Teller bonds were greater than 0.03 Å whereas equatorial bonds elongated only by around 0.01 Å indicating structural rigidity in the equatorial plane as suggested previously.[65] In light of these small geometry changes, it is unlikely that any significant magnetisation dynamics would take place based on the nuclear structure only. Therefore, it was suggested that more flexible SMMs would provide a better platform to control the magnetic properties.

Time-resolved magnetic circular dichroism is used in Chapter 6 to study the ultrafast dynamics of zinc(II) tetraphenylporphyrin. Temperature-dependent magnetic circular dichroism spectroscopy has previously been used to calculate the zero-field splitting parameters that define the anisotropy in Mn(III) complexes.[88] Therefore, the time-resolved extension could be used to measure zero-field splitting parameters in electronic excited states. To test the setup, zinc(II) tetraphenylporphyrin was chosen for study due to its large ground state magnetic circular dichroism and strong excited state optical transitions. It was shown that it is possible to measure the time-resolved magnetic circular dichroism spectrum of a molecule in solution on picosecond timescales. Through temperature-dependent measurements, the excited

state MCD was found to be dominated by MCD $\mathcal{B}_0$-terms. In addition to its potential utility for measuring spin dynamics in SMMs, this technique could have broad applications in various photophysical and photochemical problems, where optical spectroscopies alone lack specific details about the nature of excited states.

Bibliography

(1) R. L. Comstock, *Journal of Materials Science: Materials in Electronics*, 2002, **13**, 509–523.

(2) I. Tudosa, C. Stamm, A. Kashuba, F. King, H. Siegmann, J. Stöhr, G. Ju, B. Lu and D. Weller, *Nature*, 2004, **428**, 831–833.

(3) C. Back and D. Pescia, *Nature*, 2004, **428**, 808–809.

(4) D. R.-J. G.-J. Rydning, J. Reinsel and J. Gantz, *Framingham: International Data Corporation*, 2018, **16**, 1–28.

(5) D. Strickland and G. Mourou, *Optics communications*, 1985, **55**, 447–449.

(6) D. E. Spence, P. N. Kean and W. Sibbett, *Optics letters*, 1991, **16**, 42–44.

(7) P. Schatz and A. McCaffery, *Quarterly Reviews, Chemical Society*, 1969, **23**, 552–584.

(8) E. Beaurepaire, J.-C. Merle, A. Daunois and J.-Y. Bigot, *Physical review letters*, 1996, **76**, 4250.

(9) H. Zhao, B. Glass, P. K. Amiri, A. Lyle, Y. Zhang, Y.-J. Chen, G. Rowlands, P. Upadhyaya, Z. Zeng, J. Katine et al., *Journal of Physics D: Applied Physics*, 2011, **45**, 025001.

(10) A. V. Kimel, A. Kirilyuk and T. Rasing, *Laser & Photonics Reviews*, 2007, **1**, 275–287.

(11) A. V. Kimel, A. Kirilyuk, F. Hansteen, R. V. Pisarev and T. Rasing, *Journal of Physics: Condensed Matter*, 2007, **19**, 043201.

(12) A. Kirilyuk, A. V. Kimel and T. Rasing, *Reviews of Modern Physics*, 2010, **82**, 2731.

(13) A. M. Kalashnikova, A. V. Kimel and R. V. Pisarev, *Physics-Uspekhi*, 2015, **58**, 969.

(14) J. Mentink, *Journal of Physics: Condensed Matter*, 2017, **29**, 453001.

(15) K. Carva, P. Baláž and I. Radu, *Handbook of magnetic materials*, 2017, **26**, 291–463.

(16) A. V. Kimel and M. Li, *Nature Reviews Materials*, 2019, **4**, 189–200.

(17) L. Pitaevskii, *Sov. Phys. JETP*, 1961, **12**, 1008–1013.

(18) J. Van der Ziel, P. S. Pershan and L. Malmstrom, *Physical review letters*, 1965, **15**, 190.

(19) A. Kimel, A. Kirilyuk, P. Usachev, R. Pisarev, A. Balbashov and T. Rasing, *Nature*, 2005, **435**, 655–657.

(20) C. D. Stanciu, F. Hansteen, A. V. Kimel, A. Kirilyuk, A. Tsukamoto, A. Itoh and T. Rasing, *Physical review letters*, 2007, **99**, 047601.

(21) A. Khorsand, M. Savoini, A. Kirilyuk, A. Kimel, A. Tsukamoto, A. Itoh and T. Rasing, *Physical review letters*, 2012, **108**, 127205.

(22) T. Ostler, J. Barker, R. Evans, R. Chantrell, U. Atxitia, O. Chubykalo-Fesenko, S. El Moussaoui, L. Le Guyader, E. Mengotti, L. Heyderman et al., *Nature communications*, 2012, **3**, 666.

(23) F. Hansteen, A. Kimel, A. Kirilyuk and T. Rasing, *Physical review letters*, 2005, **95**, 047402.

(24) S. Tomimoto, M. Matsubara, T. Ogasawara, H. Okamoto, T. Kimura and Y. Tokura, *Physical review letters*, 2007, **98**, 017402.

(25) F. Atoneche, A. Kalashnikova, A. Kimel, A. Stupakiewicz, A. Maziewski, A. Kirilyuk and T. Rasing, *Physical Review B*, 2010, **81**, 214440.

(26) J. Stöhr and H. C. Siegmann, *Solid-State Sciences. Springer, Berlin, Heidelberg*, 2006, **5**, 294–299.

(27) A. Kirilyuk, A. Kimel, F. Hansteen, T. Rasing and R. V. Pisarev, *Low Temperature Physics*, 2006, **32**, 748–767.

(28) S. Baierl, M. Hohenleutner, T. Kampfrath, A. Zvezdin, A. V. Kimel, R. Huber and R. Mikhaylovskiy, *Nature Photonics*, 2016, **10**, 715–718.

(29) A. Stupakiewicz, K. Szerenos, D. Afanasiev, A. Kirilyuk and A. Kimel, *Nature*, 2017, **542**, 71–74.

(30) T. F. Nova, A. Cartella, A. Cantaluppi, M. Först, D. Bossini, R. V. Mikhaylovskiy, A. V. Kimel, R. Merlin and A. Cavalleri, *Nature Physics*, 2017, **13**, 132–136.

(31) D. Afanasiev, J. R. Hortensius, M. Matthiesen, S. Mañas-Valero, M. Šiškins, M. Lee, E. Lesne, H. S. van Der Zant, P. G. Steeneken, B. A. Ivanov et al., *Science advances*, 2021, **7**, eabf3096.

(32) D. Afanasiev, J. Hortensius, B. Ivanov, A. Sasani, E. Bousquet, Y. Blanter, R. Mikhaylovskiy, A. Kimel and A. Caviglia, *Nature materials*, 2021, **20**, 607–611.

(33) A. Stupakiewicz, K. Szerenos, M. Davydova, K. Zvezdin, A. Zvezdin, A. Kirilyuk and A. Kimel, *Nature communications*, 2019, **10**, 612.

(34) J. Wang, C. Sun, Y. Hashimoto, J. Kono, G. A. Khodaparast, Ł. Cywiński, L. Sham, G. D. Sanders, C. J. Stanton and H. Munekata, *Journal of Physics: Condensed Matter*, 2006, **18**, R501.

(35) D. Gatteschi, *Advanced Materials*, 1994, **6**, 635–645.

(36) J. Mroziński, *Coordination chemistry reviews*, 2005, **249**, 2534–2548.

(37) E. Coronado, P. Delhaès, D. Gatteschi and J. S. Miller, *Molecular magnetism: from molecular assemblies to the devices*, Springer Science & Business Media, 2013, vol. 321.

(38) E. Coronado, *Nature Reviews Materials*, 2020, **5**, 87–104.

(39) O. Kahn, *Molecular magnetism*, Courier Dover Publications, 2021.

(40) G. Christou, D. Gatteschi, D. N. Hendrickson and R. Sessoli, *MRS Bulletin*, 2000, **25**, 66–71.

(41) D. N. Woodruff, R. E. Winpenny and R. A. Layfield, *Chemical reviews*, 2013, **113**, 5110–5148.

(42) R. A. Layfield, *Organometallics*, 2014, **33**, 1084–1099.

(43) D. Shao and X.-Y. Wang, *Chinese Journal of Chemistry*, 2020, **38**, 1005–1018.

(44) G. Aromí and E. K. Brechin, *Single-molecule magnets and related phenomena*, 2006, 1–67.

(45) N. F. Chilton, *Inorganic Chemistry*, 2015, **54**, 2097–2099.

(46) M. Perfetti and J. Bendix, *Inorganic Chemistry*, 2019, **58**, 11875–11882.

(47) M. Perfetti, M. A. Sørensen, U. B. Hansen, H. Bamberger, S. Lenz, P. P. Hallmen, T. Fennell, G. G. Simeoni, A. Arauzo, J. Bartolomé et al., *Advanced Functional Materials*, 2018, **28**, 1801846.

(48) A. Raza and M. Perfetti, *Coordination Chemistry Reviews*, 2023, **490**, 215213.

(49) H. Bethe, *Annalen der Physik*, 1929, **395**, 133–208.

(50) J. Van Vleck, *Physical Review*, 1932, **41**, 208.

(51) J. Halpern, *3D Representation of Orbitals*, 2020, `https://chem.libretexts.org/Bookshelves/General_Chemistry/Map%5C%3A_Chemistry_-_The_Central_Science_(Brown_et_al.)/06._Electronic_Structure_of_Atoms/6.6%5C%3A_3D_Representation_of_Orbitals` (visited on 01/25/2020).

(52) M. Weller, T. Overton, J. Rourke and F. Armstrong, *Inorganic Chemistry*, Oxford University Press, 6th edn., 2014, vol. 6, pp. 515–525.

(53) S. S. Zumdahl, *Chemical Principles*, Houghton Mifflin Company, 5th edn., 2005, vol. 5, pp. 550–551.

(54) D. F. Shriver and P. W. Atkins, *Inorganic Chemistry*, Oxford University Press, 3rd edn., 2001, vol. 5, pp. 227–236.

(55) E. I. Solomon and A. B. P. Lever, *Inorganic electronic structure and spectroscopy*, Wiley, 1999, pp. 3–91.

(56) N. J. Hair and J. K. Beattie, *Inorganic Chemistry*, 1977, **16**, 245–250.

(57) S. Decurtins, P. Gutlich, K. Hasselbach, A. Hauser and H. Spiering, *Inorganic Chemistry*, 1985, **24**, 2174–2178.

(58) J. Baker and B. N. Figgis, *Journal of the Chemical Society, Dalton Transactions*, 1975, 598–602.

(59) H. A. Jahn and E. Teller, *Proceedings of the Royal Society of London. Series A-Mathematical and Physical Sciences*, 1937, **161**, 220–235.

(60) I. Bersuker, *The Jahn-Teller effect and vibronic interactions in modern chemistry*, Springer Science & Business Media, 2013.

(61) R. Englman and R. Englman, *The Jahn-Teller effect in molecules and crystals*, Wiley-Interscience New York, 1972.

(62) U. Öpik and M. H. L. Pryce, *Proceedings of the Royal Society of London. Series A. Mathematical and Physical Sciences*, 1957, **238**, 425–447.

(63) R. J. Deeth and M. A. Hitchman, *Inorganic Chemistry*, 1986, **25**, 1225–1233.

(64) M. A. Halcrow, *Chemical Society Reviews*, 2013, **42**, 1784–1795.

(65) F. Liedy, J. Eng, R. McNab, R. Inglis, T. J. Penfold, E. K. Brechin and J. O. Johansson, *Nature chemistry*, 2020, **12**, 452–458.

(66) E. Biasin, T. B. van Driel, K. S. Kjær, A. O. Dohn, M. Christensen, T. Harlang, P. Vester, P. Chabera, Y. Liu, J. Uhlig et al., *Physical review letters*, 2016, **117**, 013002.

(67) S. E. Canton, M. Biednov, M. Pápai, F. A. Lima, T.-K. Choi, F. Otte, Y. Jiang, P. Frankenberger, M. Knoll, P. Zalden et al., *Advanced Science*, 2023, 2206880.

(68) M. Iwamura, S. Takeuchi and T. Tahara, *Journal of the American Chemical Society*, 2007, **129**, 5248–5256.

(69) M. Iwamura, H. Watanabe, K. Ishii, S. Takeuchi and T. Tahara, *Journal of the American Chemical Society*, 2011, **133**, 7728–7736.

(70) M. Iwamura, S. Takeuchi and T. Tahara, *Physical Chemistry Chemical Physics*, 2014, **16**, 4143–4154.

(71) L. Hua, M. Iwamura, S. Takeuchi and T. Tahara, *Physical Chemistry Chemical Physics*, 2015, **17**, 2067–2077.

(72) M. Iwamura, S. Takeuchi and T. Tahara, *Accounts of chemical research*, 2015, **48**, 782–791.

(73) T. Katayama, T. Northey, W. Gawelda, C. J. Milne, G. Vankó, F. A. Lima, R. Bohinc, Z. Németh, S. Nozawa, T. Sato et al., *Nature communications*, 2019, **10**, 3606.

(74) G. Azzolina, H. Tokoro, K. Imoto, M. Yoshikiyo, S.-i. Ohkoshi and E. Collet, *Angewandte Chemie*, 2021, **133**, 23455–23461.

(75) K. Barlow and J. O. Johansson, *Physical Chemistry Chemical Physics*, 2021, **23**, 8118–8131.

(76) D. F. Swinehart, *Journal of chemical education*, 1962, **39**, 333.

(77) J.-M. Combes, P. Duclos and R. Seiler, in *Rigorous atomic and molecular physics*, Springer, 1981, pp. 185–213.

(78) M. Lax, *The Journal of chemical physics*, 1952, **20**, 1752–1760.

(79) B. H. Bransden and C. J. Joachain, *Physics of atoms and molecules*, Longman Group Limited, 1983, pp. 442–444.

(80) R. F. Fenske, *Journal of the American Chemical Society*, 1967, **89**, 252–256.

(81) D. J. Griffiths, *Introduction to quantum mechanics*, Pearson International Edition (Pearson Prentice Hall, Upper Saddle River, 2005), 1960.

(82) J. B. Goodenough, *Physical Review*, 1968, **171**, 466.

(83) P. Dongare, B. D. Myron, L. Wang, D. W. Thompson and T. J. Meyer, *Coordination Chemistry Reviews*, 2017, **345**, 86–107.

(84) E. U. Condon, *American journal of physics*, 1947, **15**, 365–374.

(85) P. Atkins, T. Overton, J. Rourke, M. Weller and F. Armstrong, *Shriver and Atkins' inorganic chemistry*, Oxford University Press, USA, 2010, p. 501.

(86) P. C. Bunting, M. Atanasov, E. Damgaard-Møller, M. Perfetti, I. Crassee, M. Orlita, J. Overgaard, J. van Slageren, F. Neese and J. R. Long, *Science*, 2018, **362**, eaat7319.

(87) R. Boča, *Coordination chemistry reviews*, 2004, **248**, 757–815.

(88) L. Dugad, D. Behere, V. Marathe and S. Mitra, *Chemical physics letters*, 1984, **104**, 353–356.

(89) S. Mossin, H. Weihe and A.-L. Barra, *Journal of the American Chemical Society*, 2002, **124**, 8764–8765.

(90) T. Biskup, *Frontiers in Chemistry*, 2019, **7**, 10.

(91) A.-L. Barra, D. Gatteschi, R. Sessoli, G. L. Abbati, A. Cornia, A. C. Fabretti and M. G. Uytterhoeven, *Angewandte Chemie International Edition in English*, 1997, **36**, 2329–2331.

(92) W. Browett, A. Fucaloro, T. Morgan and P. Stephens, *Journal of the American Chemical Society*, 1983, **105**, 1868–1872.

(93) B. E. Williamson, T. C. VanCott, M. E. Boyle, G. C. Misener, M. J. Stillman and P. N. Schatz, *Journal of the American Chemical Society*, 1992, **114**, 2412–2419.

(94) K. Bane, R. A. Geiger, S. A. Chabolla and T. A. Jackson, *Inorganica Chimica Acta*, 2012, **380**, 135–140.

(95) J. Sutcliffe and J. O. Johansson, *Review of Scientific Instruments*, 2021, **92**, 113001.

(96) J. Lu, I. O. Ozel, C. A. Belvin, X. Li, G. Skorupskii, L. Sun, B. K. Ofori-Okai, M. Dincă, N. Gedik and K. A. Nelson, *Chemical science*, 2017, **8**, 7312–7323.

(97) H. Kramers, *Physica*, 1934, **1**, 182–192.

(98) P. W. Anderson, *Physical Review*, 1950, **79**, 350.

(99) D. Gatteschi, R. Sessoli and J. Villain, *Molecular nanomagnets*, Oxford University Press, USA, 2006, vol. 5.

(100) O. Waldmann, *Inorganic chemistry*, 2007, **46**, 10035–10037.

(101) G. A. Craig and M. Murrie, *Chemical Society Reviews*, 2015, **44**, 2135–2147.

(102) Y.-S. Meng, S.-D. Jiang, B.-W. Wang and S. Gao, *Accounts of chemical research*, 2016, **49**, 2381–2389.

(103) R. Sessoli, D. Gatteschi, A. Caneschi and M. Novak, *Nature*, 1993, **365**, 141–143.

(104) K. Mertes, Y. Suzuki, M. Sarachik, Y. Myasoedov, H. Shtrikman, E. Zeldov, E. Rumberger, D. Hendrickson and G. Christou, *Solid state communications*, 2003, **127**, 131–139.

(105) C. J. Milios, A. Vinslava, W. Wernsdorfer, S. Moggach, S. Parsons, S. P. Perlepes, G. Christou and E. K. Brechin, *Journal of the American Chemical Society*, 2007, **129**, 2754–2755.

(106) F.-S. Guo, B. M. Day, Y.-C. Chen, M.-L. Tong, A. Mansikkamäki and R. A. Layfield, *Science*, 2018, **362**, 1400–1403.

(107) W. Kaszub, A. Marino, M. Lorenc, E. Collet, E. G. Bagryanskaya, E. V. Tretyakov, V. I. Ovcharenko and M. V. Fedin, *Angewandte Chemie*, 2014, **126**, 10812–10816.

(108) M. Schmitt, G. Knopp, A. Materny and W. Kiefer, *Chemical Physics Letters*, 1997, **270**, 9–15.

(109) A. T. Kumar, F. Rosca, A. Widom and P. M. Champion, *The Journal of Chemical Physics*, 2001, **114**, 701–724.

(110) A. T. Kumar, F. Rosca, A. Widom and P. M. Champion, *The Journal of Chemical Physics*, 2001, **114**, 6795–6815.

(111) M. Liebel, C. Schnedermann, T. Wende and P. Kukura, *The Journal of Physical Chemistry A*, 2015, **119**, 9506–9517.

(112) C. Bardeen, Q. Wang and C. Shank, *Physical review letters*, 1995, **75**, 3410.

(113) K. Ohmori, *Annual review of physical chemistry*, 2009, **60**, 487–511.

(114) G. D. Scholes, G. R. Fleming, L. X. Chen, A. Aspuru-Guzik, A. Buchleitner, D. F. Coker, G. S. Engel, R. Van Grondelle, A. Ishizaki, D. M. Jonas et al., *Nature*, 2017, **543**, 647–656.

(115) D. W. Oxtoby, *Advances in Chemical Physics*, 1979, 1–48.

(116) D. W. Oxtoby, *Advances in Chemical Physics: Photoselective Chemistry. Part 2*, 1981, 487–519.

(117) R. Kubo, *Ter Haar Oliver and J. Boyd (Edinburgh, 1962)*, 1962, 27.

(118) A. B. Myers, *Annual review of physical chemistry*, 1998, **49**, 267–295.

(119) T. Yamaguchi, *The Journal of Chemical Physics*, 2000, **112**, 8530–8533.

(120) J. M. Jean and G. R. Fleming, *The Journal of chemical physics*, 1995, **103**, 2092–2101.

(121) S. Rafiq and G. D. Scholes, *Journal of the American Chemical Society*, 2018, **141**, 708–722.

(122) E. Gershgoren, Z. Wang, S. Ruhman, J. Vala and R. Kosloff, *The Journal of chemical physics*, 2003, **118**, 3660–3667.

(123) A. F. Fidler, E. Harel, P. D. Long and G. S. Engel, *The Journal of Physical Chemistry A*, 2012, **116**, 282–289.

(124) E. A. Juban, A. L. Smeigh, J. E. Monat and J. K. McCusker, *Coordination Chemistry Reviews*, 2006, **250**, 1783–1791.

(125) P. Gütlich, Y. Garcia and H. A. Goodwin, *Chemical Society Reviews*, 2000, **29**, 419–427.

(126) J.-F. Létard, *Journal of Materials Chemistry*, 2006, **16**, 2550–2559.

(127) M. D. Woodhouse and J. K. McCusker, *Journal of the American Chemical Society*, 2020, **142**, 16229–16233.

(128) L. H. de Groot, A. Ilic, J. Schwarz and K. Wärnmark, *Journal of the American Chemical Society*, 2023, **145**, 9369–9388.

(129) I. M. Dixon, F. Alary, M. Boggio-Pasqua and J.-L. Heully, *Dalton Transactions*, 2015, **44**, 13498–13503.

(130) L. Herman, S. Ghosh, E. Defrancq and A. K.-D. Mesmaekera, *Journal of Physical Organic Chemistry*, 2008, **21**, 670–681.

(131) C. Mari, V. Pierroz, S. Ferrari and G. Gasser, *Chemical science*, 2015, **6**, 2660–2686.

(132) J. D. Knoll, B. A. Albani and C. Turro, *Accounts of chemical research*, 2015, **48**, 2280–2287.

(133) J. K. McCusker, K. N. Walda, R. C. Dunn, J. D. Simon, D. Magde and D. N. Hendrickson, *Journal of the American Chemical Society*, 1993, **115**, 298–307.

(134) C. de Graaf and C. Sousa, *Chemistry–A European Journal*, 2010, **16**, 4550–4556.

(135) P. Gütlich and H. A. Goodwin, *Spin Crossover in Transition Metal Compounds I*, 2004, 1–47.

(136) M. Chergui, *Accounts of chemical research*, 2015, **48**, 801–808.

(137) C. Consani, M. Prémont-Schwarz, A. ElNahhas, C. Bressler, F. van Mourik, A. Cannizzo and M. Chergui, *Angewandte Chemie International Edition*, 2009, **48**, 7184–7187.

(138) G. Auböck and M. Chergui, *Nature chemistry*, 2015, **7**, 629–633.

(139) M. Oppermann, F. Zinna, J. Lacour and M. Chergui, *Nature Chemistry*, 2022, **14**, 739–745.

(140) W. Gawelda, V.-T. Pham, M. Benfatto, Y. Zaushitsyn, M. Kaiser, D. Grolimund, S. L. Johnson, R. Abela, A. Hauser, C. Bressler et al., *Physical review letters*, 2007, **98**, 057401.

(141) A. Tarnovsky, W. Gawelda, M. Johnson, C. Bressler and M. Chergui, *The Journal of Physical Chemistry B*, 2006, **110**, 26497–26505.

(142) N. H. Damrauer, G. Cerullo, A. Yeh, T. R. Boussie, C. V. Shank and J. K. McCusker, *Science*, 1997, **275**, 54–57.

(143) A. T. Yeh, C. V. Shank and J. K. McCusker, *Science*, 2000, **289**, 935–938.

(144) A. Juris, V. Balzani, F. Barigelletti, S. Campagna, P. l. Belser and A. v. von Zelewsky, *Coordination Chemistry Reviews*, 1988, **84**, 85–277.

(145) A. Juris, V. Balzani, P. Belser and A. von Zelewsky, *Helvetica Chimica Acta*, 1981, **64**, 2175–2182.

(146) J. K. McCusker, *Science*, 2019, **363**, 484–488.

(147) J. R. Winkler, C. Creutz and N. Sutin, *Journal of the American Chemical Society*, 1987, **109**, 3470–3471.

(148) Y. Liu, T. Harlang, S. E. Canton, P. Chábera, K. Suárez-Alcántara, A. Fleckhaus, D. A. Vithanage, E. Göransson, A. Corani, R. Lomoth et al., *Chemical communications*, 2013, **49**, 6412–6414.

(149) B. C. Paulus, K. C. Nielsen, C. R. Tichnell, M. C. Carey and J. K. McCusker, *Journal of the American Chemical Society*, 2021, **143**, 8086–8098.

(150) B. C. Paulus, S. L. Adelman, L. L. Jamula and J. K. McCusker, *Nature*, 2020, **582**, 214–218.

(151) A. Kirk, *Coordination Chemistry Reviews*, 1981, **39**, 225–263.

(152) L. S. Forster, *Chemical Reviews*, 1990, **90**, 331–353.

(153) A. D. Kirk, *Chemical reviews*, 1999, **99**, 1607–1640.

(154) E. A. Juban and J. K. McCusker, *Journal of the American Chemical Society*, 2005, **127**, 6857–6865.

(155) E. M. Maçôas, R. Kananavicius, P. Myllyperkiö, M. Pettersson and H. Kunttu, *Journal of the American Chemical Society*, 2007, **129**, 8934–8935.

(156) E. M. Maçôas, R. Kananavicius, P. Myllyperkiö, M. Pettersson and H. Kunttu, *The Journal of Physical Chemistry A*, 2007, **111**, 2054–2061.

(157) E. M. Maçôas, S. Mustalahti, P. Myllyperkio, H. Kunttu and M. Pettersson, *The Journal of Physical Chemistry A*, 2015, **119**, 2727–2734.

(158) J. N. Schrauben, K. L. Dillman, W. F. Beck and J. K. McCusker, *Chemical Science*, 2010, **1**, 405–410.

(159) B. C. Paulus and J. K. McCusker, *Faraday Discussions*, 2022, **237**, 274–299.

(160) L. Paul, K. Enkhbold, S. Robinson, T. T. Aye, Y. Chung, D. P. Harrison, J. A. Pollock and M. R. Norris, *Journal of Inorganic Biochemistry*, 2022, **235**, 111930.

(161) M. W. Blaskie and D. R. McMillin, *Inorganic Chemistry*, 1980, **19**, 3519–3522.

(162) D. V. Scaltrito, D. W. Thompson, J. A. O'Callaghan and G. J. Meyer, *Coordination Chemistry Reviews*, 2000, **208**, 243–266.

(163) M. Feng and M.-L. Tong, *Chemistry–A European Journal*, 2018, **24**, 7574–7594.

(164) Y. Rechkemmer, F. D. Breitgoff, M. Van Der Meer, M. Atanasov, M. Hakl, M. Orlita, P. Neugebauer, F. Neese, B. Sarkar and J. Van Slageren, *Nature communications*, 2016, **7**, 10467.

(165) F. Habib, O. R. Luca, V. Vieru, M. Shiddiq, I. Korobkov, S. I. Gorelsky, M. K. Takase, L. F. Chibotaru, S. Hill, R. H. Crabtree et al., *Angewandte Chemie International Edition*, 2013, **52**, 11290–11293.

(166) F. Kobayashi, Y. Komatsumaru, R. Akiyoshi, M. Nakamura, Y. Zhang, L. F. Lindoy and S. Hayami, *Inorganic Chemistry*, 2020, **59**, 16843–16852.

(167) Y. Suzuki, K. Takeda and K. Awaga, *Physical Review B*, 2003, **67**, 132402.

(168) P. Parois, S. A. Moggach, J. Sanchez-Benitez, K. V. Kamenev, A. R. Lennie, J. E. Warren, E. K. Brechin, S. Parsons and M. Murrie, *Chemical communications*, 2010, **46**, 1881–1883.

(169) E. Rivière, B. Donnio, E. Voirin, G. Rogez, J.-P. Kappler and J.-L. Gallani, *Journal of Materials Chemistry*, 2010, **20**, 7165–7168.

(170) B. Donnio, E. Riviere, E. Terazzi, E. Voirin, C. Aronica, G. Chastanet, D. Luneau, G. Rogez, F. Scheurer, L. Joly et al., *Solid state sciences*, 2010, **12**, 1307–1313.

(171) E. Ovchenkova, N. Bichan and T. Lomova, *Russian Journal of Physical Chemistry A*, 2022, **96**, 717–723.

(172) Y. Kim, J. R. Choi, M. Yoon, A. Furube, T. Asahi and H. Masuhara, *The Journal of Physical Chemistry B*, 2001, **105**, 8513–8518.

(173) J. Jung, K. Ohkubo, K. A. Prokop-Prigge, H. M. Neu, D. P. Goldberg and S. Fukuzumi, *Inorganic chemistry*, 2013, **52**, 13594–13604.

(174) Y. H. Kim, S. D. Jung, M. H. Lee, C. Im, Y.-H. Kim, Y. J. Jang, S. K. Kim and D. W. Cho, *The Journal of Physical Chemistry B*, 2013, **117**, 9585–9590.

(175) F. A. Schaberle, A. R. Abreu, N. P. Goncalves, G. F. Sa, M. M. Pereira and L. G. Arnaut, *Inorganic Chemistry*, 2017, **56**, 2677–2689.

(176) R. Inglis, S. M. Taylor, L. F. Jones, G. S. Papaefstathiou, S. P. Perlepes, S. Datta, S. Hill, W. Wernsdorfer and E. K. Brechin, *Dalton Transactions*, 2009, 9157–9168.

(177) R. Phelps, A. Etcheverry-Berrios, E. K. Brechin and J. O. Johansson, *Chemical Science*, 2023, **14**, 6621–6630.

(178) U. Megerle, I. Pugliesi, C. Schriever, C. F. Sailer and E. Riedle, *Applied Physics B*, 2009, **96**, 215–231.

(179) N. Bloembergen, *Frontiers in Physics: Nonlinear Optics*, W. A. Benjamin, Inc, New York, 1965, pp. 96–102.

(180) A. Dubietis, G. Tamošauskas, R. Šuminas, V. Jukna and A. Couairon, *Lithuanian Journal of Physics*, 2017, **7**, 113–157.

(181) R. Smith, J. Wahlstrand, A. Funk, R. Mirin, S. Cundiff, J. Steiner, M. Schafer, M. Kira and S. Koch, *Physical review letters*, 2010, **104**, 247401.

(182) M. Gueye, M. Manathunga, D. Agathangelou, Y. Orozco, M. Paolino, S. Fusi, S. Haacke, M. Olivucci and J. Léonard, *Nature Communications*, 2018, **9**, 313.

(183) S. Rafiq and G. D. Scholes, *The Journal of Physical Chemistry A*, 2016, **120**, 6792–6799.

(184) R. M. Van Der Veen, A. Cannizzo, F. Van Mourik, A. Vlcek Jr and M. Chergui, *Journal of the American Chemical Society*, 2011, **133**, 305–315.

(185) M. Gühr and N. Schwentner, *Physical Chemistry Chemical Physics*, 2005, **7**, 760–767.

(186) K. Barlow, J. Eng, I. Ivalo, M. Coletta, E. K. Brechin, T. J. Penfold and J. O. Johansson, *Dalton Transactions*, 2022, **51**, 10751–10757.

(187) C. Mantel, H. Chen, R. H. Crabtree, G. W. Brudvig, J. Pécaut, M.-N. Collomb and C. Duboc, *ChemPhysChem*, 2005, **6**, 541–546.

(188) C. Mantel, A. K. Hassan, J. Pécaut, A. Deronzier, M.-N. Collomb and C. Duboc-Toia, *Journal of the American Chemical Society*, 2003, **125**, 12337–12344.

(189) J. Limburg, J. S. Vrettos, R. H. Crabtree, G. W. Brudvig, J. C. de Paula, A. Hassan, A.-L. Barra, C. Duboc-Toia and M.-N. Collomb, *Inorganic chemistry*, 2001, **40**, 1698–1703.

(190) N. S. Hush and J. R. Reimers, *Chemical reviews*, 2000, **100**, 775–786.

(191) F. Juliá, *ChemCatChem*, 2022, **14**, e202200916.

(192) V. Talrose, A. N. Yermakov, A. A. Usov, A. A. Goncharova, A. N. Leskin, N. A. Messineva, N. V. Trusova and M. V. Efimkina, in P.J. Linstrom and W.G. Mallard, Gaithersburg MD, 2023.

(193) A. Rosspeintner, B. Lang and E. Vauthey, *Annual Review of Physical Chemistry*, 2013, **64**, 247–271.

(194) W. Huang, C. Li, J. Wang and L. Zhu, *Spectroscopy letters*, 1998, **31**, 1793–1809.

(195) S. Schneider, G. Brehm, C.-J. Prenzel, W. Jäger, M. Silva, H. Burrows and S. Formosinho, *Journal of Raman spectroscopy*, 1996, **27**, 163–175.

(196) J. Schroeder, V. Schiemann, P. Sharko and J. Jonas, *The Journal of Chemical Physics*, 1977, **66**, 3215–3226.

(197) T. J. Penfold, C. J. Milne and M. Chergui, *Advances in Chemical Physics*, 2013, **153**, 1–41.

(198) C. Milne, T. Penfold and M. Chergui, *Coordination Chemistry Reviews*, 2014, **277**, 44–68.

(199) M. Chergui and E. Collet, *Chemical reviews*, 2017, **117**, 11025–11065.

(200) M. Chergui, *Structural Dynamics*, 2016, **3**.

(201) F. De Groot, *Chemical Reviews*, 2001, **101**, 1779–1808.

(202) J. E. Penner-Hahn et al., *Comprehensive Coordination Chemistry II*, 2003, **2**, 159–186.

(203) J. Yano and V. K. Yachandra, *Photosynthesis research*, 2009, **102**, 241–254.

(204) M. Maiuri, M. Garavelli and G. Cerullo, *Journal of the American Chemical Society*, 2019, **142**, 3–15.

(205) K. J. Gaffney, *Chemical Science*, 2021, **12**, 8010–8025.

(206) R. M. Jay, K. Kunnus, P. Wernet and K. J. Gaffney, *Annual Review of Physical Chemistry*, 2022, **73**, 187–208.

(207) H. T. Lemke, C. Bressler, L. X. Chen, D. M. Fritz, K. J. Gaffney, A. Galler, W. Gawelda, K. Haldrup, R. W. Hartsock, H. Ihee et al., *The Journal of Physical Chemistry A*, 2013, **117**, 735–740.

(208) H. T. Lemke, K. S. Kjær, R. Hartsock, T. B. van Driel, M. Chollet, J. M. Glownia, S. Song, D. Zhu, E. Pace, S. F. Matar et al., *Nature communications*, 2017, **8**, 1–8.

(209) W. Zhang, R. Alonso-Mori, U. Bergmann, C. Bressler, M. Chollet, A. Galler, W. Gawelda, R. G. Hadt, R. W. Hartsock, T. Kroll et al., *Nature*, 2014, **509**, 345–348.

(210) H. Motz, *Journal of Applied Physics*, 1951, **22**, 527–535.

(211) H. Motz, W. Thon and R. Whitehurst, *Journal of Applied Physics*, 1953, **24**, 826–833.

(212) E. Saldin, E. Schneidmiller and M. V. Yurkov, *The physics of free electron lasers*, Springer Science & Business Media, 1999.

(213) C. Pellegrini, A. Marinelli and S. Reiche, *Reviews of Modern Physics*, 2016, **88**, 015006.

(214) L. Fletcher, H. Lee, T. Döppner, E. Galtier, B. Nagler, P. Heimann, C. Fortmann, S. LePape, T. Ma, M. Millot et al., *Nature photonics*, 2015, **9**, 274–279.

(215) B. W. McNeil and N. R. Thompson, *Nature photonics*, 2010, **4**, 814–821.

(216) K. Tono, T. Togashi, Y. Inubushi, T. Sato, T. Katayama, K. Ogawa, H. Ohashi, H. Kimura, S. Takahashi, K. Takeshita et al., *New Journal of Physics*, 2013, **15**, 083035.

(217) T. Katayama, T. Hirano, Y. Morioka, Y. Sano, T. Osaka, S. Owada, T. Togashi and M. Yabashi, *Journal of synchrotron radiation*, 2019, **26**, 333–338.

(218) T. Katayama, S. Owada, T. Togashi, K. Ogawa, P. Karvinen, I. Vartiainen, A. Eronen, C. David, T. Sato, K. Nakajima et al., *Structural Dynamics*, 2016, **3**.

(219) M. Roemelt, M. A. Beckwith, C. Duboc, M.-N. Collomb, F. Neese and S. DeBeer, *Inorganic chemistry*, 2012, **51**, 680–687.

(220) T. Yamamoto, *X-Ray Spectrometry: An International Journal*, 2008, **37**, 572–584.

(221) P. Wernet, K. Kunnus, I. Josefsson, I. Rajkovic, W. Quevedo, M. Beye, S. Schreck, S. Grübel, M. Scholz, D. Nordlund et al., *Nature*, 2015, **520**, 78–81.

(222) M. Lundberg and P. Wernet, in *Synchrotron Light Sources and Free-Electron Lasers: Accelerator Physics, Instrumentation and Science Applications*, Springer, 2020, pp. 2315–2366.

(223) T. Glaser, B. Hedman, K. O. Hodgson and E. I. Solomon, *Accounts of chemical research*, 2000, **33**, 859–868.

(224) M. L. Baker, M. W. Mara, J. J. Yan, K. O. Hodgson, B. Hedman and E. I. Solomon, *Coordination chemistry reviews*, 2017, **345**, 182–208.

(225) J. Stöhr, *Journal of Magnetism and Magnetic Materials*, 1999, **200**, 470–497.

(226) S. Parchenko, A. Frej, H. Ueda, R. Carley, L. Mercadier, N. Gerasimova, G. Mercurio, J. Schlappa, A. Yaroslavtsev, N. Agarwal, R. Gort, A. Scherz, A. Zvezdin, A. Stupakiewicz and U. Staub, *Advanced Science*, 2023, DOI: 10.1002/advs.202302550.

(227) M. W. Mara, R. G. Hadt, M. E. Reinhard, T. Kroll, H. Lim, R. W. Hartsock, R. Alonso-Mori, M. Chollet, J. M. Glownia, S. Nelson et al., *Science*, 2017, **356**, 1276–1280.

(228) K. Kunnus, M. Vacher, T. C. Harlang, K. S. Kjær, K. Haldrup, E. Biasin, T. B. van Driel, M. Pápai, P. Chabera, Y. Liu et al., *Nature communications*, 2020, **11**, 634.

(229) K. Kalyanasundaram, *Coordination Chemistry Reviews*, 1982, **46**, 159–244.

(230) B. O'regan and M. Grätzel, *nature*, 1991, **353**, 737–740.

(231) F. Heinemann, J. Karges and G. Gasser, *Accounts of chemical research*, 2017, **50**, 2727–2736.

(232) S. Monro, K. L. Colon, H. Yin, J. Roque III, P. Konda, S. Gujar, R. P. Thummel, L. Lilge, C. G. Cameron and S. A. McFarland, *Chemical reviews*, 2018, **119**, 797–828.

(233) D. M. Arias-Rotondo and J. K. McCusker, *Visible Light Photocatalysis in Organic Chemistry*, 2018, 1–24.

(234) R. Harrigan and G. Crosby, *The Journal of Chemical Physics*, 1973, **59**, 3468–3476.

(235) G. A. Crosby, *Accounts of Chemical Research*, 1975, **8**, 231–238.

(236) A. Cannizzo, F. van Mourik, W. Gawelda, G. Zgrablic, C. Bressler and M. Chergui, *Angewandte Chemie International Edition*, 2006, **45**, 3174.

(237) W. Gawelda, M. Johnson, F. M. de Groot, R. Abela, C. Bressler and M. Chergui, *Journal of the American Chemical Society*, 2006, **128**, 5001–5009.

(238) P. Müller and K. Brettel, *Photochemical & Photobiological Sciences*, 2012, **11**, 632–636.

(239) J. Van Houten and R. J. Watts, *Journal of the American Chemical Society*, 1976, **98**, 4853–4858.

(240) K. Maruszewski, D. P. Strommen and J. R. Kincaid, *Journal of the American Chemical Society*, 1993, **115**, 8345–8350.

(241) J. G. Vos and J. M. Kelly, *Dalton Transactions*, 2006, 4869–4883.

(242) B. S. Howerton, D. K. Heidary and E. C. Glazer, *Journal of the American Chemical Society*, 2012, **134**, 8324–8327.

(243) L. Conti, E. Macedi, C. Giorgi, B. Valtancoli and V. Fusi, *Coordination Chemistry Reviews*, 2022, **469**, 214656.

(244) A. Soupart, F. Alary, J.-L. Heully, P. I. Elliott and I. M. Dixon, *Inorganic Chemistry*, 2018, **57**, 3192–3196.

(245) A. Soupart, F. Alary, J.-L. Heully, P. I. Elliott and I. M. Dixon, *Coordination Chemistry Reviews*, 2020, **408**, 213184.

(246) K. Eastham, P. A. Scattergood, D. Chu, R. Z. Boota, A. Soupart, F. Alary, I. M. Dixon, C. R. Rice, S. J. Hardman and P. I. Elliott, *Inorganic Chemistry*, 2022, **61**, 19907–19924.

(247) S. J. Steinke, E. J. Piechota, L. M. Loftus and C. Turro, *Journal of the American Chemical Society*, 2022, **144**, 20177–20182.

(248) A. Hauser and C. Reber, *50 Years of Structure and Bonding–The Anniversary Volume*, 2017, 291–312.

(249) Q. Sun, S. Mosquera-Vazquez, L. M. Lawson Daku, L. Guenee, H. A. Goodwin, E. Vauthey and A. Hauser, *Journal of the American Chemical Society*, 2013, **135**, 13660–13663.

(250) Q. Sun, S. Mosquera-Vazquez, Y. Suffren, J. Hankache, N. Amstutz, L. M. L. Daku, E. Vauthey and A. Hauser, *Coordination Chemistry Reviews*, 2015, **282**, 87–99.

(251) V. V. Rostovtsev, L. G. Green, V. V. Fokin and K. B. Sharpless, *Angewandte Chemie*, 2002, **114**, 2708–2711.

(252) P. Chábera, Y. Liu, O. Prakash, E. Thyrhaug, A. E. Nahhas, A. Honarfar, S. Essén, L. A. Fredin, T. C. Harlang, K. S. Kjær et al., *Nature*, 2017, **543**, 695–699.

(253) R. Z. Boota, S. J. Hardman, G. P. Ashton, C. R. Rice, P. A. Scattergood and P. I. Elliott, *Inorganic Chemistry*, 2021, **60**, 15768–15781.

(254) C. E. Welby, S. Grkinic, A. Zahid, B. S. Uppal, E. A. Gibson, C. R. Rice and P. I. Elliott, *Dalton Transactions*, 2012, **41**, 7637–7646.

(255) J. J. Snellenburg, S. Laptenok, R. Seger, K. M. Mullen and I. H. van Stokkum, *Journal of Statistical Software*, 2012, **49**, 1–22.

(256) J. S. Beckwith, C. A. Rumble and E. Vauthey, *International Reviews in Physical Chemistry*, 2020, **39**, 135–216.

(257) R. Monni, G. Capano, G. Auböck, H. B. Gray, A. Vlček, I. Tavernelli and M. Chergui, *Proceedings of the National Academy of Sciences*, 2018, **115**, E6396–E6403.

(258) J. D. Gaynor, J. Sandwisch and M. Khalil, *Nature Communications*, 2019, **10**, 5621.

(259) S. R. Rather, N. P. Weingartz, S. Kromer, F. N. Castellano and L. X. Chen, *Nature*, 2023, **620**, 776–781.

(260) J. Kim, D.-g. Kang, S. K. Kim and T. Joo, *Physical Chemistry Chemical Physics*, 2020, **22**, 25811–25818.

(261) S. Francis, C. R. Rice, P. A. Scattergood and P. I. Elliott, *Dalton Transactions*, 2022, **51**, 13692–13702.

(262) P. Scheid, Q. Remy, S. Lebègue, G. Malinowski and S. Mangin, *Journal of Magnetism and Magnetic Materials*, 2022, **560**, 169596.

(263) J.-Y. Bigot, L. Guidoni, E. Beaurepaire and P. N. Saeta, *Physical review letters*, 2004, **93**, 077401.

(264) F. Strieth-Kalthoff and F. Glorius, *Chem*, 2020, **6**, 1888–1903.

(265) J.-L. Brédas, J. E. Norton, J. Cornil and V. Coropceanu, *Accounts of chemical research*, 2009, **42**, 1691–1699.

(266) Z. Yang, Z. Mao, Z. Xie, Y. Zhang, S. Liu, J. Zhao, J. Xu, Z. Chi and M. P. Aldred, *Chemical Society Reviews*, 2017, **46**, 915–1016.

(267) H.-Z. Yu, J. S. Baskin and A. H. Zewail, *The Journal of Physical Chemistry A*, 2002, **106**, 9845–9854.

(268) B. Abraham, J. Nieto-Pescador and L. Gundlach, *The journal of physical chemistry letters*, 2016, **7**, 3151–3156.

(269) E. Sutcliffe, Ph.D. Thesis, University of Edinburgh, 2023.

(270) P. Stephens, *Annual Review of Physical Chemistry*, 1974, **25**, 201–232.

(271) P. W. Atkins and R. S. Friedman, *Molecular quantum mechanics*, Oxford university press, 4th edn., 2011, pp. 248–251.

(272) F. Leeper, *Natural product reports*, 1989, **6**, 171–203.

(273) D. Mauzerall, *Philosophical Transactions of the Royal Society of London. B, Biological Sciences*, 1976, **273**, 287–294.

(274) M. Ethirajan, Y. Chen, P. Joshi and R. K. Pandey, *Chemical Society Reviews*, 2011, **40**, 340–362.

(275) Ö. Birel, S. Nadeem and H. Duman, *Journal of fluorescence*, 2017, **27**, 1075–1085.

(276) L. Jin, S. Lv, Y. Miao, D. Liu and F. Song, *ChemCatChem*, 2021, **13**, 140–152.

(277) M. Gouterman, *Journal of Molecular Spectroscopy*, 1961, **6**, 138–163.

(278) M. Gouterman, G. H. Wagnière and L. C. Snyder, *Journal of Molecular Spectroscopy*, 1963, **11**, 108–127.

(279) J. Mack, M. J. Stillman and N. Kobayashi, *Coordination chemistry reviews*, 2007, **251**, 429–453.

(280) D. B. Moravec, B. M. Lovaasen and M. D. Hopkins, *Journal of Photochemistry and Photobiology A: Chemistry*, 2013, **254**, 20–24.

(281) V. A. Walters, J. C. de Paula, B. Jackson, C. Nutaitis, K. Hall, J. Lind, K. Cardozo, K. Chandran, D. Raible and C. M. Phillips, *The Journal of Physical Chemistry*, 1995, **99**, 1166–1171.

(282) N. Kobayashi and K. Nakai, *Chemical communications*, 2007, 4077–4092.

(283) J. P. Collman, F. Basolo, E. Bunnenberg, T. J. Collins, J. H. Dawson, P. E. Ellis Jr, M. L. Marrocco, A. Moscowitz, J. L. Sessler and T. Szymanski, *Journal of the American Chemical Society*, 1981, **103**, 5636–5648.